ENERGY TRANSFER IN (BIO)MOLECULAR SYSTEMS

Promotiecommissie

promotor:	prof. dr. J. L. Herek
assistent promotor:	dr. W. R. Browne
overige leden:	prof. dr. M. Bonn
	prof. dr. W. L. Vos
	prof. dr. D. N. Reinhoudt
	prof. dr. E. Riedle
	dr. M. S. Pchenitchnikov
	dr. B. Brüggemann

The work described in this thesis was performed at the FOM-*Institute for Atomic and Molecular Physics* (AMOLF), Science Park 104, 1098 XG Amsterdam, The Netherlands. The work is part of the research programme of the *Stichting Fundamenteel Onderzoek der Materie* (FOM), which is financially supported by the *Nederlandse Organisatie voor Wetenschappelijk Onderzoek* (NWO).

ISBN 978-90-77209-40-0

ENERGY TRANSFER IN (BIO)MOLECULAR SYSTEMS

PROEFSCHRIFT

ter verkrijging van
de graad van doctor aan de Universiteit Twente,
op gezag van de rector magnificus,
prof. dr. H. Brinksma,
volgens besluit van het College voor Promoties
in het openbaar te verdedigen
op vrijdag 12 maart 2010 om 13.15 uur

door

Maaike Theresia Wilhelmina Milder

geboren op 2 maart 1982

te Nijmegen

Dit proefschrift is goedgekeurd door:

prof. dr. J. L. Herek

'Sail away from the safe harbor. Catch the trade winds in your sails. Explore. Dream. Discover'

–Mark Twain–

Publications covered in this thesis

M. T. W. Milder, B. Brüggemann, R. Van Grondelle and J. L. Herek.
Revisiting the optical properties of FMO. *Accepted for publication in Photosynthesis Research.*

M. T. W. Milder, J. Areephong, B. L. Feringa, W. R. Browne and J. L. Herek.
Photoswitchable molecular wires: From a sexithiophene to a dithienylethene and back *Chem. Phys. Lett. 479*, 137–139 (2009).

M. T. W. Milder, J. L. Herek, J. Areephong, B. L. Feringa and W. R. Browne.
Tunable aggregation and luminescence of bis(diarylethene)sexithiophenes *J. Phys. Chem. A 113*, 7717–7724 (2009).

J. Areephong, J. H. Hurenkamp, M. T. W. Milder, A. Meetsma, J. L. Herek, W. R. Browne and B. L. Feringa.
Photoswitchable sexithiophene-based molecular wires *Org. Lett. 11*, 721–724 (2009).

Other publications

J. J. H. Pijpers, M. T. W. Milder, C. Delerue and M. Bonn
(Multi)exciton dynamics and exciton polarizability in colloidal InAs quantum dots. *Submitted*

P. Van Der Walle, M. T. W. Milder, L. Kuipers and J. L. Herek.
Revisiting the optical properties of FMO. *PNAS 106*, 7714–7717 (2009).

J. J. H. Pijpers, E. Hendry, M. T. W. Milder, F. Fanciulli, J. Savolainen, J. H. Herek, D. Vanmaekelbergh, S. Ruhman, D. Mocatta, D. Oron, A. Aharoni, U. Banin, M. Bonn.
Carrier multiplication and its reduction by photodoping in colloidal InAs quantum dots. *J. Phys. Chem. C 111*, 4146–4152 (2007).

D. Cringus, J. Lindner, M. T. W. Milder, M. S. Pshenichnikov, P. Vohringer, D. A. Wiersma.
Femtosecond water dynamics in reverse-micellar nanodroplets. *Chem. Phys. Lett. 408*, 162–168 (2005).

Contents

1 Introduction

Energy transfer is one of the most important processes on earth. It drives photosynthesis, turning solar energy into carbon based energy forms such as sugars. Organisms that do not engage in photosynthesis rely on the products of the organisms that do. The photosynthetic process can be subdivided into two initial steps [1, 2]. First the energy from the sunlight is harvested by the antenna complex; proteins containing multiple chromophores, that absorb light. The energy that is absorbed is transferred between chromophores until it reaches the reaction center. There the second stage of photosynthesis starts with electron transfer reactions that eventually lead to the fixation of carbon into larger sugars. For efficient photosynthesis it is necessary that the energy, absorbed initially, is transferred swiftly to the reaction center. The antenna complexes in general consist of several types of chromophores, often chlorophylls and carotenoids [3]. To ensure that the energy stored in the excited states of the chromophores is guided efficiently through the photosynthetic complex, the chromophores are held in specific positions with respect to each other, enforced by a protein envelop. They are positioned in such a way that the excitation of high energy chromophores will flow to low energy ones in the direction of the reaction center, acting as a funnel both in space and in energy.

Inspired in part by the well-established processes in photosynthesis, energy transfer also plays an important role in a new and upcoming line of research. Molecular electronic devices are used in a bottom up approach to overcome the size limits of classical electronics [4]. Just as in macroscopic devices, an energy source is needed to make the microscopic versions work [5]. However, it is not trivial to connect these molecular devices to a power grid. A solution is found by introducing energy into the system by the absorption of light. Energy transfer processes then ensure that the energy gets to all relevant elements in the system. In analogy to the photosynthetic antenna complexes, in synthetic systems a sophisticated scheme to allow for rapid energy transfer is required. Units that absorb light energy are in general also efficient in losing it, either by emitting a photon or releasing it as heat. To beat these processes, energy transfer, either between molecules or within an extended molecule, has to be faster. Intermolecularly, energy transfer can only happen rapidly when the molecules are in close proximity to each other as the process has a strong distance dependence. Chromophores that self-assemble could provide the necessary structure for a continuous network, over which energy can be effectively transferred. A more direct approach is to connect the chromophores to each other using linkers to control the distance between the units. However, a limitation is imposed by the size of the molecules that can be realized synthetically.

This thesis presents the results of optical experiments of energy transfer in two types of systems. The first is the Fenna-Matthews-Olson (FMO) photosynthetic antenna complex from the green sulfur bacterium *Chlorobium tepidum* [6]. In contrast to most photosynthetic organisms, this complex absorbs light in the deep red part of the absorption spectrum, around 800 nm. This means that these bacteria created a niche where they can thrive without competition from other (photosynthetic) organisms. Secondly, energy transfer in functional molecular materials is addressed. The different types of materials studied have a common element: a dithienylethene molecular switch [7]. This is a molecule that, upon irradiation with light, can make and break a covalent bond. It could serve as a molecular analogue of an electrical switch that is able to turn on and off a specific property in the system, similar to switching on and off an electrical device.

The organization of this thesis is as follows: chapter 2 addresses the experimental techniques, steady-state and time-resolved spectroscopy, used to elucidate the energy transfer processes, briefly explaining their theoretical background. Subsequently, chapter 3 gives an overview of the theory behind the different types of energy transfer processes, with focus on a description of Förster energy transfer theory. An overview of the optical properties of the FMO complex is provided in chapter 4. This chapter gives the background for the experiments on the FMO complex in chapter 5, where energy transfer under high excitation conditions is studied. Additionally, attempts to control the natural pathway of energy transfer using a closed-loop optimization scheme are described. Chapter 6 provides the introduction to the second part of this thesis, where energy transfer in molecular materials containing dithienylethene molecular switches is studied. In chapter 7, the study of a switchable molecular wire is described. Chapter 8 will refer to the design principles of energy transfer complexes. Finally, in chapter 9 another level of control is imposed on energy transfer by attaching two different chromophores to a photoswitchable unit.

2 Experimental

The first part of this chapter describes the basic interactions between light and matter, specified for the case of electronic spectroscopy. A general introduction is given after which a more detailed expression of optical transition rates is developed. This is followed by an account on nonlinear spectroscopy, in particular on transient absorption spectroscopy. In the second part of this chapter experimental details and setups of the different types of electronic spectroscopy employed are outlined.

2.1 Interaction between light and matter

2.1.1 Response of the system

The interaction between light and matter determines how and why we see. As a simple example, we see that the trees are green because the leaves do not absorb the green photons present in the sunlight, which are instead reflected and/or transmitted and get a chance to reach our eyes. There are several primary interactions between light and matter. Figure 2.1 schematically shows these interactions. An incoming beam of light will be partially reflected by the surface of the material; for glass this is about 4% in the visible region of the spectrum. Furthermore, light can be refracted since the speed of light in air/vacuum and in the material is not necessarily the same. This refraction is often wavelength dependent which gives rise to interesting optical properties as will be described in section 2.5.2. Refraction in general does not change the intensity of the light, however the intensity is affected by absorption by the medium. The transmission through the material is determined by the absorption and the reflection at the entrance and exit of the material. Losses due to scattering are in general to be avoided in electronic (absorption) spectroscopy.

There exists an empirical relation between the length of the material and the

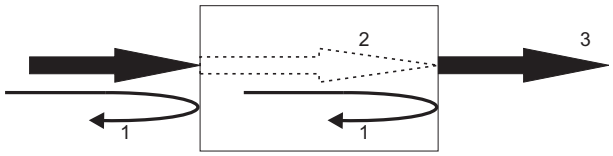

Figure 2.1. The basic interactions between light and matter. An incoming beam can be reflected (1), absorbed and refracted (2) and the remainder transmitted (3). For the sake of simplicity scattering and excited state processes, such as emission, have been omitted.

absorption, α, within. This depends, in liquids and gasses, on the concentration of the individual species that absorb the light, on the molar absorptivity, also known as the molar extinction coefficient, often represented by ϵ in $M^{-1}cm^{-1}$, and on the pathlength of the cell (l). The well known expression for the absorption in a medium is given by the Lambert-Beer law.

$$\begin{aligned} I &= I_0 10^{-\epsilon c l} \\ \alpha &= log\left(\frac{I_0}{I}\right) \\ \alpha &= \epsilon c l \end{aligned} \tag{2.1}$$

In this expression, c represents the concentration and l the length of the absorbing material. In the remainder of this thesis the absorption will often be denoted as optical density (OD), where α and OD are interchangeable.

2.1.2 RESPONSE OF THE INDIVIDUAL COMPONENTS

In a semiclassical treatment of the description of the interaction between light and matter, atoms and molecules are described as harmonic oscillators, while the light is treated classically. In electronic spectroscopy, which uses wavelengths in the ultraviolet and visible region of the spectrum, these oscillators mainly consist of electrons bound to the atoms within molecules. These bound pairs of electrons and nuclei form electric dipoles that are forced to oscillate under the influence of a resonant external electric field. A schematic representation of this oscillation is given in figure 2.2. Due to the interaction between nucleus and electron, a perturbation of the equilibrium distance between the two will lead to a restoring force, in a classical picture represented by a spring. The large difference in mass between nucleus and electron implies that during oscillations only the electron moves while the nucleus remains stationary: the Born-Oppenheimer approximation. The restoration of the equilibrium position of the electrons occurs in an oscillatory manner, where the oscillations are damped in time. These oscillations induce a microscopic, time dependent, polarization, $p(t)$, as represented in figure 2.2 which is proportional to the deviation from the equilibrium position, $x(t)$, according to equation 2.2, where e is the charge of an electron.

$$p(t) = -ex(t) \tag{2.2}$$

When light at a frequency ω interacts with matter, this can drive the oscillations of the electrons, when the frequency of the light coincides with the natural oscillatory frequency of the atom. In this case the atom can absorb the light and a quantized transition from the ground to an excited state of the atom occurs. The displacement x from equilibrium of an electron, after interaction with an electric field $E(t)$, can be expressed in terms of an equation of motion as follows [8].

$$m_0\frac{d^2x}{dt^2} + m_0\gamma\frac{dx}{dt} + m_0\omega_0^2 x = -eE(t) \tag{2.3}$$

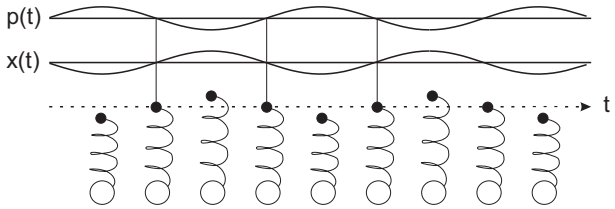

FIGURE 2.2. Schematic representation of the oscillations in a dipole, in the form of a harmonic oscillator. The electron (small black ball) has a negative charge and is bound to the positively charged heavy nucleus (big white balls). The nucleus remains stationary while the electron moves back and forth around the equilibrium position as if attached by a spring. When the position of the electrons, $x(t)$, deviates from the equilibrium position this induces a polarization $p(t)$. Figure adapted from reference [8].

In this expression the mass of the electron is represented by m_0, the dampening rate by γ and the charge of the electron by e. The three terms on the left side describe the acceleration, damping and restoring force respectively. On the right side the oscillating electric field $E(t)$, driving the motion, is described. The electric field used in this derivation takes the form of

$$E(t) = E_0 e^{-i\omega t} + c.c. \tag{2.4}$$

Where E_0 is the amplitude of the electric field, ω the frequency and $c.c.$ denotes the complex conjugate terms. A solution to equation 2.3 is given in the form of equation 2.5.

$$x(t) = \frac{-e}{m_0} \frac{E_0 e^{-i\omega t}}{\omega_0^2 - \omega^2 - i\omega\gamma} + c.c. \tag{2.5}$$

If the oscillations are driven with an electric field that has a frequency ω less than the resonance frequency ω_0, the oscillations can follow the driving force and $x(t)$ and $E(t)$ are in phase. However, when the frequency of the driving field approaches the resonance frequency, $\omega \geq \omega_0$, the oscillations are 180° out of phase with the electric field. Combining the last result with equation 2.2 also implies that the induced dipoles and the generated field are out of phase with the driving electric field.

The macroscopic polarization $P(t)$ induced by the oscillating driving field in N polarizable atoms is a sum over the individual contributions of the microscopic polarization as described in equation 2.2, leading to the following expression

$$P(t) = -\sum_N p_i(t) \tag{2.6}$$

Substituting equation 2.5 into equation 2.6 results in the following expression for the macroscopic polarization $P(t)$.

$$P(t) = \frac{Ne^2}{m_0} \frac{1}{\omega_0^2 - \omega^2 - i\omega\gamma} E(t) \tag{2.7}$$

When the frequency ω is far from the resonance frequency of the atom ω_0, the induced polarization P will be small.

In a quantum mechanical description of the interaction between light and matter, first order time-dependent perturbation theory can be employed to calculate transition probabilities and rates in spectroscopy. The Hamiltonian for a perturbed system can be described using a combination of the unperturbed, time-independent Hamiltonian $\hat{H}_0$ and a time-dependent perturbation $\hat{H}_1(t)$ [9].

$$\hat{H} = \hat{H}_0 + \hat{H}_1(t) \tag{2.8}$$

The state of such a perturbed system $\Psi(t)$ can then be expressed as a linear combination of time-dependent unperturbed states.

$$\Psi(t) = \sum a_n(t)\Psi_n(t) \tag{2.9}$$

For a solution of this equation it is required to know how the linear combination in equation 2.9 evolves in time, meaning that all the coefficients a_n must be known; this proves to be difficult already in a two level system. To simplify matters, two approximations are used: the perturbation acts only once and the perturbation is weak and short, so that all coefficients remain close to their initial value. When the system is in the initial state $|i\rangle$ at t_0, all coefficients a_n except for a_i are close to zero. The coefficient a_f of the final state is then given by substitution of Ψ into the Schrödinger equation and results in

$$a_f(t) \approx \frac{1}{i\hbar}\int_0^t H_{fi}(t)e^{i\omega_{fi}t}dt \tag{2.10}$$

Using the relation that $\hat{H}_{fi}(t)$ equals $\hbar\hat{V}(t)$, where $\hat{V} = -\hat{\mu}E(t)$ is the transition dipole operator multiplied by the field, and assuming an oscillatory perturbation such as a light wave with

$$\hat{V} = V\left(e^{i\omega t} + e^{-i\omega t}\right), \tag{2.11}$$

equation 2.10 rearranges into the following expression.

$$a_f(t) = \frac{\hat{V}}{i}\int_0^t \left(e^{i\omega t} + e^{-i\omega t}\right)e^{i\omega_{fi}t}dt \tag{2.12}$$

$$a_f(t) = \frac{\hat{V}}{i}\left(\frac{e^{i(\omega_{fi}t+\omega t)}-1}{i\left(\omega_{fi}+\omega\right)} + \frac{e^{i(\omega_{fi}t-\omega t)}-1}{i\left(\omega_{fi}-\omega\right)}\right) \tag{2.13}$$

The first term in equation 2.13 can in general be neglected because it is much smaller than the second term, especially when the frequency of the driving field, the perturbation V, approaches a resonance at $\omega_{fi} \approx \omega$. The probability, P, of finding the system in the final, excited, state is obtained by the modulus square of the transition coefficient a_f.

$$P_f(t) = \frac{4\left|\hat{V}\right|^2}{\left(\omega_{fi}-\omega\right)^2}sin^2\left(\omega_{fi}-\omega\right)t \tag{2.14}$$

Close to a resonance where ω approaches ω_{fi}, the expression for the transition probability can be approximated by

$$P_f(t) = \left|\hat{V}\right|^2 t^2. \tag{2.15}$$

This expression holds in the limit when $\omega \to \omega_{fi}$. Following first order perturbation theory, equation 2.15 is valid when $|V_{fi}|^2 t^2 \ll 1$.

The transition rate, W, for a transition from the initial state i to the final state f can be expressed as the rate of change of the probability of being in an unoccupied state.

$$W = \frac{dP}{dt} \tag{2.16}$$

Often this rate is expressed, using equation 2.14, in a more well known form as Fermi's golden rule of transitions.

$$W = \frac{2\pi}{\hbar}\left|\hat{V}\right|^2 (\delta(\omega_{fi} - \omega) + \delta(\omega_{fi} + \omega)) \tag{2.17}$$

This expression, containing the Dirac delta functions δ, implies that only near resonances the transition rate will have a considerable value. A connection to the well known Lambert-Beer law can be made by the molecular cross section σ. Since this value is often represented in the form of

$$\sigma I = W \tag{2.18}$$

where I is the intensity of the light and W is the rate of the transition [10]. Using the relation for W in equation 2.17 where $\hat{V}$ is replaced by $-\hat{\mu}_{fi}E(t)$ and the intensity by $I = (nc/2\pi)|E|^2$, where n is the refractive index and c the speed of light, the cross section at a resonance is given by the following expression

$$\sigma = \frac{4\pi^2}{nc\hbar^2}\left|\hat{\mu}_{fi}\right|^2. \tag{2.19}$$

2.2 Electronic transitions

2.2.1 Absorption

Electronic optical transitions occur at such a speed that the nuclei are unable to follow the motion of the electrons and are assumed to remain stationary during the transition. This simplification, referred to as the Born-Oppenheimer approximation, results in the description of optical transitions based on the motion of electrons only. However, once a transition has occurred, the nuclei start to alter their vibrational motion to adapt to the new excited state electron density, what leads to vibronic transitions. To keep the change in the nuclear coordinates during a transition to a minimum, transitions occur to the vibrational level in the excited state which wavefunction most resembles that of the vibrational level of the ground state, the so-called Franck-Condon approximation. Such a transition is called a vertical transition and a schematic view is

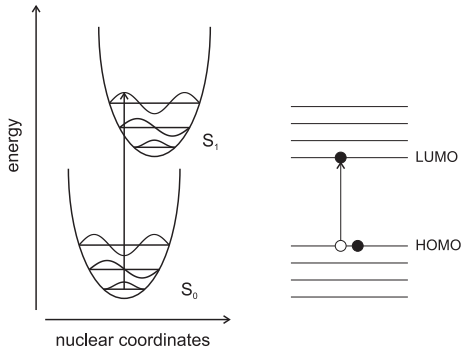

FIGURE 2.3. [Left] Schematic representation of a vertical vibronic transition in the Franck-Condon approximation. [Right] Optical transition to the first excited state from the highest occupied molecular orbital (HOMO) to the lowest unoccupied molecular orbital (LUMO).

presented in figure 2.3. The overlap between the vibrational wavefunctions is then a crucial factor in the expression of the transition dipole moment $\hat{\mu}$ between the ground and excited states.

$$\langle \epsilon_f v_f \left| \hat{\mu} \right| \epsilon_i v_i \rangle = \hat{\mu}_{\epsilon_f \epsilon_i} \int \psi^*_{v_f}(r) \psi_{v_i}(r) d^3 r \tag{2.20}$$

where $|\epsilon_i \nu_i\rangle$ and $|\epsilon_f \nu_f\rangle$ are the vibronic ground and excited state. The term $\hat{\mu}_{\epsilon_f \epsilon_i}$ in equation 2.20 is a constant since the nuclear coordinates r are unchanged for the electrons upon the transition to the excited state. The term $\int \psi^*_{v_f}(r) \psi_{v_i}(r)$ represents the overlap integral between the vibrational states in the electronic ground and excited state respectively. The intensity of the transition is proportional to the square of the transition dipole moment and hence to the square of the overlap integral in equation 2.20, that is commonly known as the Franck-Condon factor of a transition. In a potential energy curve there will be several vibrational states that give rise to substantial Franck-Condon factors. Transitions will occur to all of them resulting in a vibrational progression in the optical spectra.

A classical picture of absorption is given in figure 2.3. After an optical excitation in the visible regime one of the valence electrons of an atom is promoted from the highest occupied molecular orbital (HOMO) across an energy gap to the lowest unoccupied molecular orbital (LUMO), leaving behind a so-called hole in the HOMO.

2.2.2 EMISSION

After the perturbation by an external electromagnetic field is turned off, the oscillations of the induced transition dipoles will be damped while returning to their ground state. One of the radiative phenomena that is characteristic of this process is the emission of light by a system containing a collection of dipoles.

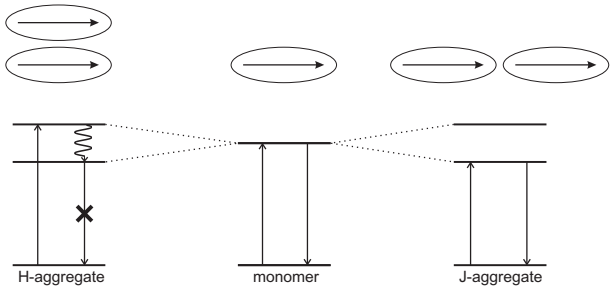

FIGURE 2.4. Splitting of the excited energy levels in molecular aggregates depending on their relative orientation. The straight arrows pointing up and downwards represent absorption and emission respectively. Decay to the lowest excited state is represented by the oscillatory arrow.

This is referred to as fluorescence by the material. In principle, emission should occur at the same frequency as the absorbed light, i.e. the resonant frequency driving the oscillations of the dipoles. However, as seen in the previous section, absorption of photons can populate many vibrational levels in the excited state, while emission in general only occurs from the lowest vibrational level in the excited state according to Kasha's rule [11]. Energy is dissipated into the surroundings while the system decays to the lowest vibrational level which results in red shift of the emission compared to the absorption. The difference between the maxima in absorption and emission is called the Stokes shift, generally given in units of cm^{-1}. Similar to absorption, emission also occurs following the Franck-Condon principle. Therefore, the emission spectra also show vibrational progression, however in this case arising from the vibrational modes of the ground state.

There are exceptions to Kasha's rule, when emission does not occur from the lowest vibrational level. In the case of aggregate formation, the molecules are sufficiently close together to generate interactions between them. These interactions cause splitting of the lowest excited state, the so-called Davydov splitting. Figure 2.4 shows the orientation of the dipoles between two interacting molecules and its effect on the excited state. In J-aggregates the dipoles are oriented in-line, resulting in a low-lying, highly fluorescent, excited state. In contrast, in H-aggregates, the dipoles have a parallel orientation. This leads to a splitting of the energy levels where the highest level carries the oscillator strength, transitions to and from the lowest level are optically forbidden. Relaxation to the lowest excited level can occur, however from thereon the decay to the ground state will occur mainly non-radiatively. In general H-aggregates show little or no fluorescence compared to their monomeric counterparts.

2.2.3 DECAY OF EXCITED STATES

Emission in the form of fluorescence is only one of the physical processes that can take place after optical transitions to the excited state. Figure 2.5 gives

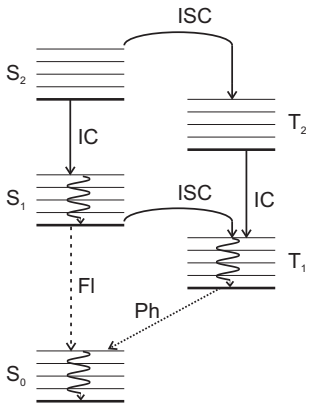

FIGURE 2.5. Different radiative and non-radiative decay pathways of exited states. Non-radiative decay associated with internal conversion (IC) is represented by the straight lines. The radiative pathways fluorescence (Fl) and phosphorescence (Ph) are labeled with the dashed and dotted straight lines respectively. The transition from the singlet to a triplet state, intersystem crossing (ISC), is labeled with a curved arrow. The oscillatory arrow represents vibrational cooling within the electronic excited and ground states.

a schematic representation of the different processes that can occur. Besides decay via direct emission of light, a second radiative decay pathway can exist in molecules. Intersystem crossing (ISC) from the initially excited singlet to a triplet state can occur. This process plays a role especially in molecules with heavy atoms, due to which the mixing of the singlet and triplet states is accommodated. The transition from the excited triplet state back to the ground state is only weakly allowed. The emission of light upon this decay is referred to as phosphorescence and is much longer lived than fluorescence. Both emission and phosphorescence are radiative decay pathways, nevertheless an important part of the decay of excited states happens non-radiatively. In this case, the excitation energy within a molecule is dissipated in the form of heat, usually by coupling to the low-frequency vibrations, i.e. phonon modes, in the surrounding molecules. As an example in section 2.2.2 H-aggregates were addressed. Due to the absence of an allowed optical transition from the excited to the ground state, energy is dissipated in the form of heat. An interesting aspect of excited states are photo-induced reactions. These are reactions, often involving structural changes, that use light as an energy source. Two typical examples are cycloaddition of alkenes and electrocyclization reactions. The latter will be extensively addressed in chapter 6.

2.3 NONLINEAR SPECTROSCOPY - TRANSIENT ABSORPTION

So far, in the description of electronic transitions we have assumed a linear relation between the electric field E and the induced polarization P. However, this is not necessarily the case as the dependence of the polarization on the incoming electric field can be expanded in a power series leading to the following expression [8]:

$$P \propto \chi_1 E + \chi_2 E^2 + \chi_3 E^3 + ... + \chi_n E^n \tag{2.21}$$

where χ_i is the susceptibility, a material property, which has linear (χ_1) and higher order terms ($\chi_2 ... \chi_n$). When the electric field strength of the incoming light is sufficiently high, as may occur in laser beams, the higher order terms of the susceptibility in equation 2.21 can no longer be neglected. Several types of nonlinear spectroscopy are based on these higher order interactions. In centro-symmetric media such as liquids, all even order responses are zero due to symmetry. Hence, the third order polarization is the lowest nonlinear polarization order that can be observed in liquids and is used in several types of nonlinear spectroscopy.

Transient absorption (TA) spectroscopy, also known as pump-probe spectroscopy, is one type of third order nonlinear spectroscopy, making use of the third order response of the polarization. It probes the time-dependent population difference between the ground and excited state. A strong pump pulse populates the excited state after which a much weaker probe pulse is applied that can be delayed in time. The transient signal is detected as the ratio between the probe intensity $\Delta OD = -log(I_{on}/I_{off})$ in the presence and absence of the pump. Figure 2.6 shows a schematic representation of the effect of the probe in a three level system. Delaying the probe in time gives information about the decay of the population to the ground state and hence the time-dependent changes in the ground and excited state spectra. The pump pulse excites part of the population of the ground state to the first excited state, leaving a 'hole' in the ground state. This makes the sample more transparent for the incoming probe pulse at the same frequency at which the pump is absorbed, i.e. bleaching the ground state (B), resulting in a higher transmission. Stimulated emission (SE), induced by the probe, from the first excited to the ground state also increases the intensity of the probe. The added contribution of these two processes appears as a negative signal in the transient spectra, because ΔOD is defined to be negative in the case of increased probe intensity induced by the pump pulse. Besides bleaching of the ground state and stimulated emission the probe can also excite the population from the first excited state to higher states, so-called induced absorption or excited state absorption (ESA). This will reduce the transmission of the probe, resulting in a positive signal in the transient spectra. The transition to the first and second excited state are generally spectrally shifted, because when the electrons are considered as particles in a box, the higher excited states are more closely spaced in energy. Figure 2.6 shows a schematic example of a transient spectrum. Transient absorption

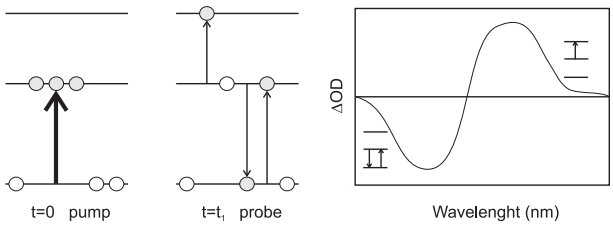

FIGURE 2.6. Effect of pump and probe on the populations of the energy levels. The pump, represented by the thick arrow, excites the population to the first excited state at $t = 0$. Subsequently the weaker probe, thin arrows and delayed to t_1, interacts in different ways with the sample. The picture on the right shows an example of a frequency resolved transient spectra.

spectroscopy can be described as a 4-wave mixing technique. This is intuitively not easy to understand, but the signal (fourth wave) is generated by a double interaction with the pump field and a single interaction with the probe field. The signal is characterized by $\omega_s = \omega_{pump} - \omega_{pump} + \omega_{probe}$ and travels in the direction of the probe according to $\overrightarrow{k_s} = \overrightarrow{k}_{pump} - \overrightarrow{k}_{pump} + \overrightarrow{k}_{probe}$.

A theoretical formulation of nonlinear spectra is often given using the semi-classical density matrix description. This description can be used to calculate the nonlinear polarization, generating the signal field, induced by the interaction of the material with the pump and probe fields. Once the density matrix $\rho(t)$ of the system is known, the polarization can be calculated according to:

$$P^{(n)}(t) = \langle \mu \rho^{(n)}(t) \rangle \tag{2.22}$$

where μ is the density matrix operator. To obtain a description of the polarization that is insightful and can be derived relatively easily, the response of the system and the interaction with the fields are separated as follows [10]:

$$\begin{aligned} P^{(3)}(t) &= \left(\frac{i}{\hbar}\right)^3 \int_0^\infty dt_3 \int_0^\infty dt_2 \int_0^\infty dt_1 S^{(3)}(t_3, t_2, t_1) \\ &\quad E(t - t_3)\, E(t - t_3 - t_2)\, E(t - t_3 - t_2 - t_1) \end{aligned} \tag{2.23}$$

The third order response of the system is governed by the response function $S^{(3)}$, that contains all the microscopic information needed to calculate the optical properties of the material. There are eight terms that contribute to the nonlinear response $S^{(3)}$. Convoluting the different terms contributing to the third order response of the system with the electric fields, of pump and probe, leads to a large amount of terms describing the third order polarization $P^{(3)}$. The multitude of terms reduces to only six terms that are relevant for transient absorption spectroscopy using some approximations. Three of the main tricks that are applied to reduce the number of terms are the time ordering, the rotating wave approximation and phase matching [12]. Time ordering reduces the number of terms in the response function, because, when the laser pulses are

shorter than the time between them, the first interaction is with the pump field $E_1(t)$ and the second interaction is with the probe field $E_2(t)$. Subsequently, the number of terms is further reduced by applying the rotating wave approximation (RWA). In short this approximation means that only terms containing either $e^{i\omega t}$ or $e^{-i\omega t}$, but not both of them, contribute. The latter will lead to rapidly oscillating terms that are in general neglected in the description of $P^{(3)}$. The last trick reducing the number of terms is the phase matching direction. For transient absorption spectroscopy, the signal is expected in the direction of the probe, hence all the combinations of the response functions and the fields that do not lead to a radiated field in the probe direction will not be taken into account. Of the six terms that survive the approximations and tricks, two describe stimulated emission, two other terms describe bleaching of the ground state and the remaining two describe induced absorption. Full treatment of this theory is beyond the scope of this thesis, but an integral description can be found in the books of Mukamel and Boyd [10, 12].

2.4 Linear spectroscopic techniques

2.4.1 Absorption and fluorescence

For linear absorption and emission spectroscopy standard equipment was employed. Absorption spectra were measured using a Jasco V-630 or a Jasco V-660 UV/Vis absorption spectrometer. Emission and excitation spectra were recorded using a Jasco FP-6200 spectrofluorimeter. Fluorescence quantum yields were calculated using a reference (r) fluorophore and the following expression [13]

$$QY = QY_r \frac{I}{I_r} \frac{OD_r}{OD} \frac{n^2}{n_r^2} \tag{2.24}$$

where QY_r is the quantum yield of the reference molecule, $I(_r)$ the intensity of the fluorescence, $OD(_r)$ the absorption at the excitation wavelength and $n(_r)$ the refractive index of the solvent.

2.4.2 Single photon counting

Time-correlated single photon counting experiments (TCSPC) for measuring fluorescence lifetimes were performed using a mode-locked Ti:Sapphire laser system (Coherent Inc: VERDI-5W, MIRA-900-F, Pulse Picker 9200, Harmonics Generator 9200), delivering subpicosecond pulses of approximately 5 pJ at a 1.9 MHz repetition rate. The fluorescence was collected at a 90° angle via an f/2 collimating lens. The emitted light was detected with a microchannel plate photomultiplier (Hamamatsu R1564U-01). The instrument response function, determined by scattering experiments, was in the order of 50 ps (fwhm). High-pass filters were placed in front of the photomultiplier to cut out possible scatter at the excitation wavelength. No further spectral selection was used, unless specifically mentioned.

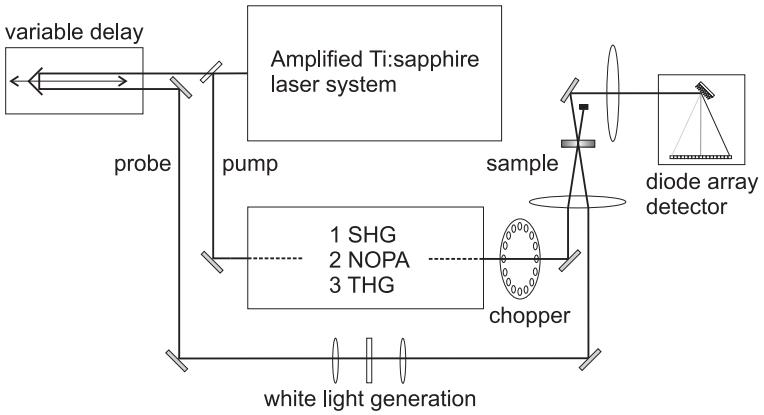

FIGURE 2.7. Schematic representation of the experimental setup used for pump-probe spectroscopy. Three different nonlinear schemes were used to generate the pump: second harmonic generation (SHG), triplet harmonic generation (THG) and a noncolinear optical parametric amplifier (NOPA). The probe is always formed by a white light supercontinuum.

2.5 NONLINEAR SPECTROSCOPIC TECHNIQUES

At the basis of the work described in this thesis lies transient absorption (i.e. pump-probe) spectroscopy. Figure 2.7 shows a schematic setup for these measurements. The output of the amplified laser system is split and the different parts are directed along separate paths in the setup forming the pump and probe respectively. The probe is delayed in time using a computer controlled delay stage. Pump and probe beams are focussed in the sample after which the pump is blocked and the signal, in the direction of the probe, is sent into a spectrograph and is detected using a home-built diode array detector. In the remainder of this section the different components in the setup will be described in detail, starting from the amplified laser system to the detector. Whenever relevant, theoretical background is supplied.

2.5.1 AMPLIFIED LASER SYSTEMS

For the experiments in this thesis, three different amplified Ti:sapphire laser systems were used. Ti:sapphire oscillators are solid state lasers that most commonly generate pulses around 800 nm but allow for tunability in the range between 700 and 1000 nm. They thank their popularity to their short pulses, down to ∼5 fs [14] and to their pulse-to-pulse stability. To achieve higher powers than can be obtained from oscillators, the output of the oscillator can be used as a seed in an amplifier system at the cost of reducing the repetition rate of the pulses. In general the output repetition rate of Ti:sapphire amplifiers is 1 KHz. The layout of the amplifiers used for the experiments described in this thesis was different and will be described below.

The system that was used most frequently was based on chirped pulse amplification (CPA-2001; Clark-MXR Inc.) and will be referred to as PUSH. A seed is generated by frequency doubling the output of a mode-locked erbium doped fibre laser to 775 nm. Subsequently, the seed is fed into a stretcher where the pulses are stretched and chirped. Amplification occurs by pumping the Ti:sapphire rod in the CPA by a frequency doubled Nd:YAG laser. The timing of this process is set by two Pockels cells. Before exiting the system, the pulses are compressed. The output of this system has a remarkable, pulse-to-pulse, stability of ∼1-2%. Pulses are generated with a 4.5 nm bandwidth, delivering a pulse length of ∼200 fs at a maximum power of ∼870 μW. The output of this system was used to pump the NOPA (vide infra).

Secondly, for experiments pumping at 266 and 400 nm a regenerative amplifier was used (Legend F-HE, Coherent Inc.). This system operates with a Vitesse oscillator as a seed, pumped by a Verdi, delivering 100 fs pulses at 80 MHz (both Coherent Inc.). The frequency doubled output of an Evolution laser, Nd:YLF with pulses at 1 KHz, is used as a pump (Coherent Inc.). It produced pulses of 12 nm bandwidth, ∼200 fs, at an output power of 2.8 W. This amplifier system will be referred to as DAVE.

The third amplifier system used in the control experiments described in chapter 5 contains two amplification steps. First, the seed is amplified in a similar Legend system as described above. This is followed by a second amplification step using a multipass amplifier. Here the Ti:sapphire crystal is cooled in a helium cryostat and is pumped from both sides by two Evolutions, amplifying the output of the regenerative amplifier by a factor ∼3. Output pulses typically had a 27 nm bandwidth, resulting in 30-50 fs pulses at a total output power of 7 W. This is a prototype system from Coherent Inc. and will be referred to as VIKTOR.

2.5.2 NONLINEAR OPTICAL PROCESSES FOR FREQUENCY CONVERSION

The samples described in this thesis all have different absorption spectra and therefore several wavelengths in the range of 266 to 800 nm are required for resonant excitation. Most femtosecond lasers produce pulses at or around 800 nm. To generate light at different wavelengths, a conversion method is used based on nonlinear optical crystals. The experimental frequency conversion procedures to generate the respective pump frequencies can be subdivided into three groups that all start with the output of a Ti:sapphire amplified laser system as described in the previous section.

At the basis of frequency conversion using crystals lies the nonlinear response of these materials when the impinging electric field has a large amplitude. Additional requirements are the transparency of the material in the region of interest and the strong birefringence needed for phase matching (vide infra). When the polarization response in the medium is instantaneous, it can be described by an expansion in the electric field as in equation 2.21. Frequency conversion in non-isotropic crystals can be attributed to second order terms in the nonlinear

susceptibility, i.e. χ_2. Assuming there are two beams that impinge on the crystal at frequencies ω_1 and ω_2, then the second order polarization will be dependent on both frequencies as expressed in equation 2.25 [8, 15, 16].

$$\begin{aligned} P^2(t) &\propto (E_1 cos(\omega_1 t) + E_2 cos(\omega_2 t))^2 \\ &\propto \frac{1}{2}\left(E_1^2 E_2^2\right) + \frac{1}{2}E_1^2 cos(2\omega_1 t) + \frac{1}{2}E_2^2 cos(2\omega_2 t) \\ &\quad + E_1 E_2\left[cos(\omega_1 + \omega_2)t + cos(\omega_1 - \omega_2)t\right] \end{aligned} \tag{2.25}$$

The oscillating polarization leads to the radiation of electric field(s) by the non-linear medium at the newly generated frequencies. From equation 2.25 it is clear to which physical processes, in the case of two incoming beams, the polarization combinations can be attributed. The first term has lost its oscillatory behavior, hence a DC polarization is created which is generally known as the process of optical rectification. Secondly, there are two similar terms with a frequency dependence of either $2\omega_1$ or $2\omega_2$. These terms describe the widely-used process of second harmonic generation (SHG), where the frequency of the incoming beam is doubled. The two last terms represent sum frequency and difference frequency generation (SFG and DFG), respectively.

The macroscopic polarization that induces the radiation field that exits the non-isotropic material consists of the contributions of microscopic dipole-like radiation that is induced in the atoms or molecules in the crystal. Only if this microscopic radiation is phased properly, an electric field will appear with considerable amplitude. In the example of second harmonic generation, where $\omega_2 = 2\omega_1$, this means that the fundamental electric field wave, with frequency ω_1, propagates with a different phase velocity through the material than the frequency doubled wave with frequency ω_2. This implies that the frequency doubled wave generated at the front of the material will be out of phase with that generated deeper in the crystal. In this case, the waves add up constructively only over a limited distance, the coherence length, usually several tens of μm. To increase the coherence length, it is required that $n_{2\omega} = n_\omega$ or by analogy using the wave vectors $\overrightarrow{k}$ of the fields $\overrightarrow{k}_{2\omega} = 2\overrightarrow{k}_\omega$. In principle this requirement cannot be fulfilled as the refractive index increases with ω. Nevertheless, in birefringent crystals, this problem can be overcome, because the index of refraction depends on the polarization of the waves. These crystals have two indices of refraction, causing light to take a different path through the crystal depending on the polarization. As the fundamental and frequency doubled waves are orthogonally polarized to each other, the polarization of the latter can be chosen to match the lower of the two refractive indices and hence the phase matching condition can in theory be fulfilled. In practice, the phase matching condition can be achieved by tuning the angle between the incoming beam and the crystal axis.

Optical parametric amplification (OPA) is a specific type of difference frequency mixing where there are two input fields, one that is strong and virtually undepleted at a frequency ω_3 and a second that acts as a seed at a frequency ω_1. These two input field generate a second output field at $\omega_2 = \omega_3 - \omega_1$. The

output beams at ω_1 and ω_2 are generally referred to as signal (shorter wavelength) and idler. The beam at ω_1 retains its original phase and is amplified by the process of OPA. The beam generated at the frequency ω_2 is dependent on both the pump and the seed [10]. The technique of OPA lies at the basis of tunable pulses with a tens of femtosecond pulse duration in the visible and near infrared (475 to 1200 nm). In this thesis a non-collinear optical parametric amplifier ($NOPA^{TM}$; Clark-MXR Inc.) was used [17–19]. Figure 2.8 shows a schematic presentation of the NOPA. Depending on the wavelength ∼20–50 fs, 20-40 nm bandwidth, pulses were obtained with a power up to 15 μW at 1kHz. The output pulses of the CPA are frequency doubled in a KDP crystal for blue light pumping of the NOPA. The mismatch between the group velocities of the signal and idler waves in the crystal, and the accompanying lengthening of the pulses, is overcome by using a non-collinear alignment of the two waves. To cancel the mismatch it is required that the projection of the group velocity of the idler onto the signal wave vector is equal to the signal group velocity. Since in a blue-pumped NOPA the group velocity of the idler always exceeds that of the signal a suitable angle to cancel the mismatch always exists. As a seed to the NOPA process, white light continuum is used. The white light is generated using a fraction of the 775 nm light from the CPA. The continuum spectrum is reasonably featureless over the total wavelength range. However, around the pump wavelength, at 775 nm, a highly structured spectrum exists due to self phase modulation. Therefore, it is not advisable to generate 800 nm short pulses in a one stage NOPA. Instead, to generate short pulses around 800 nm, a two stage NOPA is used. To ensure a seed with a featureless spectrum around 800 nm, in the first stage a small amount of 1200 nm light is generated. This light is sent into a second sapphire disk to generate a new white light seed for the second NOPA process, with a flat spectrum around 800 nm. Subsequently, the seed at 800 nm light is amplified similarly as in a single stage NOPA. The output of both single and double stage NOPAs could be easily compressed with a simple prism compressor.

Outside the tuning range of the NOPA, excitation frequencies in the UV used in the experiments described in this thesis were generated by SHG and frequency tripling. The first process was used to generate light at 388 nm directly from the CPA output. The second process was applied to generate light at 266 nm. In principle frequency tripling from 800 to 266 nm can be done in one step using a material with third order nonlinearity, however the experimental realization is often achieved by a two step procedure. In the first step, 800 nm is frequency doubled in a BBO crystal, cut at 29.2°, to 400 nm. Subsequently, the beams at 400 and 800 nm are collinearly sent into a second BBO crystal, cut at 44.3° and sum frequency mixing of the two wavelengths generates a beam at 266 nm.

A white light supercontinuum was used in most experiments as the probe beam. It is generated by splitting off part of the light from the amplified Ti:sapphire lasers and subsequently focussing it by a 50 mm lens into a 1 mm thick c-cut (zero-order) sapphire disk. There are several nonlinear processes that contribute to the formation of the supercontinuum, among which

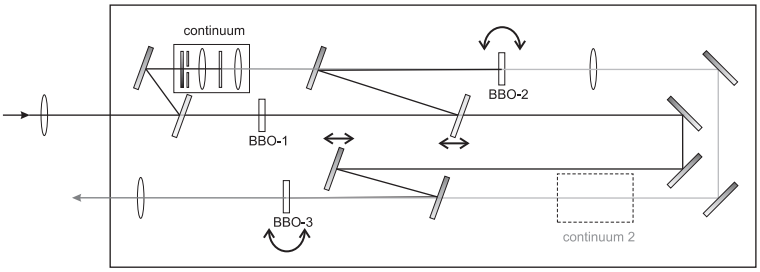

FIGURE 2.8. Schematic representation of the NOPA. The incoming beam is weakly focused and split in two. Subsequently one part enters the first continuum stage. The other part is frequency doubled in the BBO-1 crystal and split again after which one part is overlapped with the continuum in the BBO-2 crystal. The newly formed beam is sent to BBO-3 crystal, where it is overlapped with the remainder of the frequency doubled beam, to be amplified. Optionally a second continuum stage can be entered to generate wavelengths around 800 nm.

self phase modulation is the dominant process [15]. The generated white light is collected and collimated either by a lens or a parabolic mirror. The generation of stable white light continuum is very sensitive to the position of the sapphire disk with respect to the focus and the intensity of the incoming light. These two parameters have to be adjusted carefully, by means of an iris and a neutral density filter, to prevent the formation of fringes in the beam profile of the white light. At the sample position the white light is heavily chirped, i.e. not all frequency components arrive at the same time. Partially this is inherent to the nonlinear processes generating the white light, however additional optics in the beam path towards the sample tend to induce additional chirp. It is fairly simple to correct for the chirp afterwards by a mathematical procedure. For the pump-probe experiments on FMO a different approach in generating the probe was used. This experiment required a stable probe around 800 nm, that cannot be generated by pumping the sapphire disk with 800 nm. Therefore, 1200 nm was produced by a second NOPA and subsequently used to pump the sapphire to generate white light supercontinuum with a structureless spectrum around 800 nm.

2.5.3 PULSE CHARACTERIZATION

To measure the pulse lengths of the beams generated in the NOPA, autocorrelation is used. In this technique the pulse is split into two beams. In the autocorrelator employed (NOPA-Pal Clark-MXR Inc.), this was done spatially by cutting the beam in two using two closely spaced mirrors. One of these beams is delayed in time by attachment of the mirror to a piezo electric element. Subsequently, the beams are non-collinearly crossed into a BBO crystal. The obtained SH intensity versus the delay, $AC(\tau)$, is a one dimensional array

given by the following, symmetric function [20, 21].

$$AC(\tau) = \int dt \, |E(t)E(t-\tau)|^2 = \int dt I(t)I(t-\tau) \tag{2.26}$$

Depending on the assumed pulse shape, often Gaussian or sech^2, the full-width-half maximum (FWHM) of the autocorrelation can be divided by a factor of 1.41 or 1.54 to obtain an estimation of the pulse length. It is a reliable and simple method of pulse characterization, as long as the autocorrelator is properly aligned and the BBO crystal is thin enough to support phase matching, that scales as 1/length, over the whole bandwidth of the pulse that is to be characterized. An independent check is to calculate the pulse duration directly from the bandwidth of the spectrum. This gives the transform limited (TL) value of the pulse duration which is the shortest pulse duration theoretically achievable. The limitation of this technique surfaces when the TL pulse duration and the value from the autocorrelation measurement do not agree. Autocorrelation can not identify the origin of the distortion that causes lengthening of the pulse. Therefore, it is not recommended to rely only on autocorrelation for pulse characterization.

Characterizing the complex pulses emerging from a pulse shaper, see chapter 5, is especially difficult and a second, more advanced, pulse characterization technique was employed. This technique is called frequency resolved optical gating (FROG) and is used to measure a two dimensional trace, resolved in frequency and time, i.e. an autocorrelation with temporal and spectral resolution. In contrast to the autocorrelation measurements a different, known, gate pulse is used in the spectrally resolved measurements (i.e. XFROG). A mathematical description of such an XFROG trace is called a spectrogram and is given by the following relation.

$$S(\tau, \omega) = \left| \int dt E(t)E'(t-\tau)e^{-i\omega t} \right|^2 \tag{2.27}$$

With this function it is possible to quantitatively assign a FROG signal to belong to a transform limited pulse, usually a symmetric shape. Instead, if there occurs a deviation from a flat phase, corresponding to a transform limited pulse, this will be apparent in the FROG signal. A common problem is that the different frequency components of a short laser pulse do not arrive simultaneously at a given position, i.e. chirp, in a FROG measurement this results in a distinct, tilted, shape. In autocorrelation traces, deviations from transform limited pulses could only be detected qualitatively.

2.5.4 DETECTOR

The detector consists of two parts. First the pulses were dispersed in a spectrograph (Acton-SP2150i; Princeton instruments). Depending on the type of measurements different gratings with respect to the blaze wavelength and the number of lines per mm were used to disperse the probe pulse. Subsequent detection of the frequency resolved probe pulse was achieved using a home-built

diode array detector (Diablo). This detector has two arrays of 256 pixels each, enabling optional detection of a reference.

2.6 Data analysis

TA data is time and energy resolved providing a matrix with 256 wavelength components on one axis and a varying number of points on the time axis (often 100-200). Analysis of the time-resolved data was done using two approaches. First simple single trace fitting of the decay traces was used to obtain a general idea of the decay time constants involved and to look at ultrashort decay times of ∼100s fs. Subsequently, a more elaborate fitting tool was used. Software for global analysis, where a complete data matrix is analyzed in one fit, was developed by Dr R. L. A. Timmer [22]. As input for this procedure a model for the decay pathways between the different energy levels in a molecular system need to be computed. This model can be quantified in rate equations that describe the population transfer from one to the next level in the model. In this thesis often a four level sequential model, with three decay time constants, is used. The program uses a multi-component deconvolution of the data matrix to find the best spectra that belong to the levels of the model employed. The rate equations imposed by the model, are solved generating the model matrix. Subsequently, a least square fit of the difference between the calculated and the data matrix is performed. The result of the global fit, for the chosen model, is a description of the decay dynamics of the system in terms of the least square fit spectra of the different states in the model and the corresponding decay times between them.

2.7 Sample handling

This thesis describes measurements on a wide range of complex molecular systems, ranging from proteins to dyes. All of these samples require their own specific preparation procedure. Whereas the dyes are photostable, the FMO protein is very sensitive and easily bleaches.

2.7.1 FMO

The FMO protein was kindly provided by Mette Miller and was extracted and purified following the procedure developed in their lab [23]. The sample was freeze dried and was kept at -80° C until use. To prepare a sample for cryogenic measurements at 77 K the protein was first dissolved in a 50 mM TRIS buffer at pH 8 to prevent unfolding. A double quantity of glycerol (TRIS:gycerol, 1:2) was added to this solution to ensure the formation of a good glass without cracks. Before the measurement, the cryostat (Optistat CF, Oxford Instruments) was cooled down to 77 K using liquid nitrogen. The sample was diluted to reach an OD of around 0.3 at 800 nm. To prevent cracks in the glass, the use of a plastic cuvette proved to be essential. We designed a home-made cuvette where

two plastic windows were polished and bolted onto a 1 mm thick teflon spacer. The high viscosity of the sample limited leakage. The FMO protein is easily bleached even at cryogenic temperatures and low excitation power. To prevent severe photobleaching and degrading of the signal, the sample was rotated using a home-built cryo-rotator. This devices moved the sample continuously on an elliptical trajectory ensuring maximum sample volume excited in one loop made by the rotator [24].

2.7.2 SWITCHES

To prevent the possible build-up of photoproducts, measurements on molecular switches made use of a 2 mm pathlength flowcell with a 30 mL reservoir. This ensured that every laser shot saw a fresh sample. If necessary the reservoir was irradiated to return the switches to their open or closed form, depending on the measurement. This method was mainly employed while pumping the open form of the switches with UV light, because of the high QY of ring closing. The sexithiophene switches and the dye-switches were dissolved in cyclohexane and dichloromethane respectively for measurements at room temperature. Additionally, the sexithiophene switches were measured in solution at low temperatures. Isopentane was chosen as a solvent in this case, because of its low freezing point. All of the building blocks of the multi-component dye switches described in part II of this thesis were synthesized and measured individually. In contrast to the switches, the dyes were dissolved in dichloromethane in a 1 mm quartz cuvette. Absorption and fluorescence spectra were recorded in a dilution range starting from the concentrations used in the time-resolved measurements (OD $\sim$0.3 in a 2mm pathlength cell). The similarity of the absorption and fluorescence spectra at the different concentrations showed that concentration effects, such as aggregation, did not influence the experiments.

3 Energy transfer

In this chapter the basic theory behind energy transfer in molecular materials is developed. In the weak coupling limit this leads to Förster theory, that describes energy transfer as an incoherent hopping mechanism. This theory does not suffice for strongly coupled systems such as aggregates in which energy transfer can occur in a coherent manner.

3.1 Introduction

Interactions between chromophores can lead to interesting excited state behavior. An optical electronic excitation promotes an electron to a higher energy level leaving behind a hole in the ground state. In a coupled system this excited molecule can interact with similar, i.e. not solvent, molecules in its surrounding. This type of excited state is generally referred to as an exciton state. In the absence of charge transfer, i.e. the electron and hole remain on the same molecule, the system can be described using the Frenkel exciton model. Photo-excitation of one chromophore can lead via resonance energy transfer to movement of the exciton to the other chromophores. In figure 3.1 an optically prepared excited state on molecule 1 is deactivated and simultaneously the excitation energy is transferred to molecule 2. This process does not occur via emission of photons by 1 and subsequent reabsorption of the emitted photons by 2, but is a non-radiative process that reduces the lifetime of the excited state of the donating chromophore. In general energy transfer occurs downhill, i.e. the excited state of the accepting molecule must lie lower in energy than that of the donating molecule. The accounts of resonance energy transfer are numerous, two of which will be addressed in this thesis. As described in the first chapter, energy transfer is an essential step in complicated processes such as light harvesting in natural and artificial photosynthesis [25–30]. It also is an important aspect of the design and function of molecular devices [31–33].

A recurring problem in the description of energy transfer is its dependence on the strength of the electronic coupling between chromophores. In the weak coupling regime the dynamics in the system can be described by the Pauli Master equations for time dependent populations of the localized excited states [34]. Using this approach, the electronic coupling between the two molecules is taken into account perturbatively. The two assumptions that underly this approach are that vibrational relaxation within the excited state is much faster than energy transfer and that the coupling to the vibrational modes of the bath is stronger than the interchromophore coupling. The latter ensures that energy transfer occurs via an incoherent hopping mechanism and shows Markovian

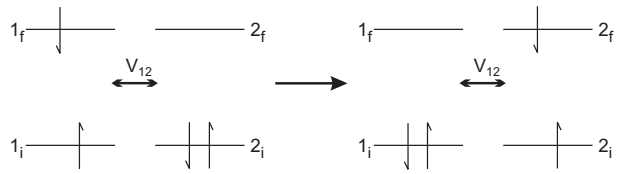

FIGURE 3.1. Exciton interaction and subsequent movement between the excited donor molecule (1) and the surrounding acceptor molecule (2). V_{12} is the Coulomb interaction between the molecules.

behavior [12, 34]. The rate of energy transfer in the weak coupling regime is generally described by Förster theory. In the strong coupling case the excited states of the chromophores mix and new delocalized states emerge. On short time scales this mixing can lead to coherent, non-Markovian dynamics. In recent years this topic has received quite some interest with respect to light harvesting systems [35,36]. In the remainder of this chapter first the dipole approximation is presented. Subsequently, energy transfer in the weak coupling regime, following Förster theory, is discussed. This theory is widely applicable, but it breaks down under certain conditions. Therefore an extension of the Förster theory is described using an additional exchange term in the case of orbital overlap, the so-called Dexter mechanism. The chapter ends by a discussion on energy transfer in the strong coupling case where the Pauli Master equations are no longer valid and possible coherent energy transfer needs to be described.

3.2 DIPOLE APPROXIMATION

In this section, following a similar line as in reference [34], a description of a weakly coupled system in which different chromophores in a system interact will be developed. When the coupling V between an arbitrary number of chromophores is turned on as is shown in figure 3.1, this results in the following Hamiltonian describing the coupled system:

$$H_{coupled} = H_{el}(R) + T_{nuc} + V_{nuc} \tag{3.1}$$

where $H_{el}(R)$ contains all electronic contributions, depending on the complete set of nuclear coordinates R. The nuclear contributions are contained in T_{nuc}, the nuclear kinetic energy, and V_{nuc}, the interaction between the nuclei. The electronic Hamiltonian can be rewritten as follows:

$$H_{el} = H_m^{el} + \frac{1}{2}\sum_{m,n} V_{mn}^{el-el}. \tag{3.2}$$

In this expression H^{el} accounts for the single molecule contributions and the interaction between the electrons localized on the chromophores m and n is represented by V_{mn}^{el-el}. The single molecule part of the Hamiltonian can be described using the electronic states of the single molecules, that is $|\phi_{ma}\rangle$ for

chromophore m in the a^{th}, i.e. S_0, S_1, etc, state. For these states a single molecule Schrödinger equation can be stated. In expression 3.3 the Schrödinger equation is specified for molecule m in state a.

$$H_m^{el}(R)\phi_{ma}(r_m;R) = \epsilon_{ma}(R)\phi_{ma}(r_m;R) \tag{3.3}$$

Using this expression, the electronic Hamiltonian in equation 3.2 can be expanded to the form

$$H_{el} = \sum_{ma} \epsilon_{ma}|\phi_{ma}\rangle\langle\phi_{ma}| + \frac{1}{2}\sum_{mn}\sum_{abcd} J_{mn}(ad,bc)|\phi_{ma},\phi_{nb}\rangle\langle\phi_{md},\phi_{nc}|. \tag{3.4}$$

Here, the matrix elements of the Coulomb interaction, $J_{mn}(a,b,c,d)$ are given by:

$$J_{mn}(a,b,c,d) = \langle\phi_{ma}\phi_{nb}|V_{mn}^{el-el}|\phi_{nc}\phi_{md}\rangle. \tag{3.5}$$

The general expression of the electronic part of a Hamiltonian of a coupled system, H_{el}, can be specified to a situation where two chromophores 1 and 2 interact. Additionally, the chromophores will be described as two-level systems with a ground state i and an excited state f. Without interaction, such a system is characterized by four different states: one ground state $|1_i2_i\rangle$, two single excited states $|1_i2_f\rangle$, $|1_f2_i\rangle$ and a double excited state $|1_f2_f\rangle$. In the two-level approximation, the labels a through d in equation 3.5 can only take the values of i and f. Even when taking into account only two levels, the Coulomb interaction J_{12} is classified by 2^4 different elements. However, the number of matrix elements in the exciton Hamiltonian can be reduced by the following assumptions [34, 37]. First, the matrix elements that describe the interaction between charges at molecules 1 and 2 can be neglected as long as the molecules do not have a large permanent dipole moment. Secondly, the non-resonant terms that correspond to simultaneous creation and annihilation of excitons on two different molecules are disregarded, the so-called Heitler-London approximation. This reduction leaves only two terms to be considered that correspond to the interaction between the transitions $1_i \rightarrow 1_f$, $2_f \rightarrow 2_i$ and vice versa. Hence, the system in figure 3.1 can be represented by the terms $\langle 1_f2_i|\hat{V}|1_i2_f\rangle$ and $\langle 1_i2_f|\hat{V}|1_f2_i\rangle$. The matrix element, J_{12}, of the Coulomb interaction, V_{12}, between the electrons at molecules 1 and 2 then can be rewritten using the transition densities, ρ_{if} that are defined as

$$\rho_{1if}(r_1,R) = \phi_{1f}^*(r_1,R)\phi_{1i}(r_1,R) \tag{3.6}$$

where $|\phi\rangle$ is the single-molecule state vector. The matrix element for an aggregate consisting of two molecules is then given by the following expression.

$$J_{12} = \int dr_m dr_n \rho_{1if}(r_m,R)V_{12}^{el-el}\rho_{2if}^*(r_n,R) \tag{3.7}$$

Where m and n describe the electronic coordinates of molecules 1 and 2 respectively and R is the distance between the nuclei. At relatively large distances

between the nuclei, the short range aspects of the transition densities do not need to be taken into account. Such a simplification is achieved by using a multipole expansion in $|r/R|$. In the dipole approximation the Coulomb interaction reduces to

$$J_{12} \approx \frac{\overrightarrow{d}_1 \overrightarrow{d}_2^*}{|\overrightarrow{R}_{12}|^3} - 3\frac{(\overrightarrow{R}_{12}\overrightarrow{d}_1)(\overrightarrow{R}_{12}\overrightarrow{d}_2)}{|\overrightarrow{R}_{12}|^5}. \tag{3.8}$$

Where both R and d are vectors and d represents the transition dipole moment $d_1 = \langle\phi_{1f}|\hat{\mu}_1|\phi_{1i}\rangle$. By introduction of the orientational factor κ_{12} the Coulomb interaction is obtained in its usual form.

$$J_{12}(R) = \kappa_{12}\frac{|\overrightarrow{d}_1||\overrightarrow{d}_2^*|}{|\overrightarrow{R}_{12}|^3} \tag{3.9}$$

Here κ is given by

$$\kappa_{12} = \overrightarrow{n}_1 \cdot \overrightarrow{n}_2 - 3(\overrightarrow{e}_{12}\overrightarrow{n}_1)(\overrightarrow{e}_{12}\overrightarrow{n}_2). \tag{3.10}$$

In this expression n and e are unit vectors in the direction of the respective transition dipole moments of molecules 1 and 2 and in the direction of the line connecting both transition dipole moments respectively.

3.3 FÖRSTER ENERGY TRANSFER

Förster resonant energy transfer, also known as FRET has proven its use in many, often biology inspired, optical measurements [38]. Fluorescent proteins or tags are often used as tools in biological imaging [39], since they are sensitive probes of distances between molecules. Whereas quenching of fluorescence by energy transfer was first described by collisions between donor and acceptor molecules, soon it was realized that a quantum mechanical coupling between the two molecules mediates energy transfer [40]. One of the first to describe this phenomenon successfully was Theodor Förster, who recognized that the rate of energy transfer can be expressed using photophysical properties of the donor and acceptor. Figure 3.2 shows a schematic picture of the process.

In the weak coupling regime the cumulative spectra of donor and acceptor in a coupled system are matched by the summed spectra of the individual components. In this case the coupling between donor and acceptor and the coupling to the bath modes can de described using a perturbative approach. This implies that the probability of an excitation on the donor to hop to the acceptor is governed by Fermi's golden rule of transitions as described in chapter 2. A further assumption is that the rate of vibrational energy relaxation exceeds the rate of energy transfer, i.e. energy transfer occurs between vibrationally equilibrated states, meaning that energy transfer occurs by an incoherent mechanism [12,34].

Our derivation of the rate of energy transfer begins with Fermi's golden rule, that was developed in chapter 2 as equation 2.17, for the rate of optical

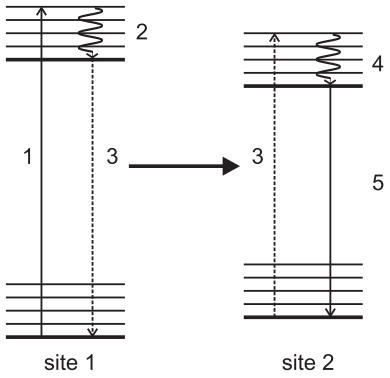

FIGURE 3.2. Schematic representation of the Förster mechanism of energy transfer. The respective steps in the process are labeled 1 through 5 and correspond to excitation (1) and vibrational relaxation of chromophore 1 (2). Subsequently, simultaneous de-excitation of chromophore 1 and excitation of 2 (3) occurs. Rapid excited state vibrational relaxation of 2 prevents back transfer to 1 (4). Relaxation of chromophore 2 by (non)radiative processes ends the energy transfer process (5).

transitions as in equation 3.11 and uses an approach similar to the work of May and Kühn [34].

$$W = \frac{2\pi}{\hbar^2} \left|\hat{V}\right|^2 (\delta(\omega_{fi} - \omega) + \delta(\omega_{fi} + \omega)) \tag{3.11}$$

The description of the molecules as two level systems leads to an expression of the coupling V as in equation 3.12. In addition to the Coulomb interaction J often truncated to the dipole-dipole interaction (section 3.2), there is a term due to spatial overlap of the orbitals of the different chromophores 1 and 2. This exchange interaction K is neglected in the description of Förster energy transfer as it decreases exponentially with the distance, R, between the chromophores and is generally not significant at an interchromophore distance larger than 10 $\mathring{A}$.

$$\begin{aligned} V_{12} &= J_{12} - K_{12} \\ &\approx J_{12} \text{ for R>10 } \mathring{A} \end{aligned} \tag{3.12}$$

Up to this point, the vibrational degrees of freedom have been assumed to be fixed. Next, the vibrational motion needs to be included in the rate equation in two ways: the energies of the electronic states depend on the complete set of vibrational degrees of freedom. The dipole-dipole coupling J_{12} depends on the distance between the chromophores 1 and 2 and following the Franck-Condon approximation does not depend on the nuclear coordinates. In this light the rate equation expressed in equation 3.11 can be rewritten as

$$W = \frac{2\pi}{\hbar^2} |J_{12}|^2 \sum_{MN} f(E_{1M}) \left|\langle \chi_{1M} | \chi_{2N} \rangle\right|^2 \delta(E_{1M} - E_{2M}). \tag{3.13}$$

In this equation chromophores 1 and 2 are characterized by their own independent set of vibrational coordinates M and N. The assumption to use two sets of independent vibrational coordinates holds for distances between 1 and 2 that are larger than 10 $\mathring{A}$. In equation 3.13 the distribution of the vibrational states at chromophore 1 is represented as $f(E_{1M})$. The initial-donor and final-acceptor states are given by χ_{1M} and χ_{2N} respectively. Since energy transfer occurs via simultaneous de-excitation of chromophore 1 and excitation of 2, equation 3.13 reorganizes to

$$W = \frac{2\pi}{\hbar^2} |J_{12}|^2 \sum_{M_1,N_1} \sum_{M_2,N_2} f(E_{1fM_1}) f(E_{2iN_2}) \langle \chi_{1fM_1} | \chi_{1iN_1} \rangle \langle \chi_{2iN_2} | \chi_{2fM_2} \rangle \times \delta(E_{1fM_1} + E_{2iN_2} - E_{2fM_2} - E_{1iN_1}). \tag{3.14}$$

Where the subscripts i and f denote the ground and excited states of the chromophores respectively. The distribution of the vibrational states of the donor and acceptor are now separated. To give a description in terms of optical observables, the emission and absorption spectra are defined. The rate of spontaneous emission, $I(\omega)$, can also be expressed in the form of a Golden rule, using the dipole approximation. The emission spectrum of the donor $I_1(\omega)$ is given by

$$I_1(\omega) = \frac{4\hbar\omega^3}{3c^3} |\hat{\mu}_{fi}|^2 \sum_{M_1 N_1} f(E_{1fM_1}) |\langle \chi_{1fM_1} | \chi_{1iN_1} \rangle|^2 \delta(E_{1fM_1} - E_{1iN_1} - \hbar\omega). \tag{3.15}$$

A similar line can be followed to define the absorption coefficient, $\alpha(\omega)$, of the acceptor, $\alpha_2(\omega)$.

$$\alpha_2(\omega) = \frac{4\pi^2 \omega n_{mol}}{3c} |\hat{\mu}_{fi}|^2 \sum_{M_2 N_2} f(E_{2fM_2}) |\langle \chi_{2iN_2} | \chi_{2fM_2} \rangle|^2 \delta(E_{2iN_2} - E_{2fM_2} + \hbar\omega) \tag{3.16}$$

By inserting equations 3.15 and 3.16 representing the emission and absorption spectra into equation 3.14 the Förster formulation for the rate of energy transfer is obtained.

$$W_{12} = \frac{9c^4}{8\pi n_{mol}} |J_{12}|^2 \int_0^\infty \frac{d\omega}{\omega^4} I_1(\omega) \alpha_2(\omega) \tag{3.17}$$

Here c and n_{mol} are the speed of light and the number of molecules in a given volume. The Coulomb interaction in the dipole approximation, J_{12}, is given by equation 3.9. The interaction strongly depends on the distance, R, between the chromophores. A useful value that can be deduced from these expressions is the Förster distance R_0. At this distance between the chromophores the radiative lifetime of the donor, τ_1, is similar to the rate of energy transfer and the efficiency of the energy transfer process is 50%.

$$W_{12}(R_0) = \frac{1}{\tau_1} = \int_0^\infty d\omega I_1(\omega) \tag{3.18}$$

The rate of energy transfer expressed in terms of the Förster distance is then given by

$$W_{12} = \frac{1}{\tau_1}\left(\frac{R_0}{R_{12}}\right)^6. \tag{3.19}$$

In practice, to obtain the value of R_0, an overlap integral $J(\lambda)$ is calculated using the emission spectrum of one chromophore, normalized to unit area, and the absorption spectrum of the accepting chromophore, the latter expressed in $\mathrm{cm}^{-1}\mathrm{M}^{-1}$. If the spectra are given on a nm scale, the expression for the Förster distance (in $\AA$) reduces to [13]

$$R_0 = 0.211\left(QY_1 J(\lambda)\frac{\kappa^2}{n^4}\right). \tag{3.20}$$

Here n is the refractive index of the solvent and QY_1 is the quantum yield of fluorescence of the donor in the absence of the acceptor. When the value of the Förster distance is close to or exceeds the distance between the donor and acceptor, the energy transfer will be efficient. In general the efficiency E of the process is described as

$$E = \frac{(R_0)^6}{(R_0)^6 + (R_{12})^6}. \tag{3.21}$$

3.4 Breakdown of Förster theory

Förster theory is not always successful in describing energy transfer. The conditions in which it fails will be described in the following two sections. First, when the distance between donor and acceptor is equal to the size of the molecules, the electronic wavefunctions can start to overlap. This result in a quantum mechanical effect known as exchange interaction that plays a significant role and needs to be included in the description of energy transfer. Exchange has no classical analogue, but for indistinguishable particles such as electrons it means that when the labels of the two electrons are changed, the total wavefunction changes its sign. Dexter theory includes the exchange interaction. Secondly, in the strong coupling regime (e.g. in the case of molecular aggregates), neither Förster nor Dexter theory suffices to describe energy transfer. Energy transfer in these systems can occur on timescales faster than vibrational relaxation, and due to the strong coupling, coherent – wavelike – energy transfer needs to be taken into account in a theoretical description.

3.5 Orbital overlap

When the interchromophore distance is sufficiently small to allow orbital-orbital overlap, the exchange interactions K cannot be neglected and need to be incorporated in the exciton Hamiltonian. Besides the terms $\langle 1_f 2_i|\hat{V}|1_i 2_f\rangle$ and $\langle 1_i 2_f|\hat{V}|1_f 2_i\rangle$ used in the Förster approach, two other types of interactions, that is $\langle 1^+2^-|\hat{V}|1^-2^+\rangle$ and $\langle 1_f 2_i|\hat{V}|1^-2^+\rangle$ are needed to form a complete basis

set [41]. In these expressions $|1^+\rangle$, $|1^-\rangle$ and $|2^+\rangle$, $|2^-\rangle$ represent the states of the charged molecules 1 and 2 respectively. In the weak coupling limit the exchange interaction is described by the Dexter mechanism of energy transfer. Where in equation 3.12 the contribution due to exchange term between electrons A and B was neglected, it is incorporated in the full description of coupling as

$$V_{12} = \frac{1}{2}\int \phi_{1f}^{(A)}\phi_{2i}^{(B)} V \phi_{1i}^{(A)}\phi_{2f}^{(B)} d\tau - \frac{1}{2}\int \phi_{1f}^{(A)}\phi_{2i}^{(B)} V \phi_{1i}^{(B)}\phi_{2f}^{(A)} d\tau. \tag{3.22}$$

The first term describes the Coulomb interaction J_{12} and the second term describes the exchange interaction, where the electron coordinates A and B are interchanged. The rate for energy transfer in the Dexter approach is given by [42–44]

$$W_{12}^{(ex)} = \frac{2\pi}{\hbar} K J_{12} e^{(-2R/L)}. \tag{3.23}$$

In this expression L is the orbital radius of the of molecules 1 and 2 and K is a constant that does not depend on experimental observables, in contrast to $J(\lambda)$ in equation 3.20. Opposed to the Förster approach, the coupling J_{12} in the exchange expression uses normalized absorption and emission spectra. This implies that optically forbidden energy levels, that do not participate in Förster energy transfer because their absorption cross section is too low, can play a role in the exchange mechanism. Since the rate of transfer shows an exponential distance dependence, this type of interaction is only relevant at short donor-acceptor distances below 10 $\mathring{A}$.

3.6 Coherent energy transfer

Förster energy transfer, describing exciton movement in the form of a hopping mechanism is not valid when the dipole coupling J_{12} is sufficiently strong. In this case, the time it takes an exciton to travel to the next molecule is shorter than the time it takes for intramolecular vibrational relaxation to occur. In contrast to the incoherent transfer described by Förster theory in the strong coupling case the exciton can be delocalized over several molecules and can travel through the system in a wavelike manner until dephasing destroys the coherence. Hence, in the strong coupling limit energy transfer occurs between non-equilibrated exciton states. In this case density matrix theory, is needed to describe the transfer of excitons [34]. The equations of motion are described in terms of the chromophores having few degrees of freedom coupled to a large heat bath. To return to the Förster rate of energy transfer, a simple perturbative method of including the vibrations in the system cannot be used. Whereas the interactions between the different chromophores is described perturbatively, the exciton-vibrational coupling needs to be done exactly. The population of the different sites can then be expressed in terms of the Generalized Master Equation that describes all regimes of energy transfer [45]. This approach uses a memory function to describe the rate of exciton transfer, connecting the probability of excitation of chromophore 1 at time $t < \tau$ to the probability of excitation of

chromophore 2 at $t = \tau$ [46]. This implies that the energy transfer follows non-Markovian dynamics and is expected to be faster than described by the incoherent hopping mechanism.

Part I

The FMO complex

4 The optical properties of the FMO complex

This chapter will give an overview of the optical properties of the FMO complex as found by spectroscopic studies of the Q_y band over the last two decades. The focus will lie on the different methods used, both experimental and theoretical, to elucidate the excitonic structure of and dynamics within this pigment-protein complex.

4.1 Introduction

In 1975 Fenna was the first to resolve the X-ray structure of the Fenna-Matthews-Olson (FMO) complex of *Prosthecochloris aestuarii*. This protein fulfills a role in the photosynthetic cycle of green sulfur bacteria, where it channels the excitation energy from the chlorosomes to the reaction center. Since it was the first photosynthetic antenna complex of which the X-ray structure became available, it triggered a wide variety of studies of spectroscopic and theoretical nature and it therefore has become one of the most widely-studied and well-characterized pigment-protein complexes. Due to its relatively simple structure amongst the light harvesting complexes, with only 7 interacting bacteriochlorophyll a (BChla) molecules, and with the level of sophistication at which the optical properties are known, it comes as no surprise that the FMO complex serves as a guinea pig for new and ever improving simulation methods as well as new optical techniques. Remarkably, FMO is still a subject of active investigation and new insights continue to emerge. Even fundamental properties, such as the pigment-protein ratio, remain controversial. The goal of this chapter is to review the mass of information that has appeared the last $\sim$20 years on the optical properties of the FMO complex. It is attempted to give an objective view of the experimental data and the parameters and methods used in simulations. Also where applicable it is indicated which data and parameter sets have become most by favored by others and for which reasons. To keep this review insightful and focused, a restriction is made to the Q_y band in the optical spectrum, that lies around 800 nm.

4.2 Structure

In 1962, John Olson isolated a water-soluble bacteriochlorophyll (BChla) protein (150 kDa) from green sulfur bacteria [47]. This specific protein is part of the light-harvesting system in green sulfur bacteria and acts as a subantenna

to collect sunlight and transfer excitation energy from the light harvesting antennas to the reaction center. Spectroscopic analysis was performed on the two species *Prosthecochloris aestuarii* and *Chlorobium tepidum* which to date have remained the most widely studied species. The spectroscopic results showed that the newly discovered protein contained only BChla chromophores, noncovalently bound to a protein envelope (figure 4.1). In 1975 Roger Fenna and Brian Matthews resolved the X-ray structure of this protein, extracted from *Prosthecochloris aestuarii* at 2.8 $\mathring{A}$ resolution and found that the complex consists of three identical subunits (C_3 symmetry), each containing seven BChla pigments [6]. It showed a protein 'cylinder' in which the BChla molecules were enclosed. The major part of the outside of the protein cylinder exposed to the solvent is composed of 15 strands of β-sheet. The side of the cylinder that is in contact with one of the other subunits in the trimer consists of four short strands of α-helix alternated by regions of the protein without a clear structure. The average distance between BChla molecules within one subunit of the trimer is 12 $\mathring{A}$ while the nearest molecule in the neighboring subunit is found at a distance of 24 $\mathring{A}$. Analysis of the X-ray data showed no evidence for interactions -be these covalent or noncovalent- between neighboring BChla molecules, however the same analysis predicted the presence of extensive interactions between the chlorophyll molecules and the protein cylinder. Besides hydrophobic interactions, also hydrogen bonding and liganding to the Mg atom in the BChla molecule occurs.

In 1997 the crystal structure of FMO from *Chlorobium tepidum* was determined at a 2.2 $\mathring{A}$ resolution [48]. Similar to *Prosthecochloris aestuarii*, the distance between the pigments within a subunit range from 4 to 11 $\mathring{A}$ while the nearest neighbor in a different subunit is over 20 $\mathring{A}$ away. The β sheet is folded in such a way that the strands at the front and the back of the cylinder are roughly perpendicular to each other. The opening in the cylinder is situated towards the center of the trimer, forming the shape of a taco shell. The six α-helices are located at the open end of the taco shell and mainly connect the separated β-strands. BChla molecule 1 and 2 are situated at the outside of the protein complex, while BChla 3 to 7 are located in the center. Polar interactions and salt bridges between amino acids ensures the formation of a stable trimer. The magnesium atom has a fivefold-coordination in all the BChla molecules, although the fifth ligand varies between the pigments. For BChla 1,3,4,6, and 7 it is a histidine residue, for BChla 5 it is an oxygen atom from a leucine residue, and for BChla 2 the electron density suggests a water molecule as the fifth ligand. The structures of the FMO protein present in the two species *Prosthecochloris aestuarii* and *Chlorobium tepidum* show a high degree of similarity (the amino acid sequences are identical to within 77%). The residues that are not conserved do not alter the interaction between the protein and the BChla molecules. Besides that, the relative positions of each of the BChla molecules in the two species match almost perfectly. The main difference is in the planarity of the tetrapyrrole ring of the BChla molecules. For a more detailed description of the comparison between the two species see reference [48].

A range of spectroscopic investigations using linear absorption spectroscopy,

circular dichroism (CD) and linear dichroism (LD) on samples of the isolated FMO protein and the protein associated with membrane vesicles, have revealed the orientation of the proteins with respect to the membrane [49]. The C_3 symmetry axis of the disc like system is perpendicular to the membrane plane. This implies that one of the flat sides of the discs is embedded in the membrane (figure 4.2).

In two recent studies, the presence of an additional BChla molecule per monomer was proposed. This observation is based on careful studies of high resolution X-ray data. Ben-Shem *et al.* noticed additional electron density at the interface between the monomers in their newly crystalized and solved structure. They attributed this to the presence of an eighth BChla molecule possibly located at the interface between the FMO protein and RC [52]. In an attempt to clarify matters, Tronrud *et al.* decided to revisit the structure of *Chlorobium tepidum* as well as collect a new diffraction dataset of *Prosthecochloris aestuarii* [50]. Their comparison indicated the presence of an eighth BChla molecule at the same location, however with different local protein structure, that could account for the difference in the optical spectra. They also showed that the amino acid sequence responsible for the binding corresponds to the spectral differences of the two species. The absence of this additional pigment in earlier studies is explained by an occupancy that is not unity, depending on the preparation method. The effect of an extra BChla molecule is expected to have a considerable influence on the optical spectra, especially on the CD spectra.

4.3 Linear spectra of *Prosthecochloris aestuarii*

4.3.1 Absorption spectra at high and low temperature

The linear absorption spectrum of the FMO complex shows several bands in the wavelength range of 200-900 nm [53]. The Q_y (S_1) absorption band around 800 nm is the most well-characterized band and the focus of the current work. This band appears in the spectral region between the absorption band of the chlorosome (720-750nm) and that of the reaction center core at ∼834 nm, to which FMO transfers its excitation energy [49]. The Q_y (S_1) absorption band has a temperature-dependent shape. At cryogenic temperatures, in a mixture of Tris buffer and glycerol, the absorption band consists of at least three distinct peaks [54,55] (figure 4.3). At elevated temperatures the fine structure disappears and the absorption spectrum appears as a broad featureless band.

Low-temperature absorption spectra of the Q_y (S_1) band show a clear difference between the FMO complex of *Prosthecochloris aestuarii* and *Chlorobium tepidum* (77% homology between the two species); the former has a strong absorption band at 815 nm, while for the latter the strongest absorption band is at 809 nm. Comparison between two species with 97 % homology (*Chlorobium limicola* and *Chlorobium tepidum*) shows a nearly identical absorption spectrum at 6K. This indicates that the local protein environment has a limited but observable influence in the spectral differences between the FMO complexes [56].

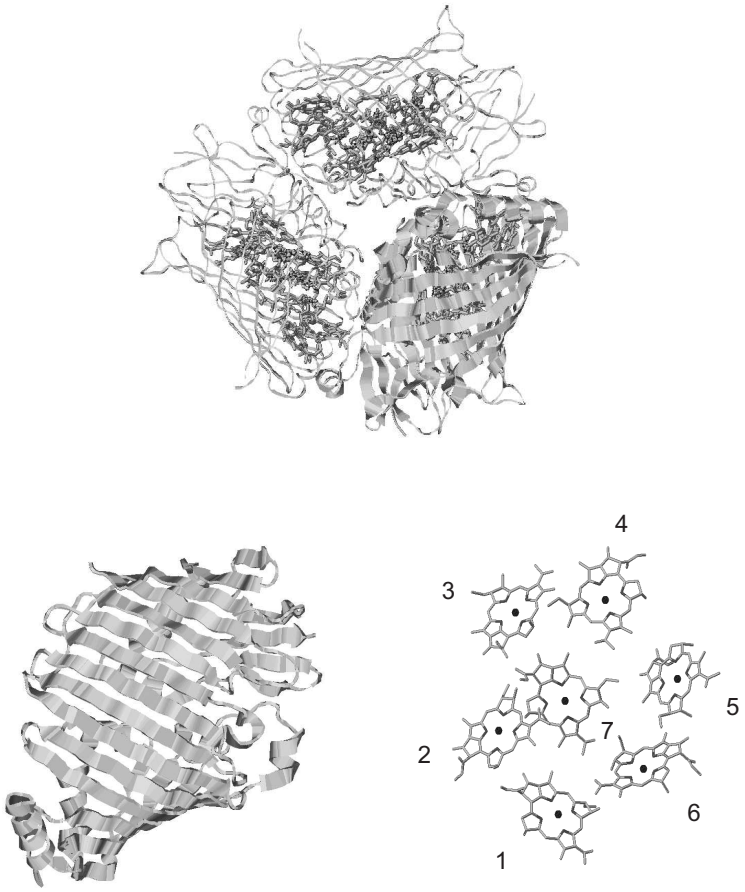

FIGURE 4.1. Representation of the FMO protein trimer of *Prosthecochloris aestuarii* showing the BChla pigments surrounded by the protein envelope [top]. Protein envelope showing the wrapping by β sheets [bottom left]. Enlarged view of the arrangement of the seven BChla pigments [bottom right]. Identifier 3eoj[5] in the Brookhaven Protein Databank. Pictures are created with rasmol. The 8th BChla is omitted for sake of clarity but can be created using the coordinates from [50].

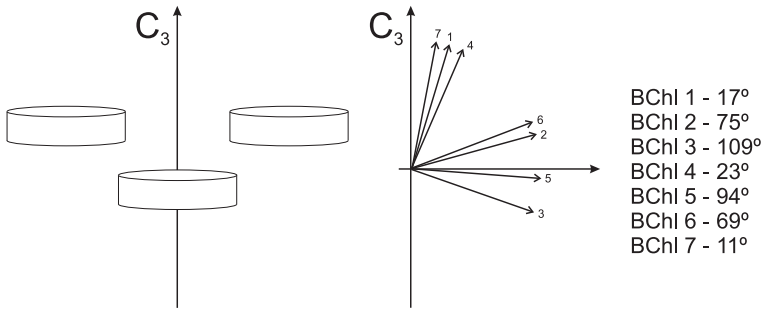

FIGURE 4.2. [Left] Orientation of the FMO protein. The C_3 axis is perpendicular to the disc plane. [Right] The angles between the Q_y transitions of the seven BChla pigments with respect to the C_3 axis [51].

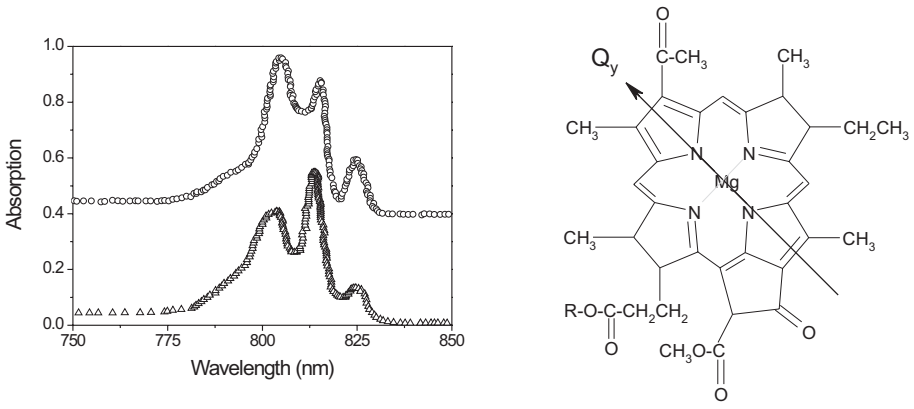

FIGURE 4.3. [Left] Absorption spectra of *Prosthecochloris aestuarii* (triangles) and *Chlorobium tepidum* (circles) offset by 0.4 for clarity. The figure is adapted from reference [56]. [Right] Structure of the BChla pigment. R represents the phytyl chain. The direction of the Q_y transition dipole moment is indicated by the arrow.

Li *et al.* showed that most ligands of the BChla pigments are conserved in both species and propose that the spectral differences find their origin in the non-planarity of the ring in the BChla molecules [48].

4.3.2 MONOMER OR TRIMER

The interaction energy between the BChla molecules within one subunit is about ten times larger than that between subunits, as a result the spectral features of the FMO complex are generally considered to be dominated by the interactions of BChla molecules within a single subunit. However, in several papers describing the modeling of a wide variety of optical spectra of the FMO complex, the issue was raised whether or not to include the interactions between subunits

within the trimer.

In subsequent simulations of the optical spectra a mixed approach is observed. While some authors are convinced of either the trimer [54, 57–59], or the monomer approach [51, 60–64], others compare both [65]. The latter show that there is no significant difference between them and that the effects of including all 21 BChla molecules can also be achieved with small adaptations in the parameters described in the remainder of this section. The main reason for rejecting the trimer approach is the assumption in this case that the three subunits of the trimer are identical: i.e. the effect of energy disorder due to structural heterogeneity (diagonal disorder) is ignored. By including this in the monomer simulations, a similar or even better result is obtained than with the trimer approach.

4.3.3 SITE ENERGIES

One of the most debated properties of the FMO complex are the site energies of the seven BChla molecules in the complex. These values are needed for exciton calculations of the linear spectra and simulations of dynamics. They are defined as the transition energy of a pigment in the absence of coupling between the pigments. It does however depend on local interactions between the BChla molecule and the protein envelope and includes electrostatic interactions and ligation. Since the interactions are difficult to identify and even harder to quantify, the site energies are usually treated as independent parameters that are obtained from a simultaneous fit to several optical spectra. Table 4.1 gives an overview of the different site energies determined by various research groups, employing a variety of approaches described in this section.

Although previous efforts to model the system using the full trimer geometry had not been very successful, Pearlstein still expected the C_3 symmetry of the system to amplify the coupling effect between the intersubunit BChla molecules [57]. In contrast to earlier simulations, in later studies different site energies were assigned to the 21 transitions, i.e. instead of a single one at 802.6 nm, they were fitting parameters and the best fit was judged by eye. Lu *et al.* improved the previous fits by making use of an algorithm to minimize the difference between the measured spectra and the simulated ones by varying adjustable parameters amongst which the seven site energies of the monomer [66]. Their fits were based on two spectra, absorption and CD, both at 77 K and obtained from different groups (referred to as 1 and 2 in table (4.1). Several years later a similar approach was used by Gülen [67]. CD spectra were excluded from these fits, since they tend to be very sensitive to the experimental conditions like the choice of solvent. The directions of the individual (not excitonic) dipole moments were shown with respect to the C_3 axis: BChla pigments 7, 1 and 4 lie almost parallel to the C_3 axis, while the orientation of the dipole moments of BChla 6, 2, 5 and 3 is almost perpendicular (figure 4.2). The spatial organization of the individual dipole moments with respect to each other could help to restrict and direct the fit. In contrast to the simulations of Pearlstein, the site energies in the trimer were taken to be equal reducing the number of fitting parameters to seven. As

a start of the fit, the energy of BChla 6 was set to lie somewhere between 815-820 nm, while the rest were set to 805 nm. Optimization was done manually. Likewise, the site energies used by Louwe *et al.* were obtained my manual adjustment starting from 809.7 nm [61]. However, using these the simulated population dynamics did not agree with the experiments. Simulations of FMO from *Chlorobium tepidum* did match the experimental data much better, a direct consequence of the choice of site energies, and therefore it was decided to adjust the values closer to that of *Chlorobium tepidum* [62]. For both species a single subunit was simulated. This approach was also adopted by Iseri *et al.*, where the site energies are free parameters in a manual fitting routine [51]. Nevertheless, the sign of the bands in the LD spectra limits choice since they pose a restriction on the direction of the dipole moments with respect to the C_3 symmetry axis, as previously described by Gülen *et al.* and Louwe *et al.* Additional, absolute values of the angles of the dipole moments with the C_3 axis, adapted from Louwe *et al.*, were obtained from a global fit of the absorption, CD and LD spectra [64] (site energies obtained with different broadening included in the simulations are denoted with number 2 in table 4.1).

Adolphs *et al.* used a different approach by calculating the "electrochromic shifts" of the site energies by taking into account the interaction between charged amino acids and the pigments [65]. The individual electrochromic shifts were calculated using the Coulomb coupling between the charged amino acids, approximated by point charges, and the difference of the permanent dipole moments of the BChla ground and excited state, estimated from Stark experiments. Remarkable is that the red shift of BChla 3 and the blue shift of BChla 6 are caused by charged amino acids that are conserved in the structures of *Prosthecochloris aestuarii* and *Chlorobium tepidum*. However, this method only partially succeeded in reproducing the site energies corresponding to the ones found by fitting the linear spectra. Therefore, a more elaborate model was needed for better agreement.

Further elaboration, and as a result a good agreement with the experimental spectra, is provided by calculations of the site energies including a detailed description of the charge distribution of both the pigment and the protein states [68]. Ab initio methods were used to describe the pigments, while a classical electrostatic method was used to describe the whole complex on the atomic level. As a result of the low dielectric constant of water/glycerol below the freezing point the standard protonation pattern of the amino acids was no longer valid and half of the usually acidic and basic groups turned out to be neutral. This complex method was simplified, without losing the main results, by assuming a standard protonation pattern and by the introduction of an effective dielectric constant for screening effects [69]. There exists an earlier account of similar quantum calculations where, amongst others, the effect of the charged amino acids was included [70]. However, the resulting site energies are spread over a range ($\sim$770-840 nm) much larger than what is observed in spectra, hence these results are not used for exciton calculations.

While for some of the earlier calculations and fits the range of site energies only spans 10 nm, the more recent ones seem to converge to a difference between

TABLE 4.1. Pigment site energies of *Prosthecochloris aestuarii* in nm. The annotation M and T stand for simulations using the monomer (M) or the trimer (T).

BChla	1	2	3	4	5	6	7
[66]-1	784.6	798.3	800.9	803.3	799.7	811.7	822.4
[66]-2	796.8	806.9	816.9	802.2	780.2	809.3	797.2
[67]-T	804.2	802.6	805.2	806.2	807.8	815.8	803.1
[61]	811.7	804.2	824.4	811.7	795.5	803.2	804.5
[62]	809.3	799.4	824.4	813.0	799.0	801.3	801.6
[51]	808.0	802.1	822.8	809.4	795.9	800.5	804.2
[64]-1	809.7	802.2	822.4	809.7	793.7	801.3	802.6
[64]-2	804.5	806.1	821.4	812.0	792.1	800.0	803.2
[65]-M	801.6	802.6	818.0	806.1	789.6	797.1	803.9
[65]-T	803.5	803.2	817.7	809.4	788.6	796.2	799.4
[68]	805.8	800.1	820.1	806.8	792.4	799.5	802.7
[69]	797.1	809.1	822.4	802.9	794.3	801.9	806.1

the highest and lowest site energy of almost 30 nm, which is comparable to the total width of the absorption spectrum.

4.3.4 LOWEST ENERGY PIGMENT

The pigment with the lowest site energy is the most likely candidate to continue the photosynthetic process by transferring the energy from the FMO complex to the reaction center. The position of this pigment within the complex cannot be detected optically because this would require a resolution below the diffraction limit, therefore it can only be assigned from the outcome of exciton simulations. However, since photosynthesis occurs at 300 K, at room temperature none of the exciton states should be excluded from, a transition dipole weighted, energy transfer to the reaction core complex. Table 4.2 shows the different 'exit pigments' that have been proposed, with consensus now leaning toward pigment 3.

Pearlstein pioneered in the approach of finding the best site energies by looking at absorption, CD and hole burned spectra, rather than just at spectra from one experimental technique. His fits showed that BChla 7 has the lowest site energy [57]. Subsequently the lowest energy pigment was assigned to be BChla 7 or 3 depending on the fitted dataset [66]. The site energies fitted to absorption, LD, and singlet-triplet spectra [67] brought BChla 6 forward as the pigment with the lowest site energy. It is the best interconnected pigment. Simulations by Buck *et al.* favored BChla 7 for that role. They obtained the best fit using parameters deduced from optical spectra of Olson *et al.*, in which BChla 7 has the lowest site energy [60]. By fitting new LD and CD data Louwe *et al.* concluded that the exciton states are mainly localized on one BChla and that the lowest energy pigment was BChla 3 [61]. This agrees with the results

Table 4.2. Lowest site energy of *Prosthecochloris aestuarii*.

Reference	Site energy (nm)	Pigment number
[57]	826.4	7
[66]	822.4	7
[67]	815.8	6
[60]	822.5	7
[61]	824.4	3
[62]	824.4	3
[51]	822.8	3
[64]	822.4, 821.4	3
[65]	817.7	3
[68]	820.1	3
[69]	822.4	3

from Stark hole burning experiments [71]. Since then, different theoretical and experimental approaches agree on BChla 3 being the pigment with the lowest site energy [51,62,64,65,68,69]. Electron microscopy showed the arrangement of the FMO complex with respect to the reaction center (RC) [72]. The technique lacks the resolution to distinguish between the top and the bottom of the FMO complex. However, from the shape of the FMO complex it can be deduced that either BChla 1 and 6 or 3 and 4 form the exit pigments from FMO protein to RC.

By taking a closer look at the environment of BChla 3, which is generally assumed to have the largest electrochromic shift to lower site energy, a curious arrangement of α-helices was observed [68]. The dipoles of the two helices can be represented by two partial charges on the ends of the helix. The positive and negative partial charges of helix 5 lie in the negative and positive region respectively of the calculated difference $(S_0 - S_1)$ electrostatic potential. This results in a red shift of the site energies of about 200 cm^{-1}. Similarly helix 6 gives an additional, however somewhat reduced, redshift of $\sim$100 cm^{-1}. Both helices have a definite effect on the site energies without being dependent on protonation states.

4.3.5 Exciton nature of the FMO complex; delocalization

The close proximity of the BChla molecules ($\sim$10 $\mathring{A}$) leads to electronic coupling between them that exceeds the electron-vibrational coupling in the FMO complex. Therefore, the system is usually described by a superposition of the seven molecular BChla states forming seven exciton states [73], and the electron-vibrational coupling is treated perturbationally. These excitonic interactions V_{ij} between two chromophores i and j are dominated by the relative orientation of the transition dipole moments and the inverse cube of the distance between the

BChla molecules. The exciton levels have different cross-sections and linewidths which together with a close energy spacing results in a dense and complex spectrum. This can be seen in the low temperature absorption spectra in which only three peaks out of seven are clearly visible.

To describe the excitonic wavefunctions in the FMO protein, the following electronic Hamiltonian is used:

$$\hat{H}_0 = \sum_j E_j |j\rangle\langle j| + \sum_{j<i} V_{ij}(|j\rangle\langle i| + |i\rangle\langle j|) \tag{4.1}$$

in which E_j represents the site energies of the uncoupled BChla molecules. The exciton wavefunctions $|\alpha\rangle$ are obtained by diagonalizing the Hamiltonian as

$$|\alpha\rangle = \sum_j C_\alpha(j)|j\rangle \tag{4.2}$$

using the exciton expansion coefficients $C_\alpha(i)$ which represent the contribution of the individual BChla molecules to an excitonic transition. The results of such calculations, as performed on the same system by a variety of research groups, are shown in the tables 4.3, 4.4 and 4.5, where α runs vertically and i horizontally. Pearlstein used a point-monopole approach to describe the interaction between the individual BChla molecules. The transition charge density is calculated for each molecule, represented by point charges at the position of individual atoms, and the interactions of all point charges with those of the other chromophore are considered. All 21 BChla of the trimeric FMO complex were included in the model and the parameters for all 21 degenerate and non-degenerate exciton transitions are displayed in the original paper [57]. It can be concluded that in each case only one or two of the BChla pigments contribute significantly to the squared amplitude of the eigenvectors of the transitions. This means that none of the exciton states is delocalized over the complete subunit let alone the trimer. Several years later this was verified by using a similar approach to model the absorption spectra [67]. However, the main difference is that now the simpler point-dipole approximation was used to model the interactions between the excitonic transitions of two chromophores by representing the electronic transition of each molecule by a single dipole moment. Later followed an approach by the same group that restricted the dipole interactions to one monomer only [51].

Results from linear-dichroic absorbance-detected magnetic resonance experiments on FMO at 1.2 K exhibited similar results as monomeric BChla molecules in organic solvents. This technique is sensitive to the triplet state of the complex and therefore it was concluded that in FMO the triplet state is localized on a single BChla pigment and not its delocalized trimeric counterpart [74]. Simultaneous simulation of the spectra obtained from this technique together with CD spectra were performed considering a single subunit only [61]. This approach was justified by the fact that the simulations predict exciton states that are mainly dominated by a single BChla, implying that the degree of exciton delocalization is limited in the FMO complex.

TABLE 4.3. Contribution of the individual BChla pigments j to the monomer exciton transitions α in *Prosthecochloris aestuarii*, occupation probabilities $|C_\alpha(j)|^2$ from reference [67].

transition number	1	2	3	4	5	6	7
1	0.004	0.001	0.004	0.082	0.340	0.510	0.059
2	0.102	0.193	0.232	0.285	0.004	0.162	0.023
3	0.409	0.255	0.010	0.196	0.003	0.061	0.064
4	0.017	0.017	0.186	0.005	0.160	0.003	0.613
5	0.024	0.001	0.482	0.034	0.275	0.167	0.017
6	0.314	0.344	0.004	0.169	0.096	0.021	0.055
7	0.130	0.189	0.081	0.229	0.122	0.076	0.169

TABLE 4.4. Contribution of the individual BChla pigments to the monomer exciton transitions in *Prosthecochloris aestuarii*, amplitudes $C_\alpha(j)$ from reference [61].

transition number	1	2	3	4	5	6	7
1	-0.066	-0.116	0.955	0.259	0.035	0.027	0.042
2	0.845	0.449	0.037	0.252	0.027	0.020	0.136
3	-0.220	-0.133	-0.268	0.794	0.243	-0.166	0.382
4	0.015	-0.143	-0.111	0.348	-0.293	0.818	-0.300
5	0.130	-0.336	0.009	-0.261	-0.310	0.236	0.807
6	-0.464	0.795	0.057	-0.007	-0.199	0.187	0.272
7	-0.018	0.043	0.014	-0.223	0.847	0.459	0.139

TABLE 4.5. Contribution of the individual BChla pigments to the monomer exciton transitions in *Prosthecochloris aestuarii*, occupation probabilities $|C_\alpha(j)|^2$ from reference [51].

transition number	1	2	3	4	5	6	7
1	0.005	0.019	0.882	0.088	0.002	0.001	0.002
2	0.547	0.286	0.000	0.126	0.007	0.000	0.034
3	0.090	0.052	0.094	0.490	0.091	0.042	0.141
4	0.001	0.028	0.018	0.132	0.140	0.667	0.013
5	0.037	0.093	0.001	0.090	0.093	0.002	0.683
6	0.319	0.520	0.003	0.000	0.051	0.016	0.091
7	0.001	0.003	0.001	0.073	0.616	0.272	0.035

4.3.6 COUPLING STRENGTHS, LINEWIDTH AND EXCITON ENERGIES

For exciton simulations of the various spectra (e.g. absorption, LD, CD) of the FMO protein there are three basic ingredients: the site energies, the dipolar coupling (coupling strength), and the optical linewidth. The first is treated in section 4.3.3, while the rest will be subject of this section. The transition dipole strength of BChla $d(D^2)$ in the FMO complex, has been reported several times in literature. It is an important parameter in simulations of the optical spectra. The values of this dipole strength vary widely and range roughly between 20 and 60 D^2. Simulations by Pearlstein revealed a dipole coupling strength with a value of 51.6 D^2 [57]. This number is similar to the one he used in previous calculations and corresponds to the value of 50.8 D^2 used by Fenna. Further successful simulations of steady state and time-resolved experiments were obtained using values of 51 D^2 [75] and 30-40 D^2 [51, 64]. This value was verified by calculations which resulted in a value of the effective dipole strength of 30 D^2 [65], obtained by reducing the dipole strength in vacuum by a factor of 1.25.

Broadening in optical spectra has two distinct origins which are both of importance in the spectroscopic studies of the FMO complex [34]. The first phenomenon that causes line broadening is static disorder. The seven pigments in the FMO complex all have a slightly different local environment, since the protein envelope that surrounds them differs from pigment to pigment. As a result there is a different mean energy, center absorption frequency, for each BChla. Due to the differences between for example the solvation of all BChla1 pigments in the sample, the center absorption frequency of this pigment is broadened. This effect is referred to as inhomogeneous broadening and can lead to a broad band in the linear absorption spectrum. Inhomogeneous broadening is included in the description of optical spectra in two ways: by including a variable linewidth or by introducing one linewidth for all transitions. An example of the first is given by Pearlstein, who employed widths in the range of $\sim$80 cm^{-1} to $\sim$170 cm^{-1} although there was no physical justification for this large difference [57]. Exciton simulations by Buck *et al.* were performed using $\sim$150 cm^{-1} for all the transitions in the complex [60] and therefore discarded the effect of inhomogeneous broadening shown by Pearlstein to be effective in simulation. Around the same time, linewidths obtained from hole burning experiments, $\sim$70–80 cm^{-1}, were employed by two sets of authors [67, 76] to simulate absorption, linear dichroism, singlet-triplet and low-temperature absorption and fluorescence line-narrowing measurements respectively. Several successful simulations of both steady-state and time-resolved spectra were performed using an inhomogeneous linewidth of $\sim$80 cm^{-1} [61, 62, 77, 78].

Besides inhomogeneous broadening, a second physical process that contributes to broadening of the linewidths is important in the FMO complex. If the changes in the molecular properties are fast compared to the duration of the measurements, dynamic disorder occurs. This causes homogeneous broadening, because it is equal for the whole system. Initially hole burning spectra

provided a way to obtain the homogeneous linewidths and revealed values of ∼70–80 cm^{-1} [54]. A better description of the spectra was subsequently obtained by fully including the effects of different types of broadening to an existing model proposed earlier by the same authors [64]. The two types of broadening were included in simulations of new LD and CD spectra at low temperatures describing the whole trimer. Inhomogeneous broadening due to the variation in site energies in between subunits and complexes could especially influence the simulations of the polarized spectra. Subsequently the authors added homogeneous broadening due to dephasing, the lifetimes of the exciton states were calculated using their exciton model. Even without changing the site energies and coupling strengths from reference [61] the absorption spectra were reproduced better taking broadening into account in the system. The simulations of the LD and CD spectra were further improved by fitting the site energies and the coupling strengths to the experiments using a global fit.

To determine the different exciton states and the accompanying transition energy, several approaches were used. To start, in reference [54] exciton energies are determined by simultaneous analysis of different hole burning spectra. In this case eight exciton components were observed of which the latter two were assigned to contribute to one band around 825 nm (vide infra). Pearlstein followed a similar procedure and fitted 21 exciton energies (of which 14 degenerate, see table 4.6) to absorption and CD spectra [57]. There are two more reports on the exciton levels in the trimer, both based on the method described by Pearlstein [66, 67]. Improvements were made by using algorithms to fit the spectra and changing the site wavelengths that are used to determine the exciton levels respectively.

In further attempts to model the spectra, only monomers containing seven BChla molecules are taken into account (see table 4.7). This results in a structure with seven interconnected exciton levels. These simulations require the site energies of the BChla molecules as input parameters. Louwe *et al.* set a standard for simulations of the spectra [61]. The interaction energies are calculated in the point-dipole approximation assuming a common linewidth for all transitions of ∼80 cm^{-1}. Screening by the protein is taken into account by a dielectric constant that was used a a global free fit parameter. The initial calculated dipole strength of 68.9 D^2, is thus reduced by a factor 2.4 leading to an effective dipole strength of 28.7 D^2, a lower value than proposed by Pearlstein. This value is close to a physically relevant value of the reduced dipole strength in the range of 25 to 40 D^2. To simulate the spectra a minimum of free parameters was used to fit the essential features of the spectra. The authors proposed that the model can be improved by inclusion of vibrations, lifetime broadening of the highest energy exciton states and by allowing for different dipole strengths for the individual BChla molecules and a variation of the dielectric constant over the protein. Simulations based on the same exciton model were performed by Vulto *et al.*, Wendling *et al.*, and Iseri *et al.* (see table 4.7).

TABLE 4.6. Exciton energies of *Prosthecochloris aestuarii* in the trimer in nm.

Exciton transition	[57]	[66] [a]	[67][a]
1	779.7	777.7	789.63
2,3	780.4	777.2	790.76
4,5	789.4	787.3	792.38
6	789.8	788.5	793.31
7,8	797.4	797.0	801.53
9	799.6	800.1	801.57
10	803.8	805.1	804.10
11,12	805.5	806.3	804.73
13	813.0	811.6	812.50
14,15	814.3	812.5	815.37
16	814.7	812.8	816.46
17,18	815.3	813.8	817.82
19	824.1	825.0	824.80
20,21	826.4	828.0	825.19

[a] The degeneracy of the exciton transitions is different than proposed by Pearlstein, given in this table, and can be found in the references.

4.3.7 NATURE OF THE LOWEST ENERGY BAND

The assignment of the bands in the absorption spectrum, especially the band lowest in energy at 825 nm, has proven to be difficult. The number of excitonic states and their respective energies have been the subject of intense debate. Spectral hole burning studies show that spectral features at higher and lower energy than the burning wavelength are affected which cannot be understood when assuming non-communicating, individual BChla molecules [54]. Furthermore, the results of spectral hole burning show the presence of eight states. Two of those eight identified exciton states, which have perpendicular symmetry, contribute to this lowest exciton band at 825 nm. Models excluding the interactions between the subunits of the trimer are not successful in describing this experimental data. Therefore, Johnson *et al.* have developed a model in which this interaction is included leading to a maximum of 14 delocalized states (21 states in total, of which 14 are degenerate) [54]. This implies that the 825 nm band in is comprised of three, slightly shifted, bands of the subunits, of which two are degenerate. For the space group C_3 the states having E symmetry are degenerate while the states with A symmetry are not [79]. Due to the varying local environment there is a certain degree of static disorder in the system leading to an inhomogeneously broadened 825 nm band. The nature of the 825 nm band was confirmed to have a double origin seven years later by means of Stark hole burning studies [71]. However in this case, the nature of these states was assumed to be much more localized, with the excitons mainly spread over one BChla molecule. Structural heterogeneity in the complex leads to a variation in the excitation energy of the lowest energy state in the subunits

Table 4.7. Exciton energies of *Prosthecochloris aestuarii* in the monomer.

Exciton	A	B	C	D	E
1	827.1 - 824.4	825.6	825.7	825.0	823.8
2	816.3	815.2	814.5	814.1	813.7
3	813.0	813.5	812.2	812.8	811.5
4	807.8	806.7	805.8	805.9	804.7
5	804.8	802.7	800.8	801.5	801.0
6	801.3	800.2	796.4	799.6	797.8
7	793.6	791.5	793.0	791.5	789.4

Where A is from [54]; B is from [61]; C is from [62]; D is from [51]; E is from [64].

of the trimer. This view was tested by temperature-dependent hole burning experiments on *Chlorobium tepidum*. The 825 nm absorption band was fitted with three Gaussian bands of $\sim$55 cm^{-1} at 823.0, 825.0, and 827.0 nm respectively. The dependence of hole width and hole growing kinetics on the burning frequency confirms that there are three bands contributing to the 825 nm band. Triplet minus singlet (T-S) spectra measured by Louwe *et al.* shows that the triplet state is localized on a single BChla since it demonstrates the same properties as monomeric BChla *a* in organic solvents [74]. The orientations of excitonic transitions in the Q_y band were determined relative to the triplet carrying molecule. In contrast to earlier measurements, fluorescence line narrowing experiments showed that the 825 nm absorption band can be accounted for by a single transition in the range of 4 K to room temperature [76]. This transition is coupled to protein phonons and vibrations in the chromophore. The effect of disorder on the lowest energy band in the trimer was further studied by Monte Carlo simulations [80]. The lowest energy band could be fitted with three nearly Gaussian bands of almost identical intensity. One of those band was centered at the λ_{max} of the 825 nm band, while the other two where shifted $\sim$-17 and $\sim$+26 respectively. Summarizing, the outcome of different experimental techniques do not agree on the nature of the 825 nm band. While some say this band is due to a single transition, others include a distribution of the lowest exciton energy in the different subunits of the trimer to account for the observations.

4.4 Linear spectra of *Chlorobium tepidum*

4.4.1 Site energies

The site energies are, as in *Prosthecochloris aestuarii*, obtained in several ways: firstly as parameters in a fit of the optical spectra [65,75,77], a second approach is to calculate the electrochromic shift of the site energies due to charged amino acids [65] in table 4.8 denoted with 'S'.

TABLE 4.8. Pigment site energies of *Chlorobium tepidum* expressed in nm. The annotations M and T stand for approaches taking into account only the monomer (M) or the trimer (T).

BChla	1	2	3	4	5	6	7
[77]	806.5	793.7	823.7	814.3	800.0	800.0	804.5
[75]	780.3	806.1	822.2	799.4	800.4	804.6	796.3
[65]-M	803.5	798.7	819.3	810.7	800.6	791.1	803.2
[65]-T	805.8	798.1	819.0	811.7	801.3	791.8	803.9
[65]-S	804.5	815.3	819.3	804.2	816.7	799.4	812.0

TABLE 4.9. Lowest site energy of *Chlorobium tepidum*.

Reference	Exciton energy (nm)	Pigment number
[77]	823.7	3
[75]	822.2	3
[65]	819.3	3

4.4.2 LOWEST ENERGY PIGMENT

Since the protein structure of the FMO complex of *Prosthecochloris aestuarii* and *Chlorobium tepidum* are relatively similar (homology of 77%), it is expected that the pigment with the lowest site energy is the same in both species. This 'exit' pigment has an important role in guiding the excitation energy from the FMO complex to the reaction center, it is therefore interesting to see that in both species the tendency is towards pigment number 3 (table 4.9).

4.4.3 EXCITON NATURE OF THE FMO COMPLEX; DELOCALIZATION

As in *Prosthecochloris aestuarii* the contributions of the individual BChla molecules to an excitonic state can be calculated. Results of such calculations, as performed by a variety of research groups, are shown in the tables 4.10 and 4.11, where α runs vertically and i horizontally.

4.4.4 COUPLING STRENGTHS, LINEWIDTH AND EXCITON ENERGIES

Renger and May included dynamical fluctuations of the BChla site energies due to the protein environment, i.e. homogeneous linewidth of the transitions, in their exciton simulations [75] (see table 4.12). The authors make use of the point-dipole approximation, taking into account that the smallest interpigment distance is 11 $\mathring{A}$. The vibrations in the protein occur on a timescale much slower

Table 4.10. Contribution of the individual BChla pigments to the monomer exciton transitions in *Chlorobium tepidum*, amplitudes $C_\alpha(j)$ from [77].

transition number	1	2	3	4	5	6	7
1	-0.04	-0.07	0.92	0.37	0.06	0.02	0.01
2	-0.06	-0.03	0.35	-0.82	0.28	0.10	-0.34
3	0.91	0.38	0.07	0.00	-0.10	0.09	-0.01
4	0.08	0.09	0.12	-0.33	0.52	-0.73	0.24
5	0.04	0.04	-0.08	0.18	0.39	-0.11	-0.89
6	0.09	-0.19	0.01	-0.22	0.68	0.64	0.17
7	-0.38	0.90	0.05	-0.02	0.11	0.18	0.04

Table 4.11. Contribution of the individual BChla pigments to the monomer exciton transitions in *Chlorobium tepidum*, amplitudes $C_\alpha(j)$ from [81].

transition number	1	2	3	4	5	6	7
1	0	0	0.875	0.115	0.005	0	0.005
2	0	0	-0.114	0.597	0.110	-0.015	0.165
3	0.776	0.225	0	0	0	0	0
4	0.225	0	0.005	-0.098	-0.108	-0.030	0.759
5	0	0	0.005	-0.126	0.453	-0.416	0
6	0	0	0.002	-0.064	0.325	0.540	0.071
7	0.225	0.776	0	0	0	0	0

than the decay of the excitonic system that occur via emission of vibrational quanta. To account for this effect static disorder was introduced in the model. The coupling between the pigments and the bath, consisting of the faster protein and the intramolecular vibrations, is small enough to use a perturbative approach. The linear absorption spectrum was fitted to obtain the necessary input parameters to solve the exciton Hamiltonian. A simplex algorithm was used to find the best fit of the spectra at 5 and 107 K. Plotting the spectral density versus the differential energy clearly shows that the transitions between neighboring exciton states (e.g. 3–4) lie in a spectrally dense area, while transitions across a state (e.g. 3–5) occur in an area with a much lower density. The probability of the latter process is therefore lower and the exciton relaxation is likely to happen step-by-step down the energetic ladder as in *Prosthecochloris aestuarii* (see for examples figure 4.5). The quality of the fit shows the importance of homogeneous linewidth and the delocalization of the vibrations, that from the fits seems to span the whole trimer. Exciton simulations by Vulto *et al.* were based on the previously successful simulations in *Prosthecochloris aestuarii* by Louwe *et al.* [61]. These lie also at the basis of simulations of Abramavicius *et al.* Subsequent simulations from the same authors were based on the refined

TABLE 4.12. Exciton energies of *Chlorobium tepidum* in nm.

Exciton transition	A	B	C	D
1	825.6	825.6	825.4	823.7
2	815.5	815.4	814.4	812.0
3	809.4	810.1	808.8	806.5
4	805.4	803.2	805.4	805.2
5	803.3	795.8	803.1	802.6
6	793.0	784.7	796.9	800.0
7	790.6	775.6	792.4	796.2

Where A is from [77]; B is from [75]; C is from [84]; and D is from [82].

Hamiltonian by Brixner *et al.* [82, 83].

4.4.5 VARIABLE FLUORESCENCE IN THE FMO COMPLEX-REDOX EFFECTS

Right from the start it was noticed that there was a difference in optical properties between oxidized and reduced FMO complexes [23]. Reduction can be achieved using a freshly made solution of sodium ascorbate. The oxidized species of the FMO-RC complex [23] can be obtained chemically by treatment with ferricyanide or by illuminating, an ascorbate reduced complex, with strong white light. At room temperatures the fluorescence increases by a factor of 3-5 upon reduction of the complex [85]. Because the X-ray structure does not show any redox sensitive groups, oxidized quinones for example are excellent quenchers of excitation energy, the origin of the quenching mechanism remains unknown. The redox effects were visible both in the steady state spectra and in time-resolved measurements, where the excited state decayed back to the ground state with 60 ps and 2 ns time constants under oxidized or neutral and reduced conditions respectively [55]. The effect of light on three species of green sulfur bacteria also was the topic of a fluorescence study [86]. After increasing the amount of illumination, the fluorescence yield shows a rapid increase, after which it slowly decreases on a timescale of minutes. The modulation of the fluorescence is mainly observed around 800 nm, where the FMO complex absorbs. However still the exact origin remained unclear. Two proposed mechanisms are direct quenching in the FMO complex, through structural changes, or an indirect mechanism in which the redox state of electron carriers in the RC influence the FMO complex.

However, changes in fluorescence can also have a different origin as was shown in a temperature dependent study of the fluorescence in the FMO complex [59]. The fluorescence intensity starts to decrease from 2 K onwards to room temperature. Addition of glycerol (cryo-solvent) or dithionite to the sample did only effect the extent of the quenching, but did not stop or alter the nature of the process. A difference fluorescence line narrowing technique was

used to determine the origin of the quenching. The authors found that the origin of the quenching must lie in the 825 nm absorption band, because that is where a sharp decrease of the electron-phonon coupling occurs. An exciton explanation for this sharp decrease within the 825 nm band is favored above the explanation of energetically coupled individual BChla molecules.

In short, although several mechanisms are put forward, there still is a lack of an accepted explanation for the quenching of fluorescence within the FMO complex.

4.5 Nonlinear spectra and dynamics of *Prosthecochloris aestuarii*

Based on the simulation of the excitonic structure and the linear optical spectra it is a small, yet complex step to simulate the time-dependent behavior of the excitons. After optical excitation, the population in the exciton states eventually decays back to the ground state. The relaxation pathways and the accompanying timescales have been studied intensely by several nonlinear optical techniques and are often accompanied by theoretical investigations. These will be divided into four sections; hole burning experiments, followed by pump-probe and photon-echo experiments, 2D electronic experiments and finally new theoretical approaches.

Theoretical description of the dynamics in chromophore complexes is done according to two main lines. The first describes energy transfer between chromophores by the incoherent Förster hopping rate equation, which is valid for weak coupling between the chromophores and a strong coupling of the electronic transition to vibrational states, precluding the formation of exciton levels. Excitation energy will hop from one molecule to the other downwards in energy. However, since the existence of exciton levels in the FMO complex is well-established, the Förster hopping rate equation seems not to be the most accurate way to describe dynamics in the FMO complex. This problem was partially overcome by Iserie *et al.* who approximated the energy transfer rate between excitons by a linear combination of the Förster rates between the BChla pigments that dominate the exciton states [51]. The second approach is to describe the light induced dissipative dynamics within the framework of the multi-exciton density matrix theory. Often the Redfield approach for the description of dissipation is used. This theory combines the time-dependent Schrödinger equation for the excitonic transitions with a linear coupling to a classical bath, given by all vibrational modes of the chromophore complex [62, 75, 87, 88]. Finally, a modified Redfield approach valid for intermediate coupling regimes has been applied in [89].

Once all light-induced coherences have vanished, the time evolution of the excitonic state populations E_α can be described by the Master equation [73].

$$\frac{d}{dt}E_\alpha = \sum_\beta k_{\beta\to\alpha}E_\beta - k_{\alpha\to\beta}E_\alpha, \tag{4.3}$$

TABLE 4.13. Frequency dependent decay times of *Prosthecochloris aestuarii* in reference [91].

Wavelength (nm)	Time constant T_2 at-6K (ps)
803	0.5
808	0.8
811.5	3.1
817	4.2
820.5	6.0
823	9.9
826.5	$\geq$18
829	$\geq$19
830	$\geq$20

using the rate constants $k_{\alpha\rightarrow\beta}$, which eventually lead to a thermal equilibrium within the singly excited states.

The proposed pathways of downward energy transfer are shown schematically in figure 4.4, as drawn by the respective authors. Although they show little agreement, a few general conclusions can be drawn from these results. The energy transfer from the highest to the lowest exciton level occurs on a very fast timescale; within 5 ps mainly E_1 is populated. The population can be transferred downward either by a few big steps or by small steps including all the exciton levels.

4.5.1 HOLE BURNING

Spectral dynamics, in terms of hole widths, obtained from hole burning experiments follow a temperature dependence power law (T^{α}, with $\alpha \sim$1.3) that is typical for spectral diffusion due to a two level system of glasses and proteins [63]. Analysis of the kinetics of the three levels underlying the 825 nm absorption band result in the low-temperature lifetimes of the different states. Fitting the hole growth traces taking into account the spectral diffusion due to the glasslike protein, the lifetime of the energy transfer between the levels within the 825 nm band are 99 and 26 ps respectively. Similar reasoning holds for *Chlorobium tepidum* [90]. To bridge the gap between steady-state and time-resolved spectroscopy an elaborate hole burning experiment was performed [91]. On top of broad (800-820 nm) uncorrelated signals, sharp holes were detected. The observed hole widths are for an inhomogeneously broadened band twice the homogeneous linewidth, from which is is straightforward to calculate the excited state lifetimes (see table 4.13). The lifetimes of the exciton states that were obtained from hole burning studies were fast, (sub)picosecond, and similar to those obtained from other methods (vide infra).

4.5.2 Pump-probe and photon-echo

When researchers started to study the excitation energy transfer within the FMO complex in the early 90's, they soon realized that the dynamics occurs on very fast, subpicosecond, timescales. By studying the bleach spectrum at 2 and 10 ps after excitation, it was shown that even at those short delay times the spectrum does not exhibit a uniform bleach [92]. In this study the anisotropy decay was 2-4 ps. As was known from the linewidths of hole burning, the relaxation between exciton levels is complete within several 100's of femtoseconds [54] and does not contribute to one color anisotropy decay. Therefore, the longer, picosecond, time constant obtained from anisotropic decay traces was attributed to hopping of excitation energy between neighboring subunits and not to lifetimes of the higher exciton states.

The obtained dephasing times from hole burning experiments are considerably faster than values that were obtained from accumulated photon echo experiments by Louwe *et al.* [93]. They demonstrated that the photon echo decay is wavelength and temperature dependent, ranging from a decay <1 ps at 790 nm to 100 ps at 824 nm at 10 K and exhibits multiexponential decay. They also observed a decrease of the decay times with increasing temperatures. The wavelength dependent decay rates from the photon echo experiments are explained on the basis of phonon assisted dephasing, where the number of lower lying states determine the dephasing time. Initially it was thought that the relaxation was governed by scattering within the exciton manifold. It was concluded from pump-probe measurements that energy transfer was favored between exciton levels that lie within an energy spacing of 10 nm (120 cm^{-1}) [94]. At this energy the density of acoustic phonons might be high, so electron-phonon coupling might be the underlying mechanism of downward energy transfer. Pump-probe transients indicated a sequential relaxation of the exciton energy along a ladder of states, as was also seen in exciton simulations [51, 60, 62, 87, 94] (see tables 4.14, 4.15, 4.16 and 4.17). Figure 4.4 shows a couple of examples of this type of decay. Only at very low temperatures the dephasing might be governed by downward coherent exciton transfer. The origin of the disagreement between the dephasing times from both measurements are unclear but might have to do with the distinct experimental conditions tuning into different mechanisms underlying the energy transfer in the complex.

In a more elaborate study Louwe *et al.* decided to take another look at the possible coherent nature of exciton transport by studying the FMO complex at 1.4 K with accumulated photon echoes and transient absorption [95] (see table 4.18). Due to the broad exciton levels, they probed several excitonic transitions at the same time resulting in traces with multiple time constants. At long wavelengths (815-830 nm) 5, 30, 110, and 385 ps were found, while at shorter wavelengths (795 nm) the decay was in the order of 100 fs. The FMO complex was described as pigments coupled to a two level system (TLS, double-well potential, in between which tunneling occurs) which is in its turn coupled to a phonon bath. Fluctuations in the interactions between pigments due to transitions in the TLS is the main dephasing pathway in glasses below 10 K. The

TLS transitions can both influence the dipole interactions between the pigments (low frequency transitions in TLS corresponding to large displacements in the protein) as well as the site energies (high frequency, smaller displacement). At low temperatures the coherent energy transfer is mainly limited by this coupling. Above 10 K, the contribution of the TLS tunneling is a minor contribution to the dephasing mechanism, that are dominated by other processes. With these measurements their earlier results from a preliminary study [93] were confirmed.

Several years later interesting features were seen in low temperature two-photon echo (2PE) signals of both *Chlorobium tepidum* and *Prosthecochloris aestuarii* [96]. At 1.27 K, the 2PE signals show oscillations that increase in intensity when the excitation is tuned to the red edge of the absorption spectrum (up to 40% of the total amplitude for excitation at 832 nm). These oscillations last up to 300 ps and are ascribed to vibrational states of the BChla molecule in the ground state. Fourier transforms of the 2PE traces show that the obtained frequencies match those from previous studies. In the same study it was shown that the general theory to describe the results of photon echo experiments did not account for the current results. The typical δ shape for dynamics in the Markov limit at initial time delays was not observed. Therefore, the dynamics was described beyond the Markov limit where a system-bath memory effect occurs which, among others, results in the delayed growing in of coherence in the system. At that time it was unclear if this had a specific function in light-harvesting.

Vulto *et al.* used a similar approach as before in the simulation of the static spectra, however to introduce dynamics, coupling of the electronic excitations to the vibrational modes in the system was included [62]. Homogeneous broadening within the system was not incorporated in the model. Due to the weak coupling, the exciton-vibrational coupling can be treated as a perturbative term in the Hamiltonian. The distinct timescales of dephasing and the bath correlation times leads to the decoupling of the dynamics of population and coherence. The excited state dynamics therefore is governed by population relaxation. Similarly, in the simulations of Renger and May the frequency dependent coupling of the electronic states in the systems to the surroundings is needed. To describe this the phonon side band in a fluorescence spectrum is fitted. Using this analytical description for the spectral density, the time resolved spectra can be fitted quite nicely. As was shown before, the exciton relaxation occurs mainly between adjacent levels. The number of states lower in energy determine the relaxation rate of an exciton level, however important additional factors are the energy difference between the two levels and the overlap between the excitation probability densities on a single pigment j (i.e. $|C_\alpha(j)|^2|C_\beta(j)|^2$). The authors noted that the spectra of *Chlorobium tepidum* fitted remarkably better than those of *Prosthecochloris aestuarii*, in particular an experimental decay time of 1.7 ps was not reproduced. This could be partially overcome by adjusting the site energies of especially BChla 1 and BChla 4. The energetic order of these pigments, which are the main contributors to the second lowest exciton states (E2), seems of importance for the dynamics in the system. This was further tested by introducing inhomogeneous broadening in the system by a Monte Carlo simulation of the

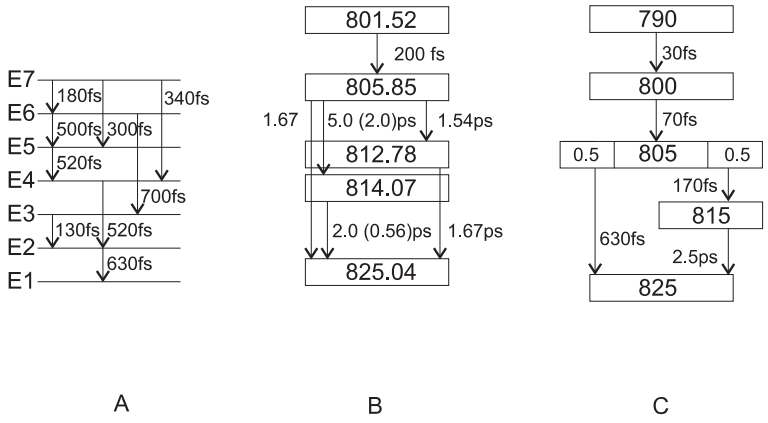

FIGURE 4.4. Proposed relaxation pathways of the exciton energy in the FMO protein, examples as given in the original references. The 7 single exciton levels are represented by E1 through E7. Model A from [62], B from [51], C from [60].

spectra and the dynamics. Additional to the decay time constants, distributions of time constants centered around the originally simulated values were found. At the exciton level E2 this distribution showed a clear distinction between two time domains; one of several 100's of fs and another of several ps, the latter is in the same order as the experimentally observed timescale. The spectra resulting from the Monte Carlo simulations are very similar to the dressed stick spectra calculated earlier [77]. Vulto *et al.* showed that the method of Renger *et al.* does not reproduce the T-S and LD spectra at all, and concluded that their description of the electronic structure of the FMO complex was not completely correct. However the ingenious way of describing the spectral broadening of the transitions by Renger *et al.* could be used to improve future simulations.

The decay time for energy transfer from the lowest exciton state to the ground state varies widely between different techniques and research groups. Table 4.19 gives a clear indication that there are two timescales concerned with the lowest exciton lifetime; one of about 100 ps and a longer one of several ns. A more elaborate description of this lifetime for *Chlorobium tepidum* is found in section 4.4.5.

4.5.3 2D-SPECTROSCOPY

In the last 5 years an additional technique was used to study exciton dynamics in the FMO complex: 2D spectroscopy. This technique directly shows the frequency correlation between excited states. When there is coupling between the different states, as is the case in the FMO complex, excitation of one state influences the others.

2D electronic spectroscopy on the FMO complex is mainly used to elucidate the time- dependent couplings between exciton states. This does not provide a direct way of measuring the site energies of the individual pigments. However, in

TABLE 4.14. Frequency dependent decay times of *Prosthecochloris aestuarii* [94].

Wavelength (range) (nm)	Time constants-10K (ps)
blue edge	<0.1
804	0.5
812	0.17
815	5.5
823	37

TABLE 4.15. Decay times from global analysis of pump-probe spectra of *Prosthecochloris aestuarii* at 19 K [60].

Number	τ (ps)
1	0.170
2	0.630
3	2.5
4	11
5	74
6	840

TABLE 4.16. Frequency dependent decay times of *Prosthecochloris aestuarii* [51].

Wavelength (range) (nm)	Time constants-10K (ps)
801.52	0.2
805.85	1.54, 5.0 (2.0)[a] , 1.67
812.78	1.67
814.07	2.0 (0.56)

[a] There was no distinct difference in the quality of the fit between the kinetic model a and b (in parenthesis).

TABLE 4.17. Lifetime of exciton states of *Prosthecochloris aestuarii* by exciton calculations [87].

Exciton number	τ (ps) 4 K	τ (ps) 77 K	τ (ps) 265 K
1	∞	193	8.5
2	82	33	3.5
3	7.4	5.8	1.8
4	8.8	6.6	2.0
5	4.0	3.3	1.4
6	2.0	1.9	1.1
7	1.8	1.8	1.2

Table 4.18. Frequency dependent accumulated photon echo decay times of *Prosthecochloris aestuarii* at 1.4 K [95].

λ_{max} of DAS [a] (nm)	Decay time (ps)
827	385
826	110
824	30
818	5

[a] DAS spectra originate from a global analysis were the amplitudes of the different decay components are plotted against the wavelength resulting in distinct bands.

Table 4.19. Decay times of the lowest exciton level at 77 K of *Prosthecochloris aestuarii*.

Reference	τ (ns)
[95]	0.25, 3
[94]	>0.8
[63]	2
[87]	0.19

2D electronic spectroscopy the coupling between the exciton states will appear in the spectra directly as so-called cross peaks [83]. In the FMO complex the cross peaks in the 2D spectra overlap with broad and strong diagonal peaks, due to the high spectral density. To overcome this problem a technique in which the diagonal peaks can be eliminated and the cross peaks are brought out was developed [97]. The technique is based on a scheme known from 2D vibrational spectroscopy and uses polarization of the first two pulses to select the cross peaks. Since most of this work has been done using *Chlorobium tepidum*, more on this topic can be found in the next section.

To extract the contributions of the various energy decay processes in a congested 2D spectrum polarization dependent 2D spectroscopy was used [89]. In contrast to the previous study [97] is the measurement of both the rephasing and non-rephasing spectra. In the non-rephasing spectra the diagonal linewidths of the exciton transitions are narrower and therefore a higher resolution can be obtained. Furthermore, the authors made use of two polarization combinations for separate 2D experiments. Theoretically it is possible to obtain the projection angle ϕ between a pair of exciton states from the ratio between these two polarization combinations. In the nonrephasing spectra a strong cross peak at 804, 814 nm appears while changing the polarization from one to the other polarization combination. By calculating the amplitude factor of the cross peaks depending on ϕ for the two polarization cases, it was shown that an angle of 40° reproduced the measured 2D data. This implies that without previous

knowledge about structural properties of the system, a tentative view of the orientation of transition dipoles can be obtained. The current models of the FMO complex predict that excitons 2 and 4 have a high dipole strength and are the main contributors to the peaks in the spectrum at 804 and 814 nm. Furthermore, the corresponding exciton states have a projection angle of 38° verifying the results from the polarization dependent 2D experiments. Using the same idea of polarized fields in a theoretical study, contributions of coherent evolution and incoherent energy relaxation to a 2D spectrum could be separated due to a specific choice of the polarizations of the incoming pulses [82].

4.5.4 New theoretical approaches

As the exciton dynamics in the FMO complex is well studied and understood a possible next step is to try and influence this dynamics. Following that route, specially shaped laser pulses are calculated using an optimal control algorithm and applied to the FMO complex [87]. These pulses lead to a superposition of excitonic states, an excitonic wavepacket, with the target to populate just a single chromophore at a given time. The theoretical framework is given by the multi-exciton density matrix, and although the dissipation is damping the wavepacket at low temperatures the target can be reached quite well. In a follow-up paper the additional effects of inhomogeneous broadening and orientational averaging were included [88]. Again, the target could be reached although to a lesser extend. The introduction of a laser field, shaped in both polarization directions, lead to a larger target state population, partially working against the energetic and oriental averaging.

Under conditions encountered by the FMO complex in vivo it is very likely that multiple excitations occur within one complex. These double excited states are more complicated than its single counterpart and are less well studied. Often 2D spectra are obscured by overlapping contributions of single and double exciton resonances. By looking at a smart representation of the 2D spectra using a particular set of pulses, the correlated dynamics of the double excited states can be probed [84]. Strong peaks are observed for double exciton states 1,7 and 18, that also happen to be the most delocalized states in the system. Additionally, weaker signals of exciton states 9, 16 and 17 are observed. Instead of calculating the wavefunctions of the different exciton states an alternative method can be used to describe the behavior of excitons in aggregates. In the quasiparticle approach, all the properties of the system are described in terms of scattering and double exciton energies are simply given by a sums of single exciton energies. Comparing the spectra resulting from the full calculation with that of the quasiparticle approach shows that the energies at which the peaks appear in the spectra agree, while the fine structure in the spectra of the quasiparticle approach is distorted. To approximate the spectra the quasiparticle approach can be used, however because the exciton coupling is strong, which is neglected in this approach, and the nonbosonic nature of the excitons a full calculation of the spectra is necessary for detailed analysis.

New types of 2D techniques can be developed by introducing pulse polariza-

tions as variables into standard 2D schemes, as described in the previous section. This, amongst others enables the dissection of the congested 2D spectra into incoherent and coherent contributions and provides interesting perspective for new control strategies [82, 98].

4.6 Nonlinear spectra and dynamics of *Chlorobium tepidum*

4.6.1 Hole burning

Pressure dependent hole burning experiments showed that the excitonic band at 825 does not change with pressure at 4.2 K. The dephasing time, corresponding to the measured hole widths, is equal to 35 ps in all cases [99]. Reddy *et al.* give two explanations for the observed decay: electron-phonon coupling destroys the C_3 symmetry and the excitation is trapped on one subunit with a rate of 35 ps, secondly dephasing could occur due to equilibration between split levels in the 827 nm exciton state induced by low-frequency phonons.

4.6.2 Pump-probe and photon-echo

Room temperature pump-probe experiments with an increased time resolution refined the findings of the earlier experiments on *Prosthecochloris aestuarii* [100]. One color experiments showed a 450 fs decay at 796 nm together with a time constant of several tens of ps (table 4.20), the latter was also observed at 821 nm. The femtosecond component was assigned to downward energy transfer to lower exciton levels. Two color experiments, 800 nm pump and 820 nm probe, showed a rise-time of 350 fs which was taken to be directly related to the decay time at higher energies in the one color experiments. These combined results indeed proved that downward energy transfer from higher excitonic states occurs on a timescale of 100's of fs [101] (table 4.21). Additional experiments by the same authors revealed that the ultrafast components ranged from 100–900 fs depending on pump and probe wavelengths. A comparison between room and low temperature pump-probe experiments showed the slowing down of some of the decay processes from several hundreds of femtoseconds at 300 K to 10 ps at 19 K [102] (table 4.22). However, even at these low temperatures some femtosecond processes still occur. Global fitting of pump-probe spectra of *Chlorobium tepidum* at 19 K resulted in several observed time constants; 170 fs, 630 fs, 2.5 ps, 11 ps, 74 ps, and 840 ps (figure 4.5).

Gulbinas *et al.* did pump-probe measurements on longer timescales in which they found three major time components using global analysis [55]. The two longest time components depended on the addition of a reducing or oxidizing agent during the sample preparation (table 4.23). At room temperature, the fits resulted in decay times of 7 ps, 60 ps and 2000 ps. At 77 K, similar time constants showed up, 7.4 ps, 104 ps and 1020 ps. When plotting the amplitudes of the different decay components a 26 ps time constant was found and attributed

to energy transfer from heated pigments to vibrational modes of the protein. Similar results where obtained by analyzing the pump-probe and fluorescence spectra in a range from 6 to 160 K with a combination of global and single-band analysis [103]. Three distinct time constants with wavelength dependent sign of their amplitudes where needed to fit the kinetic pump-probe traces: 0.25 ± 0.15 ps, 1 ± 0.2 ps and a decay constant of 150 ps spreading over the whole spectrum assigned to the excited state lifetime (table 4.24). Low temperature picosecond fluorescence were discussed in terms of solute-solvent interactions and showed four distinguishable time constants: a rise time of 10-20 ps, a fast decay that varied between 7-60 ps and two slower decay times of 200 ps and 2 ns [103]. Their respective amplitudes change depending on the detection wavelength. The interaction between solute and solvent is formally described by the relative response function, that depends on the peak energy at a given time in the time-dependent emission spectra. The relative response function for the FMO shows changes from 1 ps up to 10 ns. Fitting the curve resulted in four time constants which were linked tentatively to physical processes in the pigment protein complex. Firstly, the fast time constant of 5.4 ± 1.3 ps was linked to exciton relaxation within a monomer. Secondly, the time constant of 26.7 ± 7 ps was linked to energy transfer between the different subunits in the complex, this is in agreement with results from anisotropy measurements (vide infra). The two remaining time constants are attributed to solvation effects; in 163 ± 58 ps the protein trimer configuration relaxes followed by relaxation in the whole system including the protein and its frozen surrounding in 1930 ± 590 ps.

Savikhin *et al.* were the first to detect oscillations in the anisotropic decay dynamics at 19 K [104, 105]. These oscillations have a period of roughly 300 fs and last up to 1 ps. Since the phase of the oscillations is shifted by a factor of π in the parallel and perpendicular polarization traces, they are hardly visible in the isotropic decay dynamics. Refinement of these measurements showed that the period of the oscillations is ∼220 fs which corresponds to 150 cm^{-1}, the energy gap between the 815 and 825 nm band [104, 105]. Due to the fact that the amplitude of the oscillations was dependent on the overlap of the laser with the 815 and 825 nm bands, quantum beating between the two levels was assumed to be the origin of these rapidly dampened (<1ps) oscillations. A mathematical description required the presence of perpendicular transitions within the 815 and 825 nm band, the presence of which were verified by simulations of CD spectra. Simulations by Renger *et al.* confirmed that these oscillations arise from quantum beating between exciton levels are dampened in about 1 ps and have a period of 220 fs [75].

At higher excitation densities it is possible that exciton energy transfer between single excited monomeric subunits occurs and leads to annihilation of excitations. One way to observe this is in the anisotropy decay of pump-probe experiments. There are only a few reports for singlet annihilation with timescales of 26 ps and 13 ps respectively [103, 104] (table 4.25). Because energy transfer within one monomer occurs as seen above on a much faster timescale (∼100 fs) it is likely that the energy transfer between monomers leading to annihilation proceeds mainly between the pigments on which the lowest energy excitons are

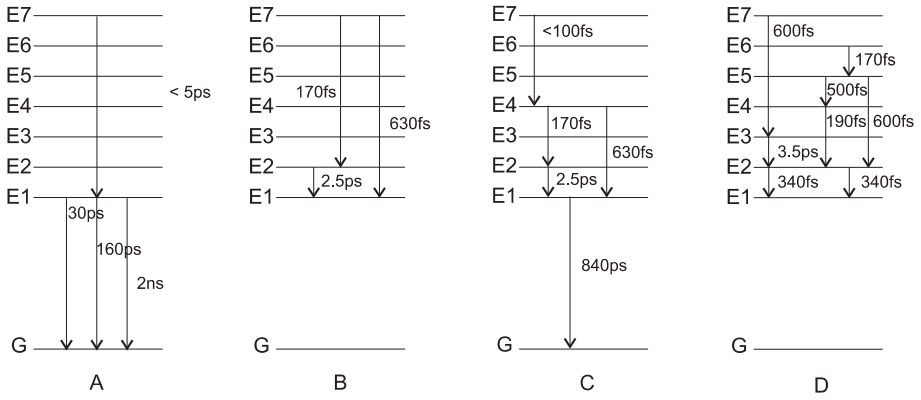

FIGURE 4.5. Proposed relaxation pathways of the exciton energy in the FMO protein. G denotes the ground state and the 7 single exciton levels are represented by E1 through E7. Model A from [103], B from [104], C from [105] and D from [83].

TABLE 4.20. Frequency dependent decay times of *Chlorobium tepidum*, room T, one-color experiments from [101] [a].

Wavelength (nm)	Time constants (ps)
773	0.011, 0.318, 152
790	0.058, 0.417, 21.8
798	0.047, 0.424, 25.3
806	0.018, 0.253, 13.3
815	0.064, 23.8
825	0.108, 27.6
835	0.066, 22.8

[a] In the case of more experiments per wavelength, the first one stated in the original paper is used in the table.

located. Another way of determining the singlet annihilation time constant is by changing the fluence in transient absorption spectroscopy. Under high excitation conditions, generating more than one exciton per trimer, the kinetics could be fit with multiple exponents [55]. The amplitude of only one of the components, 7 ps, was found to change upon increasing fluence and therefore must correspond to the energy equilibration between the monomers. Temperature dependent pump-probe spectra showed isotropic decay traces depending on the laser fluence [102]. Decay rates longer than 10 ps were accelerated, mainly coming from the annihilation of excited singlet states with triplet states that were accumulated due to the high repetition rate in this experiment.

TABLE 4.21. Frequency dependent decay times of *Chlorobium tepidum*, room T, two-color experiments from [101] [a].

Wavelength (pump-probe) (nm)	Time constants (ps)
800-830	-0.159 [b], -0.412, 52.5
830-800	-0.228, -0.991, 53.5
790-820	-0.067, -0.348, 47.5
780-810	-0.152, -0.838, 43.1
770-800	-0.405, 45.4
810-780	-0.110, -0.941, 27.1

[a] In the case of multiple experiments per wavelength, the first one stated in the original paper is used in the table. [b] The negative signs in front of the decay times correspond to a rise component.

TABLE 4.22. Frequency dependent decay times of *Chlorobium tepidum*, room T, two-color experiments in [102] [a].

Temperature (K)	Time constants (ps)
19	-0.64 [b], -3.1, -13, 765
52	-0.92, -7.5, 56, 483
130	-0.64, -4.3, 25, 292

[a] Pump 812, probe 829 nm. In the case of more experiments per wavelength, the fits from experiments with 70/100 μW pump-probe power are used in the table. [b] The negative signs in front of the decay times correspond to a rise component.

TABLE 4.23. Temperature dependent decay times (ps) of *Chlorobium tepidum* at 77 K and room T, from [55], results are from global analysis of the data.

τ	298 K	77 K
1	7	7.4
2 [a]	60	104
3 [b]	2000	1020

[a] Oxidized and neutral form of the FMO complex. [b] Reduced state of the FMO complex.

TABLE 4.24. Decay times of the lowest exciton level of *Chlorobium tepidum* at 77 K.

Reference	τ (ns)
[103]	0.15, 2
[105]	0.84 (300 K)
[101]	0.1
[55]	0.1, 1

Table 4.25. Anisotropy decay of *Chlorobium tepidum*.

Reference	decay (ps)
[101]	75-135, 1.4-2.0 (298K)
[102]	8.4 (19K)
[102]	4.5 (28K)
[102]	1.9 (52K)
[102]	0.5, 3.5 (101K)
[104]	0.140-0.180 (between 815–825 at 19K)

4.6.3 2D-spectroscopy

Brixner *et al.* started with 2D electronic measurements on the FMO protein [83]. This technique indirectly reveals the energy transfer pathways by means of the off-diagonal cross peaks in a 2D plot where one axis corresponds to the pump pulse, and one axis to the probe pulse. The dynamics is represented by a change of these peaks depending on the delay time between pump and probe. A model of the 2D spectra was obtained by adjusting the site energies, as proposed by Vulto *et al.*, slightly and by reducing the coupling between BChl 5 and BChl 6 [77]. Further simulations of the spectra employed Förster or modified Redfield theory depending on the coupling strengths (cutoff at 30 cm^{-1}). It revealed two energy decay pathways along exciton levels: $7 \rightarrow 3 \rightarrow 2 \rightarrow 1$ and $6 \rightarrow 5 \rightarrow 4/2 \rightarrow 2/1 \rightarrow 1$ (see figure 4.5 and tables 4.26 and 4.27) [81]. Important in the analysis of the 2D spectra is that rapid energy transfer between exciton levels can occur without occurrence of cross peaks in the spectra if the corresponding combination of transition dipole moments is small.

To simulate 2D electronic spectra of an ensemble of FMO complexes from *Chlorobium tepidum* a non-perturbative approach in the field strength was used [106]. The signal in different, phase-matched, directions was calculated by summing over an ensemble of distributed molecules. As a result this technique is not limited to the 3rd order in the field, but also higher orders are obtained in their respective phase matched directions. Exciton dynamics of the system was calculated using a multi-exciton density matrix approach including up to two excitons. The cross peaks observed in the experiments by Brixner *et al.* relate via the simulations to relaxation between the following exciton levels: $E_3, E_4, E_5 \longrightarrow E_2$; $E_4, E_5 \longrightarrow E_1$; $E_2 \longrightarrow E_1$ and weaker $E_7, E_6 \longrightarrow E_5 .... E_2$ (see table 4.28). Under high excitation conditions mainly the two-exciton states are populated. The spectrum remains its general shape although it is slightly broader and less structured.

By exciting the FMO complex with a laser pulse that spans several exciton levels a coherent superposition of states is created, analogue to a wavepacket in the vibrational regime. Theory predicts that this coherence manifests itself by beating signals with frequencies that correspond to the energy difference in the excited exciton states. Indeed this beating appeared in 2D electronic

spectroscopy, e.g. in the 825 nm crosspeak the oscillations remained up to 660 fs [35]. Not only are the oscillations visible in the amplitude of the cross peak, they also appear in the shape. The oscillations in the peak width, ratio between the diagonal (inhomogeneous broadening) and anti-diagonal width (homogeneous broadening), are anti-correlated with the oscillations in the amplitude. The protein envelope might play an important role in sustaining the coherence during energy transfer and might even be creating new coherences. To model the energy transfer within the FMO accurately long lasting coherence needs to be taken into account, complicating current models.

TABLE 4.26. Transfer times between of the exciton levels of *Chlorobium tepidum* at 77 K from [83].

Exciton transition	transfer time (ps)
7-3	0.63
3-2	3.6
6-5	0.17
5-4	0.5
5-2	0.63
4-2	0.19
2-1	0.34

TABLE 4.27. Lifetime of exciton states of *Chlorobium tepidum* by exciton calculations in reference [81].

Exciton Number	total decay time (ps)
1	8.3
2	0.28
3	2.2
4	0.15
5	0.21
6	0.12
7	0.41

4.7 CURRENT CONSENSUS AND FUTURE DIRECTIONS

Slowly the choice of parameters used to simulate the results obtained from various optical techniques are converging. About 15 to 20 years ago, little agreement existed on whether to include the whole trimer or just the monomer in the simulations of the spectra, on the values of the site energies and how to obtain them, and on the location of the lowest energy pigment. Nowadays these issues seem more or less resolved: Only the monomer is taken into account in

Table 4.28. Transfer times between of the exciton levels of *Chlorobium tepidum* at 77 K in reference [106][a].

Exciton transition	transfer time (ps)
7-3	0.16
3-2	2.9
6-5	0.32
5-4	1.2
5-2	0.34
4-2	0.34
2-1	0.22

[a] for direct comparison to the 2D data in table 4.26, only the rates mentioned by Brixner *et al.* are given in this table

simulations, as is inhomogeneous broadening due to structural changes, BChla 3 is principally assigned to have the lowest site energy. The parameter set from Louwe *et al.*, including the site energies, are widely used in increasingly complex simulations. The latest addition to this is a new approach to calculate site energies instead of fitting them, using amongst others quantum chemical methods. The possible influence of the recently proposed eight BChla molecule on the variety of optical spectra could invoke new studies. It is conceivable that new detailed simulations including this pigment can lift the remaining discrepancies between experimental and theoretical spectra.

While the exact energy transfer timescales within the exciton manifold vary between techniques, it is agreed upon that decay to the lowest exciton state occurs within several picoseconds. Despite this rapid decay, an interesting fact is the prolonged presence of coherence observed in the complex. This coherence, and its potential role in mediating efficient energy transfer, is the topic of current research using advanced techniques such as 2D electronic spectroscopy and coherent control strategies with shaped excitation pulses.

5 Ultrafast spectroscopy on the FMO complex

This chapter addresses different aspects of measurements on energy transfer within the FMO complex. At first the exciton energy equilibration within the complex is described at high excitation fluence. In this case multiple photons excite one complex and energy is dissipated by annihilation. Secondly, control over the exciton energy decay within the complex by control schemes was pursued.

5.1 Exciton annihilation in the FMO complex

5.1.1 Introduction

The primary steps of photosynthesis comprise of the generation of electronically excited states in a so-called antenna system by the absorption of light. The antennas often consist of a multitude of pigments such as chlorophylls [25,107–110]. Due to the interaction between these, often closely spaced, pigments the description in terms of localized, electronically excited states no longer holds and the system must be described in terms of excited states that are 'shared' between some of the pigments, the exciton states [34]. Subsequent decay within the exciton manifold is followed by energy transfer from the antenna pigments to a reaction center where the excitons are trapped and electronic energy is transformed into chemical energy. This process is well-known to occur in plants, but it also plays an important role in the metabolism of green sulfur bacteria. These organisms also rely on sunlight as an energy source. In between the antenna and the reaction center in green sulfur bacteria lies another, secondary, antenna. This antenna is referred to as the FMO protein, named after its discoverers Fenna, Matthews and Olson, and consists of a trimer, each of the subunits containing seven bacteriochlorophyll a pigments. In chapter 4 an extensive overview of this protein and its optical properties was given.

A little studied, but highly interesting aspect of energy transfer within the FMO complex is the energy dissipation at high exciton densities, as generated by excitation with intense laser pulses. When two excitations in the S_1 state of the pigments are sufficiently close, their excitation energy can be used to create a higher excited state S_n at one chromophore, leaving the other in the ground state. This process of exciton-exciton annihilation can be used to study the electronic structure of antenna complexes [111]. It can further be used to determine the coherence length of the exciton and the exciton hopping time [112]. The exciton energy transfer, underlying annihilation, between monomeric subunits

of the FMO protein can be observed using several experimental techniques. One of the possible ways to observe this type of energy transfer is through the anisotropy decay in pump-probe experiments. There are only a few accounts on exciton annihilation in the FMO complex. One of them has assigned time constants of 26 ps and 13 ps to singlet annihilation [103, 104]. Since energy transfer to the lowest exciton level within one monomer occurs on much faster timescales (∼100 fs), it is likely that the energy transfer between monomers proceeds mainly between the pigments that participate in the lowest exciton levels. Another way to determine the singlet-singlet annihilation time is by changing the fluence in transient absorption spectroscopy. Under high excitation conditions, generating more than one exciton per trimer, the time traces could be fit with multiple exponents [55]. The amplitude of only one of the exponents, a 7 ps time constant, changed upon increasing fluence and therefore was assigned to annihilation between the monomers.

Here, in contrast to previous studies, exciton annihilation within one monomer of the FMO complex is studied. Data obtained by pump-probe spectroscopy at high pump intensities is compared to exciton simulations to extract the effects of excitation annihilation.

5.1.2 EXPERIMENTAL

Time-resolved transient absorption spectroscopy was performed using an amplified Ti:Sapphire system (Clark CPA-2001) producing pulses at a 1 kHz rate (PUSH). Part of the output was sent into a non-collinear optical parametric amplifier (NOPA) to generate near transform-limited pulses centered at 795 nm with a bandwidth of ∼30 nm. These pulses were used to excite the sample (pump). Broadband probe pulses (740-850 nm) were obtained from a white light continuum by focusing the output of a second NOPA centered at 1100 nm into a 2 mm sapphire crystal. The time resolution in the transient absorption measurements was determined by cross correlation to be approximately 80 fs. The diameter d of the pump beam in the focus was 150 μm. FMO complexes from *Chlorobium tepidum* were kindly provided by Prof. Mette Miller of the University of Southern Denmark. The complexes were dissolved in 50 mM Tris/HCl (pH 8.0) and 30 mM sodium ascorbate. Glycerol was added (66 % v/v) to obtain a clear glass at low temperatures. The sample was placed in a plastic 1 mm cuvette and inserted into a cryostat (Optistat CF, Oxford instruments), where it was cooled down to 77 K. The cuvette was rotated, in the plane perpendicular to the laser axis, using a home-built cryo-rotator [24] to avoid photo-degradation of the FMO complexes. The excitation energy E_{exc} was varied between 40 and 400 nJ/pulse in steps of approximately 40 nJ. At these excitation energies the transient spectrum was measured at four different pump-probe delay times (-0.5, 0.5, 5 and 15 ps) to obtain a saturation/linearity curve. Full kinetic traces, up to 400 ps, were measured for excitation energies of 120 and 240 nJ/pulse.

5.1.3 Transient absorption spectroscopy

To observe exciton-exciton annihilation within one FMO monomer, it is important that there is a sufficient amount of double excitations. To calculate the amount of absorbed photons per FMO monomer, the following set of equations, beginning with the well-known Lambert-Beer law for absorption, were used.

$$\begin{aligned} A = \epsilon C l = -log\left(\frac{I}{I_0}\right) \\ N_{mol} = \frac{A}{\varepsilon l}\frac{\pi d_{laser}^2 l}{4} \end{aligned} \tag{5.1}$$

Here the absorption A at 800 nm in the experiments is 0.5 and the value for the molar absorption coefficient ϵ is 153.10^3 $M^{-1}L^{-1}$ for BChla molecules in the FMO complex [113]. The concentration C is unknown, but can be calculated using equation 5.1. The number of photons absorbed per FMO monomer N_{phabs} follows by a summation over the absorption, $s(\alpha)$, of the seven respective exciton levels α.

$$N_{phabs}(\alpha) = s(\alpha)N_{ph} \tag{5.2}$$

In this expression the absorption of the exciton levels is obtained by integrating the overlap of the linear absorption spectrum $D_\alpha(E)$ with the laser spectrum used to excite the complex $N_{ph}(E)$.

$$s(\alpha) = \int dE D_\alpha(E) N_{ph}(E) \tag{5.3}$$

The absorption spectra of the individual exciton states were calculated and are shown in figure 5.1. The experimental laser spectrum is simulated using a Gaussian shape according to

$$N_{ph}(\omega(E)) = N_{ph}\frac{1}{\sqrt{2\pi\sigma^2}}\exp\left(-\frac{(E-E_0)^2}{2\sigma^2}\right). \tag{5.4}$$

Due to spectral mismatch between the laser and the linear absorption spectrum, the maximum number of photons absorbed is reduced by a factor 2. Figure 5.2 shows the saturation curve for the excitation energies in the range of 40-400 nJ. It is apparent that the relation between the excitation energy and the signal is not linear, especially above 300 nJ the signal does not increase any longer, i.e. the transition is saturated. The same figure also shows the number of absorbed photons per FMO monomer, that varies linearly with excitation energy between 1 and 10 for the range of excitation energies. At 240 nJ, the highest excitation power used in the pump-probe experiments, about 7 photons per FMO monomer are absorbed. This implies that the 7 pigments are all singly excited and by using the Poisson distribution, the amount of double excitations is ∼3-4 per FMO monomer. As this calculation does not take into account the saturation of the transition, figure 5.2 will present a rough estimate.

The transient absorption matrix, wavelength vs pump-probe delay, at an excitation energy of 240 nJ is shown in figure 5.3. Clearly visible are the three

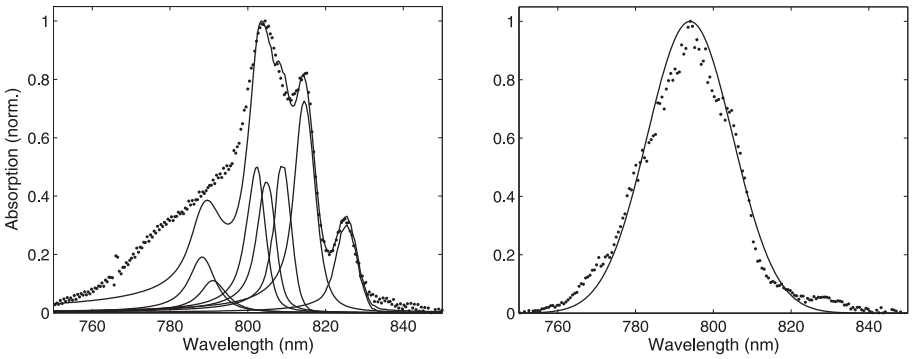

FIGURE 5.1. [Left] Linear absorption spectrum of the FMO complex at 77 K (dots) and simulations of the seven exciton levels and the total spectrum (line). [Right] The experimental and simulated laser spectrum are represented by the dots and the line respectively.

distinct peaks at 805, 815 and 825 nm that are characteristic for the FMO complex at 77 K. These peaks correspond to the inverse of the linear absorption spectra indicating that the majority of the signal can be attributed to ground state bleach and stimulated emission since it is known that the pigments in the FMO complex show a small, $\sim$18 cm^{-1}, Stokes shift [59]. For further inspection, the transient spectra – horizontal cuts from the matrix – are plotted in figure 5.4. In addition to the three peaks, the blue side of the probe range (765 nm and lower) shows a small positive signal, most likely coming from excited state absorption from single to double or higher exciton states [62,100,101,103]. Figure 5.4 also shows vertical cuts from the matrix that represent the time decay of the TA signals. Single trace fits do not give representative decay times of downward energy transfer in the complex. For example, the spectral band at 805 nm consists of contributions from several, broadened, exciton states, hence at this frequency a weighted sum of transitions between the exciton states will be probed, instead of a single transition. Since there are seven exciton states, theoretically there are nearly hundred distinct decay pathways between these states. Nevertheless, some preference is imposed by the coupling between the exciton levels, i.e. transfer between levels that correspond to pigments that are relatively far apart is not likely to occur. A better description of the data is obtained from simulations, based on the electronic structure of the pigment-protein complex. The outcome of such simulations in comparison to the data can be used to assign the relevant decay pathways and their corresponding decay time constants [87]. A full treatment of the different simulation methods can be found in chapter 4.

The dynamic traces in figure 5.4 do reveal an interesting feature that supports the notion of downward population transfer of the exciton levels after excitation at the top of the manifold with an 800 nm pump. Whereas the sub-picosecond decay at 805 nm has a relatively large amplitude compared to the

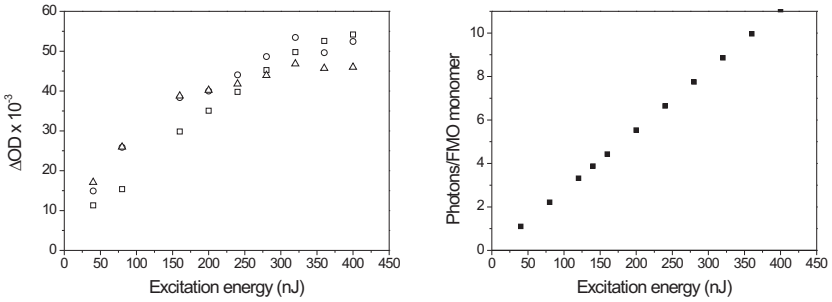

Figure 5.2. [Left] Experimental saturation curve showing the TA signal at 5 ps at frequencies 805 (squares), 815 (circles) and 825 nm (triangles). [Right] Calculated number of photons absorbed per FMO monomer versus the excitation energy. The calculation does not take into account the possible saturation of the transitions around 800 nm, as shown in the left panel.

other decay time constants, at 825 nm a rise of the signal is observed with a comparable short time constant. Similarly, in the transient spectra the relative amplitude of the band at 825 nm increases. This implies that in the course of time the population of the lowest exciton level increases. All wavelength components in the probe range show a long decay constant of several hundreds of picoseconds. This time constant can be assigned to several processes, most likely it corresponds to the lifetime of the lowest exciton state that varies, depending on the preparation method of the sample, between 200 ps and 3 ns [63,87,94,95]. Although single trace fitting is not the preferred tool to analyze this complex data, it has revealed qualitative information about the dynamics within the exciton manifold. The high energy exciton states decay to the bottom of the exciton manifold within 1 ps. This decay leads to a rise of the transient signal at longer wavelengths, the spectral region that corresponds to the lower exciton states. Also, the fits show a long decay component of several tens of ps that is assigned to the relaxation of the lowest exciton state to the ground state. However, for further quantitative analysis of the data, sophisticated simulations are needed.

5.1.4 Simulations

Simulations of exciton-exciton annihilation are not straightforward as they require the system to be described at least as a three level system, using S_0 as the ground state and S_1 and S_n as the first and higher excited states. Upon annihilation between two excitons, a second excited S_n state is occupied. From this level usually fast internal conversion to the S_1 state occurs. Exciton simulations, performed by Dr B. Brüggemann, make use of density matrix theory [114]. This method has been described in the previous chapter and details can be found

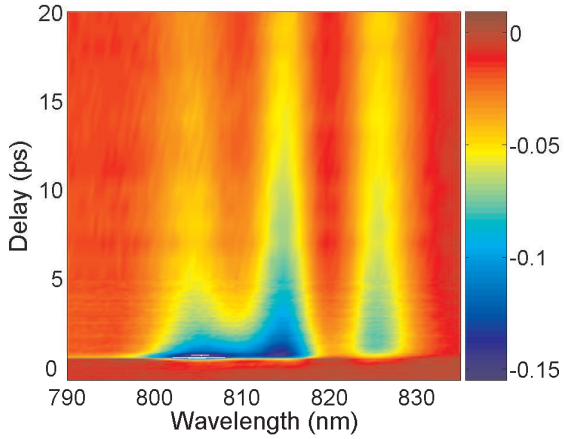

FIGURE 5.3. Transient absorption spectra at 77 K, pump 800 nm, 80 fs FWH, 240 nJ/pulse. Plotted on the horizontal axis is the wavelength range of the experiment, the vertical axis represents the delay time between pump and probe.

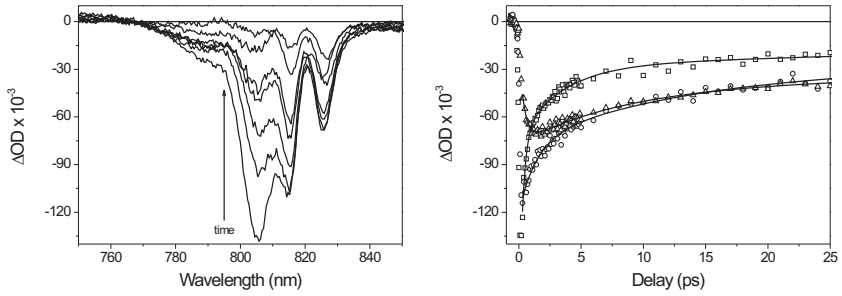

FIGURE 5.4. Transient absorption spectra at 77 K, pump 800 nm, pulse duration 80 fs, 240 nJ/pulse. [Left] Transient spectra at 0.2, 0.5, 1, 2.5, 3.5, 3.5 and 350 ps, the arrow indicates the time evolution. [Right] Transient kinetics at 805 (squares), 815 (circles) and 825 nm (triangles). The data and the single trace fits are represented by the symbols and lines respectively. The fits are to guide the eye.

in reference [34]. Briefly, the coupling between the electronic transitions is described by the dipole-dipole approximation. Diagonalizing the Hamiltonian gives the respective exciton states. An important factor in the density matrix simulations is the spectral density J, that describes how effective the energy difference between the states can be deposited into vibrational modes of the chromophore and the protein envelop. The description of the spectral density is obtained from hole burning experiments [115] and assumes a local spectral density on a single chromophore.

The exciton simulations show that the rate of exciton-exciton annihilation is proportional to the square of the overlap of the one-exciton wavefunction with the respective molecular part of the two-exciton wavefunction at the same pigment. The annihilation rate as extracted from the simulations is $1/1.5$ ps^{-1}. Additionally, the simulations can reveal the timeconstant associated with the relaxation between the exciton levels, which turns out to be 0.65 ps. Since annihilation and the decay within the manifold occur on similar timescales, both processes will occur simultaneously. The transient spectra were simulated using the parameters described above according to a method developed previously [114, 116] and were subsequently fit to the experimental spectra. In this fit, the site energies of the BChla pigments were slightly shifted from the literature values [77]. It was found that the internal conversion rate between the S_n and S_1 exciton states was fast at $1/200$ fs^{-1}. We found an additional, unexpected effect, of the annihilation of excitations on the transient spectra. Double excitations, as can be obtained at high pump fluence, rapidly decay to two single excitations, increasing the number of single excitations. The additional excitations are transformed into heat at longer decay times. Based on the simulations, time constants of 10 and >100 ps can be assigned to the heating processes. Hence, the local temperature can deviate from 77 K, depending on the excitation power. At 15 ps the local temperature, after excitation with 240 nJ, is about 130 K. The heat changes the relaxation rates between the exciton levels and hence leads to different transient absorption spectra. A comparison between the kinetics at 120 and 240 nJ is shown in figure 5.5.

Whereas the single trace fits give qualitative information on the exciton dynamics in the FMO complex, the simulations provide supplementary, quantitative information. Using simulations, time constants can be assigned to processes such as annihilation and heating of the sample. It is impossible to extract this information from the transient absorption data without sophisticated simulations.

5.1.5 Conclusion

At high pump fluence, multiple excitations per FMO monomer are generated. We have studied the dissipation of energy in the presence of double excitations. Simulations have shown that within an FMO monomer, exciton-exciton annihilation occurs at a rate of $1/1.5$ ps^{-1}. Additionally, the simulations reveal a relaxation time within the exciton manifold of 0.65 ps. Therefore, annihilation occurs simultaneous to exciton decay. The effect of annihilation is locally heat-

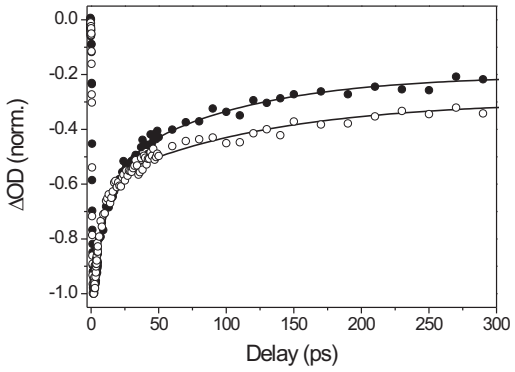

FIGURE 5.5. Transient absorption kinetics at 77 K, pump 800 nm, pulse duration 80 fs. A comparison between excitation with 120 (black circles) and 240 nJ/pulse (open circles). The data are normalized by their maximum signal at t_0.

ing the sample with time constants of 10 and >100 ps. Therefore, a higher effective temperature needs to be taken into account to fit the transient absorption data. As the dynamics within the FMO complex are now relatively well understood, in the remainder of this chapter a study is described, in which it was attempted to control the exciton dynamics and guide the energy within the system in a desired direction.

5.2 Control of the energy flow in the FMO complex

5.2.1 Introduction

After studying the energy transfer processes in the FMO complex, the next step was to try and control the energy flow through the system. The target of the control experiment in the FMO complex, was to deviate from the natural energy decay pathways and to spatially localize the excitation energy on a specific pigment at a given time (see figure 5.6). The initial idea was to obtain such a localized state by a coherent control experiment, using a shaped pump pulse. Since the FMO complex is an excitonic system, the shaped pump pulse can generate a wavepacket on the basis of the exciton states as

$$|\psi\rangle = \sum_{n=1}^{7} I_n A_n e^{i\phi_n} |E_n\rangle. \tag{5.5}$$

The laser pulse exciting the system controls the relative phase ϕ and amplitude I of the components, where A_n corresponds to the absorption of transition n. There exists a direct relation between the seven exciton states and the seven states localized on each pigments. This relation can be written using the complex matrix $C_n(k)$ as

$$|E_n\rangle = \sum_{k=1}^{7} C_k(n) |L_k\rangle. \tag{5.6}$$

In this expression the excitonic states are represented by $|E_n\rangle$ and the localized states by $|L_k\rangle$. When the phase (and amplitude) of the pump pulse are controlled, the initial condition of the wavepacket can be engineered so that, at a given time, the relative phases of the exciton states correspond to those describing the localized states

Shaping of the laser pulse for this control task can be achieved by an adaptive learning process during which an experimental signal is used as a feedback signal in an iterative (closed) learning loop (vide infra). This approach has been widely used to guide systems towards a specific state [117,118] and has also proven to be effective in large and complex biomolecules [119,120]. A theoretical account has indicated the feasibility of of such a control process in the FMO complex [87]. The experimental details of the closed loop approach will be further addressed in the next section.

5.2.2 Experimental

One of the important challenges in coherent control is the stability of the laser system, i.e. the noise has to be smaller than the changes induced by the different pulse shapes tested. This is not trivial in most amplified laser systems and tricks might need to be applied to reach sufficient stability. The laser system

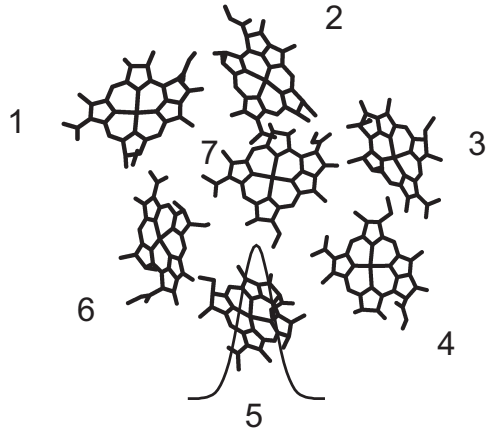

FIGURE 5.6. Target of the optimization in the FMO complex using a closed learning loop: localization of the excitation energy at a given pump-probe delay on one of the pigments.

used for these experiments is the two-stage amplifier described in chapter 2 (VIKTOR). Due to the unstable pointing vector over the long distances from the compressor to the sample, a solution was achieved in the form of spatially selecting the center of the beam with an iris. This should be avoided for more stable systems as spatial selection by a round aperture creates a diffraction (Airy) pattern leading to a distorted beam profile. The output of the amplifier is split in two of which the weaker one acts as the probe and the stronger is sent into the pulse shaper.

As mentioned in the introduction, a closed loop approach was used to optimize a feedback signal. In this loop, shown in figure 5.7, there are three main components which are represented by the computer (the algorithm driving the optimization), the pulse shaper (generating the pulse shapes to be tested) and the sample (generating the feedback signal). This section will describe these three components in detail starting with the pulse shaper.

The function of a pulse shaper can best be considered using the musical analogy of a laser pulse (figure 5.7) [121]. The shortest sound, containing many frequencies, can be produced by playing all these frequencies at the same time. In a short laser pulse, of a certain spectral bandwidth, all these frequencies would have the same phase generating a transform limited pulse. The pulse shaper can then act on the individual frequency components, changing their relative phase and amplitude (and in some shapers even polarization) generating the equivalent of a melody [122]. The pulse shaper used was a dual mask spatial light modulator (SLM-1280-VN-R; Cambridge Research & Instrumentation Inc.). Details of this particular shaper and its calibration can be found

in reference [123]. The mask is placed in the focus of a folded 4f-compressor setup. At the back of the mask a mirror was attached to reflect the output of the first transmission back through the mask. Such a reflection setup is necessary to allow full, 2π, modulation of the phase at 800 nm. In this folded setup the output of the shaper is sent back slightly lower than the input, so that it can be picked up by a mirror and sent to the sample. The small deviation does not significantly influence the quality of the pulse shaping. However, it does induce an alignment problem. Since both surfaces of the mask are partially reflective, several 'false' reflections will end up close to, or on top of, the reflected shaped pulse. These problems are overcome in two steps. The polarizer that is attached to the front of the mask is removed; this precludes using amplitude shaping but is not an issue here since the experiment will employ phase shaping only. Secondly, the polarization of the pulse is changed by 90° in the pulse shaping process. Discrimination between the false reflections and the shaped pulse is achieved by a polarizer cube instead of a mirror. It selects the shaped pulse by its polarization and sends it off at a 90° angle. Due to the uneven thickness of the liquid crystal pixels that shape the individual frequencies, the output pulse no longer has a flat phase over the spectrum and therefore is not transform limited. The start of each control experiment is to find a phase function for the shaper that counteracts these distortions and leaves a flat phase over the spectrum of the shaped pulse. In practice this is achieved by frequency doubling the shaped pulse at the sample position with a nonlinear crystal and optimizing the intensity, i.e. a flat phase results in the shortest pulse and the highest intensity.

The second element in the loop is the algorithm. A simplistic explanation of the operation of an evolutionary algorithm is as follows: the learning loop starts with a random guess of a set of pulse shapes that are tested on the sample, after which the feedback signal is evaluated and selection of pulse shapes, the parents, occurs. New shapes are created by recombining the parents after which mutations are made, generating the new set of pulse shapes that are applied. The loop continues until the optimization has converged. The specific optimization algorithm used in this experiment is an evolutionary strategy. The covariance matrix adaptation (CMA) searches the parameter space in parallel and adapts the step size of the mutations on the basis of the success of the previous generation [124]. This allows for an effective search where local minima can be avoided. A downside of this approach is the unique pathway the optimization follows and in theory no two experiments will result in the same learning curve. More information on CMA and comparison to other algorithms can be found in [123].

The third component in the loop is the sample. The FMO complex is dissolved in a mixture of TRIS buffer and glycerol (1:2) to form a good glass at 77 K. To prevent photobleaching the sample is continuously moved in an oval trajectory [5]. Experiments could be continued for several hours before the quality of the data decreased due to degradation of the sample.

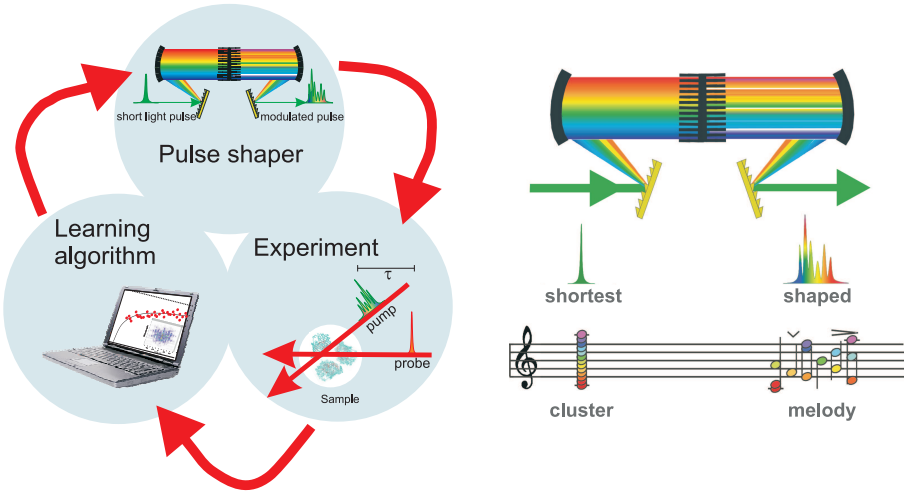

FIGURE 5.7. [Left] Learning loop used in coherent control, consisting of the pulse shaper, the algorithm and the sample. [Right] Analogy between the acoustic and optical domain. Like music, a pulse shape can be represented in the time and frequency domain.

5.2.3 PROOF OF PRINCIPLE

Using simple simulations, it was shown that in theory it is possible to use coherent control to localize excitation energy in the system. Based on the absorption spectra of the seven single exciton levels and a shaped laser pulse a wavepacket was created. The localized states were written on the basis of the exciton states by inversion of equation 5.6. The feedback signal in the closed loop optimization was the probability of finding the wavepacket of the localized states corresponding to pigment number 5 and is defined as follows:

$$\text{Fitness} = \frac{\sum_{n\neq 5} |\langle \Psi_n(x,t)|n\rangle|^2}{|\langle \Psi_{n5}(x,t)|n_5\rangle|^2}. \tag{5.7}$$

This value can be easily probed in a simulation. To minimize the fitness value, a similar algorithm as described in the previous section was used. Also, only phase only shaping was allowed. Figure 5.8 shows the optimization curve associated with the simulated localization on pigment number 5. The system is guided towards localization on pigment 5 up to generation 50, after which it seems to have converged. Since the optimization uses a localized basis, the population of the different pigments can be probed during the optimization which is shown in figure 5.9. The population of pigment 5 increases at the cost of the populations of the other pigments, i.e. in the course of the optimization spatial localization on pigment 5 occurs before the coherence and excited state population have decayed. Unfortunately, an experimental observable, equivalent to the fitness value as given in equation 5.7, is not available. In the experiment, described below, a different goal – population control – was pursued.

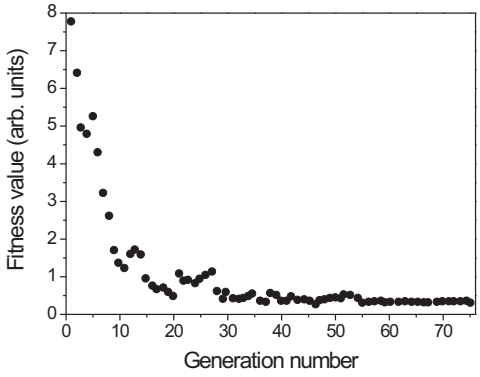

Figure 5.8. Fitness value versus the generations of the optimization to localize the wavepacket on pigment number 5.

5.2.4 Preliminary results

An inherent shortcoming of the use of TA spectroscopy in the experiment is the absence of phase information of the electric field. Therefore, in the control experiments information is obtained about the populations of the exciton states, but not about the relative phases between them as in equation 5.6. As was shown these phases are essential to indicate if, at a given time, localization occurs. Hence, a population control experiment was pursued, trying to retain population of the higher exciton states beyond their natural lifetime.

The goal of the experimental closed loop population optimization was to maximize the area in the TA spectra belonging to the 805 nm exciton band from 795 to 808 nm at 3 ps delay (figure 5.10). This specific target was chosen to try to prolong population of the higher exciton states. Because of the short lifetime of these states, the optimization had to be run at 3 ps. This is risky, since at such short delay times the algorithm can easily find a trivial solution that shifts the pump pulse in time by 3 ps. The fitness of the optimization run was defined as the amount with which the area had increased, normalized to the starting area using the transform limited pump pulse. The optimization shows an initial jump from a fitness value of 1 to $\sim$1.2 after which the feedback signal increases up to generation 160 (figure 5.10). The initial jump is assigned to a trivial incoherent control mechanism and has been observed before [125, 126]. Because of the high excitation power, 200 nJ, there exists the possibility that the system is saturated, i.e. the maximum number of single exciton states and therefore the maximum transient signal is reached. The pulse at the start of the learning loop will likely be longer than the transform limited pulse and will open the opportunity of re-excitation of the sample. This can occur either by the trailing end of the elongated pulse or by subsequent pulses in a pulse train.

Figure 5.11 shows the XFROG traces of the transform limited pulse and the

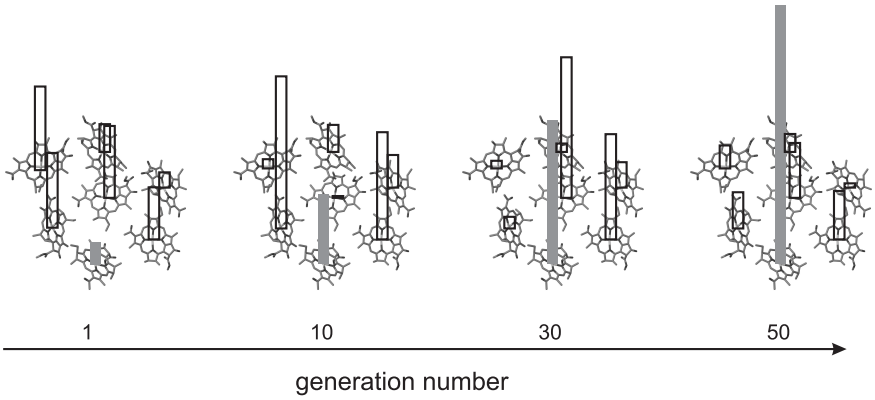

FIGURE 5.9. Results of the simulation to localize the wavepacket on pigment number 5 compared at different generation numbers in the optimization. The relative population of the pigments is represented by the bars, at pigment number 5 the population is shown in grey.

optimized pulse at generation 150 respectively. The transform limited starting pulse is a short, clean pulse with a pulse duration of ∼50 fs fwhm. In contrast, the optimized pulse is highly structured. It shows several sub-pulses, of which the main one is at 3 ps delay (figure 5.12). Figure 5.11 also shows the transient absorption matrix for the transform limited pulse and the optimized pulse. The sub-pulse at 3 ps seems to re-excite the sample. This is further illustrated in figure 5.12 that shows the comparison between the decay kinetics of the sample excited with the transform limited pulse and the optimized pulse.

5.2.5 RECOMMENDATIONS

The results in this chapter show the feasibility to control the natural flow of energy through the FMO complex using a closed loop optimization routine with a genetic algorithm. Whereas coherent control experiments could not be performed due to an inherent shortcoming of TA spectroscopy, population control was pursued. In the course of this complicated experiment three main recommendations for improvements and alterations came forward. The first, and at the same time the most obvious is to use a different type of 4-wave mixing technique, such as 2D electronic spectroscopy, to allow for phase knowledge needed for a feedback signal in coherent control experiments. Secondly, the use of open loop control experiments is advised, especially for coherent control experiments on systems that have a short excited state lifetime. In open loop experiments, the optimization is not guided by a genetic algorithm, but instead series of pulses (i.e. chirps, pulse trains, double pulses, etc.) are tested. Such open loop experiments can result in the observation of a possible trend in the target transient signal with respect to the series used. In the open loop experiments, the pulse shapes that have either a positive or negative effect on the

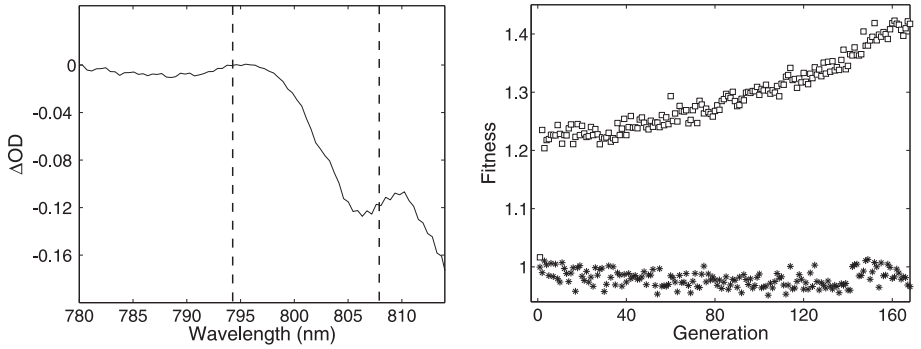

FIGURE 5.10. [Left] Transient absorption spectrum of FMO. The dashed lines indicate the region that was integrated and used as feedback in the optimization. [Right] The obtained learning curve is represented by the squares. The stars show the fitness value of the TL pulse taken before each generation.

transient signal can be readily identified as they are computed by the researcher. This is in stark contrast to the optimal pulse shapes resulting from closed loop experiments: these pulses often are complex, highly structured and demanding to interpret. An additional advantage of the open loop experiments is that the programmed series can be repeated an infinite number of times to increase the signal to noise level and reveal features in these scans, depending on the phase applied. Finally, scatter should be avoided at all costs when doing coherent control experiments. A drawback of the generation of apparent series such as double pulses and pulse trains is the mark they leave in the spectrum of the excitation pulse, which will carry on in possible scatter. When a double pulse is created using phase only shaping, this appears in the spectrum as fringes of which the spacing depends on the time between the double pulses. In a scattering sample, like a glass, this is unmistakably visible in the transient absorption spectra. Hence, the effect of the changing delay between the double pulses on the transient signal can be obscured by the changing spectrum of the scatter. Several subtraction tricks to remove the scatter were tested in our lab. Whereas for standard TA measurements scatter can be nearly completely removed at the end of a measurements, with a prerequisite that the signal to noise is sufficient, this was never achieved adequately in the control measurements using the laser system described in section 5.1.2.

The results of the experiment show that it is possible to reach sufficiently stable conditions required for (coherent) control experiments with a feedback loop using a moving sample, pulse shaper and a cryostat. Both the XFROG and the transient absorption spectra show that the result of the preliminary experiment control the excited state population, as the obtained pulse shape seems to re-excite the system up to a delay of 3 ps, the delay time chosen for the optimization run. Future experiments will further explore the possibilities of exciton control in the FMO complex.

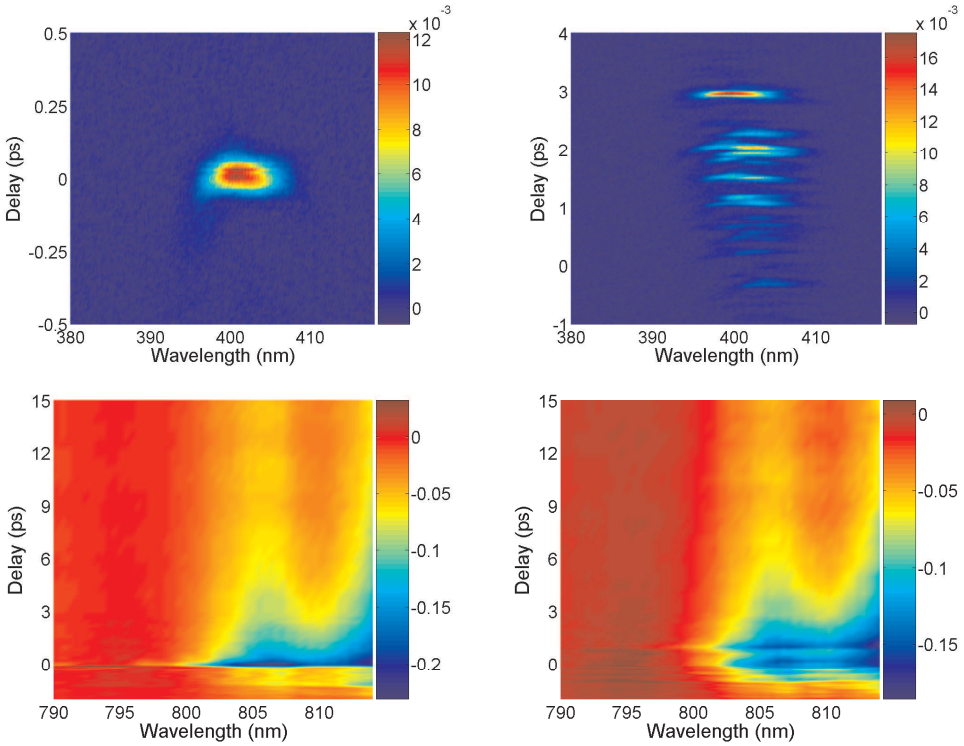

FIGURE 5.11. [Top] The XFROG traces of the TL pulse (left) and the optimized pulse at generation 150 (right). [Bottom] Transient absorption matrices, wavelength vs pump-probe delay, pumping with the TL (left) and the optimized pulse (right). The signal before pump-probe delay time 0 in the TL case is caused by the deviation of the starting pulse from its optimized transform limited shape during the time of the experiment.

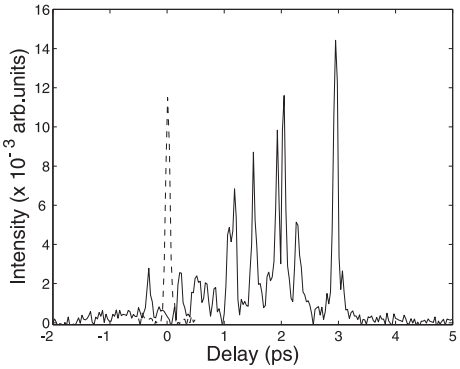

FIGURE 5.12. FROG traces of the transform limited pulse and the optimized pulse in the time domain at 400 nm.

Part II

Molecular switches

6 Introduction to diarylethene molecular switches

This chapter gives a basic introduction to diarylethene molecular switches. First, the theoretical background of the cyclization reaction is described using the Woodward/Hoffmann rules. This is followed by accounts on the ring closing and opening reactions as observed in optical experiments. Finally, switches with special side groups, as will be encountered in the remainder of this thesis, will be discussed.

6.1 Photochromic switches

Photochromic switches come in many shapes and sizes, but all have one thing in common: they undergo a reaction between two isomeric forms under the influence of light. In recent years, photochromic switches have successfully made their way into industry, where they are widely used in applications such as photochromic sunglasses that change, reversibly, the level of transmission of the lenses upon UV irradiation. In research, the main focus lies on the development of molecular electronics and devices. As the top-down limits of conventional fabrication methods of electronics are drawing closer, the need for a bottom up technology based on a molecular approach is becoming increasingly attractive. Photochromic switches are interesting candidates in this development as they can serve as bifunctional components that are readily addressable by an external stimulus such as light.

Amongst other photoreactions, photoisomerization (cis–trans) and photocyclization have been studied intensely. Indeed azobenzene is a paradigm compound in research on photoisomerization [127–129]. However two drawbacks of the photoisomerization of azobenzene are the thermal reversion of the *cis* form to the more stable *trans* form and secondly the addressability of each of the individual molecular states. The absorption spectra of both the *trans* and *cis* form are in the same spectral region ($\lambda_{max-cis} = 300$ nm vs. $\lambda_{max-trans} = 350$ nm). This creates a problem in addressing these states individually (e.g. with a broadband,ultrafast, light source). Luckily, there are other molecules that do not suffer from these inherent shortcomings.

6.2 Diarylethenes

A myriad of structurally varied diarylethenes have been studied for a diverse range of research fields [130]. These photochromic systems have two thermally stable states, with sufficient spectral differences to be addressed indi-

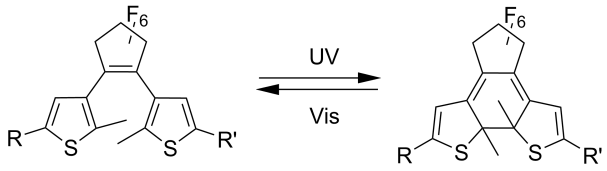

FIGURE 6.1. Dithienylethene photochromic molecular switch. The bridging cyclopentene group here has fluoro substituents (F_6). The side groups R and R'can be, but are not necessarily, different.

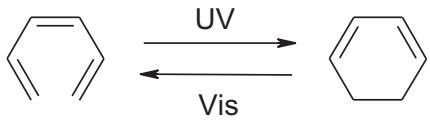

FIGURE 6.2. Ring closing reaction of hexatriene (HT) into cyclohexane (CH).

vidually. The open form typically absorbs in the UV. However, after the (electro)cyclization reaction, i.e. ring closing, an absorption band appears in the visible region of the spectrum. Irradiation with UV light (< 400 nm) results in ring closing, the reverse reaction can be driven by irradiation with visible light resonant with the absorption band of the closed form. The absorption bands of both forms extend into the UV region, therefore it is not possible to excite the open form independently and obtain complete conversion to the closed form. A photostationary state (PSS) is expected for which the maximum percentage of closed isomer can be determined by NMR spectroscopy [131]. Since the quantum yield of ring closing is considerably higher than that of ring opening in most diarylethenes, the amount of closed isomer at the PSS state in general exceeds 90%.

In this thesis the focus lies on diarylperfluorocyclopentene molecular switches (figure 6.1). The diarylethene is locked in the *cis* form by the cyclopentene bridge that prevents *cis-trans* isomerization. Nevertheless, in the open form the rotation around the single bond that connects this bridge to the thiophene groups is still possible. This flexibility is essential for the formation of the closed form (vide infra).

6.3 ELECTROCYCLIC REACTIONS - WOODWARD/HOFMANN RULES

The basic process underlying the electrocyclic reaction observed in diarylethenes is the cyclization of a hexatriene, HT, to form a cyclohexadiene, CH (figure 6.2).

This reaction is essentially the formation of a ring by replacing one π by a σ bond. It is a well characterized reaction both theoretically and experimentally

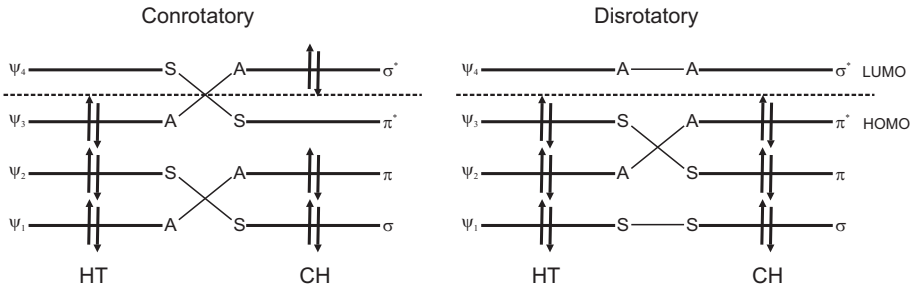

FIGURE 6.3. Molecular orbital picture of the ring closing reaction of hexatriene. The orbitals are denoted as S (symmetric) when they remain unchanged under C_2 or σ_v operation in the conrotatory and disrotatory reaction pathway respectively. In case of a sign change in the orbitals under the operation, the orbitals are denoted as A (antisymmetric).

[132–135]. A simple description of the electrocyclic bond formation can be obtained from frontier orbital theory, under the assumption that the reaction occurs in a symmetric and concerted manner (i.e. no intermediates) [136]. Using this theory the chemical reactivity of a compound is correlated to the properties of the molecular orbitals. Specifically, the highest occupied molecular orbital (HOMO) and the lowest unoccupied molecular orbital (LUMO) dominate the reaction. Ring closure of the hexatriene can take place by following two reaction paths: the two CH_3 groups can rotate either in the same direction (conrotatory) or in opposite direction (disrotatory). While hexatriene and cyclohexadiene are both characterized by a C_2 and a σ_v symmetry element, during the reaction only one is preserved depending on the reaction pathway. In the conrotatory reaction the C_2 element is conserved, while in the disrotatory pathway the σ_v, (often denoted as C_s) element is conserved. This has implications for the potential energy surface and possible activation barriers to the reaction as can be seen from the molecular orbital (MO) picture sketched in figure 6.3.

The orbitals of a certain symmetry (irreducible representation of a group) can only convert to orbitals of the same symmetry when undergoing a reaction. This is represented in a simplified way by S (symmetric) and A (antisymmetric) in the MO picture. Orbitals that remain unchanged under a C_2 or σ_v symmetry operation are denoted as S, orbitals that change (sign) are denoted as A. In a reaction, orbitals denoted with S in the reactant do not correlate to an A orbital in the product of the reaction. As can be seen from this figure, in conrotatory fashion, the molecule starts off in the ground state of HT and ends up in the excited state of CH. This is energetically unfavorable and therefore the reaction is thermally inactive. Photo-activation of one electron from ψ_3 to ψ_4 overcomes this barrier. The conrotatory pathway is only followed upon photoexcitation. A similar explanation holds for the disrotatory reaction pathway. The inherent absence of an energy barrier in the ground state allows for thermal ring closing.

The Woodward/Hoffmann rules can be used to predict on the basis of frontier orbital theory via which pathway the thermally allowed ground state reac-

tion occurs. This depends on the number of carbon atoms n in the ring after cyclization. If the number of occupied orbitals $n/2$ is odd (e.g. as in HT where $n/2 = 3$) the ground state process proceeds in a disrotatory fashion, while where $n/2$ is even, the conrotatory pathway is favored. These rules especially apply for simple non-polar systems without bulky groups that can interfere with the pathways described above. Although allowed, cyclization in the ground state, via the disrotatory pathway, does not occur in diarylethenes. There is a high energy barrier between the ring open and ring closed form due to steric interactions. Hence, the only route to ring closing is via a photoexcited state making both the open and closed states thermally stable.

In these systems the quantum yield of ring closing can never reach 100%, because of the presence of the unreactive C_s conformer in a fixed proportion on the timescale of the experiment.

6.4 Ring closing reaction

Over the past ten years it has been established that ring closing dynamics of diarylethenes proceeds to completion within several picoseconds [137, 138], indicating a high quantum yield of the reaction. Often, indirect estimations of the ring closing timescale make use of the quantum yield of ring closing and the lifetime of the open form [138]. The ring closing reaction (QY ∼86% in CHO-diarylethene) occurs within 2.3 ps assuming

$$QY = \frac{k_{RC}}{k_{RC} + k_\tau} \tag{6.1}$$

where k_{RC} is the rate of ring closing and k_τ the lifetime of the S_1 state and the measured decay time of 2 ps corresponds to $k_{RC} + k_\tau$.

After excitation of the open form, the build-up of photoproduct can be followed by transient differential spectroscopy. Especially if the quantum yield is sufficiently high and the form of the transient signal resembles that of the linear absorption spectrum in the closed form. However, often the presence of additional transient signals of several other species, such as the unreactive conformer, obscure these observations. The latter has a longer lived excited state than the reactive conformer, since it cannot decay through fast ring closing [139, 140].

The underlying mechanism for the ring-closure reaction is complex and not as simple as sketched in figure 6.3. Several experimental and theoretical techniques have been utilized to come up with a solid mechanism that explains all observations made for the ring closing dynamics. Time-resolved fluorescence is one of those techniques and discriminative in the sense that it is only sensitive to the emissive excited states. A limitation of the technique is that possible 'dark' intermediate states being involved cannot be excluded. Using this technique two emissive states are observed: one exhibiting a time constant of ∼100 ps and another showing a fast component of ∼1 ps [141]. Both time constants are mainly attributed to the reactive C_2 conformer. The observation of two time

constants is interpreted as due to the presence of two minima on the excited electronic state potential energy surface, where the fast reaction pathway is assigned to direct ring closing, possibly through a conical intersection (CI), while the slow component undergoes ring closure due to conformational changes [141].

Essential evidence to support the assignment of two minima in the excited state was reported by Uchida *et al.* [142]. Surprisingly, a positive correlation between the reactive C_2 population and the quantum yield of ring closing was not observed. Ab initio calculations predicted the presence of two minima in the excited state: one reactive and one non-reactive. The presence of the non-reactive minimum, that leads to decay to the ground state of the open isomer, reduces the ring closing quantum yield.

All observations were unified with the description of ring closing by Hania *et al.* [143]. The evolution of the transient signal was divided into three time regimes; subpicosecond over the whole spectral window, followed by a delay of several picoseconds that is omnipresent with varying amplitude, and finally a decay that occurs over tens of picoseconds. These regimes were assigned as pre-switching, ring-closing and post-switching dynamics. The assignment of pre-switching dynamics is supported by the detection of subpicosecond evolutions of the transient signal in several studies, that were attributed to conformational changes on the S_1 potential energy surface towards ring closing [139]. At wavelengths below 500 nm a non-switching conformer is observed, it does show the subpicosecond delay, however the picosecond component that is assigned to switching is absent. Instead, the ultrashort decay is followed by a relatively long decay of ∼100 ps, that is attributed to the lifetime of the excited state of the non-switching conformer. At 100 ps the transient spectrum begins to resemble the steady state absorption spectrum of the closed state, this long decay is assigned to vibrational cooling. Due to the radiationless transition from the S_1 state in the open form to the ground state of the closed form, the molecule ends up in a hot ground state and has to get rid of a large amount of excess vibrational energy.

6.5 Ring opening reaction

Whereas transient signals attributed to ring closing can be assigned based on empirical data due to the relatively high quantum yield of the reaction, dynamics belonging to the ring opening reaction are much harder to detect. The quantum yield for ring opening is, in most switches, low and typically does not exceed ∼1%. It is therefore difficult to extract a mechanism for ring opening from (time-resolved) experiments. However, several groups reported a viable mechanism often based on a combination of experimental and theoretical studies. Due to these difficulties it is therefore not unexpected that reports on the ring-opening time vary between several picoseconds [140] to several hundreds of picoseconds [144].

Ern *et al.* used pump-probe spectroscopy where the excitation wavelength and temperature were changed. Excitation of the closed form to either its S_1

or S_2 state resulted in identical transients. Therefore it was concluded that the $S_2 - S_1$ relaxation occurs on a timescale within the instrumental response (∼100 fs) [144]. The decay $S_1 - S_0$ of the closed form is described well by a single exponential decay with a time constant of ∼13 ps. On the other hand, the excited state absorption shows different behavior: the transients could be fitted by a sum of two exponentials with time constants of 0.9 and 13 ps respectively. The underlying mechanism based on their observations combined with a calculation of the potential energy surfaces of the S_0, S_1, and S_2 states lead to the following model [144]. The system is initially excited to the S_1 state after which it undergoes structural relaxation (0.9 ps) to a minimum on the potential energy surface, P^*. From this state, there is a weakly avoided crossing by a potential energy barrier to the CI where the ring opening reaction takes place. The lifetime of P^* returning back to the ground state is 13 ps. Using rate equations and the time constants obtained from the fits to the transients a ring opening time constant from P^* was determined to be 325 ps. The existence of a potential barrier on the S_1 potential energy surface is supported by the enhancement of the quantum yield of ring opening at increasing temperatures [145, 146].

Similar reasoning after detection of a biexponential decay (0.3–0.5 ps and 5–11 ps) of the excited state of the closed form lead to the proposal of a barrier between the potential energy minimum on the S_1 state and the CI via which relaxation takes place [139]. The branching between the open and closed isomer takes place at the CI and is sensitive to the excess energy in the system, i.e. irradiation with 514 nm increases the quantum yield of ring opening with respect to irradiation at 690 nm, this in contrast to previous observations. The model is supported by ab initio calculations where it was shown that the barrier towards the ring open isomer decreases for higher excited states [147, 148]. However because the oscillator strength of the higher lying states is relatively small, direct pumping of these states is less probable than a multiphoton absorption including a state with a high(er) oscillation strength, so-called multi photon gated reaction. Experimental verification for this model was provided by Murakami *et al.* [149]. They showed that excitation with a picosecond pulse lead to considerable enhancement of the ring opening quantum yield in comparison to a femtosecond pulse. The explanation offered is a subsequent excitation of the system from the S_1 to S_2 state by a second photon within one pulse after relaxation from a hot to a cold S_1 state has taken place. The Franck Condon factor from the hot S_1 to the S_2 state is low, this is the state a femtosecond pulse would doubly excite, however, the Franck Condon factor from the cold S_1 to the S_2 state is high, allowing for double absorption by a picosecond pulse. As in reference [147] the quantum yield of ring opening from the S_2 state is higher than in the S_1 state. However in contrast to the predictions based on calculations, by tuning the excitation pulse around 600 nm, they demonstrated that excess vibrational energy does not play a role in this mechanism.

Subsequently, a purely theoretical report based a mechanism for ring opening on internal conversion through a CI [150]. Ab initio molecular orbital calculations are employed in the prediction of a CI at which the system crosses from the excited to the ground state. Directly after the crossing there are a, theo-

retically, infinite number of reaction paths. This explains why the CI can act as a branching point between two product states; the closed and open isomer. According to the model they obtain from calculations, the decay back to the closed ground state is more efficient than the ring opening reaction because the latter needs two steps with considerable use of vibrational modes.

After ring opening the molecule ends up, as for ring closing, in a hot ground state. As observed by anti-Stokes Raman spectroscopy, it takes the molecule several tens of picoseconds to dissipate all the excess vibrational energy to its surrounding solvent molecules [140].

6.6 Special switches

6.6.1 Switches with extended side chains

The extension of molecular switches with different thiophene based sidegroups has been reported in several studies. The switching functionality is unaffected by this addition as the switching process runs to completion within 1.5 ps [151,152]. The influence of carotenoid side groups on the switching efficiency is interesting. Both the quantum yields of the ring opening and closing reaction decrease sharply at a specific carotenoid chain length. The increase in the length of the side chains reduces the excitation density on the central switch unit, thereby decreasing the excited state lifetime and the switching efficiency [153].

6.6.2 Photoswitchable fluorophores

Covalent addition of a fluorescent molecule onto a molecular switch leads to photoswitchable emission levels both in solution and on a surface. Ern *et al.* showed that the fluorescence of anthracene is quenched upon ring closing [154]. Additional calculations show that this is explained by localization of the lowest excited state. While in the open form this state is predominantly localized on the anthracene substituent, the situation is inverted in the closed form where this state is localized on the dithienylethene center. In the closed form all signals decay monoexponentially within 8 ps, assigned to the lifetime of the excited state. In contrast, in the open form the transient signal is more complicated, it is composed of contributions of the anthracene, the switch in the reactive and non-reactive form and of the closed form. Both conformers undergo fast (0.9 ps) conformational relaxation. The reactive conformer decays within 10 ps to a state from which ring opening takes place. However, the non-reactive conformer decays with a distribution of lifetimes ranging from 100 to 400 ps. The fluorescence of a perylene unit attached to a switch also resulted in fluorescence quenching upon ring closing [155]. In contrast to the previous example, quenching occurred due to electron transfer to the switch. This is supported by the appearance of the spectral signature of the radical cation of the perylene (at 613 nm) in the transient spectra of the closed form when excited at 400 nm to the S_2 state of the perylene. That a similar quenching process works reversibly for single molecules in a matrix was demonstrated by Irie *et al.* [156].

The quantum yield of an anthracene unit bound to a switch was reduced from 0.73 in the open form to < 0.001 in the closed form. Based on the fluorescence lifetimes of 4.9 ns and 4.5 ps of the open and closed forms respectively, an energy transfer rate from anthracene to switch was estimated to be $2.2.10^{11}$ s^{-1} with an efficiency of 99.9%. In contrast with the previous system, the emission of a metal-ligated switch was increased upon ring closure [157]. Hence, by tuning both the switch and the fluorophore it is possible to develop reversibly photoswitchable fluorescent molecules with a modulation of the intensity that can reach over 90% [158].

6.7 In this thesis

The molecular switches used in the experiments described in this thesis are all based on diarylethenes. However, their functional side groups are different. In chapter 7 two switches are connected by a sexithiophene linker, forming a molecular wire. Interesting is the effect of the sexithiophene on the (optical) properties of the switch and vice versa. The chapters 8 and 9 describe switchable fluorescence in multicomponent systems. In the first chapter, the effect of a small structural change in the fluorophore on the energy transfer process and hence fluorescence quenching is studied. By connecting two different fluorophores to the diarylethene switch a molecular triad is obtained. The energy flow in this system can be controlled by means of the switch.

7 Diarylethene-substituted sexithiophenes

Two different aspects of a sexithiophene molecular wire connected at both ends to dithienylethene molecular switches are discussed. First, the temperature-dependent optical properties of this multicomponent system are studied when the switch is in the open form. This behavior is, unexpectedly, strongly influenced by the peripheral side groups of the switches. Secondly, the system is ring closed and the optical properties are compared to those of its open counterpart. The character of the molecule turns out to be changed completely depending on the state of the switch.

7.1 Tunable aggregation and luminescence of bis-diarylethene-sexithiophenes

7.1.1 Introduction

Since the discovery of conducting polymers by Heeger and MacDiarmid in the late 1970s, [159] π-conjugated systems have seen increasing application in areas as diverse as supramolecular chemistry and organic electronics in FETs, [160] OLEDs, [161] molecular wires, [162] photovoltaic cells [163] and electrochromic materials [164, 165]. Oligothiophenes in particular show remarkable optical and electronic properties [166]. Their widespread use is due to their stability towards molecular oxygen and water [167]. From a supramolecular perspective, oligothiophenes are especially attractive as components in molecular devices where they can act as bridging units, i.e. molecular wires, between functional units, as well as active components in their own right [168]. The distinct advantage that oligothiophenes provide over their polymeric analogues is their precisely defined structure. Furthermore in contrast to conventional semiconducting materials, subtle structural changes can yield dramatic effects in conductivity and luminescence properties [169–172]. Whereas in polythiophene the material properties are affected by kinks and bends in their structures, oligothiophenes can form rigid, well-ordered structures more easily. The type of order determines the luminescence and electronic properties of oligothiophenes, providing the tunability required for application in optoelectronic devices [173–176]. A wide range of substituted oligothiophenes have been reported, [177] in solution, as well as in thin films and single crystals, with sexithiophene-based systems receiving the most attention [178–180]. The properties of oligothiophenes can be tuned via synthetic modification and processing [181, 182]. The impact of strong intermolecular interactions between oligothiophenes on solubility typi-

cally requires that long alkyl side chains are employed to improve solubility and/or control aggregation. However, while such an approach improves solubility and processibility, the steric interactions introduced by the alkyl side chains at the positions impact on the photophysical and electronic properties in comparison to non-substituted oligothiophenes [183]. An alternative approach is to modify oligothiophenes by end-capping the α,α-positions with functional groups, for instance, to control aggregation [184]. This approach limits the steric hindrance and therefore the effects of functionalization on electronic and spectroscopic properties. A further extension is the introduction of added functionality such as photochromism to change the conjugation pathlength of oligothiophenes [152, 185, 186]. The synthesis, photochemical and electrochemical properties of two α,α-sexithiophene compounds **1** and **2** were reported previously (figure 7.1) [187]. These molecules incorporate two photo-responsive units in the form of photoswitchable dithienyl hexafluoro-cyclopentenes. These molecular photochromic switching units have proven their versatility in optoelectronic memory and display devices due to their fatigue resistance and thermal stability [7, 130, 188, 189]. Surprisingly, despite the fact that the substituent (phenyl- in **1** and Cl- in **2**; figure 7.1) on the outermost thiophene unit is well removed from the sexithiophene core, these substituents have a pronounced effect on the spectroscopic and electrochemical properties of the compounds, in particular on the energy of the HOMO level. However, in order to apply the functional behavior of these photochromic oligothiophenes in particular in materials applications such as polymer modified electrodes, [190] it is necessary that the effect of aggregation on their photochemical and photophysical properties be understood.

This part of the chapter describes the study of compounds **1** and **2** in their fully open states (figure 7.1) by temperature dependent steady state and ultrafast time resolved spectroscopies. Particular attention is paid to the effect of the peripheral substituents on aggregation phenomena. The steady state and transient spectroscopic techniques provide complementary information regarding the behavior of the compounds over the temperature range 120-298 K. As for the electrochemistry and steady state spectroscopy at room temperature, a considerable difference between the temperature dependent behaviors of **1** and **2** in the open form is noted. The results indicate that the hexafluoro-cyclopentene unit provides for effective electronic communication between the sexithiophene and the phenyl/chloro-thienyl groups, and furthermore, provides for additional intermolecular interactions that can control aggregation properties in solution.

7.1.2 EXPERIMENTAL

n-Hexane, cyclohexane, isopentane (m.p. 113 K) and ethanol/methanol (4:1, Tg 115-125 K) were of spectroscopic grade or better and used as received. Hexane was used for steady state absorption spectroscopy carried out at room temperature; cyclohexane was employed in the room temperature time-resolved measurements; isopentane and ethanol/methanol were used in temperature dependent measurements. The synthesis and characterization of compounds **1o**

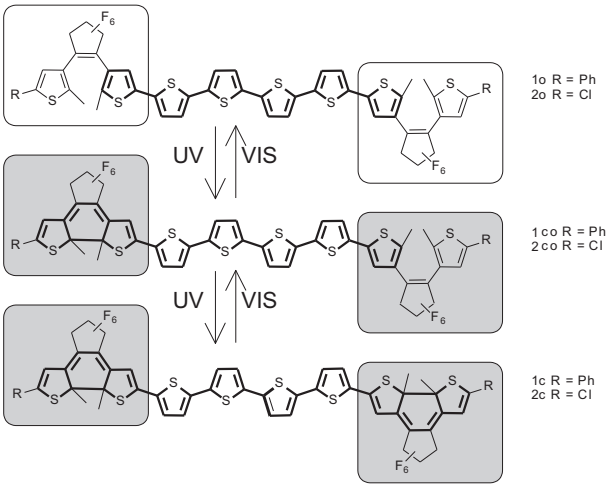

FIGURE 7.1. Molecular structures of compounds **1** and **2** in the fully open (**1o**/**2o**), singly closed (**1co**/**2co**) and fully closed (**1c**/**2c**) forms. Compound **1** is end-capped with peripheral phenyl groups and compound **2** with peripheral chloro groups. The suffixes **o** and **c** indicate that both photochromic units are in the open and closed states, respectively. The suffix **oc** indicates that one each of the photochromic units are in the open and closed state.

and **2o** is reported elsewhere [187]. For the decomposition of the spectra into Gaussian bands, the nanometer scale was changed to reciprocal centimeters and the intensities of the spectra were corrected according to $I(\nu) = I(\lambda).\lambda^2$ [13]. The time resolution in the transient absorption measurements, performed at the PUSH setup, was determined by cross correlation to be 45 fs for excitation at 475 nm and ∼100 fs at 388 nm. Room temperature measurements were collected using a 2 mm flow cell with a 50 ml reservoir to avoid the build-up of photoproducts. Steady state absorption spectra of the samples before and after the time-resolved measurement were taken to assure the absence of ring-closed species (figure 7.1). Low temperature measurements were performed by placing the sample in a 1 mm cuvette and inserting it into a cryostat (Optistat CF, Oxford instruments), where it was cooled to 150 and 125 K for measurements in ethanol/methanol and isopentane, respectively. The excitation energy was limited to a maximum of 100 nJ for most measurements. The system response was linear (15-20% of the molecules are excited at an excitation power of 200 nJ) up to an excitation power of 100 W (200 nJ per pulse). Kinetics obtained at 30 and 100 W could be fitted with identical time constants.

7.1.3 STEADY STATE ABSORPTION SPECTROSCOPY

The steady state absorption spectrum of **1o** in solution and in the solid state as a powder and as a drop cast film at room temperature are shown in figure 7.2. In solution, the absorption spectrum consists of two absorption bands

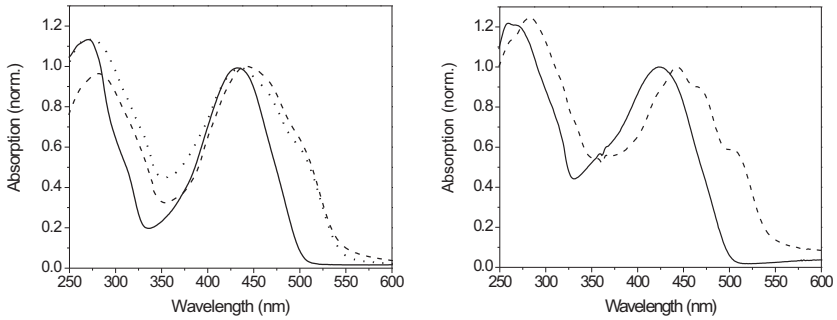

FIGURE 7.2. [Left] Room temperature absorption spectra of **1o** in hexane (solid line), as a powder (dotted line), and as a drop cast film (dashed line). [Right] Temperature dependent absorption spectra of **1o** in isopentane at 280 K (solid line) and 120 K (dashed line). Spectra in both panels are normalized with respect to the absorption band at ∼430-450 nm.

showing little structure. The lowest energy absorption ($S_0 - S_1$, λ_{max} 432 nm, 23150 cm^{-1}) is decomposed into three Gaussian bands (21870, 23170 and 25560 cm^{-1}, respectively). The solid state diffuse reflectance spectrum of a powdered solid sample is red-shifted and significantly more structured than the absorption spectrum in solution, suggesting partial ordering in the solid state. The lowest energy absorption feature in the solid state spectrum is decomposed into four Gaussian bands (19530, 20780, 22880, 26180 cm^{-1}). The absorption spectrum of a thin film of **1o** is comparable to that of the diffuse reflectance spectrum of the powdered solid. Decomposition of the lowest absorption band into Gaussian bands indicates maxima at 19580, 20750, 22590, 26700 cm^{-1}. The spectral features in the solid state can be assigned to a vibronic progression as observed in other sexithiophene based systems at room and low temperature [130]. However, it is probable that in the solid state, either as a powder or a drop cast film, there will be a mixture of amorphous and microcrystalline material, the former reducing the resolution of the vibronic progression.

The temperature dependence of the absorption spectrum of **1o** in isopentane is shown in the right panel of figure 7.2. The shape of the absorption spectrum is strongly temperature dependent; the absorption band undergoes a bathochromic shift of ∼20 nm and shows resolved spectral features below 220 K. At 120 K, the main absorption band in the visible region, λ_{max} at ∼430-440 nm, can be deconvoluted into five bands centered at 19560, 21060, 22460, 22540 and 26500 cm^{-1}. The vibrational progression (∼1500 cm^{-1}) is similar, although considerably more pronounced compared to that observed in the (solid state) absorption and diffuse reflectance spectra. Furthermore, the better resolution of the vibrational progression, in the absorption spectra of a solution at 120 K, compared with the solid state spectra suggest that the sample is aggregated with a greater degree of intermolecular order. The change in the

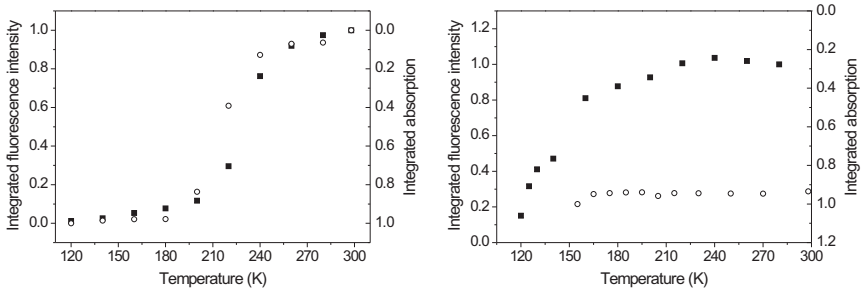

FIGURE 7.3. [Left] Temperature dependence of the absorption (circles) and fluorescence (squares) spectra of **1o** in isopentane. The fluorescence spectra are integrated over the range 450-800 nm and subsequently the intensity at a given temperature is scaled relative to that at 298 K. Similarly, the absorption spectra were integrated over the interval 443-550 nm. A constant background was subtracted and the integrated spectra were scaled to that at 120 K. [Right] Integrated temperature dependent absorption spectra of **2o** in ethanol (circles) and integrated temperature dependent fluorescence spectra of **2o** in isopentane (squares).

visible spectrum from a broad unstructured absorption to a red shifted structured spectrum occurs over a relatively narrow temperature range (180-220 K), well above the onset of the glass transition temperature of the solvent (∼115 K) and is independent of concentration between 10^{-6} and 10^{-4} M (figure 7.3).

Compound **1o** is strongly emissive in solution at room temperature ($\Phi_{fl} = 0.2$) and the fluorescence spectrum shows a vibrational progression typical of sexithiophenes (figure 7.4) [191]. The asymmetry between the featureless absorption and structured fluorescence spectra for oligothiophenes in solution has been noted previously [192]. The fluorescence spectrum is decomposed into three bands centered at 17570, 18690, and 19980 cm^{-1}, corresponding to a vibrational progression of ∼1100-1200 cm^{-1}. Comparison with the Raman and IR spectra of **1o** indicates that the progression is coupled primarily to a C=C stretching vibration of the thiophene and that the emission originates from the sexithiophene unit [187]. The mismatch between the vibrational progression in the absorption and emission spectra is due to the fact that in the absorption spectra the vibrational levels of the excited state are represented in the spectra. However, emission occurs from the lowest vibrational level in the excited state to the different vibrational states in the ground state. Hence, the vibrational levels of the ground state leave their mark in the emission spectra. The Stokes shift in hexane is determined, by comparison of the origins of the deconvoluted absorption and fluorescence spectra (21570 and 19980 cm^{-1}, respectively), to be 1600 cm^{-1}. This value is less than the typical Stokes shift observed for unsubstituted oligothiophenes of 3000-3500 cm^{-1} [193]. In the solid state, either as a powder or a drop cast film, **1o** is essentially non-fluorescent (i.e. the intensity is of the same order of magnitude as the Raman scattering

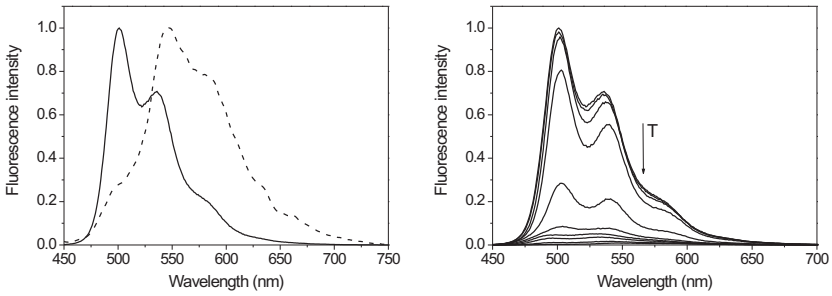

FIGURE 7.4. [Left] Fluorescence spectra at 300 K (solid) and 120 K (dash) normalized at the respective λ_{max}. [Right] Temperature dependence of the fluorescence of **1o** in isopentane, at an excitation wavelength of 445 nm.

from the sample), in stark contrast to **1o** in solution. The lack of fluorescence at low temperature and the increase in the resolution of the vibrational progression in the absorption spectra indicate that the molecules are assembled in an ordered structure. The X-ray single crystal diffraction structure of crystals of **1o** (grown from dichloromethane solution) was reported earlier [187]. The molecules are stacked with their long axis parallel making an angle to the horizontal (so-called herringbone structure). Molecules of **1o** stack together with an offset of one thiophene ring between the layers, i.e. the first thiophene of layer A lies below the second thiophene of layer B. This specific stacking of chromophores with their transition moments lying along their long axes, parallel to one another, is described as an H-aggregate [34]. In this type of aggregate the transition from the lowest exciton state to the ground state is optically forbidden due to symmetry selection rules [173]. Relaxation therefore occurs mainly via non-radiative processes resulting in a lower fluorescence quantum yield than observed in solution. Intermolecular interactions between the closely spaced molecules in these aggregates will cause splitting of the molecular energy levels into a series of exciton states. Between 250 and 300 K, the fluorescence of **1o** is essentially temperature independent, but the fluorescence spectrum changes considerably between 200-250 K. Below 180 K the fluorescence is weak ($\sim$1% of the intensity observed at 298 K) and red-shifted (figures 7.3 and 7.4). As with the temperature dependence of the absorption spectrum, this effect is still observed after a 30 fold decrease in concentration. The fluorescence spectrum obtained at 120 K is a sum of that of the weakly-fluorescent aggregates of **1o** and of non-aggregated molecules of **1o**. After scaling and subtraction of residual fluorescence of non-aggregated **1o** (scaling at λ_{max} 501 nm, figure7.4), the low temperature fluorescence spectrum was fitted with three Gaussian bands (16350, 17030 and 18260 cm^{-1}). The observed Stokes shift at 120 K is $\sim$2800 cm^{-1}. The sharp decrease in fluorescence indicates that aggregates are forming in solution upon decreasing temperature. Since this structural transition is characterized by the decrease in fluorescence it is probable that H-aggregates,

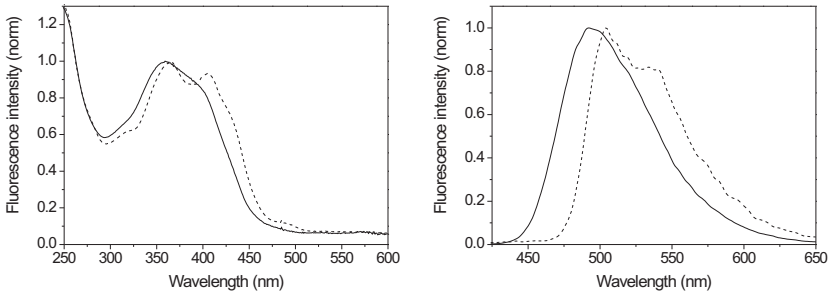

FIGURE 7.5. [Left] Absorption spectra of **2o** in ethanol/methanol (1:4) at 280 K (solid line) and 120 K (dashed line). [Right] Fluorescence spectra of **2o** at 280 K (solid line) and 120 K (dashed line). In panels a and b the spectra are normalized individually at their λ_{max} in the region $\sim$ 350-370 nm and $\sim$490-510 nm respectively.

analogous to those observed in the X-ray crystal structure, form in low temperature solutions. The effective absence of the 0-0 transition at 120 K ($\sim$500 nm at room temperature, figure 7.4), which is forbidden in H-aggregates, provides additional support to this hypothesis [194]. However, formation of H-aggregates typically results in a blue shift in the absorption spectrum. In the present system the blue shift may be masked by conformational changes, i.e. the transition to the solid state is accompanied by increased planarity and a loss of torsional modes [195].

7.1.4 COMPARISON BETWEEN THE STEADY STATE SPECTROSCOPY OF **1o** AND **2o**

As for **1o**, the lowest energy absorption band of **2o** at room temperature is decomposed into three bands, centered at 24670, 27640 and 30780 cm^{-1}. However, the most noticeable difference between the two compounds in the effects of the peripheral chloro and phenyl groups is already visible in the absorption and fluorescence spectra at room temperature; for **2o**, the spectra are blue shifted compared to **1o** (see figure 7.5 for comparison). This implies that although the end groups are connected to the sexithiophene unit via an electron deficient alkene bond (by virtue of the electron withdrawing properties of the perfluorocyclopentene), electronic communication is not precluded. The temperature dependence of the integrated absorption spectrum of **2o** shows a gradual red shift and increase in intensity with decreasing temperature and the distinct phase transition observed for **1o** is absent (figure 7.3).

The fluorescence of **2o** is less structured than that of **1o**. Nevertheless, the fluorescence spectrum can be decomposed into three bands centered at 18800, 19040 and 20415 cm^{-1}, respectively. Again an abrupt temperature dependent phase transition in the fluorescence spectra is absent. It is apparent that the phenyl substituent plays a key role in driving specific intermolecular interac-

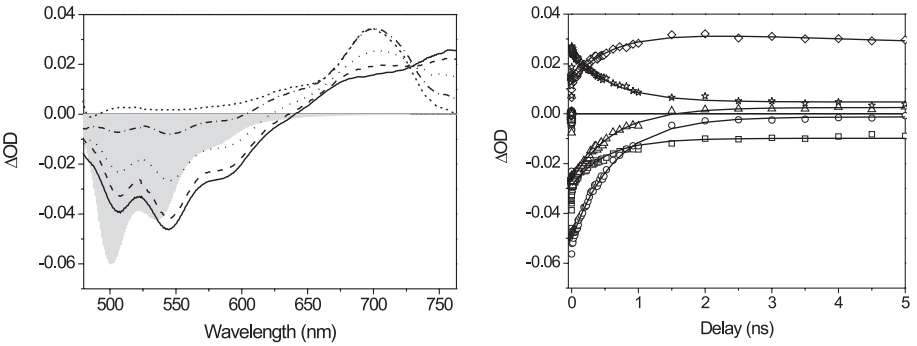

FIGURE 7.6. Transient absorption spectra of **1o** in cyclohexane T = 298 K. Pump 475 nm, 45 fs, 100 μW. [Left] Spectral evolution of **1o** at 10 ps (solid line), 100 ps (dashed line), 320 ps (dotted line), 1 ns (dash-dotted line) and 4.5 ns (short dashed line). The inverted steady state fluorescence spectrum of **1o** is superimposed, with scaling (grey shading). [Right] Temporal evolution of the transient signal at 450 (squares), 545 (circles), 585 (triangles), 685 (diamonds) and 750 (stars) nm. The solid lines are the fits.

tions. Comparison with **2o** shows that aggregation occurs to a lesser extent, i.e. the intermolecular interactions are less strong, or that aggregates, different to those of **1o**, are formed. Hence minor changes to the peripheral groups affect aggregation behavior and consequently the temperature dependence of the luminescence properties can be tuned.

7.1.5 TRANSIENT ABSORPTION SPECTROSCOPY

Steady-state spectroscopy indicated formation of H-aggregates at lower temperatures for **1o**, and to a lesser extent for **2o**. These results would predict a difference in the photoexcited state dynamics at low (125 K) and high (298 K) temperatures. In order to further elucidate the nature of these systems, their ultrafast dynamics were measured under a range of conditions. Transient absorption spectroscopy can provide deeper insight into the effect of the peripheral phenyl and chloro groups on aggregate formation. The steady-state spectra assist in the assignment of features in the transient absorption spectra. At low temperature, there is no evidence of ring closing, even after prolonged (>2 h) irradiation at 365 nm. Hence, at these temperatures ring closing reactions are not observed in the spectroscopic studies. Furthermore time-resolved spectra show that even at room temperature the ring closing reaction and resulting permanent absorption changes are negligible.

Figure 7.6 shows the transient absorption spectra and single wavelength kinetic traces of **1o**. From the steady state absorption spectrum at 298 K (figure 7.2) it is apparent that **1o** does not show significant absorption at wavelengths <500 nm; hence within the spectral window examined here (480-760 nm) ground state bleaching will not be observed. A structured negative sig-

nal (pump-induced transmission increase) is observed between 480 and 650 nm, while between 650 and 760 nm a positive signal (pump-induced absorption) dominates the spectrum. At longer time delays (>1 ns) the main spectral feature is a relatively narrow positive band centered at 700 nm. The negative signal in the transient spectra is comparable with the inverse of the steady state fluorescence spectrum of **1o** at room temperature (figure 7.4 and grey shading figure 7.6), indicating that the negative transient signal is due to stimulated emission (SE) from the S_1 to S_0 state. The positive signal between 650 and 760 nm is assigned to excited state absorption (ESA) from S_1 to S_n. The nature of the band at 700 nm cannot be assigned directly on the basis of the steady state spectra. The decay over the whole spectral window can be fitted globally to a biexponential function with time constants of 11 and 625 ps using the model described in figure 7.8. The first time constant is tentatively assigned to a vibrational cooling process. The second time constant matches the fluorescence lifetime determined by single photon counting (600 ± 30 ps), and is similar to the lifetime of the lowest excited state in unsubstituted T6 in solution (800 ps) [196, 197] and agrees closely with the lifetime of substituted T5 (300 ps) [196]. Both SE and ESA regions can be fitted with identical decay constants, indicating that the ESA at ∼750 nm is due to the S_1 to S_n transition. The ESA signal at 700 nm grows in with a ∼600 ps time constant, hence the corresponding state must be populated from the S_1 state. The lifetime of the state centered at 700 nm is beyond the resolution of the present system (maximum scan range ∼6 ns). However, the absence of a depletion at 700 nm prior to the t_0 of the pump-probe scan sets an upper limit for the lifetime of this state to be much less than the inverse of the repetition rate of the laser (500 μs). In assigning the transient absorption band at 700 nm, the formation of the mono-cationic state of the compound (the spectrum of **1o**+ was measured and shows a band at ∼750-800 nm) or formation of **1c**, which absorbs at 640 nm, can be excluded. The rate of the process is typical of intersystem crossing (ISC) in oligothiophenes from a singlet to a triplet state. The shape of the band compares closely with the T_1 to T_n transition in sexithiophene (T6) [198] in dichloromethane at 680 nm. Hence the ESA in **1o** at 700 nm is assigned to the T_1 to T_n transition.

The transient spectra of **1o** recorded at 125 K are shown in figure 7.7. The transient spectra are similar in certain respects to those observed at 298 K, i.e. negative signals are observed in the region 500-700 nm and a positive signal is seen at wavelengths longer than 700 nm. As at 298 K the ESA at 700-750 nm is again assigned to the S_1-S_n transition. However, there are also distinct differences between the spectra at the two temperatures. The steady state absorption spectrum at 125 K is red-shifted compared to that at 298 K. The lowest energy absorption in the steady state absorption spectra of **1o** at 125 K is relatively intense at ∼505 nm (figure 7.2), and falls within the spectral window examined (500-750 nm). Hence, in contrast to 298 K, a ground state bleaching signal is expected and indeed a negative signal centered at ∼515 nm is observed in the transient spectra of **1o** at 125 K that is assigned to ground state bleaching of the S_0 - S_1 transition. The steady state fluorescence spectrum at 125 K is

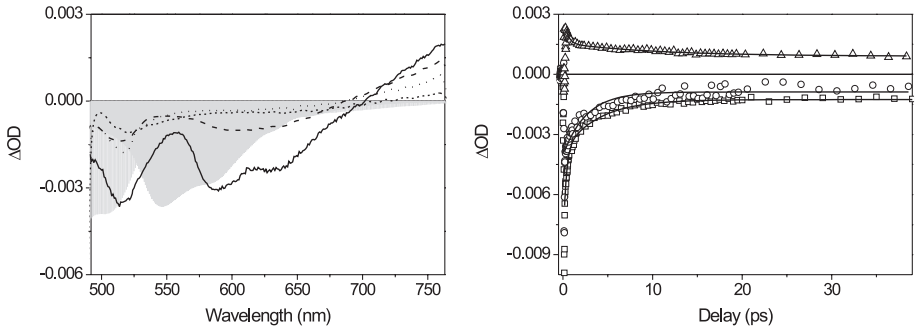

FIGURE 7.7. Transient absorption spectra of **1o** in isopentane T = 125 K. Pump 475 nm 45 fs, 30 μW. [Left] Spectral evolution of **1o** at 1 ps (solid line), 10 ps (dashed line), 100 ps (dotted line) and 4.5 ns (dash dotted line). The inverted steady state fluorescence and absorption spectra of **1o** at 125 K are superimposed, after scaling (dark and light grey shading respectively). [Right] Temporal evolution of the transient signal at 515 (squares), 615 (circles) and 750 (triangles) nm. The solid lines are fitted to the data

red shifted compared with that observed at 298 K (figure 7.4). The transient spectra show a similar red shift in the SE signal with maxima (i.e. at 1 ps after excitation in figure 7.7) at 544 and 588 nm at 298 and 125 K, respectively. Although the vibrational progression at 125 K differs between the transient SE and the steady state fluorescence spectra, the characteristic vibrational substructure remains recognizable (i.e. maxima at 588 and 631 nm for SE and 546, 588, 628 and 667 nm for the steady state fluorescence). The fact that not all the bands visible in the steady state fluorescence spectra are observed in the transient SE spectra can be explained by overlapping signals, i.e. ESA both at the red and the blue side of the SE can distort the shape compared with the steady state fluorescence spectrum. The decrease in fluorescence intensity at low temperature (vide supra) was attributed to the formation of H-aggregates. Therefore, it is expected that the dynamics, observed at 125 K and 298 K are different. The dynamics, obtained from a global fit using the model in figure 7.8, are considerably faster at 125 K with components of 5 and 200 ps, the latter having a smaller amplitude (by a factor of 4-40) than the fast components (figure 7.7). Although, not resolved by global analysis, in single trace fitting an ultrafast component of 650 fs ($\pm$170 fs), with a considerable amplitude, was observed, absent at room temperature . In addition to these decay constants a longer-lived signal is observed. This long-lived signal has a time constant that is beyond the maximum scan range of the system, but with an upper limit of $<<$500 μs. The sharp decrease in the transient signal that is observed especially at 515 nm (figure 7.7) is not assigned to ultrafast kinetics in the system but instead to a coherent artifact. The presence of two distinct species, one of which is in the aggregated state, and a small amount still present as isolated molecules, is based on the assignment of the several decay time constants at 125 K. The latter, as seen at 298 K, give rise to the $\sim$400 ps and $<<$500 μs decay

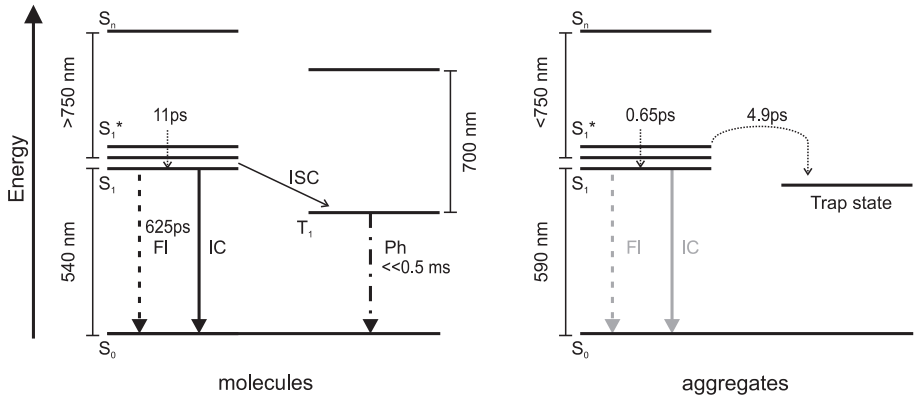

FIGURE 7.8. Energy diagram for **1o** in the form of isolated molecules (left) and aggregates (right). At room temperature only isolated molecules are present, while aggregation is observed at lower temperatures. At low temperatures there is a mixture of a (minor fraction of) isolated molecules and of the aggregates. Therefore, at 125 K both energy level diagrams are relevant and a combination of time constants, long for the isolated molecules and short for the aggregates, and spectral features belonging to both cases can be expected in the transient absorption experiments at low temperatures

times. Therefore the faster time constants are characteristic of the aggregated species with efficient non-radiative deactivation expected due to the intermolecular interactions present. The fastest time constant of 650 fs is assigned to rapid relaxation to the lowest vibrational state in S_1 [199–201]. The nature of the state that decays with the 4.9 ps time constant is unclear. Lanzani *et al.* tentatively attributed a similar ps time constant to charge separation [196]. It is perhaps more probable that there are local defects and impurities in the H-aggregates that cause the trapping of the excitons after rapid intermolecular energy transfer. Figure 7.8 shows tentative energy diagrams for the molecules and the aggregates.

7.1.6 COMPARISON BETWEEN THE TRANSIENT ABSORPTION SPECTROSCOPY OF **1o** AND **2o**

Table 7.1 shows the results of the fitting of the transients in **1o** and **2o**. At room temperature the different bands in the transient spectra agree well with those observed for **1o**. As expected, the spectral features mirror the steady state spectra and therefore the SE in **2o** shows few spectral features (figure 7.9). The three time constants that are needed to fit the transients in **2o** are similar and have the same physical origin as those of **1o**. The excited state lifetime in **2o** is considerably longer than in **1o**. A possible explanation is a difference in the destabilization of the planar configuration of the molecules by the substituent [196]. Along these lines, the chloro substituent allows for

TABLE 7.1. Transient absorption kinetics from exponential fits for **1o** and **2o**.

Sample	T(K)	Decay constant
1o	298	11 ps
		625 ps
		$\ll 500$ μs
1o	125	650 fs
		4.9 ps
		196 ps
		$\ll 500$ μs
2o	298	6.9 ps
		830 ns
		$\ll 500$ μs
2o	125	8.6 ps
		1.5 ns

The error in the decay times determined by global analysis of the data is in the order of 10%. Because of the lack of qualitative data for **2o** at 125 K, the decay times are determined by single trace fitting.

more planar molecules, lowering the efficiency of low energy torsional modes as acceptor modes in the radiationless decay to the ground state. The shape of the triplet state in **2o**, unlike the distinct band around 700 nm in **1o**, is spread out over the whole spectrum.

The transients of **2o** at 125 K are of poorer quality, due to the low concentrations achievable in solution. However, it is clear that a short time constant dominates the dynamics. The presence of an 8 ps time constant in both the 298 and the 125 K transients appears to be coincidental, however the quality of the data precludes identification of a similar subpicosecond time constant as in **1o**. The results from steady state spectroscopy could not discriminate between the formation of aggregates showing smaller intermolecular interactions or different types of aggregates in **1o** and **2o**. The decrease in fluorescence intensity in **2o** indicated the formation of H-aggregates. Moreover, no additional spectral features typical for different arrangements such as J-aggregates, superradiance and a narrow J-aggregate peak, were observed [175]. However the time-resolved data provide a definite answer. While for **1o** the temperature dependence of the transient absorption decay time constants is indicative of aggregation, the data is less clear for **2o**. The decay time constants at 298 K and 125 K are coincidentally similar, however the amplitudes are not. As for **1o**, the amplitude of the fast component at 125 K in **2o** exceeds the amplitude of the long component. Based on this similarity, we conclude that H-aggregates are formed by both compounds. Nevertheless, the intermolecular interactions are stronger for **1o**, indicating that the phenyl group in **1o** contributes considerably to the intermolecular interactions by additional $\pi - \pi$ interactions.

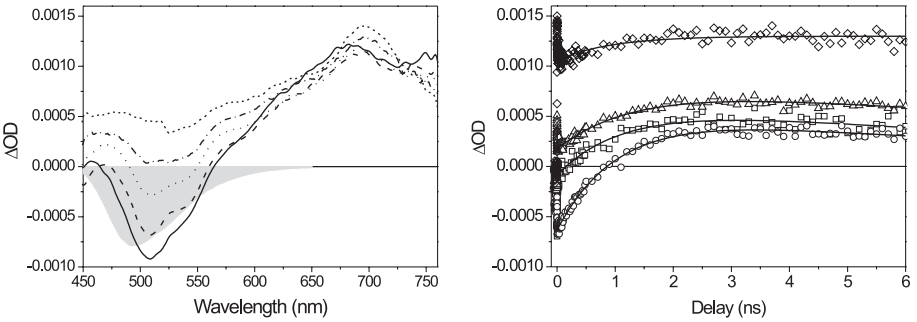

FIGURE 7.9. Transient absorption spectra of **2o** in cyclohexane T = 298 K. Pump 388 nm 150 fs, 30 μW. [Left] Spectral evolution of **2o** at 5 ps (solid line), 200 ps (dashed line), 500 ps (dotted line), 1 ns (dash-dotted line), 4 ns (short-dashed line). The inverted steady state fluorescence spectrum of **2o** is superimposed, after scaling (grey shading). [Right] Temporal evolution of the transient signal, cuts made at 475 (squares), 535 (circles), 585 (triangles), and 685 nm (diamonds). The solid lines are the fits through the data.

7.1.7 CONCLUSION

Two α-substituted sexithiophene compounds with two peripheral side groups (i.e. phenyl and chloro) have been studied in solution under several different conditions by steady state and time-resolved spectroscopies. The absorption, fluorescence and transient spectra of **1o** and their respective temperature dependence manifest the formation of aggregates upon decreasing temperature. While at 298 K the system consists of isolated molecules, below 180 K specific intermolecular interactions drive the system to form H-aggregates. Likewise, H-aggregates have also been observed in solid state samples of **1o** as revealed by absorption and X-ray spectroscopy. Similar measurements of **2o** indicate a markedly different aggregation behavior; quenching of the fluorescence was not complete and occurred gradually over the whole temperature range. The transient spectral data for **1o** and **2o** at 125 K provides strong evidence that both compounds form H-aggregates. Nevertheless, the interactions between the molecules of **2o** are weaker and lack the potential for $\pi - \pi$ stacking of the peripheral phenyl rings of **1o**. This result leads to the conclusion that there is a pronounced effect of the peripheral substituent (i.e. phenyl- vs chloro-) on both the electronic and aggregative properties of these systems. The hexafluorocyclopentene groups facilitate communication between the sexithiophene and the chloro and phenyl substituted monothiophene unit. These results demonstrate that well-structured intermolecular aggregation can be achieved in the absence of more traditional functional units such as amides and ureas. Furthermore these data provides an understanding of the electronic properties of these compounds essential to their application in multicomponent molecular systems.

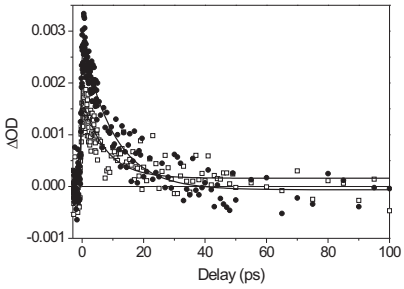

FIGURE 7.10. Transient absorption spectra of **2o** in isopentane T = 125K. Pump 338 nm 150 fs, 4.8 mW. Temporal evolution of the transient signal at 700 (open squares) and 740 nm (circles). The solid lines are the fits through the data. The reduced solubility of **2o** at lower temperatures in isopentane results in considerable levels of scatter and hence the signal obtained is significantly reduced in quality.

7.2 PHOTOSWITCHABILITY IN BIS-DIARYLETHENE-SEXITHIOPHENES: FROM A SEXITHIOPHENE TO A DITHIENYLETHENE AND BACK

7.2.1 INTRODUCTION

In the bottom-up approach to molecular electronics, highly conjugated molecules with multiple functionalities provide important properties, including high charge mobility and the possibility to form rigid structures, together with the possibility to modify materials reversibly after synthesis and even after incorporation into devices. Within the context of functional molecular materials dithienylethenes and oligothiophenes stand out. Photochromic dithienylethene switches are especially interesting because of their often excellent fatigue resistance and the thermal stability in both photochromic states [7, 130]. Oligothiophenes form materials that have already proven their versatility in electronic devices such as FEDs, OLEDs, photovoltaic cells and molecular wires [166, 168, 179]. They provide for high charge mobilities and emission quantum yields, regular morphologies, and show excellent stability. The combination of these two functional units allows for interesting new materials, such as switchable molecular wires. Recently, we introduced photoswitchable units at both α-ends of a sexithiophene (figure 7.11). These units allow for tuning of the properties of these systems after the compounds are synthesized [187]. In these systems the absorption and fluorescence spectra of the open form exhibit a remarkable dependence on temperature [202]. In the open form the UV/Vis spectrum at 298 K shows a broad unstructured absorption band in solution that becomes increasingly structured below 260 K and is accompanied by a near complete loss in fluorescence intensity. The changes in the absorption

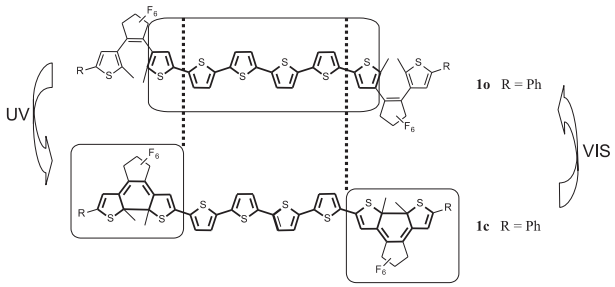

FIGURE 7.11. Molecular structure of compound **1** in the fully open (**1o**) and fully closed (**1c**) state. Compound **1** is end-capped with phenyl groups. The suffixes **o** and **c** indicate that both photochromic units are in the open and closed states, respectively. The dotted lines between the open and closed form indicate the overlap in structure of the sexithiophene and the dithienylethene unit.

spectrum and the dramatic decrease in fluorescence observed with decreasing temperature were ascribed to the formation of aggregates at temperatures below 260 K. A fundamental challenge facing the design of multifunctional systems arises when the two functional units in a molecular system overlap structurally (figure 7.11); can both units retain their individual characteristics. In the present case, for example, will the sexithiophene unit or the molecular dithienylethene unit dominate the properties of this multi-component system. These questions are of key importance in the development of switchable molecular devices. When two functional components are combined to form a single molecular system, often its properties are determined primarily by only one of the functional units with the second component serving to modify and/or tune these properties. However, it would be highly interesting to design systems in which the fundamental nature of a multicomponent system can be changed through reversible switching. In this part of the chapter steady state and ultrafast time-resolved spectroscopies are employed to explore the behavior of these dithienylethene-sexithiophene multicomponent compounds. It is shown that the fundamental character of the molecule can be toggled between two states: in the open form the molecule behaves as a sexithiophene and in the closed form as a dithienylethene.

7.2.2 EXPERIMENTAL

Ring-closure of the compound was achieved by irradiation with a UV lamp (Spectroline 312 nm) for approximately one minute. HPLC analysis showed that full ring closure proceeded through the intermediate **co** state [187]. However, isolation of **co** and **c** was precluded by thermal instability with respect to ring opening. Transient spectra show that during the experiments on the closed state the system is in the **c** state.

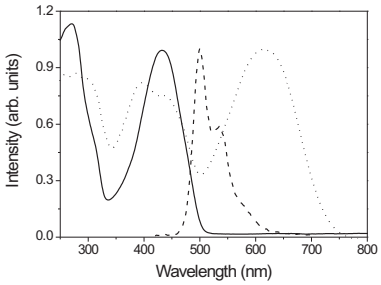

FIGURE 7.12. Absorption spectra of **1o** (solid) and **1c** (dots) and the fluorescence spectrum of **1o** (dashed). The closed form is non-fluorescent. The individual spectra are normalized to their maxima in the region 430-620 nm.

7.2.3 RESULTS AND DISCUSSION

Figure 7.12 summarizes the results of steady-state spectroscopy. The absorption spectrum of the sample closed photochemically shows a pronounced bathochromic shift of ∼180 nm compared to that of the open form (**1o**). Such a shift is typical for dithienylethene photochromic switches and is due to changes in the energies of the frontier orbitals [7, 189]. The absorption spectrum undergoes a red shift of ∼40 nm over a 180 K temperature range (see figure 7.2) and is broadened slightly compared with that at room temperature. Even at 120 K, the absorption spectrum does not show structure that would indicate aggregation, in contrast to **1o**. Furthermore in the open form, the compound is highly fluorescent ($\Phi_{fl} = 0.2$), whereas the closed form is non-fluorescent ($\Phi_{fl} < 10^{-5}$). In summary, the steady state spectra show that the behavior of the closed form does not resemble that of the open form; **1c** is non-fluorescent and there is no evidence for H-aggregate formation at low temperature. We now proceed to the analysis of the ultrafast dynamics with particular focus on selective excitation of the closed form. The quantum yield of photochemical ring opening for dithienylethenes is low, typically 1% or less [139]. Therefore, the transient spectra and kinetic traces are virtually free of contributions from the photochromic reaction and the formation of **1o**. Furthermore, permanent bleaching is not observed in the transient data, allowing for unencumbered analysis of the photophysics of **1c**.

Figure 7.13 shows the room temperature transient spectra and decay kinetics of **1c**. The negative signal (minimum at 614 nm) corresponds in shape to the steady state absorption spectrum. Hence, this signal is assigned to ground state bleach. Between 670 nm and 750 nm, the end of the detection window, a positive signal is observed, that can be assigned to excited state absorption (ESA) from S_1 to S_n. The kinetic traces at 298 K can be fitted globally with a three level sequential model with time constants of 140 fs, 1.6 ps and 6.3 ps. The shapes of the transient spectra of the **1c** at 125 K and 298 K are similar (see figure 7.14). The kinetic traces at 125 K are fitted globally with the same

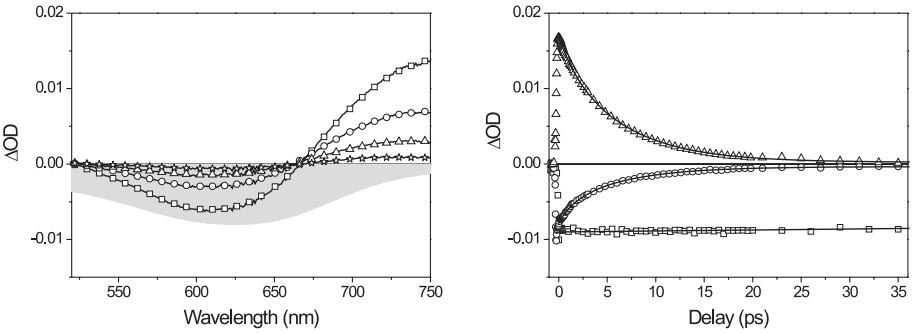

FIGURE 7.13. Transient absorption spectra of **1c** in cyclohexane at 298 K. Pump 620 nm, 33 fs, 30 W. [Left] Spectral evolution of the closed form at 1 ps (squares), 5 ps (circles), 10 ps (triangles), and 20 ps (stars). The symbols represent the spectra obtained from global analysis of the data. [Right] Temporal evolution of the transient signals at 600 nm (circles), and 750 nm (triangles). The steady state absorption spectrum is presented scaled and in grey shading. As a comparison the left panel shows the time evolution of the open form at 545 nm (squares). The solid lines are global fits of the data.

model as at room temperature. Time constants resulting from this fit are 90 fs, 1.5 ps and 5.0 ps. Fitting the data at 125 K with the same parameters as the room temperature data resulted in a decrease of the χ_2 of the fit by less than 4%. The errors in the time constants from the global fits are ∼10%. Because of the close resemblance in spectral shape of the levels involved in the model, the different time constants cannot be directly linked to a physical process, however comparison with previous studies is strongly suggestive of certain underlying processes [132, 135, 142, 150, 203]. The subpicosecond time constant observed in our data corresponds well with a time constant assigned to the initial decay of the excited state by level crossing (1B-2A) in cyclohexadiene, the core of the dithienylethene molecular switches. From this point onwards the decay proceeds to a minimum on the potential energy surface from which the molecule returns via a conical intersection to its electronic ground state. This process is followed by vibrational cooling to allow for relaxation to the minimum of the ground state potential.

Figure 7.13 shows a kinetic trace for **1o** as a comparison [202]. The closed form (**1c**) decays by a factor of a hundred times faster than the open form (**1o**); within the lifetime of **1c** the signal of the open form is virtually static. Previously we assigned the properties of the **1o** – the shape and intensity of the fluorescence spectra and the temperature dependent aggregation – to behavior typical of a sexithiophene [202]. However, the properties of the closed state examined here are markedly different from those of sexithiophenes. Instead, the results of both steady state and time resolved spectroscopy are consistent with previous studies of ring closed dithienylethenes [139, 204]. Hence, the state – open (**1o**) or closed (**1c**) – of the dithienylethene functional units has a profound influence on the nature of this multicomponent compound: in the open form it

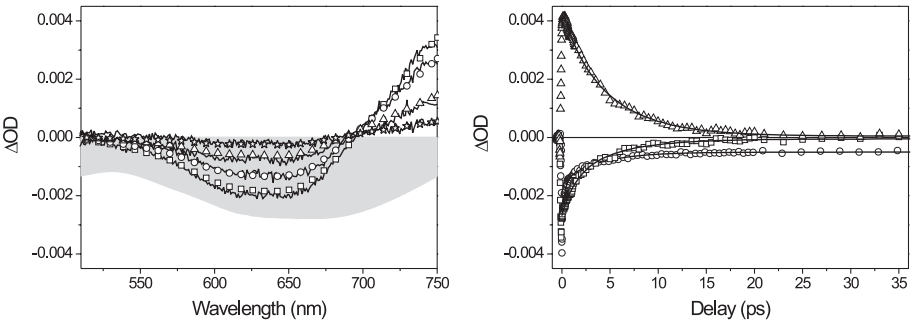

FIGURE 7.14. Transient absorption spectra of **1c** in isopentane T=125 K. Pump 620 nm, 33 fs, 30 W. [Left] Spectral evolution of the closed form at 1 ps (squares), 2 ps (circles), 5 ps (triangles), and 10 ps (stars). The steady state absorption spectrum is presented scaled and in grey shading. The symbols represent the spectra from global analysis of the data. [Right] The temporal evolution of the transient signals at 650 nm (squares), 750 nm (triangles). As a comparison on the right side the time evolution of the open form at 515 nm (circles)is shown. The solid lines are global fits of the data.

behaves as a sexithiophene and in the closed form as a dithienylethene. This observation is supported by electrochemical measurements reported earlier [187], where it was shown that cyclic voltammetry of **1o** is typical of end-capped sexithiophenes. However, upon ring closing to **1c**, the reduction potential observed is characteristic of dithienylethenes in the closed form. The shift in reduction potential corresponds closely to the shift of the lowest absorption in the UV/Vis absorption spectrum.

7.2.4 CONCLUSION

The behavior of this molecular wire can be changed reversibly between that of a sexithiophene with photochromic end groups and that of an oligothiophene bridged bis-dithienylethene. This change is manifested by a dramatic difference in fluorescence intensity and excited state lifetime between **1o** and **1c**. Thus, by adding dithienylethene photochromic groups to the α-ends of a sexithiophene a simple stimulus, light, can be used for post-synthetic tuning of the molecule. In the open state the electronic and excited state properties are essentially those of an oligothiophene molecular wire perturbed by the thienylethene end groups. In the closed state the molecule shows photochemical behavior that is essentially that of a dithienylethene molecule substituted with thiophene units. This ability to toggle the primary functionality of a multicomponent molecular system opens interesting prospects for the development of bifunctional molecular electronic systems, not least in the fundamental concept of switching of molecular conductance.

8 Energy transfer in coumarin substituted dithienylethenes

The optical properties of two structurally similar coumarins attached to a diarylethene molecular switch are compared. The fluorescence of the dimethoxy-coumarin has a high quantum yield in the open form and is nearly completely quenched upon ring closing. In stark contrast, the fluorescence of the monomethoxy-coumarin is already quenched by the switch in the open form and limited quenching is seen upon ring closing. Hence, the ability to switch fluorescence intensity on and off depends strongly on the structure of the fluorophore and therefore also on the electronic energy levels of the fluorophore with respect to the switch.

8.1 Introduction

Molecular switching of fluorescence is receiving increasing attention because of the possibilities for non-destructive readout of information at the molecular level. Control of energy transfer using molecular design principles allows for manipulation of the fluorescence output in multicomponent systems based on dithienylethene molecular switches [154, 205–207]. Since conventional top-down lithographic methods for data storage are running towards their fundamental limits, a molecular based bottom-up approach is an interesting development. Dithienylethene molecular switches are good candidates in this regard, due to their high fatigue resistance and advantages in terms of writing speed and resolution (see chapter 6) [127, 130]. However, such switchable systems raise many fundamental questions, such as how to build systems in which energy flow can be directed. The type of components that are needed in what form and why, are key issues which need to be addressed to design compounds with specific functions.

In this chapter, the basic design principles for the construction of compounds showing switchable fluorescence are addressed. Two highly fluorescent chromophores are linked covalently to a dithienylethene molecular switch as shown in figure 8.1. This class of switches has shown excellent stability, high efficiency in the formation of the photo-stationary state and a high degree of reversible fluorescence quenching [127, 156, 205, 206]. The two coumarin-substituted dithienylethene switches were synthesized with only minor differences in their structures, but as will be shown with significant differences in their optical properties. While the monomethoxy coumarin (MMCS) shows little fluorescence, independent of the state of the switch, the dimethoxy coumarin (DMCS) is highly fluorescent in the open form, but not in the closed. That is,

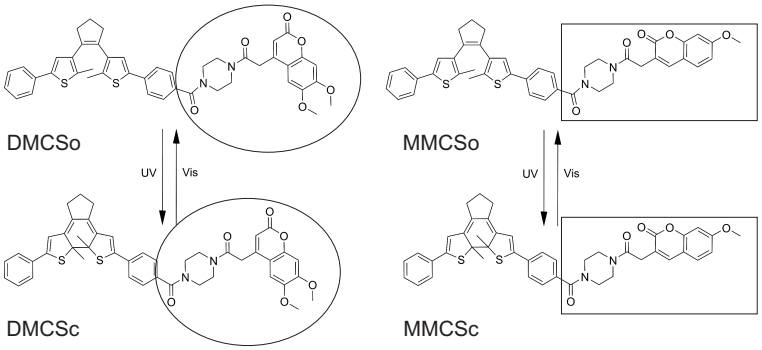

Figure 8.1. Molecular structures of the di-methoxy coumarin functionalized diphenyl switch (DMCS) in the open and closed form (left) and of the mono-methoxy coumarin functionalized diphenyl switch (MMCS) in the open and closed form (right). The coumarin units are pointed out by the lines drawn around them. The suffixes o and c will be used throughout the chapter to refer to the open and closed form of the compounds.

for DMCS after ring closing to the photostationary state, the fluorescence is almost completely quenched (>90%), thus acting as a reversible on/off switch of the fluorescence. Usually fluorescence quenching behavior is described by Förster energy transfer theory in which, amongst others, the overlap between the emission spectrum of the donor and absorption spectrum of the acceptor is important [40]. Changes to molecular structures are then made to modify the energy levels resulting in a change in the optical spectra. However, in the present case this approach breaks down and other aspects need to be taken into account. This unexpected result holds considerable implications regarding the design of these types of molecules.

8.2 Experimental

Dichloromethane, employed in all measurements, was of spectroscopic grade or better and used as received. DMCS, MMCS, the model coumarins DMCpipboc and MMCpipboc and the dithienylethene switch were provided by Dr J. H. Hurenkamp and Dr J. Areephong [208]. Fluorescence lifetimes were measured using time-correlated single photon counting (for a detailed description see section 2.4.2). The instrument response function at this wavelength was estimated from scattering to be about 50 ps. The excitation power was reduced to 10 nW at a repetition rate of 1.9 MHz. Under these experimental conditions the yield of ring closing is negligible, as confirmed by linear UV/Vis absorption spectroscopy. The time resolution in the transient absorption measurements, using the DAVE amplifier, was 200 fs at an excitation wavelength of 266 nm. Room temperature measurements were collected using a 2 mm flow cell with a 50 ml reservoir to avoid the build-up of photoproducts. For the transient absorption

measurements an excitation wavelength of 266 nm was available. At 388 nm, the second harmonic of the CPA (see chapter 2), the molecular absorptivity is too low, increasing the concentration would cause further problems. Due to the relatively high excitation powers required for the measurements, frequency doubling of the output of the NOPA would not result in a sufficiently high power for excitation. Linear UV/Vis absorption spectra of the samples before and after the time-resolved measurement were taken to verify that a minimal concentration of ring-closed species was formed (figure 8.1). The quantum yield of fluorescence of the compounds is determined using diphenylanthracene [209] as a reference and normalizing the fluorescence spectra to the absorption of the coumarin at the excitation wavelength.

8.3 Steady state absorption spectra

UV/Vis absorption spectra of DMCS and MMCS in the open and closed form (photostationary state after irradiation at 365 nm) are shown in figure 8.2. As a comparison the respective spectra of the coumarins, DMCpipboc and MMCpipboc are plotted. The lowest absorption peak for the two coumarins is shifted by 20 nm, from 346 nm for DMCpipboc to to 323 nm for MMCpipboc. However, in the absorption spectra of DMCS and MMCS in the open form the shift in the lowest absorption band is only 3 nm between both compounds. Photochemical ring closing, by irradiation at 365 nm, leads to the appearance of an additional red shifted band centered around 550 nm. This band is well known for dithienylethene switches and can therefore be ascribed to the switch unit [130]. This confirms that in these compounds the ring closing reaction (yield >95 %) proceeds and is not hindered by the addition of coumarin subunits.

Summation of the individual spectra of the switch and coumarin units provides a spectrum that closely resembles that of DMCS or MMCS both in the open and closed form, assuming that the quantum yield of ring closing in DMCS and MMCS is similar to that of the unconnected units (figures 8.3 and 8.4). This implies that, since the absorption spectra of the individual components are not perturbed by the covalent connection between the units, the coupling is not strong and there is little or no, through-bond, electronic communication between the two components.

8.4 Emission and excitation spectra

Figure 8.5 shows the fluorescence spectra of DMCS and MMCS in the open and closed form. The fluorescence spectra of DMCS and MMCS in the open form are identical in shape to their coumarin counterparts. In the open form the maximum of the fluorescence is at 420 and 415 nm for DMCS and MMCS respectively. Upon ring closing, the maximum of the fluorescence spectrum of DMCS shows a red shift to 435 nm. In contrast, in the case of MMCS it shifts to the blue at 394 nm, which coincides with the emission maximum of the switch in the closed form. When the 'absorption corrected' intensity of fluorescence of

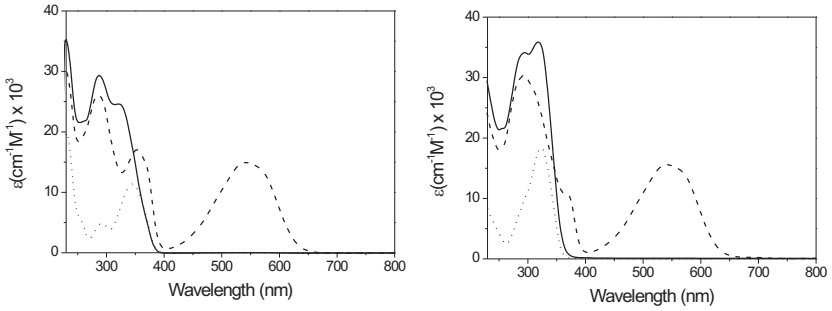

Figure 8.2. [Left] UV/Vis spectra of DMCS in the open form (line), closed form (dashed) and of the coumarin DMCpipboc (dots), spectra recorded in dichloromethane at 298K. [Right] UV/Vis spectra of MMCS in the open form (line), closed form (dashed) and of the coumarin MMCpipboc (dots), spectra recorded in dichloromethane at 298K.

DMCSo and MMCSo are compared with their respective coumarins two aspects stand out. Firstly, the fluorescence intensity of the DMCSo is equal to that of DMCpipboc, that is, the covalent attachment to the switching unit does not quench the fluorescence. This is contrasted by the near absence of fluorescence in MMCSo. Quantum yield measurements show that the fluorescence QY is about 30 times lower in MMCSo than in DMCSo (table 8.1). The presence of the switch in the open state, quenches the fluorescence intensity by at least 80% in MMCSo. This effect is independent of the excitation wavelength (i.e. unchanged upon excitation to S_1 or a higher excited state). Upon ring closing the fluorescence intensity of DMCS decreases dramatically. The respective QY shows that in the closed form, the emission is only 2% of the intensity observed in the open form, making the ring closed form of the switch an efficient fluorescence quencher. In contrast, ring closing has only a minor effect on the fluorescence intensity of MMCS, it is reduced to 30% of its value in the open form. Comparison of the shape of the fluorescence of the closed form of MMCS with the switch shows that these are equal, indicating that the switch is the emitting unit in the closed form of MMCS.

The excitation spectra of DMCS and MMCS in the open and closed form are shown in figure 8.6. In DMCS, in both forms the shape of the excitation spectra resembles that of the absorption of DMCpipboc, indicating that this is the main emissive unit in DMCS. It does not exclude that the switch fluoresces, but the intensity of its fluorescence at 440 nm is not significant in comparison to that of the coumarin. In MMCS, in addition to the absorption of MMCpipboc, the open and closed form show a band centered around 290 nm. Since this wavelength corresponds to the absorption maximum of the switch, it is concluded that the fluorescence at 440 nm is partially due to the switch unit. Whereas the fluorescence of the switch in DMCS was not significant compared to that of the

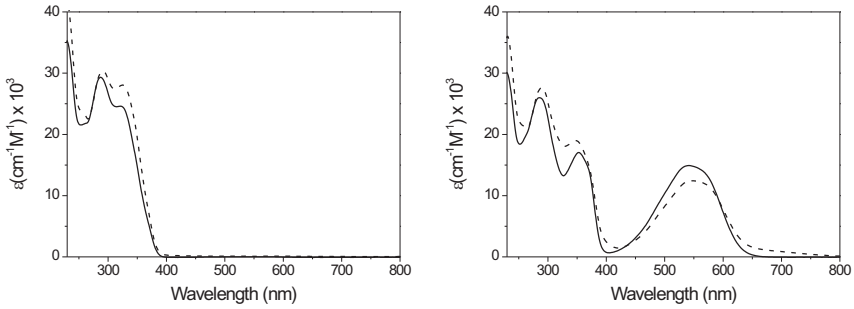

Figure 8.3. [Left] UV/Vis spectra of DMCS (line) and the summed spectra of the coumarin DMCpipboc and the switch (dashed) in the open form. [Right] UV/Vis spectra of DMCS (line) and the summed spectra of the coumarin DMCpipboc and the switch (dashed) in the closed form. Spectra recorded in dichloromethane at 298K.

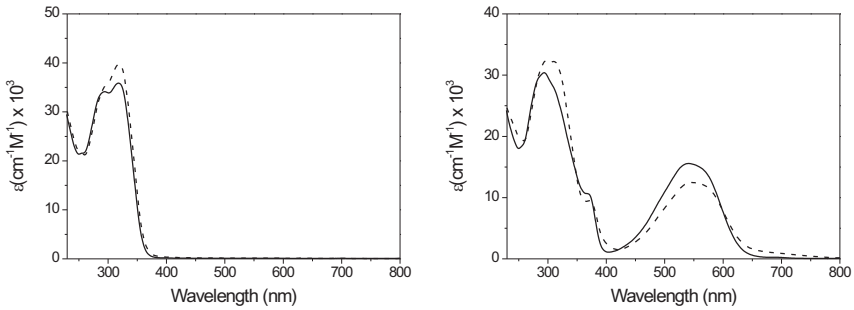

Figure 8.4. [Left] UV/Vis spectra of MMCS (line) and the summed spectra of the coumarin MMCpipboc and the switch unit (dashed) in the open form. [Right] UV/Vis spectra of MMCS (line) and the summed spectra of the coumarin MMCpipboc and the switch (dashed) in the closed form. Spectra recorded in dichloromethane at 298K.

Table 8.1. Fluorescence quantum yields in the open and closed form.

Compound	QY
DMCpipboc	0.3
MMCpipboc	0.3
DMCSo	0.3
MMCSo	0.01
DMCSc	0.007
MMCSc	0.004

The uncertainty of the values of the QY is estimated to be ∼10%. The PSS after ring closing is 98%.

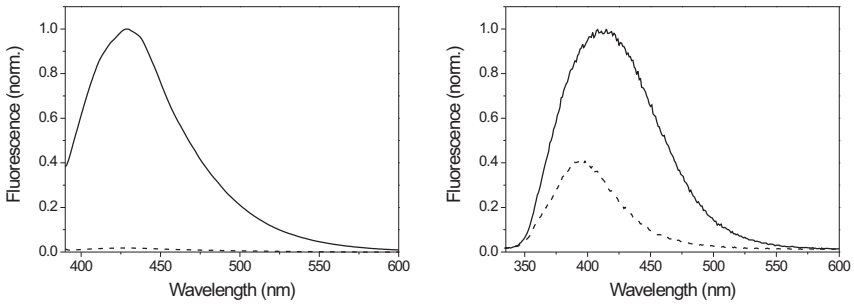

Figure 8.5. [Left] Fluorescence spectra of DMCSo (line) and DMCSc (dashed). Spectra are corrected for differences in the absorption at the excitation wavelength of 380 nm and are normalized to the maximum of DMCSo. [Right] Fluorescence spectra of MMCSo (line) and MMCSc (dashed). Spectra are corrected for differences in the absorption at the excitation wavelength of 330 nm and are normalized to the maximum of MMCSo.

coumarin, the intensity of the fluorescence of the coumarin in MMCS is lower and matches that of the switch.

The observations made in this section lead to the conclusion that there is energy transfer from the coumarin to the switch unit in both DMCS and MMCS, however the conditions needed for this to occur differ between the two compounds. Whereas energy transfer, resulting in fluorescence quenching, takes place both in the open form and closed form of MMCS, energy transfer is only efficient for DMCS in the ring closed form.

8.5 Förster energy transfer

In general when through bond interactions between molecular subunits are absent, i.e. in the weak coupling regime, energy transfer is described using Förster theory. Förster energy transfer theory is described in detail in chapter 3. Briefly, the rate of energy transfer relates linearly with the overlap integral between the emission spectrum of the donor, the coumarin, and the absorption spectrum of the acceptor, the switch. This is reflected in the equations describing the Förster radius (R_0), rate of energy transfer (k_T) and the efficiency of energy transfer (E) as follows.

$$\begin{aligned} R_0 &= 0.211 \left(\kappa^2 n^{-4} Q_D J(\lambda)\right)^{\frac{1}{6}} \\ k_T(r) &= \frac{1}{\tau_D}\left(\frac{R_0}{r}\right)^6 \\ E &= \frac{R_0^6}{R_0^6 + r^6} = \frac{k_T(r)}{\tau_D^{-1} + k_T(r)} \end{aligned} \tag{8.1}$$

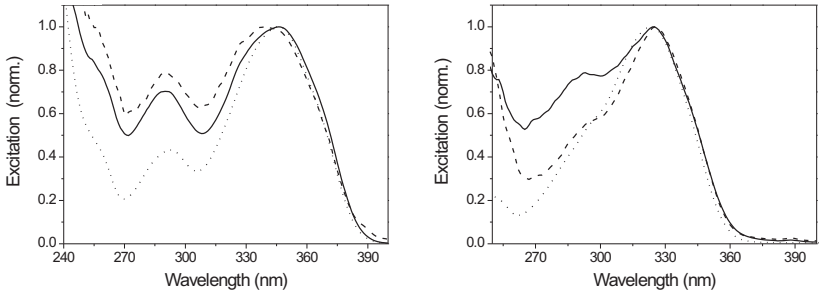

Figure 8.6. [Left] Excitation spectra of DMCSo (line) and DMCSc (dashed) compared to the absorption spectrum of DMCpipboc (dotted). [Right]Excitation spectra of MMCSo (line) and MMCSc (dashed) compared to the absorption spectrum of MMCpipboc (dotted). Excitation spectra are taken at 440 nm.

Table 8.2. Energy transfer efficiency

Compound	R_0 ($\mathring{A}$)	k_T (ps)	E^a	E^b
DMCpipboc-switch$_{open}$	18	64	1	0
MMCpipboc-switch$_{open}$	19	22	0.98	0.78
DMCpipboc-switch$_{closed}$	30	3	1	0.93
MMCpipboc-switch$_{closed}$	22	8	0.97	0.89

[a] The efficiency according to equation 8.1 using the spectra of the model coumarin and switch. [b] The experimental efficiency from the fluorescence intensities according to equation 8.2

Here κ is the orientational factor, n is the refractive index of the solvent, Q_D is the quantum yield of the donor, in the absence of the acceptor, and $J(\lambda)$ is the overlap integral between the area normalized emission of the donor and the absorption of the acceptor and r is the distance between donor and acceptor modeled as point dipoles [13]. The overlap is calculated by using 'absorption corrected' spectra of the unconnected coumarin and switch units. This can be justified by the minimal through-bond coupling between the two units. There are several assumptions made in the calculation of the energy transfer efficiency. The flexibility around the single bonds in the system justifies the orientational factor of 2/3 in the calculation of the Förster distance (see table 8.2). Both in the calculation of the transfer rate and efficiency, the distance between donor and acceptor is a variable. From molecular stick modeling, this distance r is approximated to be 10 $\mathring{A}$ for both DMCS and MMCS. When Förster theory can be applied to the system, equation 8.1 must give similar values for the energy transfer efficiency as found by comparison of the experimental fluorescence

intensities according to

$$E = 1 - \frac{F_{DA}}{F_D}. \tag{8.2}$$

Here, F_D is the fluorescence intensity of the donor and F_{DA} is the fluorescence intensity of the donor attached to the acceptor. Clearly, the values of the efficiencies from the two equations do not match (table 8.2). For MMCS the actual energy transfer efficiencies in the open and closed form agrees quite well with those calculated from the Förster equations. The open form of DMCS shows a large discrepancy between the two approaches. A different underlying mechanism such as Dexter energy transfer is not likely to explain the difference in behavior between the two compounds. The remainder of this chapter will focus on understanding the origin of this fundamental difference.

8.6 Time correlated single photon counting

To better understand the processes underlying the different behavior of the two compounds time correlated single photon counting (TCSPC) measurements were performed on the individual components of DMCS and MMCS. Figure 8.7 shows the fluorescence decay traces of the two coumarins, DMCpipboc and MMCpipboc, with excitation at 266 nm. At this wavelength $S_0 - S_n$ transitions are excited [210]. From table 8.3 the double exponential behavior of the decay of both coumarins is apparent. For the coumarins the time constants from the fit are 800 ps and 2-3 ns. It should be noted that DMCpipboc has a longer lifetime than MMCpipboc. The nanosecond decay time is likely to correspond to the lifetime of the S_1 state [211]. Coumarins are known for their complex solvation and rotation behavior and hence it comes as no surprise that their time-dependent emission shows multi-exponential behavior. Previous accounts on solvation and rotation dynamics of coumarins have assigned timescales ranging from subpipcosecond up to several hundreds of picoseconds to these processes [212–214]. Figure 8.7 shows the fluorescence decay traces of the switch. As for the coumarins, two time constants are required for a reasonable fit of the data both in the open and closed form. The fluorescence decay time constants change only by a small amount upon ring closing and the time constants needed for the fit of the data, 0.3-0.5 and 1-1.2 ns, are similar.

Excitation of a multicomponent system leads to a complex decay trace that shows contributions of all emitting units, depending on their respective absorption and fluorescence QY. In the case of DMCS and MMCS, at an excitation wavelength of 266 nm, both the coumarin and the switch are excited. Hence, decay time constants obtained from fitting the fluorescence decay traces of the coumarin and the switch are expected to be present in the DMCS and MMCS data. Figure 8.8 shows the results of the fluorescence lifetime measurements on DMCS and MMCS in the open and closed form. It turns out that only two exponents are required for fitting. The decay time constants of coumarin and switch units are similar (table 8.3) and can therefore not be resolved individually in the data of DMCS and MMCS. Table 8.3 shows that the dominating

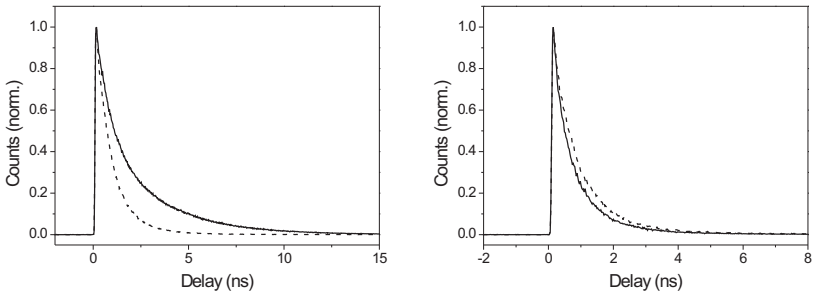

Figure 8.7. [Left] Fluorescence decay trace of DMCpipboc (line) and MMCpipboc (dashed). [Right] Fluorescence decay trace of the switch in the open (line) and closed form (dashed). Excitation wavelength 266 nm.

fast decay time constants of 200-300 ps both in the open and closed form of DMCS resemble that of the switch, the decay times of the coumarin is ∼3 times longer. The slowest time constant of 2.4 ns is too long to be assigned to the switch that shows a 1.2 ns decay constant. Hence, this decay time is assigned to fluorescence of the coumarin molecules that are unquenched. In the open form MMCS shows a similar behavior as DMCS; the dominating time constant of 220 ps resembles that of the switch. The contribution of coumarin fluorescence, present in the fluorescence lifetime measurements of DMCpipboc, is not detected in MMCS neither in the open nor in the closed form. As described in section 8.4 the fluorescence of MMCS, especially in the closed form, can be attributed to the weakly fluorescent switch. This is confirmed by comparison of the fluorescence lifetime measurements where the decay traces of the switch and MMCS, both in the closed form, are essentially indistinguishable. As expected by the values of the energy transfer rate from the coumarin to the switch stated in table 8.2, the actual process cannot be resolved with the current temporal resolution of 50 ps.

8.7 Transient absorption spectroscopy

To improve the time resolution of the fluorescence lifetime experiments, transient absorption spectroscopy is employed. Since the energy transfer is expected to occur on ultrafast timescales, improvement of the time resolution is expected to increase the knowledge about this process. At 266 nm, however, the absorption of the coumarin unit is 13% and 12% in the case of DMCS and MMCS respectively. Hence, the contribution of the coumarin dynamics, including energy transfer, to the transient absorption data will not exceed ∼10%. As in the fluorescence lifetime measurements, the individual components, coumarins and switch, were examined first. Figure 8.9 shows the transient spectra and decay kinetics of both coumarins. The transient absorption data are fitted globally

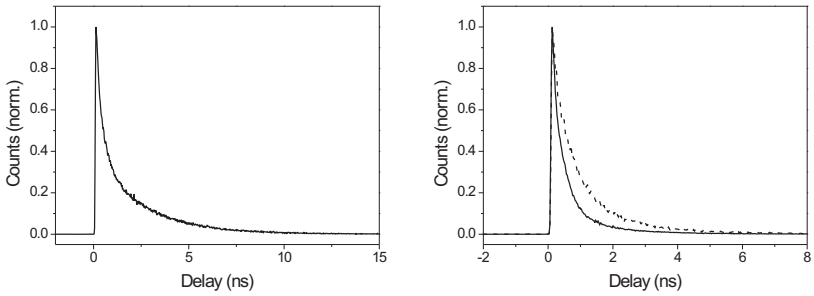

Figure 8.8. Left: Fluorescence decay trace of DMCS in the open form (line), as the decay trace of the closed form is virtually identical it is not shown. [Right] Fluorescence decay trace of the MMCS in the open (line) and closed form (dashed). Excitation wavelength 266 nm.

Table 8.3. Single photon counting decay times after excitation at 266 nm

Compound	t_1 (ns)	t_2 (ns)
DMCpipboc	0.8	3.0
MMCpipboc	0.8	1.9
switch$_{open}$	0.3	1.0
switch$_{closed}$	0.5	1.2
DMCS$_{open}$	0.3	2.4
DMCS$_{closed}$	0.2	2.4
MMCS$_{open}$	0.2	0.8
MMCS$_{closed}$	0.3	1.2

The error in the time constants is about 10%.

using a 4-level sequential model. This model uses three time constants, the minimum needed to fit the data in an acceptable way both in the frequency and time domain. The spectra show broad ESA with decay time constants of 2.8, 24 and 190 ps for DMCpipboc and 2.2, 23 and 240 ps for MMCpipboc. The signal has not decayed completely within the time window of the measurement (∼900 ps), hence there is an additional longer time component to the relaxation that cannot be extracted given the experimental resolution. This is in agreement with the nanosecond time constant observed in fluorescence lifetime measurements. Comparing the time constants from the TA measurements to those from the fluorescence lifetime experiments it is clear that the fastes two, 2-3 and 23-24 ps, were not resolved in the latter. Nevertheless, the third time constant is on the same order as the fastest time constant observed in the fluorescence lifetime data. The similarity of the time constants and the shape of the spectra of both coumarins is remarkable. This shows the similarity of their

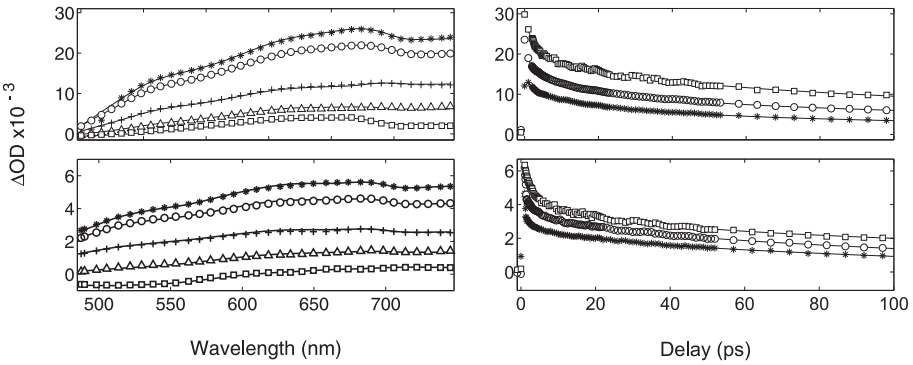

Figure 8.9. [Left] Transient absorption spectra of DMCpipboc (top) and MMCpipboc (bottom) at 2 (stars), 5 (circles), 50 (crossed), 200 (triangles) and 550 ps (squares). [Right] Transient kinetics of DMCpipboc (top) and MMCpipboc (bottom) at 500 (stars), 550 (circles) and 750 nm (squares). Excitation wavelength 266 nm, 1.3 μJ/pulse. The symbols represent the data, the lines are results of the global fits.

excited state dynamics. Previous studies show a broad excited state absorption band in the visible region of the spectrum similar to the ESA observed in figure 8.9 and assign this to $S_1 - S_n$ absorption [215]. As stated in the previous section, coumarins show complex solvation and rotation dynamics, mainly due to their large dynamic and static Stokes shifts. A wide range of time constants, subpicosecond to several hundreds of picoseconds are attributed to these processes, in addition to the nanosecond lifetime of the S_1 state. Specifically, 5 and 10 ps time constants were assigned to solvation dynamics [214] and vibrational cooling in the excited state [216] respectively and can explain the fast dynamics observed for both coumarins in the TA experiments.

The transient absorption spectra of the switch in the open and closed form show broad ESA (figure 8.10). In the open form there is a broad maximum around 550 nm. This maximum changes into a minimum upon ring closing, leaving the remainder of the spectrum unchanged. Time constants of the global fits of the open form are 1.6, 7.7 and 150 ps, as for the coumarins there is an unresolved time constant which is beyond the time window of the experiment. The deconvoluted spectra from global analysis will allow to draw some conclusions. The state that is initially excited decays with 1.6 ps to a level that has a similar, though slightly changed spectrum. In agreement with previous studies this change is assigned to relaxation to the S_1 state of the open form of the switch [139]. Subsequently, with a 7.7 ps decay time the system relaxes to a level that has a completely different spectrum and shows a maximum around 550 nm, similar to the absorption spectrum of the closed form. Hence, this time constant is assigned to the formation of the ring closed form [137, 139, 217]. After ring closing there is excess vibrational energy in the system that needs to be released. This corresponds to the time constant of 147 ps with which the system decays to the ground state of the closed switch [217]. The ns time constant in the

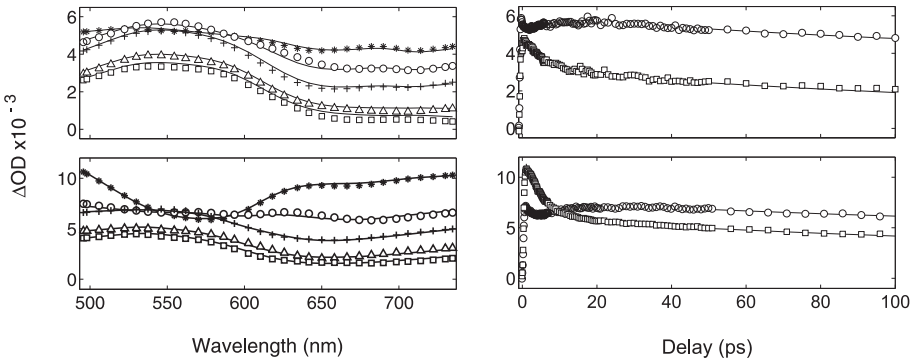

Figure 8.10. [Left] Transient absorption spectra of the switch in the open (top) and closed form (bottom) at 2 (stars), 10 (circles), 50 (crossed), 250 (triangles) and 550 ps (squares). [Right] Transient kinetics of switch in the open (top) and closed form (bottom) at 550 (circles) and 750 nm (squares). Excitation wavelength 266 nm, 300 nJ/pulse. The symbols represent the data, the lines are results of the global fits.

measurements is not straightforward to assign. However it might corresponds to the presence of the non-switching conformer, see section 6.3 [141, 217].

The closed form of the switch shows a similar decay pattern with time constants of 3.1, 8.2 and 156 ps and a small ns component. Unlike the case of the open form, it is not expected that spectral features belonging to the ring opening reaction will be observed, since the QY of ring opening does usually not exceed 1%. At 266 nm, the ring closed form of the switch is excited to a higher excited state. Within 3.1 ps the switch equilibrates to the S_1 state of the closed form. The 8.2 ps lifetime can be assigned to the lifetime of the S_1 state of the ring closed form [144, 149]. This is supported by the shape of the deconvoluted spectrum of this state. It resembles the spectrum of the state that appeared upon ring closing. The ground state relaxes with a 156 ps time constant.

Figure 8.11 shows the transient spectra and dynamics of DMCS and MMCS in the open form excited at 266 nm. For both compounds, the spectra consist of a broad positive signal that can be assigned to ESA. Since the contributions of the coumarins to the transient spectra will not exceed 10%, it is expected that both DMCS and MMCS should show similar transient absorption spectra as the switch. Time constants from global analysis are 1.6, 9.1 and 175 ps with an error margin of 10%. An additional long decay time, observed in the switch and the coumarins, remains. When the spectra and transients of MMCS are fit with the same parameters as DMCS, the χ_2 of this forced fit only reduced by $\sim$1% as compared to a fit with all parameters left free. This is an indication that DMCS and MMCS behave similarly, not only structurally, but also energetically after 266 nm excitation.

Figure 8.12 shows the transient spectra and dynamics of the ring closed form of DMCS and MMCS. These spectra consists of a broad positive band that can be assigned to ESA. There is a broad dip in the spectra centered around 550 nm.

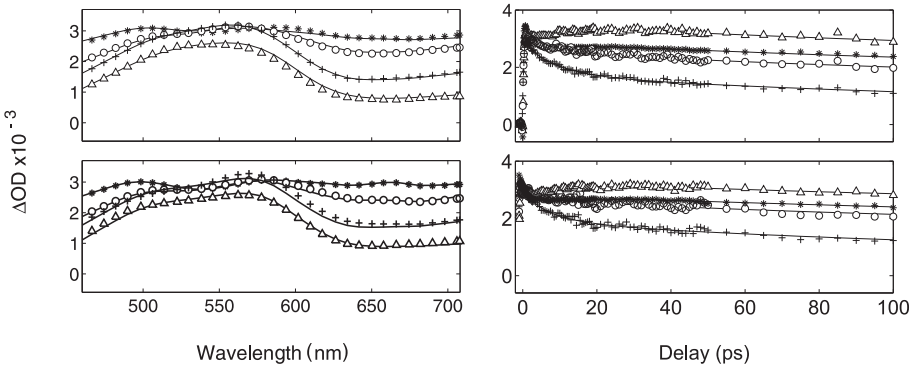

Figure 8.11. [Left] Transient absorption spectra of DMCSo excitation wavelength 266 nm, 200 nJ/pulse (top) and MMCSo, excitation wavelength 266 nm, 100 nJ/pulse (bottom). Spectral cuts at 1 ps (stars), 5 ps (circles), 50 ps (crosses) and 200 ps (triangles). [Right] Transient kinetics of DMCSo excitation wavelength 266 nm, 200 nJ/pulse (top) and MMCSo, excitation wavelength 266 nm, 100 nJ/pulse (bottom). Temporal cuts at 500 nm (stars), 550 nm (triangles), 600 nm (circles) and 650 nm (crosses). The symbols represent the data; the lines are the fits from global analysis.

As in the open form, the spectra of the two compounds show close resemblance. Nevertheless, there is a clear difference in the shape of the spectra comparing the open and the closed form. This change can be attributed to the switch unit, as similar changes were observed in transient spectra of the open and closed form of the switch unit when excited at 266 nm (see figure 8.10). As in the open form, the kinetic transients in the ring closed form are similar for DMCS and MMCS. Time constants from global analysis are 2.9, 16 and 270 ps with an error margin of 10%. As in the open form a long-lived state gives rise to an additional time constant on the order of ns that is not well resolved in our fit. When the spectra and transients of MMCS are fit with the same parameters as DMCS, the χ_2 of this restricted fit is reduced by $\sim$6% compared to a free fit. Comparing the transient spectra and kinetics of the open and closed form of the compounds (figures 8.11 and 8.12), they look different on first glance. However, the clear rise in the signal up to $\sim$25 ps observed for 550 nm in the open form is still present in the closed form only with a reduced amplitude. The three time constants that are used in the respective fits of the open and closed form also resemble each other and therefore do not show a distinct effect of ring closing.

Overall there seems to be little difference between the two compounds when looking at them with pump-probe spectroscopy. This is surprising, since the dramatic decrease of the fluorescence of DMCS upon ring closing, absent in MMCS, was expected to leave some marks in the ultrafast time domain.

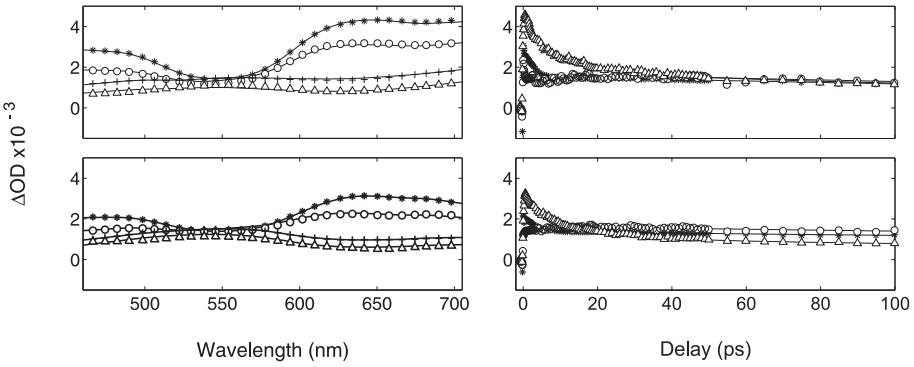

Figure 8.12. [Left] Transient absorption spectra of DMCSc excitation wavelength 266 nm, 660 nJ/pulse (top) and MMCSc, excitation wavelength 266 nm, 100 nJ/pulse (bottom). Spectral cuts at 1 ps (stars), 5 ps (circles) , 50 ps (crosses) and 200 ps (triangles). [Right] Transient kinetics of DMCSc excitation wavelength 266 nm, 660nJ/pulse and MMCSc, excitation wavelength 266 nm, 100nJ/pulse (bottom). Temporal cuts at 500 nm (stars), 550 nm (circles) and 650 nm (triangles). The symbols represent the data; the lines are the fits from global analysis.

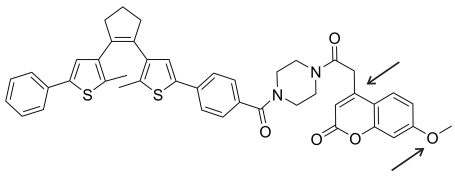

Figure 8.13. Molecular structure of a second mono-methoxy coumarin functionalized diphenyl switch (4-MMCS). The connection of the coumarin to the switch is similar as in DMCS. Both the connection and the single methoxy group are highlighted with an arrow.

8.8 The missing link

The difference in structure between DMCS and MMCS is not limited to the methoxy groups. Figure 8.1 shows that the connection of the coumarin to the switch differs between both molecules. Whereas the connection to the switch in DMCS is via the 4-position, in MMCS this is via the 3-position. Hence, the difference in the energy transfer and subsequent quenching can thus be assigned to the methoxy groups and/or the connection. To narrow down the effect further to one of the two possibilities, a new coumarin-switch was synthesized. In this coumarin, the switch is attached via the 4-position, but has only one methoxy group as is shown in figure 8.13, in the remainder of this chapter this compound will be referred to as 4-MMCS.

To distinguish, UV/Vis absorption and fluorescence spectra were measured. Figure 8.14 shows the absorption and emission spectra of 4-MMCS. The ab-

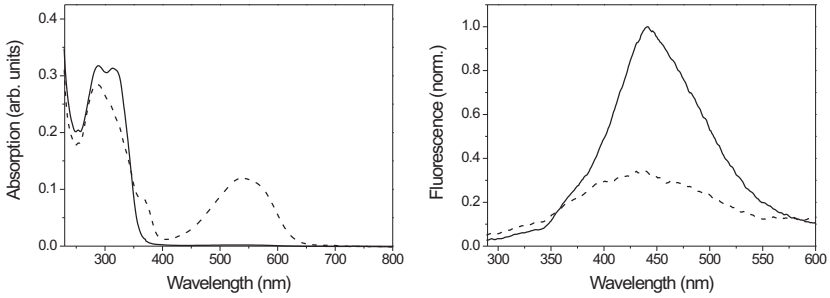

Figure 8.14. [Left] Absorption spectra of the 4-MMCS in the open (line) and closed form (dashed). [Right] Fluorescence spectra of 4-MMCS in the open (line) and closed form (dashed). Spectra are corrected for differences in the absorption at the excitation wavelength of 260 nm and are normalized to the maximum of the open form.

sorption spectra in the open and closed form resemble that of MMCS with the lowest absorption maximum at 313 nm. The same figure also shows the fluorescence spectra which have a maximum at 440 nm. The fluorescence of the open form can hardly be detected and upon ring closing the fluorescence intensity reduced to 30% of the open form. This behavior is similar to that of MMCS, that was also quenched in the open form and did not show as large a change as DMCS upon ring closing. These findings lead to the conclusion that it is the extra methoxy in DMCS that makes this molecule fluorescent in the open form of the switch.

8.9 Conclusion

Comparing the results of steady state and time-resolved spectroscopy it can be concluded that the fluorescence of the coumarin in DMCS, that is unquenched in the open form, is nearly completely quenched upon ring closing. This occurs by energy transfer from the coumarin to the closed form of the switch. In contrast, the fluorescence of MMCS is quenched in both form of the switch. Whereas the effect of quenching is unmistakably manifested in the fluorescence spectra, in the time-resolved data this is hidden. Quenching of the coumarin fluorescence by resonance energy transfer is expected to effect the lifetime of the coumarin excited state. This would decrease by fast and effective energy transfer to the switch. However, as described above at an excitation wavelength of 266 nm the contribution of coumarin to the signal is on the order of 10%. By designing and synthesizing a new coumarin-switch (4-MMCS)), the difference in fluorescence behavior of DMCS and MMCS could be assigned to the presence of an extra methoxy group in DMCS and not to the altered connection of the coumarins to the switch.

9 Switchable energy transfer in molecular triads

Molecular triads, consisting of two highly fluorescent molecules covalently attached to a molecular switch, were studied using several optical techniques. Steady state absorption and fluorescence, time-correlated single photon counting and transient absorption measurements were employed to elucidate the energy transfer processes within the triads.

9.1 Introduction

Energy transfer plays an important role in photosynthesis [25]. To mimic the efficient energy transfer in the natural light-harvesting complexes, artificial complexes have to be designed taking into account the spatial and energetic prerequisites for this process [28, 218]. To collect as much light as possible, both the natural and artificial complexes depend on antenna systems consisting of a large amount of (different) chromophores [108, 219]. In an attempt to imitate the fast downhill energy transfer process, a donor (D)-acceptor (A) system was synthesized containing a coumarin and a perylene bisimide chromophore. Both molecules have, on their own, received considerable attention in the field of artificial light harvesting and energy transfer. Whereas coumarins are widely used as sensitizing dyes for solar cells [220–224], perylene bisimides are often employed in complex systems for energy transfer [225–228].

In a multichromophore complex intramolecular energy transfer in principle occurs from the chromophore with larger $S_0 - S_1$ transition energy (D) to the chromophore that has the lowest $S_0 - S_1$ transition energy (A). If there are chromophores in the complex that have an intermediate $S_0 - S_1$ energy (I) they may be involved in the energy transfer route. However, if, based on Förster theory, the emission of chromophore D overlaps with the absorption of chromophore A and A and I are at a comparable distance from D, chromophore I might be bypassed [229]. In this chapter the energy transfer pathway is controlled by introducing a photoswitchable dithienylethene molecule as the central unit in a molecular triad. These complex molecules consist of a coumarin (D) and a perylene (A) chromophore attached on either side of the photoswitch that potentially acts as an intermediate (I) (figure 9.1). Ring closure of the switch leads to the appearance of an additional absorption band in the region where D and A emit and A absorbs. Figure 9.2 shows the structure of the different triads studied. The goal of the experiments was to see the effect of ring closing on the energy transfer pathway in the multichromophore molecular triads.

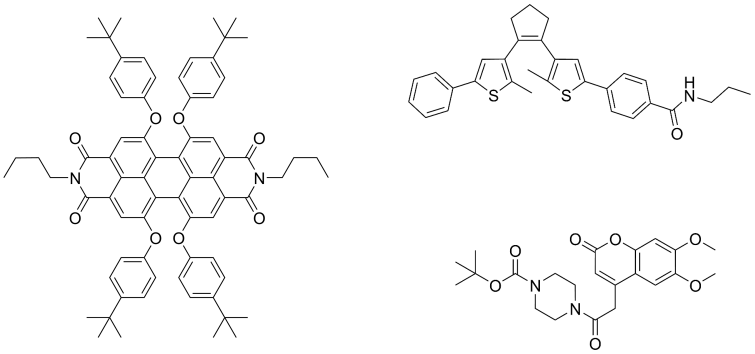

FIGURE 9.1. Model compounds for the donor-acceptor systems: perylene bisimide, PrPhSPh and DMCpipboc

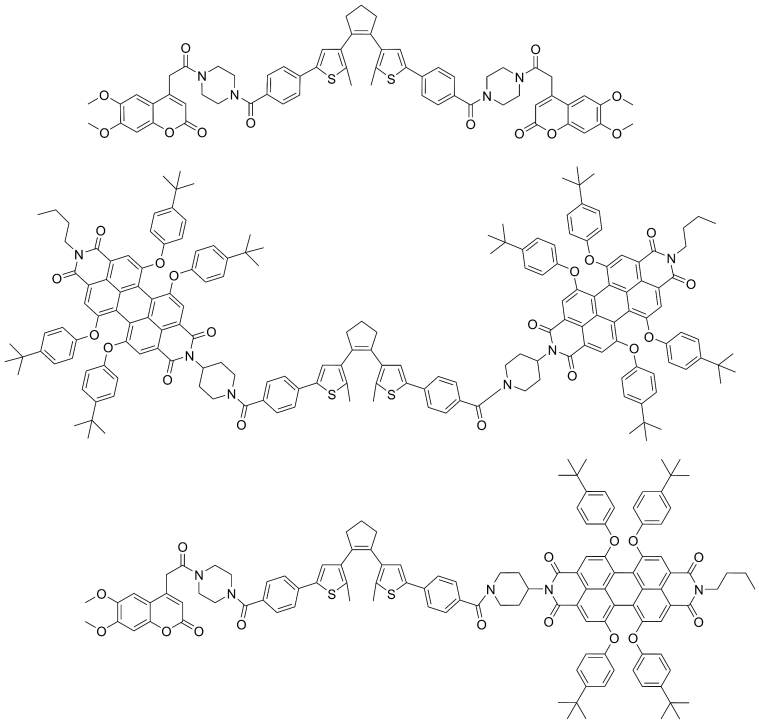

FIGURE 9.2. Molecular structures of the symmetric donor-acceptor compounds coumarin-switch-coumarin, CSC (top), perylene-switch-perylene, PSP (middle) and the asymmetric donor-acceptor system coumarin-switch-perylene, CSP (bottom) in the open form.

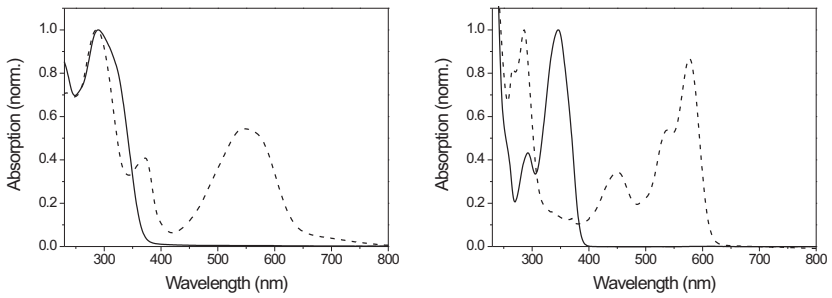

FIGURE 9.3. [Left] UV/Vis absorption spectra of PrPhSPh in the open (line) and closed form (dashed). [Right] UV/Vis absorption spectra of DMCpipboc (line) and perylene bisimide (dashed). Spectra were recorded at 298 K in dichloromethane.

9.2 EXPERIMENTAL

For experimental details of the spectroscopic measurements see chapter 8. Additional transient absorption measurements were carried out at an excitation wavelength of 550 nm. The time resolution in these transient absorption measurements was about 50 fs. The wavelength was obtained by frequency converting the output of an amplified Ti:sapphire laser with a repetition rate of 1 kHz making use of a NOPA (PUSH). The quantum yields of the compounds were calculated using 9,10-diphenylanthracene and perylene as references [209]. Steady-state fluorescence and pump scatter were carefully removed from the transient absorption data.

9.3 STEADY STATE ABSORPTION SPECTRA

Figure 9.3 gives an overview of the absorption spectra of the model compounds used in this chapter. The absorption spectra of the switch and the model coumarin are described in detail in chapter 8. The absorption spectrum of perylene bisimide shows several absorption bands over the detection window (230-800 nm) with a characteristic peaked structure at the low energy energy side of the spectrum with maxima at 450, 538 and 577 nm.

Figure 9.4 shows the absorption spectra of CSC in the ring open and closed form. The spectra are similar to those of the switch, nevertheless around 300 nm there is a clear difference. When compared to the absorption of DMCS (figure 8.2 in chapter 8), it appears that in the double peak structure around 300 nm, the peak at 330 nm is due to the coumarin absorption. Because in CSC the absorption of the coumarin is twice as high as compared to DMCS, the intensity of the peak at 330 nm is increased.

The UV/Vis absorption spectrum of PSP in the open and photostationary state are shown in figure 9.5. The structure as observed in the perylene model

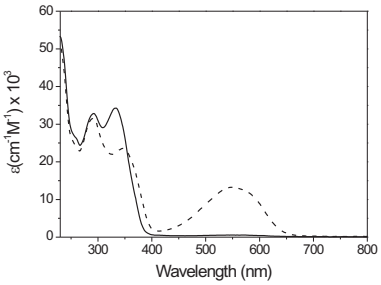

FIGURE 9.4. UV/Vis spectra of CSC in the ring open (line) and closed (dashed) form. Spectra were recorded at 298 K in dichloromethane.

compound are also observed in PSP both in the open and closed form. Upon ring closing, the absorption is unchanged below 300 nm, it decreases in the region between 300 and 350 nm, whereas it increases at wavelengths >350 nm. These changes are similar to those observed in the spectra of the model switch (figure 9.3) in which the intensity increases upon ring closing at wavelengths >350 nm onwards. Hence, the changes in the absorption spectrum of PSP upon ring closing are assigned to the switching unit. Both in the open and closed form connection by a covalent bond has a limited influence on the absorption spectra as compared to the model compounds. Summation of the spectra of the perylene and the switch units closely resembles the spectrum of PSP (not shown). This holds for the open and the closed form, indicating that the coupling between the elements is weak, and does not influence the electronic structure of one another. Figure 9.5 further shows the UV/Vis spectra of CSP in the ring open and closed form. The absorption spectrum resembles that of PSP. However, due to the presence of only a single perylene moiety in CSP vs two in PSP, the molar absorptivity, ϵ, is roughly reduced by a factor of $\sim$2. Upon ring closing the same behavior, albeit more pronounced, as in PSP is observed, which can again be ascribed to changes in the absorption spectrum due to the switch unit.

9.4 EMISSION AND EXCITATION SPECTRA

The emission spectra of the model compounds, switch, coumarin and perylene, are shown in figure 9.6. The fluorescence of the switch is asymmetric with a maximum at 384 nm. Upon ring closing the maximum remains at the same wavelength, the width of the spectrum slightly decreases at the red side of the spectrum. The coumarin has a fluorescence spectrum that lies to the red of that of the switch and has a maximum at 430 nm. The red most fluorescence originates from the perylene that has a characteristic fluorescence spectrum, mirroring the absorption spectrum, with maxima at 607 and 651 nm. The dip at 703 nm is due to an instrumental artifact and obscures another local maximum. The shape of the emission spectrum of perylene is independent of

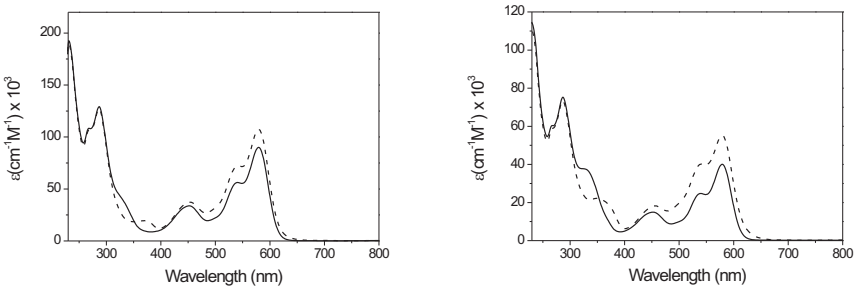

FIGURE 9.5. [Left] UV/Vis spectra of PSP in the ring open (line) and closed (dashed) form. [Right] UV/Vis spectra of CSP in the ring open (line) and closed (dashed) form. Spectra were recorded at 298 K in dichloromethane.

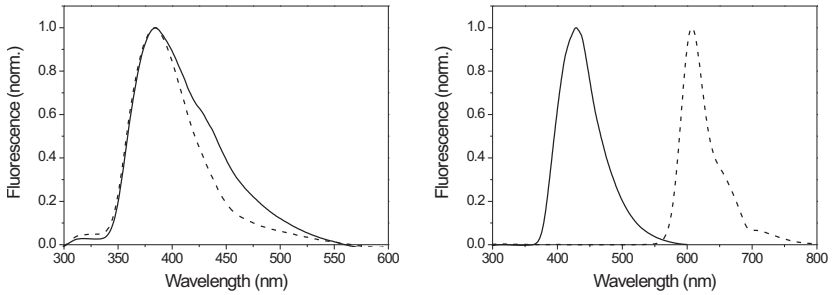

FIGURE 9.6. [Left] Fluorescence spectra of the switch in the ring open (line) and closed (dashed) form. [Right] Fluorescence spectra of the coumarin (line) and the perylene (dashed). Spectra were recorded at 298 K in dichloromethane, excitation at 266 nm.

excitation wavelength in the range from 266 to 550 nm as expected (Kasha's rule). A dilution experiment did not support the presence of intermolecular stacking of the perylene or the coumarin molecules at the concentrations used in the experiments.

The fluorescence spectra of CSC are presented in figure 9.7. As for the model coumarin, DMCpipboc, the maximum intensity of the fluorescence is at 430 nm. The intensity of the fluorescence of CSC in the open form is equal to that of DMCpipboc. Hence, no quenching of the fluorescence by the switch in the open form is observed. Upon ring closing the shape of the fluorescence remains unchanged, however the fluorescence intensity is reduced by a factor of fifteen, due to energy transfer to the closed switch as is discussed in chapter 8. This is less than in DMCS, however now twice the amount of coumarin is

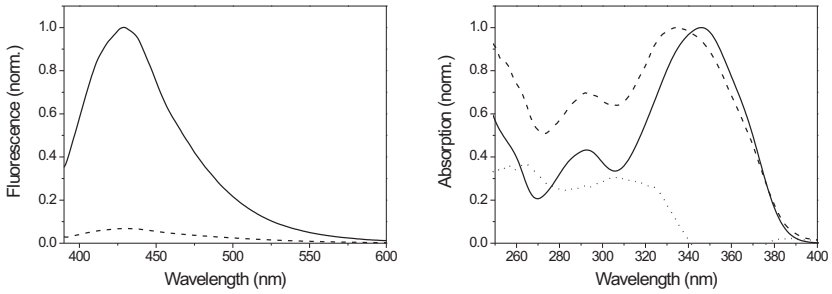

FIGURE 9.7. [Left] Fluorescence spectra of CSC in the ring open (line) and closed (dashed) form. Spectra were recorded at 298 K in dichloromethane, excitation at 380 nm. The data is normalized to the fluorescence intensity of the open form. [Right] Comparison between the absorption spectrum of coumarin (line) with the excitation spectra of CSC in the ring open form (dashed) and the difference between the two (dots), excitation spectrum measured at 440 nm.

present. The shape of the fluorescence of CSC is, both for the open and closed form, independent of excitation wavelength (266 and 380 nm).

Figure 9.8 shows the emission spectra of PSP in the open and closed form. The spectra of PSP are nearly identical to the fluorescence spectrum of the model perylene with maxima at 609 and 655 that remain unchanged upon ring closing. This indicates that perylene is the emissive unit in this system. The intensity of the fluorescence in PSP in the open form is similar to that of free perylene. Upon ring closing the intensity is reduced by 55%. The quenching in the closed form is due to energy transfer to the closed switch that in the ring closed form shows an absorption band, centered at 550 nm, overlapping with the fluorescence spectrum of the perylene. This situation provides for efficient energy transfer [40].

Figure 9.8 also shows the emission spectra of CSP. Both the coumarin, switch and the perylene fluorophores are excited at 266 nm. This is apparent in the fluorescence spectra where in addition to the intense perylene fluorescence at the blue side of the spectrum a second, weaker, emission is observed with a maximum around 420 nm. Since this emission is absent in the fluorescence spectrum of PSP and the shape is as expected by fluorescence of the coumarin, the fluorescence is assigned to the DMCS unit. The intensity of the fluorescence of the coumarin is similar to that of free coumarin. This value only changes by 5% upon ring closing. From the results in chapter 8 it was concluded that DMCS in the open form is not quenched by the switch. The reason for the absence of quenching of the coumarin fluorescence in CSP is not known. The intensity of the perylene fluorescence in the open form of CSP is similar to that of the free perylene as was also observed in PSP. Upon ring closing the intensity is reduced by 65%. Hence, the behavior of the perylene fluorescence is similar in PSP and CSP, indicating that the electronic coupling between the fluorophores

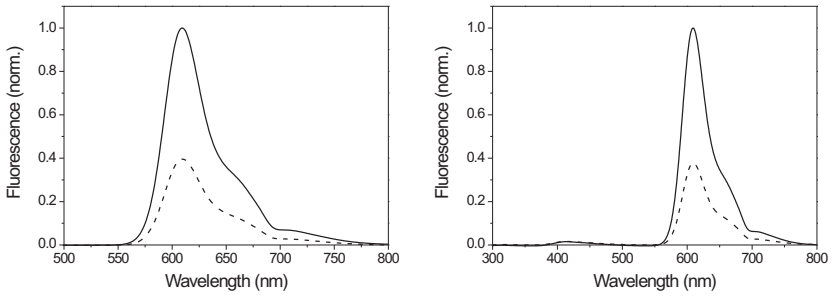

FIGURE 9.8. [Left] Fluorescence spectra of PSP in the ring open (line) and closed (dashed) form. [Right] Fluorescence spectra of CSP in the open (line) and closed form (dashed). Spectra were recorded at 298 K in dichloromethane, excitation at 266 nm. The data are normalized to the fluorescence intensity of the open form.

via the switching unit is limited. As in the model compounds, the fluorescence of PSP and CSP in the open and closed form are independent of excitation wavelength (266, 400 or 550 nm) precluding higher energy states playing a role in the energy transfer mechanism.

The excitation spectra of CSC in the open and closed form closely resembles the shape of the absorption spectrum of DMCpipboc (see figure 9.7). Around 300 nm there is a small intensity difference that can be due to the absorption of the switch. Hence, the emission in CSC can be attributed to the coumarin as was seen previously in DMCS. Figure 9.9 shows the excitation spectra of PSP compared to the absorption spectra. The similarity between the excitation spectra of the open and closed form of PSP is remarkable. This means that the emission in the photostationary state (PSS) of the switch, not 100% of the molecules can be ring closed, is due to the open form. Additionally this implies that in the closed form, the switch does not transfer energy to the perylene unit. The comparison between the excitation spectrum of CSP with its absorption spectrum and the difference between the two spectra are also shown in figure 9.9. After subtraction of the excitation spectrum from the absorption spectrum it is apparent that an extra band is present, which resembles the absorption spectrum of DMCpipboc. The meaning of this band is not entirely clear and is subject of ongoing research. Monitoring the fluorescence at 440 nm, the excitation spectra of CSP in the open and closed form are nearly identical to the absorption spectrum of DMCpipboc (data not shown), confirming that the low intensity fluorescence peak at 440 nm in CSP (see figure 9.8) can be ascribed to the coumarin unit.

Using a simple relation between the total absorption of the compound and the absorption of the switch in the closed form, the PSS for the triads can be

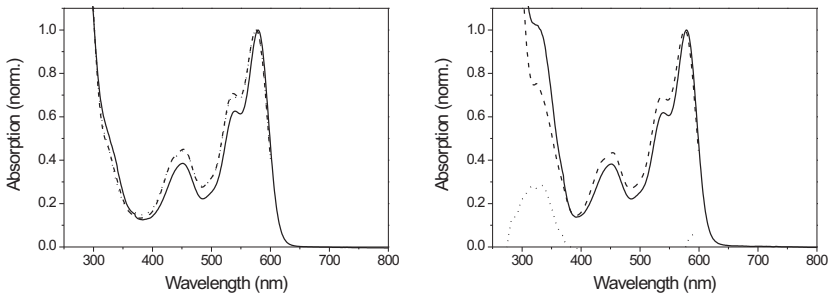

FIGURE 9.9. [Left] Comparison between the absorption spectrum of PSPo (line) with the excitation spectra of PSPo (dashed) and PSPc (dots), excitation spectrum measured at 625 nm. Note that the excitation spectra of PSPo and PSPc lie on top of each other [Right] Comparison between the absorption spectrum of CSPo (line) with the excitation spectra of CSPo (dashed) and the difference between the two (dots), excitation spectrum measured at 625 nm. Spectra were recorded at 298 K in dichloromethane.

calculated. The fraction of open form in the PSS is defined as follows.

$$\begin{aligned} \frac{[\text{open}]}{[\text{closed}]} &= F_o \\ F_o &= \frac{1}{\text{PSS}} - 1 \end{aligned} \tag{9.1}$$

To calculate the PSS of an unknown switch an expression based on molar absorptivities and the known PSS of a reference switch can be used.

$$\frac{\text{PSS}_2}{\text{PSS}_1} = \frac{A_c + A_{per} + A_{coum}}{A_c} \tag{9.2}$$

Here A_c, A_{per} and A_{coum} are the molecular absorption coefficients (ϵ) of the closed switch, the perylene and the coumarin at the switching wavelength of 365 nm. The PSS of the model switch, PrPhSPh (figure 9.1), used in this chapter is denoted as PSS_1. Expression 9.2 assumes that in the closed form all fluorescence is quenched an the remaining fluorescence is due to the fraction open molecules present in the PSS. Using this assumption and the ratio between the fluorescence intensities of the open and closed form of PSP and CSP (figure 9.8), the PSS of these triads can be calculated and result in 0.71 and 0.73 for the two compounds respectively. This value has implications for the value of the PSS of the switch, which normally lies around 0.98. However, using relation 9.1, the PSS of the model switch is estimated to lie around 0.85.

TABLE 9.1. Quantum yields of fluorescence of the various compounds, where the closed form refers to the PSS at 365 nm.

Sample	QY
Perylene	1.0
CSC_{open}	0.4
CSC_{closed}	0.08
PSP_{open}	0.9
PSP_{closed}	0.4
CSP_{open}	0.9^a
CSP_{closed}	0.4^a

[a] Monitoring perylene fluorescence.

9.5 TIME-CORRELATED SINGLE PHOTON COUNTING

Time-correlated single photon counting (TCSPC) was employed to get more insight in the fluorescence decay of the different components and especially on the possible changes upon ring closing. Three different excitation wavelengths, 266, 370 and 490 nm, were chosen to study energy transfer from coumarin to the switch and perylene to the switch selectively. To start off, the fluorescence lifetimes of the model compounds were measured. The fluorescence decays of the switch in the open and closed form and the coumarin are shown in figure 8.7 in chapter 8. Figure 9.10 shows the decays of perylene excited at two different wavelengths. Interestingly, at an excitation wavelength of 266 nm, perylene shows a rise in the fluorescence signal with a time constant of ∼200-300 ps (see table 9.2). This rise is followed by a decay of 6.5 ns, a lifetime typical of perylenes [230]. A possible explanation for this rise time is that at 266 nm an excited state higher than the S_1 state is populated. Since fluorescence generally occurs from the lowest vibrational level in the S_1 state, the 200 ps component could be due to the decay process from the higher excited states to S_1. If so, then at longer excitation wavelengths this rise should no longer be present. At an excitation wavelength of 370 and 490 nm, indeed this rise time is no longer present but is replaced by a small decay component of several hundreds of ps. The closed form of the switch shows less pronounced differences when excited with 266, 370 and 490 nm respectively. Especially the traces excited at the longest two wavelengths are similar, with decay time constants of ∼400 ps and ∼3 ns. This last time constant is longer than observed at an excitation wavelength of 266 nm.

Comparing the decay time constants of CSC with that of DMCS in the previous chapter, several aspects stand out (table 8.3). As expected, at an excitation wavelength of 266 nm, DMCS and CSC both in the open and closed form resemble each other. Both show a biexponential decay with time constants of ∼200-400 ps and 2.4-2.7 ns (table 9.3). Excitation at 490 nm shows the same characteristics. However, at 490 nm the coumarin should no longer absorb and hence coumarin fluorescence should be absent. Fluorescence detected should

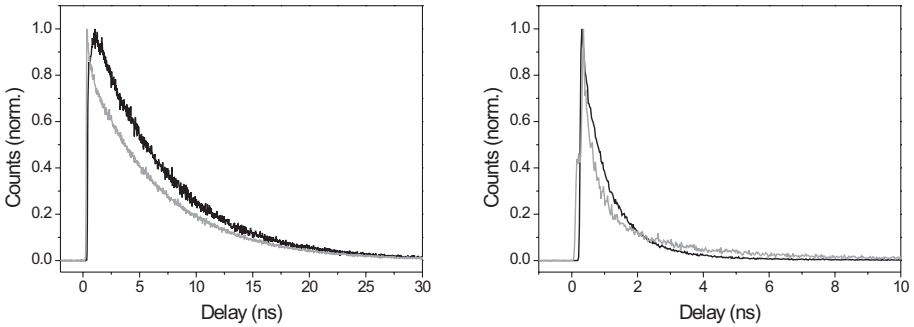

FIGURE 9.10. [Left] Fluorescence decay traces of perylene excited at 266 nm (black) and 490 nm (grey) form. [Right] Fluorescence decay traces of the switch in the closed form excited at 266 nm (black) and 370 nm (grey). Spectra were recorded at 298 K in dichloromethane.

TABLE 9.2. Single photon counting decay times of the model compounds after excitation at 266, 370 and 490 nm.

Compound	t_1 (ns)	t_2 (ns)
Perylene-266	(-)0.3[a]	6.5
Perylene-370	0.3	6.6
Perylene-490	0.3	6.5
switch$_{closed}$-266	0.5	1.2
switch$_{closed}$-370	0.4	2.9
switch$_{closed}$-490	0.4	3.3

[a] The negative time constant corresponds to a rise times in the fluorescence decay traces. The error in the time constants is about 10%.

come from the switch, when there is no energy transfer from switch to coumarin. In the closed form, the fluorescence signal can be fit with 400 ps and 1.8 ns similar to the decay constants obtained from the switch in the closed form.

As in the emission decay times of perylene, both in the open and closed form of PSP, a rise time of ∼200 ps is observed at an excitation wavelength of 266 nm (see figure 9.12). The second time constant needed to fit the traces is 6 ns. At longer excitation wavelengths this rise time is not observed and in addition to the 6 ns decay, a 1 ns decay component is used in the fits for the open and closed form (table 9.4).

As described in section 9.4, at 266 and 370 nm both fluorophores in the system are excited. However, the fluorescence decay traces of CSP in the open and closed form only show signatures of perylene fluorescence (figure 9.12). Given the low absorption of coumarin, about 5%, the presence of coumarin fluorescence is not expected. The behavior is similar to that of PSP and perylene, with a rise time of ∼200-300 ps at 266 nm that is replaced by a decay time of 700-900

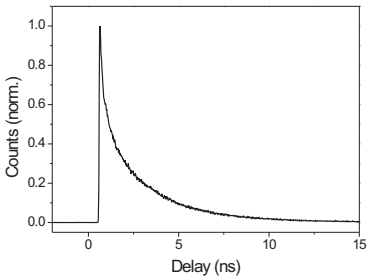

FIGURE 9.11. Fluorescence decay trace of CSC excited at 266 nm in the open form, as the decay trace of the closed form is virtually identical it is not shown. Spectra were recorded at 298 K in dichloromethane.

TABLE 9.3. Single photon counting decay times of CSC in the open and closed form after excitation at 266, 370 and 490 nm.

Compound	t_1 (ns)	t_2 (ns)
CSC_{open}-266	0.3	2.7
CSC_{open}-370	0.6	2.6
CSC_{closed}-266	0.4	2.8
CSC_{closed}-370	0.4	2.7
CSC_{closed}-490	0.4	1.8

The error in the time constants is about 10%.

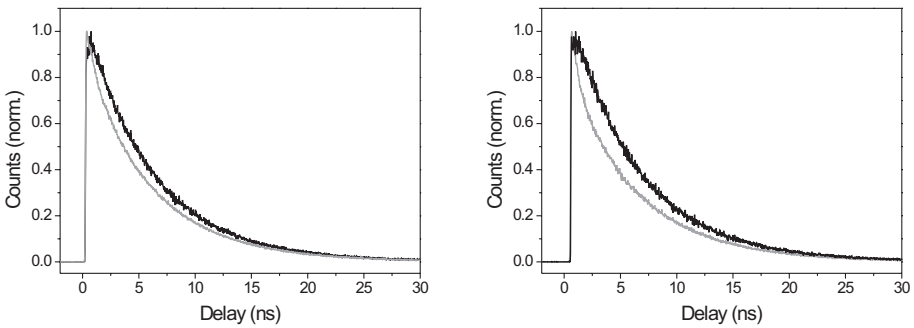

FIGURE 9.12. [Left] Fluorescence decay traces of PSP in the open form excited at 266 nm (black) and 490 nm (grey) form. [Right] Fluorescence decay traces of CSP in the open form excited at 266 nm (black) and 490 nm (grey) form. Spectra were recorded at 298 K in dichloromethane.

TABLE 9.4. Single photon counting decay times of PSP in the open and closed form after excitation at 266, 370 and 490 nm.

Compound	t_1 (ns)	t_2 (ns)
PSP_{open}-266	(-)0.2[a]	6.0
PSP_{open}-370	1.1	6.1
PSP_{open}-490	1.1	6.1
PSP_{closed}-266	(-)0.2[a]	5.7
PSP_{closed}-370	1.2	6.0
PSP_{closed}-490	1.0	5.9

[a] The negative time constant corresponds to a rise times in the fluorescence decay traces. The error in the time constants is about 10%.

TABLE 9.5. Single photon counting decay times of CSP in the open and closed form after excitation at 266, 370 and 490 nm.

Compound	t_1 (ns)	t_2 (ns)
CSP_{open}-266	(-)0.3[a]	6.1
CSP_{open}-370	1.7	5.3
CSP_{open}-490	0.7	6.2
CSP_{closed}-266	(-)0.3[a]	5.8
CSP_{closed}-370	0.9	5.5
CSP_{closed}-490	0.7	6.7

[a] The negative time constant corresponds to a rise times in the fluorescence decay traces. The error in the time constants is about 10%.

ps (table 9.5). To test for the presence of coumarin fluorescence, the region of interest, around 420 nm, was selected using an interference filter. With the current excitation energy, with which even the relatively weak fluorescence of the switch is clearly visible, no evidence of coumarin fluorescence was detected.

9.6 TRANSIENT ABSORPTION SPECTROSCOPY

To elucidate the processes of energy transfer further and to be able to follow these processes at shorter timescales, ultrafast transient absorption spectroscopy was employed. As in the previous section, the study began by examining the individual components of the triads; the two fluorophores coumarin and perylene and the switch. Two excitation wavelengths were chosen, 266 and 550 nm, to be able to study selectively energy transfer between the different components in the triad (e.g. coumarin to switch and perylene to switch).

TABLE 9.6. Transient absorption decay times from global analysis for the model compounds

Compound	t_1 (ps)	t_2 (ps)	t_3 (ps)
DMCpipboc	2.8	24	190
$DMCS_{open}$	1.6	9.1	180
$DMCS_{closed}$	2.9	16	270
$switch_{open}$	7.2	14	150
$switch_{closed}$	3.1	7.7	160

9.6.1 EXCITATION AT 266 NM

At 266 nm all three components, coumarin, perylene and switch, have significant absorption and therefore all three units are excited directly. However, compared to the switch ($\sim$18-20.10^3 $M^{-1}cm^{-1}$) and the perylene ($\sim$40.10^3 $M^{-1}cm^{-1}$), the coumarin has a relatively low molar absorptivity ($\sim$3.10^3 $M^{-1}cm^{-1}$). In chapter 8 the transient absorption spectra of the switch in the open and closed form, of the coumarin and of the coumarin attached to the switch (DMCS) were discussed (see section 8.7). Table 9.6 gives an overview of the decay time constants from these model compounds.

Figure 9.13 shows the transient absorption spectra and kinetics for perylene. The transient spectra are structured, with a negative signal, corresponding to bleach and stimulated emission (B/SE), from 490-660 nm and a positive signal, corresponding to excited state absorption (ESA), from $\sim$660 nm to the end of the detection window around 750 nm. A similar absorption band attributed to the S_1 to S_n transition has been observed in several derivatives of perylene [231–233]. When comparing maxima, by differentiation, of the bands in the transient spectra with the linear absorption and emission spectra the relaxation process can be observed. Up to $\sim$20 ps the maxima in the B/SE appear at 540, 580 and 650 nm are in good agreement with the maxima of the linear absorption spectrum at 538 and 577 nm. Between $\sim$20 and 200 ps, the central peak in the transient spectra undergo a red shift to settle at 540, 609 and 650 nm. This matches the steady state emission spectra that has maxima at 607 and 650 nm. In summary, it appears that at early times the bleach dominates the spectrum, while at longer times, when the system relaxes to the vibrationally cold S_1 state, this changes to the stimulated emission spectrum. In section 9.5 it was shown that after excitation at 266 nm, there is a similar, although longer, rise time in the fluorescence amplitude. This rise was also assigned to the decay of the system from higher excited states back to the lowest vibrational level in the S_1 state from which fluorescence occurs. Figure 9.13 also shows the decay kinetics. Global analysis using a 4-level sequential model gave rise to three distinct decay times; decay time constants of 3 and 20 ps and a rise time of $\sim$800 ps which was poorly resolved (table 9.7). The first time constant can be assigned to vibrational cooling to the lowest vibrational level in the S_1 state as was shown for perylene in previous studies [234–236]. The deconvoluted spectra

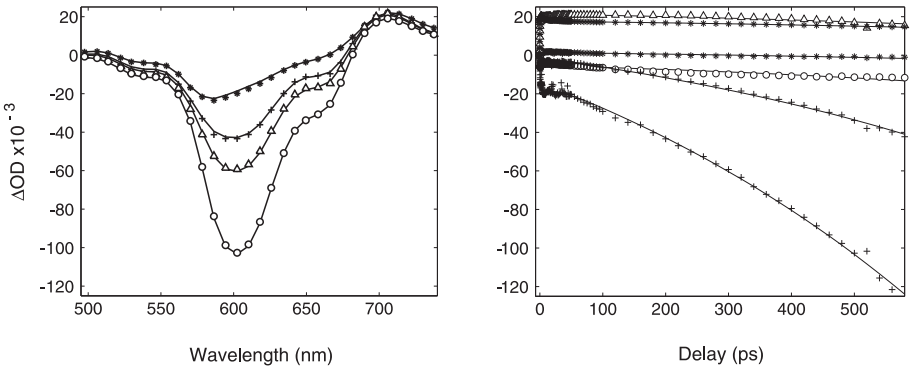

FIGURE 9.13. [Left] Transient spectra of perylene at 5 (stars), 200 (crosses), 300 (triangles) and 500 ps (circles). [Right] Transient kinetics of perylene at 500 (stars), 550 (circles), 600 (crosses), 650 (dots), 700 (triangles) and 725 nm (stars). Excitation wavelength 266 nm, 700 nJ/pulse. The symbols represent the data, the lines are results of the global fits.

from global analysis support this by showing that the spectra of the highest two levels resemble each other except for a small shift. Since the orientation of pump and probe are parallel, contributions from rotational decay cannot be excluded. Previously it was shown that a time constant of ∼15 ps can be assigned to a rotational diffusion process, similar to the second time constant. Interestingly the large increase of the transient signal at 600 nm proceeds with a time constant of ∼800 ps. The transient spectra show that during the growth, the signal resembles the steady state fluorescence spectrum. The origin of this process, possible triplet formation or charge separation [232, 233, 236], is topic of ongoing research.

As in the previous chapter for DMCS, the transient absorption spectra will show contributions from coumarin and switch. However, whereas the contribution of the coumarin was small in DMCS, in CSC its presence is doubled, further complicating the data analysis. In chapter 8 it was shown that the electronic coupling between the switch and the coumarin in DMCS is weak, therefore addition of an additional coumarin to form CSC is not expected to change the behavior of the system dramatically. Due to the high level of fluorescence of coumarin, the transient spectra of CSC are shown from ∼550 nm onwards (figures 9.14 and 9.15). Spectrally, the open and closed form are very similar and show a broad positive excited state absorption signal. The decay time constants used to fit the transients globally are given in table 9.7. For the open and closed form the decay time constants are comparable; 4, 20 and 140 ps in the open form versus 3, 15 and 200 ps in the closed form. These decay time constants for CSC are similar to those of DMCS, however the features in the transient spectra are different (i.e. the rise time characteristic of the switch is not observed), possibly due to a smaller contribution of the switch to the amplitude of signal. From previous studies it is known with which physical

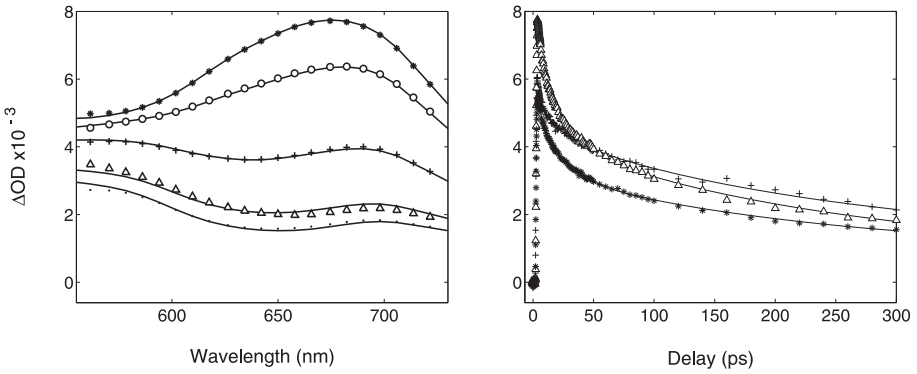

FIGURE 9.14. [Left] Transient spectra of CSC in the open form at 5 (stars), 10 (circles), 50 (crosses), 200 (triangles) and 300 ps (dots). [Right] Transient kinetics of CSC in the open form at 600 (crosses), 700 (triangles), and 730 nm (stars). Excitation wavelength 266 nm, 1400 nJ/pulse. The symbols represent the data, the lines are results of the global fits.

processes the respective time constants can be associated. The fastest two time constant of 3-4 and 15-20 ps were assigned to vibrational cooling and solvent reorganization [214, 216]. Since, pump and probe are parallel, rotation can also play a role. The longest component of 200 ps is comparable to the dominating component in the fluorescence decay traces. Section 9.4 discussed the changes in the emission spectra of CSC upon ring closing. The quenching process was attributed to resonance energy transfer from the coumarin to the switch. A decrease in the fluorescence intensity by a factor of fifteen leads, in combination with the dominant decay time in the fluorescence lifetime (200 ps), to an energy transfer time from the coumarins to the switch of ∼14 ps. In the TA data a similar time is expected to emerge upon ring closing. Depending on the wavelength, this can either appear as a decay, due to loss of population of the coumarin or as a rise, since the population lost in the coumarin will be transferred to the switch. In a direct comparison of the fits of the open and closed form it appears that a short decay time of ∼10 ps increases by about a factor 5 in amplitude upon ring closing at 600 nm. The amount with which the amplitude increases is strongly wavelength dependent and is especially pronounced at the blue side of the spectrum. Such an effect was not observed upon ring closing in the switch. Hence, the increased 14 ps decay component is assigned to the rate of energy transfer from coumarin to switch upon ring closing.

Figures 9.16 and 9.17 show the transient spectra and dynamics of PSP in the open and closed form after excitation at 266 nm. The resemblance to the perylene spectra is remarkable (figure 9.13), indicating that in this triad perylene is clearly the emitting component, as was indicated from the steady state emission spectra. A similar shift of the peaks in the transient spectra as described for perylene is visible in both forms of PSP. The similarity is also reflected in the time constants that are needed to fit the data (table 9.7), 5.1

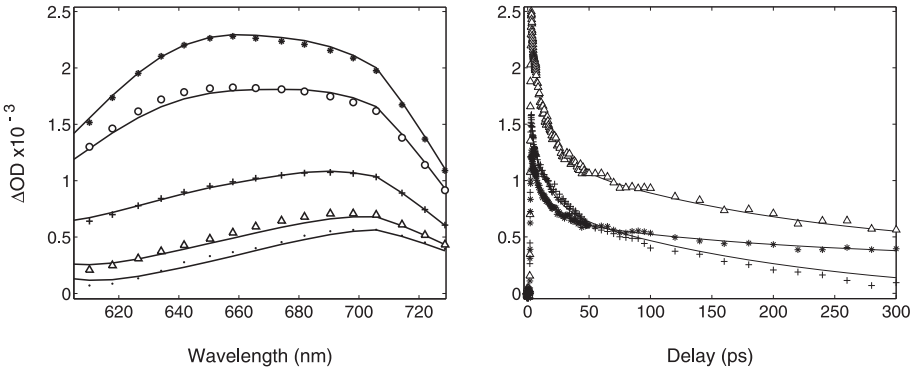

FIGURE 9.15. [Left] Transient spectra of CSC in the closed form at 5 (stars), 10 (circles), 50 (crosses), 200 (triangles) and 300 ps (dots). [Right] Transient kinetics of CSC in the closed form at 600 (crosses), 700 (triangles), and 730 nm (stars). Excitation wavelength 266 nm, 400 nJ/pulse. The symbols represent the data, the lines are results of the global fits.

and 55 for the open and 2.3 and 24 for the closed form. As in perylene, an additional slow rise time was observed. The changes upon ring closing are less visible than in CSC. However, when comparing directly decay traces at 700 and 730 nm, the amplitude of the fast decay components turns out to increase by a factor of two. The slow rise of the signal, resembling the steady state fluorescence, is independent of the state of the switch in PSP.

The transient absorption spectra for CSP in the open and closed form are shown in figures 9.18 and 9.19. The transient spectra in both forms of the switch are similar to the spectra of perylene and PSP. Signatures of coumarin fluorescence, as in CSC, are not observed. This is in agreement with the 5% relative absorption of the coumarin and the near absence of the coumarin fluorescence in the steady state emission spectra of CSP. The bands in the transient spectra shift from bleach to SE, as described for perylene. Comparison of the open and closed form shows an increase in the amplitude of the short decay time constants, this is especially pronounced in the red side of the spectrum at 700 and 725 nm.

9.6.2 EXCITATION AT 550 NM

Excitation at 550 nm gives a more refined view of the energy transfer processes in the triads. While at 266 nm the switch, the coumarin and the perylene all have significant absorption and are therefore all excited, at 550 nm only the closed switch and the perylene absorb. Therefore, this choice of excitation wavelength should give a cleaner view of energy transfer from the perylene to the switch.

Figure 9.20 shows the dynamics of the switch in the closed form, after excitation at 550 nm. Chapter 7 describes the transient spectra in the closed form.

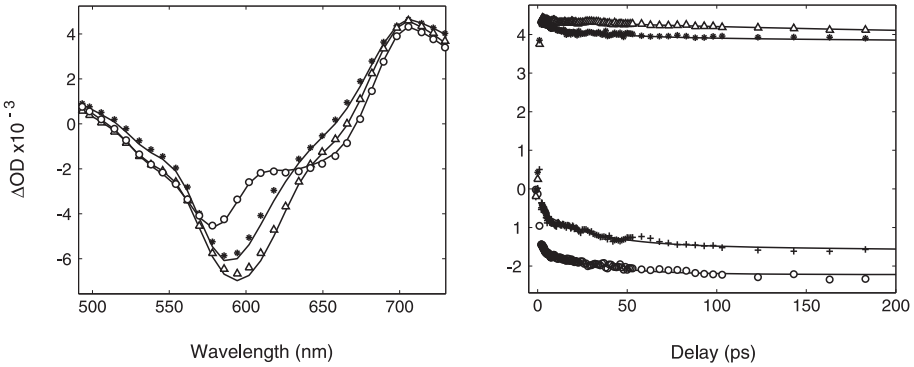

FIGURE 9.16. [Left] Transient spectra of PSP in the open form at 2 (stars), 50 (triangles) and 500 ps (circles). [Right] Transient kinetics of PSP in the open form at 550 (circles), 650 (crosses), 700 (triangles) and 725 nm (stars). Excitation wavelength 266 nm, 440 nJ/pulse. The symbols represent the data, the lines are results of the global fits.

In short, the negative signal centered at 575 nm corresponds with the linear absorption spectrum of the closed form of the switch and represents the ground state bleach. Vibrational cooling is observed in this band in the red-shift of the maximum of the bleach signal. The positive signals from 475 to 525 nm and 610-725 nm can be assigned to excited state absorption from S_1 to S_n. The decay time constants are typical for dithienylethene switches [204, 217]. However, the 30 ps time constant, which has a small amplitude and is difficult to fit, is slightly longer than previously observed.

Exciting perylene at 550 nm gives, at first glance, similar results to those after excitation at 266 nm as shown in figure 9.21. At 540 nm a small, but pronounced, negative band can be assigned to the bleach of the ground state. The amplitude of this band decreases, but it persists for up to 3 ns. As with 266 nm excitation the transient spectra shift from a maximum at 580 nm to 610 nm. This shift is completed in several hundreds of picoseconds, i.e. between the spectra at 500 ps and 3 ns there is little difference in the absorption maximum. The rise of the signal with a similar shape as the fluorescence that was observed after excitation at 266 nm, is absent when exciting with 550 nm. Instead, there is an additional decay constant of ∼300 ps. Since at the end of the detection window of 3 ns the signal has not decayed back to zero, there is an additional long decay time constant that is not resolved, but most likely corresponds to the lifetime of the S_1 state. From fluorescence lifetime measurements the lifetime of perylene is known to be 6.5 ns.

Since the coumarin does not absorb at 550 nm, it is expected that the transient spectra of CSC in the closed form will resemble that of the switch. This would mean that there is no energy transfer from the switch to the coumarin. Figure 9.22 shows the transient spectra of CSC in the closed form. Both the spectra and the dynamics show close resemblance to the switch in the closed

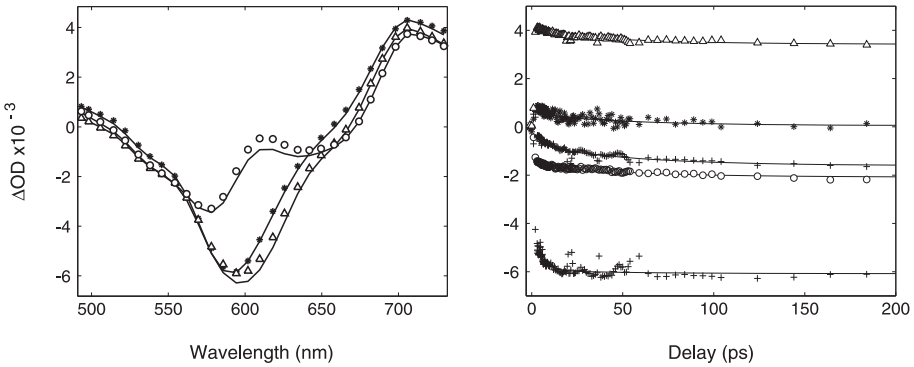

FIGURE 9.17. [Left] Transient spectra of PSP in the closed form at 2 (stars), 50 (triangles) and 500 ps (circles). [Right] Transient kinetics of PSP in the closed form at 550 (circles), 650 (crosses) and 700 nm (triangles). Excitation wavelength 266 nm, 440 nJ/pulse. The symbols represent the data, the lines are results of the global fits.

form as shown in chapter 7. Global analysis shows decay time constants of 1.5, 2.6 and 32 ps, similar to the decay times for the model switch (table 9.7). As a consequence, energy transfer from the switch to the coumarin is ruled out.

The transient absorption spectra of PSP in the open and closed form excited at 550 nm are similar to the spectra of perylene. The band at 540 nm is less distinct and seems to disappear within several hundreds of picoseconds. In contrast to perylene, the long rise time is still present both in the open and closed form. Notably, the dynamics change upon ring closing. The signal drops within 5 ps to less than half of its original value, a dramatic decrease compared to the open form. Interestingly, this agrees with the decrease of the fluorescence intensity in section 9.4. Tentatively in the ring closed form the 2 ps time constant from global analysis (table 9.7) is assigned to the energy transfer rate from perylene to switch. Compared to the nanosecond lifetime of perylene, this energy transfer pathway is expected to be the dominant decay pathway in the closed form. However, as observed in section 9.4 there is a low PSS, implying a relatively high fraction of open form, for both PSP and CSP. This suggests that in the TA spectra of the closed form, i.e. of the PSS, signatures of the open form will be present. Most likely figures 9.23 and 9.24 both show measurements of a mixture of the open and closed form. It is experimentally difficult to avoid any accumulation of the closed form during measurements of the open form. The remaining long time constant in the PSS is assigned to the unquenched form of perylene, i.e. with a lifetime of ∼6.5 ns corresponding to the remaining open form.

At an excitation wavelength of 550 nm, the coumarin does not absorb and is therefore not excited. The TA spectra of CSP will therefore consist of contributions from the closed switch and the perylene. Hence it is expected that similar dynamics as in PSP will appear for CSP. Figures 9.25 and 9.26 show the transient spectra and the dynamics for CSP in the open and closed form

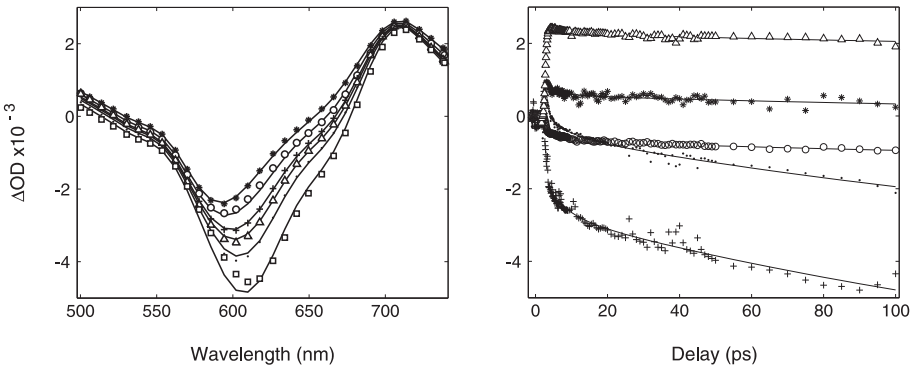

FIGURE 9.18. [Left] Transient spectra of CSP in the open form at 5 (stars), 10 (circles), 20 (crosses), 30 (triangles), 50 (dots) and 100 ps (squares). [Right] Transient kinetics of CSP in the open form at 500 (stars), 550 (circles), 600 (crosses), 650 (dots) and 700 nm (triangles). Excitation wavelength 266 nm, 400 nJ/pulse. The symbols represent the data, the lines are results of the global fits.

respectively. As expected, the shape of the transient spectra and the dynamics appear to be similar to those of PSP. Here also, the slow decay time constant is assigned to the fraction of open form in the PSS after ring closing.

9.7 CONCLUSION

By combining the results of the different optical techniques it is possible to sketch a picture of energy transfer in the photoswitchable triads. Whereas linear techniques, especially fluorescence spectroscopy, gives a direct indication of energy transfer by a reduction of the fluorescence intensity, transient absorption spectroscopy revealed the rates of the respective processes.

In the open form CSC behaves similar to DMCS. An additional coumarin, not electronically coupled to the switch, did not change the dynamics. However, since there are now twice as many coumarin units present, their signal will be more distinct than in DMCS at an excitation wavelength of 266 nm. This is manifested in the presence of an additional fast decay upon ring closing, which could not be detected in DMCS and switch. Tentatively this ∼10 ps decay time is assigned to energy transfer from coumarin to switch. This time constant agrees with the energy transfer time expected from the decrease in the steady state emission intensity upon ring closing.

PSP shows a 2 ps time constant for energy transfer from perylene to switch. This is not clearly visible in the transients with 266 excitation, however with 550 nm excitation the appearance of the fast time constant upon ring closing is apparent. Due to the low photo-stationary state (PSS), formation of the closed form is not complete. Hence, a mixture of the open and closed form are measured after ring closing. This explains the fluorescence and long decay times, due to the unquenched open form, measured after ring closing for both

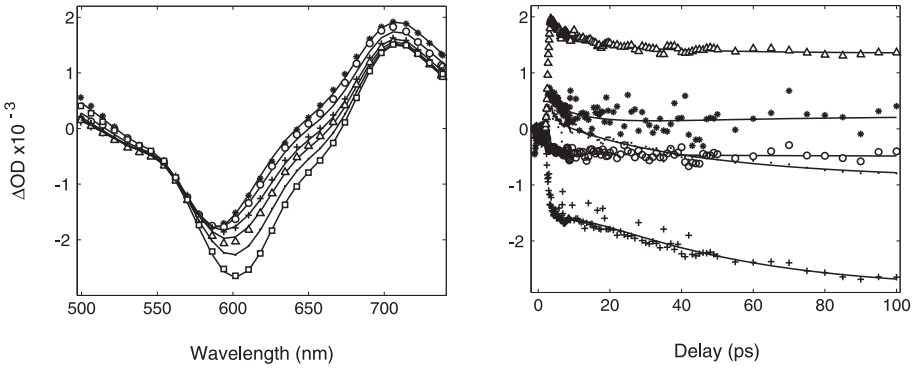

FIGURE 9.19. [Left] Transient spectra of CSP in the closed form at 5 (stars), 10 (circles), 20 (crosses), 30 (triangles), 50 (dots) and 100 ps (squares). [Right] Transient kinetics of CSP in the closed form at 500 (stars), 550 (circles), 600 (crosses), 650 (dots) and 700 nm (triangles). Excitation wavelength 266 nm, 400 nJ/pulse. The symbols represent the data, the lines are results of the global fits.

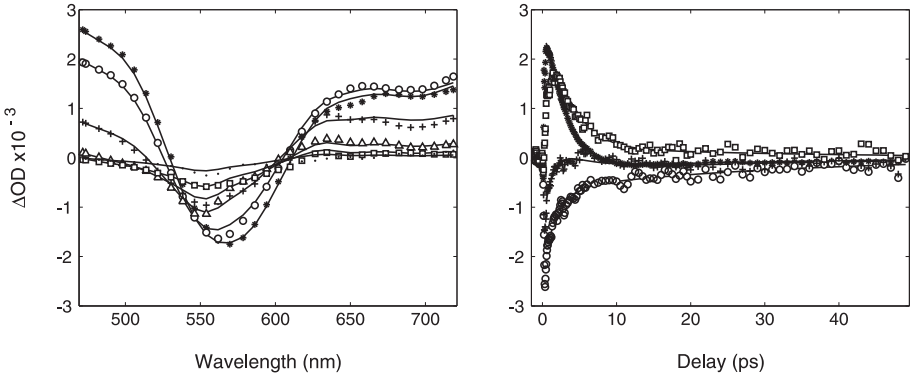

FIGURE 9.20. [Left] Transient spectra of the switch in the closed form at 1 (stars), 2 (circles), 5 (crosses), 10 (triangles), 20 (squares) and 45 ps (dots). [Right] Transient kinetics of the switch in the closed form at 500 (stars), 575 (circles), 600 (crosses) and 750 nm (squares). Excitation wavelength 550 nm, 400 nJ/pulse. The symbols represent the data, the lines are results of the global fits.

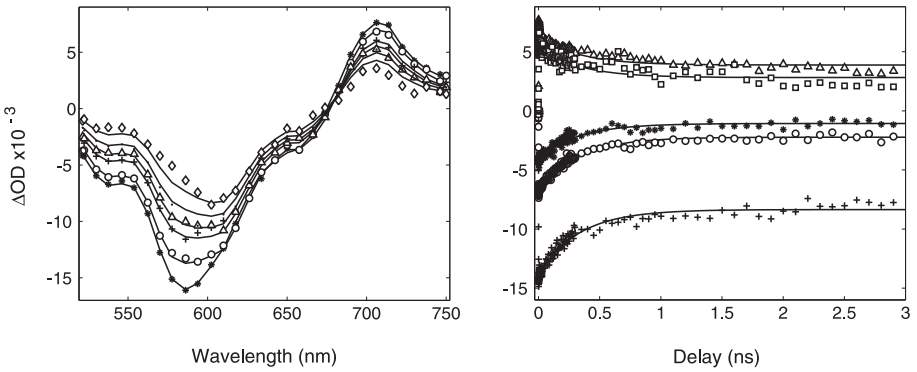

FIGURE 9.21. [Left] Transient spectra of perylene at 5 (stars), 50 (circles), 200 (crosses), 300 (triangles), 500 (dots) and 3000 ps (diamonds). [Right] Transient kinetics of perylene at 500 (stars), 550 (circles), 600 (crosses), 700 nm (triangles) and 725 nm (squares). Excitation wavelength 550 nm, 400 nJ/pulse. The symbols represent the data, the lines are results of the global fits.

PSP and CSP.

CSP shows similar dynamics as PSP. Energy transfer from coumarin to perylene, if any, is not observed, due to the relatively low molar absorptivity of the coumarin.

The particular design of the molecular triads, allows for rapid energy transfer between the coumarin and switch and between the perylene and switch due to resonance energy transfer. Hence, CSC is a reversibly photoswitchable fluorescent molecule with a modulation of the intensity that reaches over 90%. CSP and PSP show potential as frequency converters that allow photons absorbed in the UV region of the visible spectrum, to be emitted in the red part of the spectrum. Additionally, the efficiency of the emission can be controlled by the switch. In the closed form, rapid energy transfer to the switch occurs, however, due to the lack of complete ring closing, so far this process does not reach 100% efficiency.

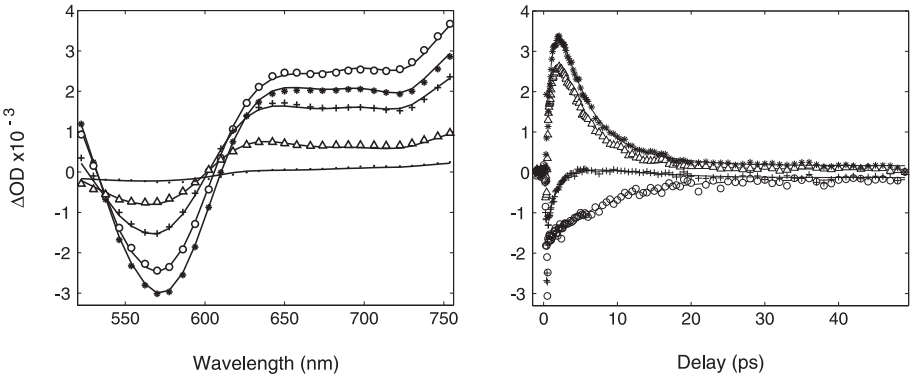

FIGURE 9.22. [Left] Transient spectra of CSC in the closed form at 1 (stars), 2 (circles), 5 (crosses), 10 (triangles) and 50 ps (dots). [Right] Transient kinetics of CSC in the closed form at 550 (circles), 600 (crosses), 700 (triangles) and 750 nm (stars). Excitation wavelength 550 nm, 420 nJ/pulse. The symbols represent the data, the lines are results of the global fits.

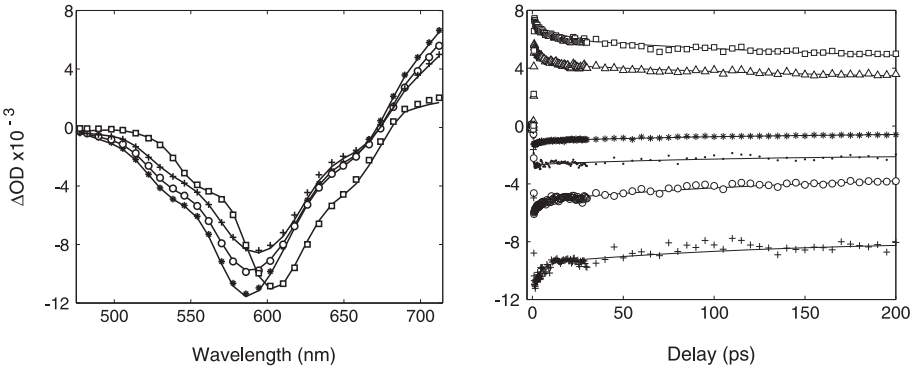

FIGURE 9.23. [Left] Transient spectra of PSP in the open form at 5 (stars), 50 (circles), 200 (crosses) and 3000 ps (squares). [Right] Transient kinetics of PSP in the open form at 500 (stars), 550 (circles), 600 (crosses), 650 (dots), 700 (triangles) and 713 nm (squares). Excitation wavelength 550 nm, 200 nJ/pulse. The symbols represent the data, the lines are results of the global fits.

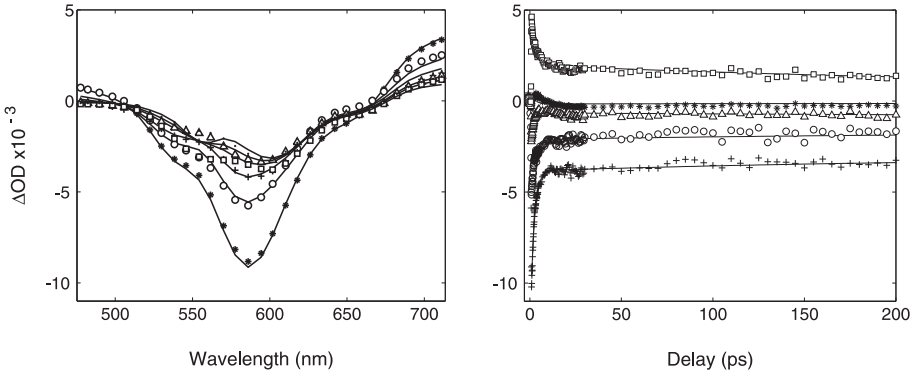

FIGURE 9.24. [Left] Transient spectra of PSP in the closed form at 2 (stars), 5 (circles), 50 (crosses), 200 (triangles), 300 (squares) and 500 ps (dots). [Right] Transient kinetics of PSP in the closed form at 500 (stars), 550 (circles), 600 (crosses), 650 (triangles) and 710 nm (squares). Excitation wavelength 550 nm, 200 nJ/pulse. The symbols represent the data, the lines are results of the global fits.

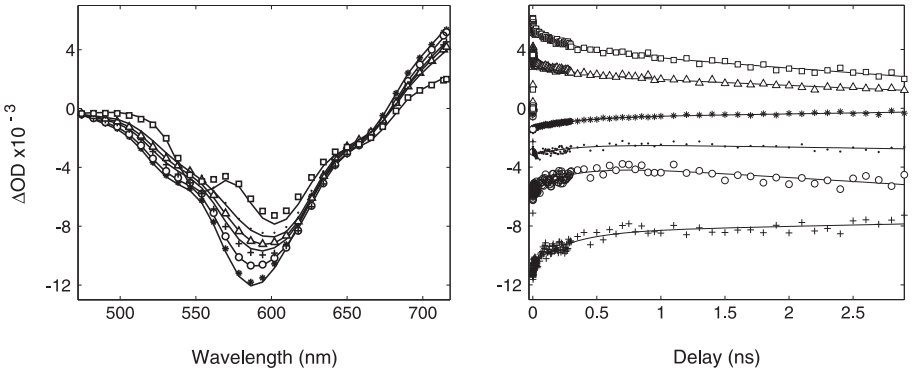

FIGURE 9.25. [Left] Transient spectra of CSP in the open form at 5 (stars), 50 (circles), 200 (crosses), 300 (triangles), 500 (dots) and 3000 ps (squares). [Right] Transient kinetics of CSP in the open form at 500 (stars), 550 (circles), 600 (crosses), 650 (dots), 700 (triangles) and 718 nm (squares). Excitation wavelength 550 nm, 400 nJ/pulse. The symbols represent the data, the lines are results of the global fits.

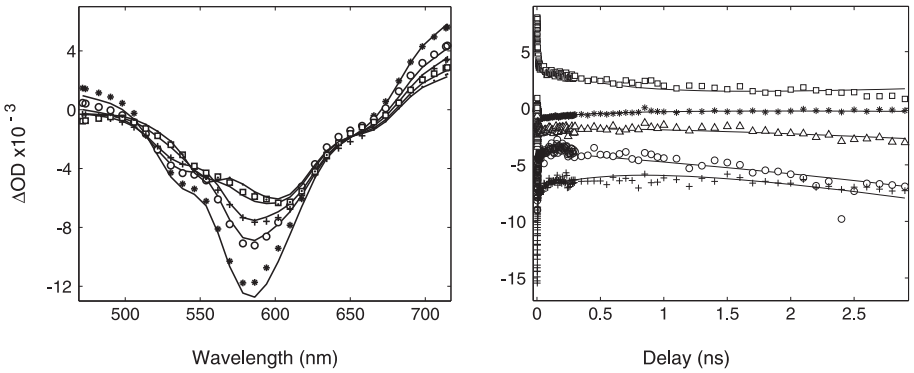

FIGURE 9.26. [Left] Transient spectra of CSP in the closed form at 5 (stars), 10 (circles), 50 (crosses), 300 (squares) and 500 ps (dots). [Right] Transient kinetics of CSP in the closed form at 500 (stars), 550 (circles), 600 (crosses), 650 (triangles) and 750 nm (squares). Excitation wavelength 550 nm, 400 nJ/pulse. The symbols represent the data, the lines are results of the global fits.

TABLE 9.7. Transient absorption decay times from global analysis

Compound	t_1 (ps)	t_2 (ps)	t_3 (ps)
Perylene-266	2.9	18	[a]
Perylene-550	1.7	10	320
switch$_{closed}$-550	1.5	2.6	32
CSC$_{open}$-266	3.7	21	240
CSC$_{closed}$-266	3.2	15	200
CSC$_{closed}$-550	0.9	3.2	7.1
PSP$_{open}$-266	5.1	55	[a]
PSP$_{closed}$-266	2.3	24	[a]
PSP$_{open}$-550	3.7	154	[a]
PSP$_{closed}$-550	2.0	320	[a]
CSP$_{open}$-266	1.0	30	120 [a]
CSP$_{closed}$-266	1.5	5.3	250 [a]
CSP$_{open}$-550	3.5	310	[a]
CSP$_{closed}$-550	3.3	590	[a]

[a] Additional rise time needed to fit the data could not be resolved properly.

Bibliography

1. B. Ke. *Photosynthesis: Photochemistry and Photobiophysics*. Kluwer Academic Publishers, 2001.

2. B. Blankenship. *Molecular Mechanisms of Photosynhtesis*. Blackwell Science, 2002.

3. G. H. Krause and E. Weis. Chlorophyll fluorescence and photosynhtesis - the basics. *Annual Review of Plant Physiology and Plant Molecular Biology*, 42:313–349, 1991.

4. J. M. Lehn. Perspectives in supramolecular chemistry - from molecular recognition towards molecular information-processing and self-organization. *Angewandte Chemie-International Edition*, 29:1304–1319, 1990.

5. W. R. Browne and B. L. Feringa. Making molecular machines work. *Nature-nanotechnology*, 1:25–35, 2006.

6. R. E. Fenna and B. W. Matthews. Chlorophyll arrangement in a bacteriochlorophyll protein from *Chlorobium limicola*. *Nature*, 258:573–577, 1975.

7. B. L. Feringa. *Molecular Switches*. Wiley-VCH, Weinheim, 2001.

8. M. Fox. *Optical Properties of Solids*. Oxford University Press, 2003.

9. P. W. Atkins and R. S. Friedman. *Molecular Quantum Mechanics*. Oxford University Press, 2000.

10. R. W. Boyd. *Nonlinear Optics*. Academic Press Inc, 2003.

11. M. Kasha. Characterization of electronic transitions in complex molecules. *Discussions of the Faraday Society*, 9:14–19, 1950.

12. S. Mukamel. *Principles of Nonlinear Optical Spectroscopy*. Oxford University Press, 1995.

13. J. R. Lakowicz. *Principles of Fluorescence Spectroscopy*. Kluwer Academic/Plenum Publishers, New York, 2nd ed. edition, 1999.

14. A. Baltuska, Z. Wei, M. S. Pshenichnikov, D. A. Wiersma, and R. Szipocs. All-solid-state cavity-dumped sub-5-fs laser. *Applied Physics B-Lasers and Optics*, 65:175–188, 1997.

15. J. C. Diels and W. Rudolph. *Ultrashort Laser Pulse Phenomena*. Academic Press-Elsevier, 2006.

16. W. Demtröder. *Laser Spectroscopy*. Springer-Verlag, 1982.

17. T. Wilhelm, J. Piel, and E. Riedle. Sub-20-fs pulses tunable across the visible from a blue-pumped single-pass noncollinear parametric converter. *Optics Letters*, 22:1494–1496, 1997.

18. E. Riedle, M. Beutter, S. Lochbrunner, J. Piel, S. Schenkl, S. Spörlein, and W. Zinth. Generation of 10 to 50 fs pulses tunable through all of the visible and the NIR. *Applied Physics B*, 71:457–465, 2000.

19. J. Piel, M. Beutter, and E. Riedle. 20-50-fs pulses tunable across the near infrared from a blue-pumped noncollinear parametric amplifier. *Optics Letters*, 25:180–182, 2000.

20. R. Trebino. *Frequency-Resolved Optical Gating: The Measurement of Ultrashort Laser Pulses*. Kluwer Academic Publishers, 2002.

21. A. A. Walmsley and C. Dorrer. Characterization of ultrashort electromagnetic pulses. *Advances in Optics and Photonics*, 1:308–437, 2009.

22. R. L. A. Timmer. *Molecular reorientation and transport in liquid water and ice*. PhD thesis University of Amsterdam, 2009.

23. M. Miller, R. P. Cox, and J. M. Olson. Low-temperature spectroscopy of isolated FMO-protein and a membrane-free reaction-center complex from the green sulfur bacterium *Chlorobium tepidum*. *Photosynthesis Research*, 41:97–103, 1994.

24. R. Fanciulli, I. Cerjak, and J. L. Herek. Low-noise rotating sample holder for ultrafast transient spectroscopy at cryogenic temperatures. *Review of Scientific Instruments*, 78:053102, 2007.

25. R. Van Grondelle, J. P. Dekker, T. Gillbro, and V. Sundström. Energy-transfer and trapping in photosynthesis. *Biochimica et Biophysica Acta-Bioenergetics*, 1187:1–65, 1994.

26. H. A. Frank and R. J. Cogdell. Carotenoids in photosynthesis. *Photochemistry and Photobiology*, 63:257–264, 1996.

27. H. Kurreck and M. Huber. Model reactions for photosynthesis-photoinduced charge and energy-transfer between covalently-linked porphyrin and quinone units. *Angewandte Chemie-International Edition*, 34:849–866, 1995.

28. D. Gust, T. A. Moore, and A. L. Moore. Mimicking photosynthetic solar energy transduction. *Accounts of Chemical Research*, 34:40–48, 2001.

29. H. Imahori, H. Norieda, H. Yamada, Y. Nishimura, I. Yamazaki, Y. Sakata, and S. Fukuzumi. Light-harvesting and photocurrent generation by cold electrodes modified with mixed self-assembled monolayers of boron-dipyrrin and ferrocene-porphyrin-fullerene triad. *Journal of the American Chemical Society*, 123:100–110, 2001.

30. D. M. Guldi. Fullerene-porphyrin architectures; photosynthetic antenna and reaction center models. *Chemical Society Reviews*, 31:22–36, 2002.

31. A. P. de Silva and N. D. McClenaghan. Molecular-scale logic gates. *Chemistry-A European Journal*, 10:574–586, 2004.

32. J. L. Bredas, D. Beljonne, V. Coropceanu, and J. Cornil. Charge-transfer and energy-transfer processes in pi-conjugated oligomers and polymers: A molecular picture. *Chemical Reviews*, 104:4971–5003, 2004.

33. F. J. M. Hoeben, P. Jonkheijm, E. W. Meijer, and A. P. H. J. Schenning. About supramolecular assemblies of pi-conjugated systems. *Chemical Reviews*, 105:1491–1546, 2005.

34. V. May and O. Kühn. *Charge and Energy Transfer Dynamics in Molecular Systems*. Wiley-VCH, Berlin, Germany, 2000.

35. G. S. Engel, T. R. Calhoun, E. L. Read, T.-K. Ahn, T. Mančal, Y.-C. Cheng, R. E. Blankenship, and G. R. Fleming. Evidence for wavelike energy transfer through quantum coherence in photosynthetic systems. *Nature*, 446:782–786, 2007.

36. Y. C. Cheng and G. R. Fleming. Dynamics of light harvesting in photosynthesis. *Annual Review of Physical Chemistry*, 60:241–262, 2009.

37. L. D. Bakalis and J. Knoester. Optical properties of one-dimensional exciton systems: Beyond the Heitler-London approximation. *Journal of Chemical Physics*, 106:6964–6976, 1997.

38. B. N. G. Giepmans, S. R. Adams, M. H. Ellisman, and R. Y. Tsien. Review - The fluorescent toolbox for assessing protein location and function. *Science*, 312:217–224, 2006.

39. N. C. Shaner, P. A. Steinbach, and R. Y. Tsien. A guide to choosing fluorescent proteins. *Nature-Methods*, 2:905–909, 2005.

40. T. Förster. Zwischenmolekulare energiewanderung und fluoreszenz. *Annalen der Physik*, 2:55–75, 1948.

41. D. Beljonne, C. Curutchet, G. D. Scholes, and R. J. Silbey. Beyond Forster resonance energy transfer in biological and nanoscale systems. *Journal of Physical Chemistry B*, 113:6583–6599, 2009.

42. D. Dexter. A theory of sensitized luminescence in solids. *Journal of Chemical Physics*, 21:836–851, 1953.

43. M. Inokuti and F. Hirayama. Influence of energy transfer by the exchange mechanism on donor luminescence. *Journal of Chemical Physics*, 43:1978–1983, 1965.

44. S. Hassoon, H. Lustig, M. B. Rubun, and S. Speiser. The mechanism of short-range intramolecular electronic energy transfer in bichromophoric molecules. *Journal of Physical Chemistry*, 88:6367–6374, 1984.

45. V. M. Kenkre and R. S. Knox. Generalized-master-equation theory of excitation transfer. *Physical Review B*, 9:5279–5290, 1974.

46. G. D. Scholes and K. Ghiggino. Rate expressions for excitation transfer. IV. energy migration and superexchange phenomena. *Journal of Chemical Physics*, 103:8873–8883, 1995.

47. J. M. Olson and C. A. Romano. A new chlorophyll from green bacteria. *Biochimica Biophysica Acta*, 59:726–728, 1962.

48. Y. F. Li, W. Zhou, R. E. Blankenship, and J. P. Allen. Crystal structure of the bacteriochlorophyll *a* protein from *Chlorobium tepidum*. *Journal of Molecular Biology*, 271:456–471, 1997.

49. A. N. Melkozernov, J. M. Olson, Y.-F. Li, J. P. Allen, and R. E. Blankenship. Orientation and excitonic interactions of the Fenna-Matthews-Olson bacteriochlorophyll *a* protein in membranes of the green sulfut bacterium *Chlorobium tepidum*. *Photosynthesis Research*, 56:315–328, 1998.

50. D. E. Tronrud, J. Wen, L. Gay, and R. E. Blankenship. The structural basis for the difference in absorbance spectra for the FMO antenna protein from various green sulfur bacteria. *Photosynthesis Research*, 100:79–87, 2009.

51. E. I. Iseri and D. Gülen. Electronic excited states and excitation transfer kinetics in the Fenna-Matthews-Olson protein of the photosynthetic bacterium *Prosthecochloris aestuarii* at low temperatures. *European Biophysical Journal*, 28:243–253, 1999.

52. A. Ben-Shem, F. Frolow, and N. Nelson. Evolution of photosystem I - from symmetry through pseudosymmetry to asymmetry. *FEBS Letters*, 564:274–280, 2004.

53. J. M. Olson. The FMO protein. *Photosynthesis Research*, 80:181–187, 2004.

54. S. G. Johnson and G. J. Small. Excited-state structure and energy-transfer dynamics of the bacteriochlorophyll *a* antenna complex from *Prosthecochloris aestuarii*. *Journal of Physical Chemistry*, 95:471–479, 1991.

55. V. Gulbinas, L. Valkunas, D. Kuciauskas, E. Katilius, V. Liuolia, W. Zhou, and R. E. Blankenship. Singlet-singlet annihilation and local heating in FMO complexes. *Journal of Physical Chemistry*, 100:17950–17956, 1996.

56. C. Francke and J. Amesz. Isolation and pigment composition of the antenna system of four species of green sulfur bacteria. *Photosynthesis Research*, 52:137–146, 1997.

57. R. M. Pearlstein. Theory of the optical spctra of the bacteriochlorophyll *a* antenna protein trimer from *Prosthecochloris aestuarii*. *Photosynthetic Research*, 31:213–226, 1992.

58. F. Van Mourik, R. R. Verwijst, J. M. Mulder, and R. Van Grondelle. Singlet-triplet spectroscopy of the light-harvesting bchl*a* complex of *Prosthecochloris aestuarii*: The nature of the low-energy 825 nm transition. *Journal of Physical Chemistry*, 98:10307–10312, 1994.

59. M. Rätsep and A. Freiberg. Unusual temperature quenching of bacteriochlorophyll *a* fluorescence in FMO antenna protein trimers. *Chemical Physics Letters*, 434:306–311, 2007.

60. D. R. Buck, S. Savikhin, and W. S. Struve. Ultrafast absorption difference spectra of the Fenna-Matthews-Olson protein at 19K: Experiments and simulations. *Biophysical Journal*, 72:24–36, 1997.

61. R. J. W. Louwe, J. Vrieze, A. J. Hoff, and T. J. Aartsma. Toward an integral interpretation of the optical steady-state spectra of the FMO-complex of *Prosthecochloris aestuarii*. 2. exciton simulations. *Journal of Physical Chemistry B*, 101:11280–11287, 1997.

62. S. I. E. Vulto, M. A. De Baat, S. Neerken, F. R. Nowak, H. Van Amerongen, J. Amesz, and T. J. Aartsma. Excited state dynamics in FMO antenna complexes from photosynthetic green sulfur bacteria: A kinetic model. *Journal of Physical Chemistry B*, 103:8153–8161, 1999.

63. S. Matsuzaki, V. Zazubovich, M. Rätsep, J. M. Haynes, and G. J. Small. Energy transfer kinetics and low energy vibrational structure of the three lowest energy Q_y-states of the Fenna-Matthews-Olson antenna complex. *Journal of Physical Chemistry B*, 104:9564–9572, 2000.

64. M. Wendling, M. A. Przyjalgowski, D. Gülen, S. I. E. Vulto, T. J. Aarstma, R. Van Grondelle, and H. Van Amerongen. The quantative relationship between structure and polarized spectroscopy in the FMO complex of *Prosthecochloris aestuarii*: refining experiments and simulations. *Photosynthesis Research*, 71:99–123, 2002.

65. J. Adolphs and T. Renger. How proteins trigger excitation energy transfer in the FMO complex of green sulfur bacteria. *Biophysical Journal*, 91:2778–2897, 2006.

66. X. Lu and R. M. Pearlstein. Simulations of *Prostechochloris* bacterioschlorophyll a protein optical spectra improved by parametric computer search. *Photochemistry and Photobiology*, 57:86–91, 1993.

67. D. Gülen. Interpretation of the excited-state structure of the Fenna-Matthews-Olson pigment protein complex of *Prosthecochloris aestuarii* based on the simultaneous simulation of the 4 K absorption, linear dichroism and singlet-triplet absorption difference spectra: A possible excitonic explanation? *Journal of Physical Chemistry*, 100:17683–17689, 1996.

68. F. Müh, M. E. Madjet, J. Adolphs, A. Abdurahman, B. Rabenstein, H. Ishikita, E.-W. Knapp, and T. Renger. Alpha-helices direct excitation energy flow in the Fenna-Matthews-Olson protein. *Proceedings of the National Academy of Sciences*, 104:16862–16867, 2007.

69. J. Adolphs, F. Müh, F. El-Amine, and T. Renger. Calculation of pigment transition energies in the FMO protein. *Photosynthesis Research*, 95:197–209, 2008.

70. E. Gudowksa-Nowak, M. D. Newton, and J. Fajer. Confromational and environmental effects on bacteriochlorophyll optical spectra: Correlations of calculated spectra with structural results. *Journal of Physical Chemistry*, 94:5795–5801, 1990.

71. M. Rätsep, H.-M. Wu, J. M. Hayes, R. E. Blankenship, R. J. Cogdell, and G. J. Small. Stark hole-burning studies of three photosynthetic complexes. *Journal of Physical Chemistry B*, 102:4035–4044, 1998.

72. H.-W. Rémigy, H. Stahlberg, D. Fotiadis, S.A. Müller, B. Wolpensinger, A. Engel, G. Hauska, and G. Tsiotis. The reaction center complex from the green sulfur bacterium *Chlorobium tepidum*: A structural analysis by scanning transmission electron microscopy. *Journal of Molecular Biology*, 290:851–858, 1999.

73. H. Van Amerongen, L. Valkunas, and R. Van Grondelle. *Photosynthetic Excitons*. World Scientific Publishing, 2000.

74. R. J. W. Louwe, J. Vrieze, T. J. Aartsma, and A. J. Hoff. Toward an integral interpretation of the optical steady-state spectra of the FMO-complex of *Prosthecochloris aestuarii*. 1. an investigation with linear-dichroic absorbance-detected magnetic resonance. *Journal of Physical Chemistry B*, 101:11273–11279, 1997.

75. T. Renger and V. May. Ultrafast exciton motion in photosynthetic antenna systems: The FMO complex. *Journal of Physical Chemistry A*, 102:4381–4391, 1998.

76. M. Wendling, T. Pullerits, M. A. Przyjalgowski, S. I. E. Vulto, T. J. Aartsma, R. Van Grondelle, and Van Amerongen H. Electron-vibrational coupling in the Fenna-Matthews-Olson complex of *Prosthecochloris aestuarii*. determined by temperature-dependent absorption and fluorescence line-narrowing measurements. *Journal of Physical Chemistry B*, 104:5825–5831, 2000.

77. S. I. E. Vulto, M. A. De Baat, R. J. W. Louwe, H. P. Permentier, T. Neef, M. Miller, H. Van Amerongen, and T. J. Aartsma. Exciton simulations of optical spectra of the FMO complex from the green sulfer bacterium *Chlorobium tepidum* at 6K. *Journal of Physical Chemistry B*, 102:9577–9582, 1998.

78. S. I. E. Vulto, S. Neerken, R. J. W. Louwe, M. A. De Baat, J. Amesz, and T. J. Aartsma. Excited-state structure and dynamics in FMO antenna complexes from photosynthetic green sulfur bacteria. *Journal of Physical Chemistry B*, 102:10630–10635, 1998.

79. P. W. Atkins. *Physical Chemistry.* Oxford University Press, 1995.

80. J. M. Hayes, M. Ruehlaender, C. Soukoulis, and G. J. Small. Monte Carlo simulations of energy transfer rates: application to downward energy transfer within the 825 nm absorption band of the FMO complex of *Prosthecochloris aestuarii*. *Journal of Luminescence*, 98:246–255, 2002.

81. M. Cho, H. M. Vaswani, T. Brixner, J. Stenger, and G. R. Fleming. Exciton analysis in 2D electronic spectroscopy. *Journal of Physical Chemistry B*, 109:10542–10556, 2005.

82. D. Abramavicius, D. V. Voronine, and S. Mukamel. Unravelling coherent dynamics and energy dissipation in photosynthetic complexes by 2D spectroscopy. *Biophysical Journal*, 94:3613–3619, 2008.

83. T. Brixner, J. Stenger, H. M. Vaswani, M. Cho, R. E. Blankenship, and G. R. Fleming. Two-dimensional spectroscopy of electronic couplings in photosynthesis. *Nature*, 434:625–628, 2005.

84. D. Abramavicius, D. V. Voronine, and S. Mukamel. Double-quantum resonances and exciton-scattering in coherent 2D spectroscopy of photosynthetic complexes. *Proceedings of the National Academy of Sciences*, 105:8525–8530, 2008.

85. W. L. Zhou, R. Lobrutto, S. Lin, and R. E. Blankenship. Redox effects on the bacteriochlorophyll-a containing Fenna-Matthews-Olson protein from *chlorobium tepidum*. *Photosynthesis Research*, 41:89–96, 1994.

86. M. F. Hohmann-Marriott and R. E. Blankenship. Variable fluorescence in green sulfur bacteria. *Biochimica et Biophysica Acta*, 1767:106–113, 2007.

87. B. Brüggemann and V. May. Ultrafast laser pulse control of exciton dynamics: A computational study on the FMO complex. *Journal of Physical Chemistry B*, 108:10529–10539, 2004.

88. B. Brüggemann, T. Pullerits, and V. May. Laser pulse control of exciton dynamics in the FMO complex: Polarization shaping versus effects of structural and energetic disorder. *Journal of Photochemistry and Photobiology A: Chemistry*, 180:322–327, 2006.

89. E. L. Read, G. S. Schlau-Cohen, G. S. Engel, J. Wen, R. E. Blankenship, and G. R. Fleming. Visualization of excitonic structure in the fenna-matthews-olson photosynthetic complex by polarization-dependent two-dimensional electronic spectroscopy. *Biophysical Journal*, 95:847–856, 2008.

90. M. Rätsep, R. E. Blankenship, and G. J. Small. Energy transfer and spectral dynamics of the three lowest energy Q_y-states of the Fenna-Matthews-Olson antenna complex. *Journal of Physical Chemistry B*, 103:5736–5741, 1999.

91. E. M. Franken, S. Neerken, Louwe R. J. W., J. Amesz, and T. J. Aartsma. A permanent hole burning study of the FMO antenna complex of the green sulfur bacterium *Prosthecochloris aestuarii*. *Biochemistry*, 37:5046–5051, 1998.

92. P. A. Lyle and W. S. Struve. Evidence for ultrafast exciton localization in the Q_y band of bacteriochlorophyll a-protein from *Prosthecochloris aestuarii*. *Journal of Physical Chemistry*, 94:7338–7339, 1990.

93. R. J. W. Louwe and T. J. Aartsma. Optical dephasing and excited state dynamics in photosynthestic pigment-protein complexes. *Journal of Luminescence*, 58:154–157, 1994.

94. S. I. E. Vulto, A. M. Streltsov, and T. J. Aartsma. Excited state energy relaxation in the FMO complexes of the green bacterium *Prosthecochloris aestuarii* at low temperatures. *Journal of Physical Chemistry B*, 101:4845–4850, 1997.

95. R. J. W. Louwe and T. J. Aartsma. On the nature of energy transfer at low temperatures in the bchl *a* pigment-protein complex of green sulfur bacteria. *Journal of Physical Chemistry B*, 101:7221–7226, 1997.

96. V. I. Prokhorenko, A. R. Holzwarth, F. R. Nowak, and T. J. Aartsma. Growing-in of optical coherence in the FMO antenna complexes. *Journal of Physical Chemistry B*, 106:9923–9933, 2002.

97. E. L. Read, G. S. Engel, T. R. Calhoun, T. Mančal, T.-K. Ahn, R. E. Blankenship, and Fleming G. R. Cross-peak-specific two-dimensional electronic spectroscopy. *Proceedings of the National Academy of Sciences*, 104:14203–14208, 2007.

98. D. V. Voronine, D. Abramavicius, and S. Mukamel. Chirality-based signatures of local protein environments in two-dimensional optical spesctroscopy of two species photosynthetic complexes of green sulfur bacteria: Simulation study. *Biophysical Journal*, 95:4896–4907, 2008.

99. N. R. S. Reddy, R. Jankowiak, and G. J. Small. High-pressure hole-burning studies of the bacteriochlorophyll *a* antenna complex from *Chlorobium tepidum*. *Journal of Physical Chemistry*, 99:16168–16178, 1995.

100. S. Savikhin, W. Zhou, R. E. Blankenship, and W. S. Struve. Femtosecond energy transfer and spectral equilibration in bacteriochlorophyll a-protein trimers from the green bacterium *Chlorobium tepidum*. *Biophysical Journal*, 66:110–114, 1994.

101. S. Savikhin and W. S. Struve. Ultrafast energy transfer in FMO trimers from the green bacterium *Chlorobium tepidum*. *Biochemistry*, 33:11200–11208, 1994.

102. S. Savikhin and W. S. Struve. Low-temperature energy transfer in FMO trimers from the green photosynthetic bacterium *Chlorobium tepidum*. *Photosynthesis Research*, 48:271–276, 1996.

103. A. Freiberg, S. Lin, K. Timpmann, and R. E. Blankenship. Exciton dynamics in FMO bacteriochloroplhyll protein at low temperatures. *Journal of Physical Chemistry B*, 101:7211–7220, 1997.

104. S. Savikhin, D. R. Buck, and W. S. Struve. Oscillating anisotropies in a bacteriochlorophyll protein: Evidence for quantum beating between exciton levels. *Chemical Physics*, 223:303–312, 1997.

105. S. Savikhin, D. R. Buck, and W. S. Struve. Towards level-to-level energy transfer in photosynthesis: The Fenna-Matthews-Olson protein. *Journal of Physical Chemistry B*, 102:5556–5565, 1998.

106. B. Brüggemann, P. Kjellberg, and T. Pullerits. Non-perturbative calculation of 2D spectra in heterogeneous systems: Exciton relaxation in the FMO complex. *Chemical Physics Letters*, 444:192–196, 2007.

107. J. Koepke, X. C. Hu, C Muenke, K. Schulten, and H. Michel. The crystal structure of the light-harvesting complex II (B800-850) from Rhodospirillum molischianum. *Structure*, 4:581–597, 1996.

108. G. McDermott, S. M. Prince, A. A. Freer, A. M. Hawthornthwaitelawless, M. Z. Papiz, R. J. Cogdell, and N. W. Isaacs. Crystal-structure of an integral membrane light-harvesting complex from photosynthetic bacteria. *Nature*, 374:517–521, 1995.

109. S. Karrasch, P. A. Bullough, and R. Ghosh. The 8.5-Angstrom projection map of the light-harvesting complex-I from Rhodospirillum-Rubrum reveals a ring composed of 16 subunits. *EMBO Journal*, 14:631–638, 1995.

110. W. Kuhlbrandt, D. N. Wang, and Y. Fujiyoshi. Atomic model of plant light-harvesting complex by electron crystallography. *Nature*, 367:614–621, 1994.

111. B. Brüggemann, N. Christensson, and T. Pullerits. Temperature dependent exciton-exciton annihilation in the LH2 antenna complex. *Chemical Physics*, 357:140–143, 2009.

112. G. Trinkunas, J. L. Herek, T. Polívka, V. Sundström, and T. Pullerits. Exciton delocalization probed by excitation annihilation in the light-harvesting antenna LH2. *Physical Review Letters*, 18:4167–4170, 2001.

113. C. Griesbeck, C. Hager-Braun, H. Rogl, and G. Hauska. Quantitation of P840 reaction center preparations from Chlorobium tepidum: chlorophylls and FMO-protein. *Biochimica and Biophysica Acta-Bioenergetics*, 1365:285–293, 1998.

114. B. Brüggemann, J. L. Herek, V. Sundström, T. Pullerits, and V. May. Microscopic theory of exciton annihilation: Application to the LH2 antenna system. *Journal of Physical Chemistry B*, 105:11391–11394, 2001.

115. A. Freiberg, M. Ratsep, K. Timpmann, G. Trinkunas, and N. W. Woodbury. Self-trapped excitons in LH2 antenna complexes between 5 K and ambient temperature. *Journal of Physical Chemistry B*, 107:11510–11519, 2003.

116. B. Brüggemann and V. May. Exciton exciton annihilation dynamics in chromophore complexes. ii. intensity dependent transient absorption of the LH2 antenna system. *Journal of Chemical Physics*, 120:2325–2336, 2004.

117. T. Brixner and G. Gerber. Quantum control of gas-phase and liquid-phase femtochemistry. *ChemPhysChem*, 4:418–438, 2003.

118. D. Goswami. Optical pulse shaping approaches to coherent control. *Physics Reports*, 374:385–481, 2003.

119. T. Brixner, N. H. Damrauer, P. Niklaus, and G. Gerber. Photoselective adaptive femtosecond quantum control in the liquid phase. *Nature*, 414:57–60, 2001.

120. J. L Herek, W Wohlleben, R. J. Cogdell, D. Zeidler, and M. Motzkus. Quantum control of energy flow in light harvesting. *Nature*, 417:533–535, 2002.

121. M. Wollenhaupt, A. Assion, and T. Baumert. *Femtosecond Laser Pulses: Linear Properties, Manipulation, Generation and Measurement*. Springer Science and Business Media, 2007.

122. A. M. Weiner. Femtosecond pulse shaping using spatial light modulators. *Review of Scientific Instruments*, 71:1929, 2000.

123. J. Savolainen. *Coherent control of biomolecules*. PhD thesis University of Twente, 2008.

124. O. M. Shir and T. Bäck. *Parallel Problem Solving from Nature - PPSN IX-Niche Radius Adaptation in the CMA-ES Niching Algorithm*. Springer-Verlag, 2006.

125. J. Savolainen, R. Fanciulli, N. Dijkhuizen, A. L. Moore, J. Hauer, T. Buckup, M. Motzkus, and J. L. Herek. Controlling the efficiency of an artificial light-harvesting complex. *Proceedings of the National Academy of Sciences*, 105:7641–7646, 2008.

126. P. Van der Walle, L. Kuipers, J. Savolainen, and J. L. Herek. Controlling the efficiency of an artificial light-harvesting complex. *Chemical Physics Letters*, 483:164–167, 2009.

127. B. L. Feringa, R. A. van Delden, N. Koumura, and E. M. Geertsema. Chiroptical molecular switches. *Chemical Reviews*, 100:1789–1816, 2000.

128. T. Ikeda and O. Tsutsumi. Optical switching and image storage by means of azobenzene liquid-crystal films. *Science*, 268:1873–1875, 1995.

129. N. Tamai and H. Miyasaka. Ultrafast dynamics of photochromic systems. *Chemical Reviews*, 100:1875–1890, 2000.

130. M. Irie. Diarylethenes for memories and switches. *Chemical Reviews*, 100:1685–1716, 2000.

131. J. J. D. de Jong, L. N. Lucas, R. Hania, A. Pugzlys, R. M. Kellogg, B. L. Feringa, K. Duppen, and J. H. van Esch. Photochromic properties of perhydro- and perfluorodithienylcyclopentene molecular switches. *European Journal of Chemistry*, (10):1887–1893, 2003.

132. S. Pullen, L. A. Walker, B. Donovan, and R. J. Sension. Femtosecond transient absorption study of the ring-opening reaction of 1,3-cyclohexadiene. *Chemical Physics Letters*, 242:415–420, 1995.

133. P. J. Reid, S. J. Doig, and R. A. Mathies. Direct measurement of the photochemical ring-opening in 1,3-cyclohexadiene by picosecond time-resolved UV resonance Raman. *Chemical Physics Letters*, 156:163–168, 1989.

134. P. J. Reid, S. J. Doig, S. D. Wickham, and R. A. Mathies. Photochemical ring-opening reactions are complete in picoseconds - A time-resolved UV resonance Raman-study of 1,3-cyclohexadiene. *Journal of the American Chemical Society*, 115:4754–4763, 1993.

135. M. O. Trulson, G. D. Dollinger, and R. A. Mathies. Excited-state structure and femtosecond ring-opening dynamics of 1,3-cyclohexadiene from absolute resonance raman intensities. *Journal of Chemical Physics*, 90:4274–4281, 1989.

136. K. Fukui. *Noble lecture: The role of frontier orbitals in chemical reactions.* 1981.

137. J. C. Owrutsky, H. H. Nelson, A. P. Baronavski, O. K. Kim, G. M. Tsivgoulis, S. L. Gilat, and J. M. Lehn. Optical properties and dynamics of a photochromic bisthienylethene in solution and in a polymer film. *Chemical Physics Letters*, 293:555–563, 1998.

138. J. Ern, A. Bens, H. D. Martin, S. Mukamel, D. Schmid, S. Tretiak, E. Tsiper, and C. Kryschi. Femtosecond reaction dynamics of a photochromic dithienylethene derivative. *Journal of Luminescence*, 87-9:742–744, 2000.

139. J. Ern, A. T. Bens, H. D. Martin, K. Kuldova, H. P. Trommsdorff, and C. Kryschi. Ring-opening and -closure reaction dynamics of a photochromic dithienylethene derivative. *Journal of Physical Chemistry A*, 106:1654–1660, 2002.

140. C. Okabe, T. Nakabayashi, N. Nishi, T. Fukaminato, T. Kawai, M. Irie, and H. Sekiya. Picosecond time-resolved stokes and anti-stokes Raman studies on the photochromic reactions of diarylethene derivatives. *Journal of Physical Chemistry A*, 107:5384–5390, 2003.

141. S. Shim, I. Eom, T. Joo, E. Kim, and K. S. Kim. Ring closure reaction dynamics of diarylethene derivatives in solution. *Journal of Physical Chemistry A*, 111:8910–8917, 2007.

142. K. Uchida, D. Guillaumont, E. Tsuchida, G. Mochizuki, M. Irie, A. Murakami, and S. Nakamura. Theoretical study of an intermediate, a factor determining the quantum yield in photochromism of diarylethene derivatives. *Journal of Molecular Structure-Theochem*, 579:115–120, 2002.

143. P. R. Hania, R. Telesca, L. N. Lucas, A. Pugzlys, J. Van Esch, B. L. Feringa, J. G. Snijders, and K. Duppen. An optical and theoretical investigation of the ultrafast dynamics of a bisthienylethene-based photochromic switch. *Journal of Physical Chemistry A*, 106:8498–8507, 2002.

144. J. Ern, A. T. Bens, H. D. Martin, S. Mukamel, D. Schmid, S. Tretiak, E. Tsiper, and C. Kryschi. Reaction dynamics of photochromic dithienylethene derivatives. *Chemical Physics*, 246:115–125, 1999.

145. K. Kuldova, K. Tsyganenko, A. Corval, H. P. Trommsdorff, A. T. Bens, and C. Kryschi. Photo-switchable dithienylethenes: threshold of the photoreactivity. *Synthetic Metals*, 115:163–166, 2000.

146. D. Dulic, T. Kudernac, A. Puzys, B. L. Feringa, and B. J. Van Wees. Temperature gating of the ring-opening process in diarylethene molecular switches. *Advanced Materials*, 19:2898–2902, 2007.

147. D. Guillaumont, T. Kobayashi, K. Kanda, H. Miyasaka, K. Uchida, S. Kobatake, K. Shibata, S. Nakamura, and M. Irie. An ab initio MO study of the photochromic reaction of dithienylethenes. *Journal of Physical Chemistry A*, 106:7222–7227, 2002.

148. S. Nakamura, S. Yokojima, K. Uchida, T. Tsujioka, A. Goldberg, A. Murakami, K. Shinoda, M. Mikami, T. Kobayashi, S. Kobatake, K. Matsuda, and M. Irie. Theoretical investigation on photochromic diarylethene: A

short review. *Journal of Photochemistry and Photobiology A-Chemistry*, pages 10–18, 2008.

149. M. Murakami, H. Miyasaka, T. Okada, S. Kobatake, and M. Irie. Dynamics and mechanisms of the multiphoton gated photochromic reaction of diarylethene derivatives. *Journal of the American Chemical Society*, 126:14764–14772, 2004.

150. Y. Asano, A. Murakami, T. Kobayashi, A. Goldberg, D. Guillaumont, S. Yabushita, M. Irie, and S. Nakamura. Theoretical study on the photochromic cycloreversion reactions of dithienylethenes; on the role of the conical intersections. *Journal of the American Chemical Society*, 126:12112–12120, 2004.

151. N. Tamai, T. Saika, T. Shimidzu, and M. Irie. Femtosecond dynamics of a thiophene oligomer with a photoswitch by transient absorption spectroscopy. *Journal of Physical Chemistry*, 100:4689–4692, 1996.

152. G. M. Tsivgoulis and J. M. Lehn. Photoswitched sexithiophenes: Towards switchable molecular wires. *Advanced Materials*, 9:39–42, 1997.

153. A. T. Bens, D. Frewert, K. Kodatis, C. Kryschi, H. D. Martin, and H. P. Trommsdorff. Coupling of chromophores: Carotenoids and photoactive diarylethenes - Photoreactivity versus radiationless deactivation. *European Journal of Chemistry*, (10):2333–2338, 1998.

154. J. Ern, A. T. Bens, H. D. Martin, S. Mukamel, S. Tretiak, K. Tsyganenko, K. Kuldova, H. P. Trommsdorff, and C. Kryschi. Reaction dynamics of a photochromic fluorescing dithienylethene. *Journal of Physical Chemistry A*, 105:1741–1749, 2001.

155. M. Berberich, A. Krause, M. Orlandi, F. Scandola, and F. Wuerthner. Toward fluorescent memories with nondestructive readout: Photoswitching of fluorescence by intramolecular electron transfer in a diaryl ethene-perylene bisimide photochromic system. *Angewandte Chemie-International Edition*, 47:6616–6619, 2008.

156. M. Irie, T. Fukaminato, T. Sasaki, N. Tamai, and T. Kawai. Organic chemistry: A digital fluorescent molecular photoswitch. *Nature*, 420:759–760, 2002.

157. A. Fernandez-Acebes and J. M. Lehn. Optical switching and fluorescence modulation in photochromic metal complexes. *Advanced Materials*, 10:1519, 1998.

158. M. Bossi, V. Belov, S. Polyakova, and S. W. Hell. Reversible red fluorescent molecular switches. *Angewandte Chemie-International Edition*, 45:7462–7465, 2006.

159. C. K. Chiang, Y. W. Park, A. J. Heeger, H. Shirakawa, , E. J. Louis, and A. G MacDiarmid. Electrical conductivity in doped polyacetylene. *Physical Review Letters*, 39:1098–1101, 1977.

160. F. Garnier. Organic-based electronics a la carte. *Accounts of Chemical Research*, 32:209–215, 1999.

161. F. Garnier, R. Hajlaoui, A. Yassar, and P. Srivastava. All-polymer field-effect transistor realized by printing techniques. *Science*, 265:1684–1686, 1994.

162. J. Nishida, T. Miyagawa, and Y. Yamashita. Novel thiophene oligomers containing a redox active hexaarylethane unit. *Organic Letters*, 6:2523–2526, 2004.

163. W. A. Gazotti, A. F. Nogueira, E. M. Girotto, L. Micaroni, M. Martini, S. das Neves, and M. De Paoli. *Handbook of Advanced Electronic and Photonic Materials and Devices*. Academic Press, San Diego, CA, 2001.

164. A. Durmus, G. E. Gunbas, P. Camurlu, and L. Toppare. A neutral state green polymer with a superior transmissive light blue oxidized state. *Chemical Communications*, (31):3246–3248, 2007.

165. R. Berridge, S. P. Wright, P. J. Skabara, A. Dyer, T. Steckler, A. A. Argun, J. R. Reynolds, W. H. Ross, and W. Clegg. Electrochromic properties of a fast switching, dual colour polythiophene bearing non-planar dithiinoquinoxaline units. *Journal of Materials Chemistry*, 17:225–231, 2007.

166. J. Roncali. Conjugated poly(thiophenes) - synthesis, functionalization, and applications. *Chemical Reviews*, 92:711–738, 1992.

167. D. Lorcy and M. P. Cava. Poly(isothianaphthene bithiophene) - a new regularly structured polythiophene analog. *Advanced Materials*, 4:562–564, 1992.

168. H. Klauk. *Organic Electronics*. Wiley-VCH, Weinheim, Germany, 2006.

169. K. Watanabe, T. Asahi, H. Fukumura, H. Masuhara, K. Hamano, and T. J. Kurata. Ultrafast decay dynamics of excited and charged states in alpha-sexithienyl film as revealed by femtosecond transient absorption and picosecond fluorescence spectroscopy. *J. Phys. Chem. B.*, 101:1510–1519, 1997.

170. P. Bauerle. *Electronic Materials: The Oligomer Approach*. Wiley-VCH, Weinheim, Germany, 1998.

171. J. Roncali. Oligothienylenevinylenes as a new class of multinanometer linear pi-conjugated systems for micro- and nanoelectronics. *Accounts of Chemical Research*, 33:147–156, 2000.

172. J. M. Tour. Molecular electronics. synthesis and testing of components. *Accounts of Chemical Research*, 33:791–804, 2000.

173. E. Da Como, M. A. Loi, M. Murgia, R. Zamboni, and M. Muccini. J-aggregation in alpha-sexithiophene submonolayer films on silicon dioxide. *Journal of the American Chemical Society*, 128:4277–4281, 2006.

174. S. Westenhoff, A. Abrusci, W. J. Feast, O. Henze, A. F. M. Kilbinger, A. P. H. J. Schenning, and C. Silva. Supramolecular electronic coupling in chiral oligothiophene nanostructnres. *Advanced Materials*, 18:1281–1285, 2006.

175. J. Clark, C. Silva, R. H. Friend, and F. C. Spano. Role of intermolecular coupling in the photophysics of disordered organic semiconductors: Aggregate emission in regioregular polythiophene. *Physical Review Letters*, 98, 2007. 206406.

176. Y. F. Feng, Y. L. Yan, S. Wang, W. H. Zhu, S. X. Qian, and H. Tian. Photochromic thiophene oligomers based on bisthienylethene: syntheses, photochromic and two-photon properties. *Journal of Materials Chemistry*, 16:3685–3692, 2006.

177. A. Alberti, B. Ballarin, M. Guerra, D. Macciantelli, A. Mucci, F. Parenti, L. Schenetti, R. Seeber, and C. Zanardi. Radical ions from 3,3 "',3 ""-tris(butylsulfanyl)-2,2 ': 5 ',2 ": 5 ",2 "',5 "',2 "": 5 "",2 ""'-sexithiophene: An experimental and theoretical study of the p- and n-doped oligomer. *ChemPhysChem*, 4:1216–1225, 2003.

178. P. Bauerle, U. Segelbacher, A. Maier, and M. Mehring. Electronic-structure of monomeric and dimeric cation radicals in end-capped oligothiophenes. *Journal of the American Chemical Society*, 115:10217–10223, 1993.

179. D. Fichou. *Handbook of Oligo- and Polythiophenes*. Wiley-VCH, 1999.

180. H. E. Katz, Z. N. Bao, and S. L. Gilat. Synthetic chemistry for ultrapure, processable, and high-mobility organic transistor semiconductors. *Accounts of Chemical Research*, 34:359–369, 2001.

181. G. Sonmez, H. B. Sonmez, C. K. F. Shen, R. W. Jost, Y. Rubin, and F. Wudl. A processable green polymeric electrochromic. *Macromolecules*, 38:669–675, 2005.

182. I. Schwendeman, R. Hickman, G. Sonmez, P. Schottland, K. Zong, D. M. Welsh, and J. R. Reynolds. Enhanced contrast dual polymer electrochromic devices. *Chemistry of Materials*, 14:3118–3122, 2002.

183. P. F. van Hutten, J. Wildeman, A. Meetsma, and G. Hadziioannou. Molecular packing in unsubstituted semiconducting phenylenevinylene oligomer and polymer. *Journal of the American Chemical Society*, 121:5910, 1999.

184. A. P. H. J. Schenning, A. F. M. Kilbinger, F. Biscarini, M. Cavallini, H. J. Cooper, P. J. Derrick, W. J. Feast, R. Lazzaroni, Ph. Leclère, L. A. McDonnel, E. W. Meijer, and S. C. J. Meskers. Supramolecular organization of a,a'-disubstituted sexithiophenes. *Journal of the American Chemical Society*, 124:1269–1275, 2002.

185. G. M. Tsivgoulis and J. M. Lehn. Photoswitched and functionalized oligothiophenes: Synthesis and photochemical and electrochemical properties. *Chemistry-a European Journal*, 2:1399–1406, 1996.

186. A. Peters, R. McDonald, and N. R. Branda. Regulating pi-conjugated pathways using a photochromic 1,2-dithienylcyclopentene. *Chemical Communications*, 19:2274–2275, 2002.

187. J. Areephong, J. H. Hurenkamp, M. T. W. Milder, A. Meetsma, J. L. Herek, W. R. Browne, and B. L. Feringa. Photoswitchable Sexithiophene-Based Molecular Wires. *Organic Letters*, 11:721–724, 2009.

188. J. N. Yao, K. Hashimoto, and A. Fujishima. Photochromism induced in an electrolytically pretreated MoO_3 thin-film by visible-light. *Nature*, 355:624–626, 1992.

189. H. Tian and S. J. Yang. Recent progresses on diarylethene based photochromic switches. *Chemical Society Reviews*, 33:85–97, 2004.

190. J. Areephong, T. Kudernac, J. J. D. de Jong, G. T. Carroll, D. Pantorott, J. Hjelm, W. R. Browne, and B. L. Feringa. On/off photoswitching of the electropolymerizability of terthiophenes. *Journal of the American Chemical Society*, 130:12850, 2008.

191. A. Yassar, G. Horowitz, P. Valat, V. Wintgens, M. Hmyene, F. Deloffre, P. Srivastava, P. Lang, and F. Garnier. Exciton coupling effects in the absorption and photoluminescence of sexithiophene derivatives. *Journal of Physical Chemistry*, 99:9155–9159, 1995.

192. J. Gierschner, H. G. Mack, L. Luer, and D. Oelkrug. Fluorescence and absorption spectra of oligophenylenevinylenes: Vibronic coupling, band shapes, and solvatochromism. *Journal of Chemical Physics*, 116:8596–8609, 2002.

193. H. Chosrovian, S. Rentsch, D. Grebner, D. U. Dahm, and E. Birckner. Time-resolved fluorescence studies on thiophene oligomers in solution. *Synthetic Metals*, 60:23–26, 1993.

194. D. Oelkrug, H. J. Egelhaaf, J. Gierschner, and A. Tompert. Electronic deactivation in single chains, nano-aggregates and ultrathin films of conjugated oligomers. *Synthetic Metals*, 76:249–253, 1996.

195. J. Cornil, D. Beljonne, J. P. Calbert, and J. L. Bredas. Interchain interactions in organic pi-conjugated materials: Impact on electronic structure, optical response, and charge transport. *Advanced Materials*, 13:1053–1067, 2001.

196. G. Lanzani, G. Cerullo, S. Stagira, and S. De Silvestri. Excited state dynamics of oligothiophenes studied by transient pump-probe spectroscopy. *Jounal of Photochemistry and Photobiology A: Chemistry*, 144:13–19, 2001.

197. R. Colditz, D. Grebner, M. Helbig, and S. Rentsch. Theoretical studies and spectroscopic investigations of ground and excited electronic states of thiophene oligomers. *Chemical Physics*, 201:309–320, 1995.

198. V. Wintgens, P. Valat, and F. Garnier. Photochemical generation of radical cations from thiophene oligomers. *Journal of Physical Chemistry*, 98:228–232, 1994.

199. J. P. Yang, W. Paa, and S. Rentsch. Femtosecond investigations of photophysics of ultrafast intersystem crossing in terthiophene by wavelength dependent excitation. *Chemical Physics Letters*, 320:665–672, 2000.

200. D. V. Lap, D. Grebner, and S. Rentsch. Femtosecond time-resolved spectroscopic studies on thiophene oligomers. *Journal of Physical Chemistry A*, 101:107–112, 1997.

201. G. Lanzani, M. Nisoli, S. DeSilvestri, and R. Tubino. Femtosecond vibrational and torsional energy redistribution in photoexcited oligothiophenes. *Chemical Physics Letters*, 251:339–345, 1996.

202. M. T. W. Milder, J. L. Herek, J. Areephong, B. L. Feringa, and W. R. Browne. Tunable aggregation and luminescence of bis(diarylethene)-sexithiophenes. *Journal of Physical Chemistry A*, 113:7717–7724, 2009.

203. M Garavelli, CS Page, P Celani, M Olivucci, WE Schmid, SA Trushin, and W Fuss. Reaction path of a sub-200 fs photochemical electrocyclic reaction. *Journal of Physical Chemistry A*, 105:4458–4469, 2001.

204. J. Ern, A. T. Bens, A. Bock, H. D. Martin, and C. Kryschi. Femtosecond transient absorption studies on photochromism of dithienylethene derivates. *Journal of Luminescence*, 76-7:90–94, 1998.

205. F. M. Raymo and M. Tomasulo. Fluorescence modulation with photochromic switches. *Journal of Physical Chemistry A*, 109:7343–7352, 2005.

206. F. M. Raymo and M. Tomasulo. Electron and energy transfer modulation with photochromic switches. *Chemical Society Reviews*, 34:327–336, 2005.

207. Y.-C. Jeong, S. I. Yang, E. Kim, and K.-H. Ahn. Development of highly fluorescent photochromic material with high fatigue resistance. *Tetrahedron*, 62:5855–5861, 2006.

208. J.H. Hurenkamp. *Tuning energy transfer between chromophores.* PhD thesis Groningen University, 2008.

209. M. Mardelli and J. Olmsted. Calorimetric determination of the 9,10-diphenyl-anthracene fluorescence quantum yield. *Journal of Photochemistry*, 7:277–285, 1977.

210. S. A. Kovalenko, J. Ruthmann, and N. P. Ernsting. Ultrafast stokes shift and excited-state transient absorption of coumarin 153 in solution. *Chemical Physics Letters*, 271:40–50, 1997.

211. G. Jones II, W. R. Jackson, C. Y. Choi, and W. R. Bergmark. Solvent effects on emission yield and lifetime for coumarin laser dyes. Requirements for a rotatory decay mechanism. *Journal of Physical Chemistry*, 89:294–300, 1985.

212. M. L. Horng, J. A. Gardecki, A. Papazyan, and M. Maroncelli. Subpicosecond measurements of polar solvation dynamics-coumarin-153 revisited. *Journal of physical chemistry*, 99:17311–17337, 1995.

213. M. L. Horng, J. A. Gardecki, and M. Maroncelli. Rotational dynamics of coumarin 153: Time-dependent friction, dielectric friction, and other nonhydrodynamic effects. *Journal of Physical Chemistry A*, 101:1030–1047, 1997.

214. T. Gustavsson, L. Cassara, V. Gulbinas, G. Gurzadyan, J. C. Mialocq, S. Pommeret, M. Sorgius, and P. van der Meulen. Femtosecond spectroscopic study of relaxation processes of three amino-substituted coumarin dyes in methanol and dimethyl sulfoxide. *Journal of Physical Chemistry A*, 102:4229–4245, 1998.

215. F. Morlet-Savary, C. Ley, P. Jacques, and J. P. Fouassier. Photophysics of a bridged 7-diethylamino-4-methyl-coumarin C102: Studying the hydrogen bonding effect by time resolved stimulated emission. *Journal of Physical Chemistry A*, 105:11026–11033, 2001.

216. K. Ohta, T. J. Kang, K. Tominaga, and K. Yoshihara. Ultrafast relaxation processes from a higher excited electronic state of a dye molecule in solution: a femtosecond time-resolved fluorescence study. *Chemical Physics*, 242:103–114, 1999.

217. P. R. Hania, A. Pugzlys, L. N. Lucas, J. J. D. de Jong, B. L. Feringa, J. H. Van Esch, H. T. Jonkman, and K. Duppen. Ring closure dynamics of BTE-based photochromic switches: Perfluoro- versus perhydrocyclopentene derivatives. *Journal of Physical Chemistry A*, 109:9437–9442, 2005.

218. C. Devadoss, P. Bharathi, and J. S. Moore. Energy transfer in dendritic macromolecules: Molecular size effects and the role of an energy gradient. *Journal of the Americam Chemical Society*, 118:9635–9644, 1996.

219. V. S. Y. Lin, S. G. Dimagni, and M. J. Therien. Highly conjugated acetylenyl bridged porphyrins-new models for light-harvesting antenna systems. *Science*, 264:1105–1111, 1994.

220. B. Valeur, J. Pouget, J. Bourson, M. Kaschke, and N. P. Ernsting. Tuning of photoinduced energy-transfer in a bichromophoric coumarin supermolecule by cation binding. *Journal of Physical Chemistry*, 96:6545–6549, 1992.

221. J. M. Rehm, G. L. McLendon, Y. Nagasawa, K. Yoshihara, J. Moser, and M. Gratzel. Femtosecond electron-transfer dynamics at a sensitizing dye-semiconductor (TiO2) interface. *Journal of Physical Chemistry*, 100:9577–9578, 1996.

222. K. Hara, T. Sato, R. Katoh, A. Furube, Y. Ohga, A. Shinpo, S. Suga, K. Sayama, H. Sugihara, and H. Arakawa. Molecular design of coumarin dyes for efficient dye-sensitized solar cells. *Journal of Physical Chemistry B*, 107:597–606, 2003.

223. W. R. Dichtel, S. Hecht, and J. M. J. Frechet. Functionally layered dendrimers: A new building block and its application to the synthesis of multichromophoric light-harvesting systems. *Organic Letters*, 7:4451–4454, 2005.

224. R. Augulis, A. Pugzlys, J. H. Hurenkamp, B. L. Feringa, J. H. van Esch, and P. H. M. van Loosdrecht. Optical energy transport and interactions between the excitations in a coumarin-perylene bisimide dendrimer. *Journal of Physical Chemistry A*, 111:12944–12953, 2007.

225. J. M. Serin, D. W. Brousmiche, and J. M. J. Frechet. A FRET-based ultraviolet to near-infrared frequency converter. *Journal of the American Chemical Society*, 124:11848–11849, 2002.

226. F. Wurthner. Perylene bisimide dyes as versatile building blocks for functional supramolecular architectures. *Chemical Communications*, (18), 2004.

227. S. M. Melnikov, E. K. L. Yeow, H. Uji-i, M. Cotlet, K. Muellen, F. C. De Schryver, J. Enderlein, and J. Hofkens. Origin of simultaneous donor-acceptor emission in single molecules of peryleneimide-terrylenediimide labeled polyphenylene dendrimers. *Journal of physical chemistry B*, 111:708–719, 2007.

228. C. Flors, I. Oesterling, T. Schnitzler, E. Fron, G. Schweitzer, M. Sliwa, A. Herrmann, M. van der Auweraer, F. C. de Schryver, K. Muellen, and J. Hofkens. Energy and electron transfer in ethynylene bridged perylene diimide multichromophores. *Journal of physical chemistry C*, 111:4861–4870, 2007.

229. M. Cotlet, T. Vosch, S. Habuchi, T. Weil, K. Mullen, J. Hofkens, and F. De Schryver. Probing intramolecular forster resonance energy transfer in a naphthaleneimide-peryleneimide-terrylenediimide-based dendrimer by ensemble and single-molecule fluorescence spectroscopy. *Journal of the Americam Chemical Society*, 127:9760–9768, 2005.

230. C. R. Goldschmidt and M. Ottolenghi. Laser photolysis of perylene solutions. *Journal of Physical Chemistry*, 75:38943897, 1971.

231. C. Hippius, I. H. M. van Stokkum, E. Zangrando, R. M. Williams, and F. Wuerthner. Excited state interactions in calix[4]arene-perylene bisimide dye conjugates: Global and target analysis of supramolecular building blocks. *Journal of Physical Chemistry C*, 111:13988–13996, 2007.

232. N. Van Anh, F. Schlosser, M. M. Groeneveld, I. H. M Van Stokkum, F. Wuerthner, and R. M. Williams. Photoinduced interactions in a pyrene-calix[4]arene-perylene bisimide dye system: probing ground-state conformations with excited-state dynamics of charge separation and recombination. *Journal of Physical Chemistry C*, 113:18358–18368, 2009.

233. A. Sautter, B. K. Kaletas, D. G. Schmid, R. Dobrawa, M. Zimine, G. Jung, I. H. M. van Stokkum, L. De Cola, R. M. Williams, and F. Wurthner. Ultrafast energy-electron transfer cascade in a multichromophoric light-harvesting molecular square. *Journal of the American Chemical Society*, 127:6719–6729, 2005.

234. T. Kasajima, S. Akimoto, S. Sato, and I. Yamazaki. Vibrational energy relaxation of S-1 perylene in solution. *Journal of Physical Chemistry A*, 108:3268–3275, 2004.

235. T. Kiba, S. Sato, S. Akimoto, T. Kasajima, and I. Yamazaki. Solvent-assisted intramolecular vibrational energy redistribution of S-1 perylene in ketone solvents. *Journal of Photochemistry and Photobiology A-Chemistry*, 178:201–207, 2006.

236. Y. H. Meyer and P. Plaza. Ultrafast excited singlet-state absorption gain spectroscopy of perylene in solution. *Chemical Physics*, 200:235–243, 1995.

Summary

This thesis reports, using a variety of optical techniques, the energy transfer pathways in different potential building blocks for molecular electronic devices, namely an antenna, a molecular wire and fluorescent switches. Using pump-probe spectroscopy the time constants of these transfer processes were determined. In the future, the knowledge obtained by these studies can be used to design and build novel and/or improved molecular devices. Controlling energy transfer, as described in this thesis, will be a crucial design criterium when it comes to building a functional molecular device.

Today, many of the properties of digital electronic devices, such as speed and storage capacity, are ruled by Moore's law. This law predicts that the amount of transistors that can be placed on a chip roughly doubles every two years. For example, where a floppy disk back in the 1980's could only contain several hundreds of kilobytes of data, nowadays a memory stick easily fits up to gigabytes. However, the technology that is used to create the transistors runs into its fundamental limits and therefore it becomes more difficult to keep reducing their size. A completely different approach is to make similar transistors and other electronic elements using molecules as building blocks. Such molecular devices have the advantage that they are versatile, flexible and small as compared to the current materials used for fabricating chips. A large group of researchers is working on the development of electronics based on molecular building blocks. This development brings along many new challenges that require inventive solutions. One of these challenges is associated with the transport of energy, both as a carrier of information or to provide a means to perform work.

Since the term energy encompasses several concepts, its meaning in the context of this thesis should be defined first. A simple representation of the type of energy transfer described here is given by figure 1. Light consists of energy quanta, i.e. photons, that can be absorbed by molecules. Absorption in general only happens when photons are resonant with an optically active transition in the molecule. After absorption of a photon, the molecule is no longer in its ground state but has gained some energy and is in an excited state. This molecule will be referred to as the donor, since it has some excess energy that it can loose. When there are molecules in proximity that are still in the ground state, they can reach the excited state by accepting the energy of the donor. Hence, these molecules are called acceptors. It is this type of energy transfer that is the topic of the research outlined in this thesis. To allow for energy transfer molecular devices can be made that consist of donor and acceptor molecules. However, in designing these devices, there are several fundamental challenges that need to be overcome. One of them is that molecules that gain energy by absorption of a photon are usually very efficient in losing it. Relaxation to the

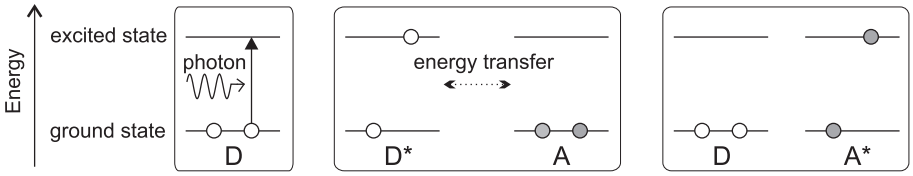

FIGURE 1. Absorption of a photon excites molecule D from the ground to the excited state. This increases the energy of the molecular system. When a second molecule A is in close proximity to molecule D, energy transfer can occur from D to A.

ground state can occur via emission of a photon or generation of heat. These two processes usually occur on a picosecond to nanosecond timescale (10^{-12}–10^{-9} s). To beat loss processes and therefore achieving energy transfer between donor and acceptor molecules certain design principles need to be followed in making a functional molecular device. Preferably, the donor and acceptor molecules are in proximity to one another as the energy transfer efficiency scales with the inverse distance between the molecules to the power six. This can be achieved in different ways. One possibility is to anchor the molecular building blocks to a surrounding structure as is shown in figure 2. Such a configuration often occurs in large biological molecules and serves as a funnel for the energy leading it into a desired direction. Furthermore, supramolecular structures can be formed by intermolecular forces driving aggregation. In these aggregates the molecules are often closely spaced allowing energy to hop between the different elements. A third option, that is synthetically the most difficult to achieve, is the connection of donor and acceptor molecules by a covalent bond as in figures 5 and 6.

A better understanding of why a certain design allows energy transfer from donor to acceptor and others do not, can be obtained by performing time resolved studies. To follow energy transfer between donor and acceptor molecules in real time, a fast probe is needed since the process is complete on a femtosecond to picosecond (10^{-15}– 10^{-12} second) timescale. While normal frame rates of cameras do not exceed several hundreds of Hz (0.01 s) for these experiments a probe is needed that is more than a billion times faster. Nowadays, ultrafast lasers produce flashes –pulses– of light, similar to a stroboscope but much shorter, that have a sufficiently short duration to follow energy transfer real time. Figure 3 shows diagrammatically the technique that was used to study energy transfer. The pump pulse excites molecules, after which a weak probe pulse is used to determine how long it takes before the energy is transferred from one molecule to the next. From start to finish stepwise 'images' of the energy transfer process are taken by the probe that, glued together, show the movement of the excitation through the system.

In this thesis studies of energy transfer in three different components that can act as building blocks for molecular electronic devices –antennas, wires and switches– are described. The antennas originate from green sulfur bacteria. These organisms are photosynthetic and use this complex antenna to gather as

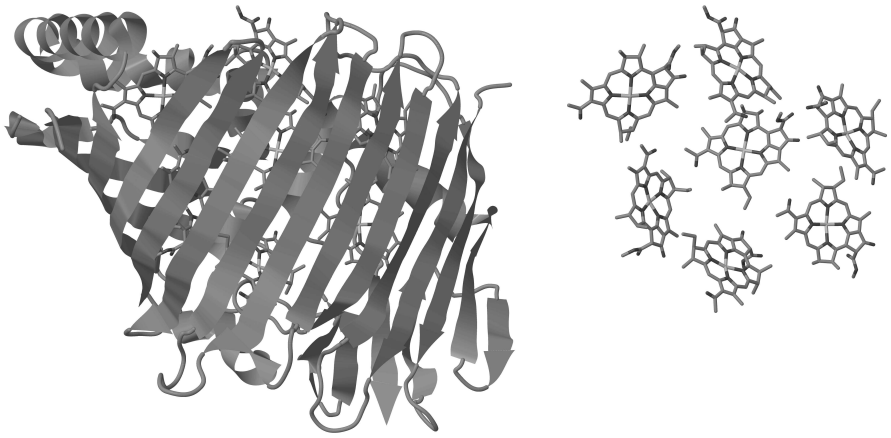

Figure 2. FMO antenna complex. [Left] Protein envelop anchoring seven bacteriochlorophyll a molecules. [Right] Spatial arrangement of the seven bacteriochlorophyll a molecules.

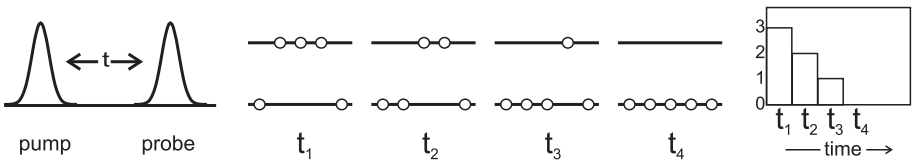

Figure 3. Schematic representation of the ultrafast pump probe technique. The probe records the state of the system at different times t, after the pump pulse has brought the system to the excited state. This results in a similar picture as sketched on the right, where the 'amount' of excited states is plotted against the time.

much light as possible and transfer it to the reaction center, where the light energy is converted to chemical energy. Secondly, small strands of thiophene polymer, connected to molecular switches, act as molecular wires. Interestingly, their behavior as individual molecules and as aggregates is completely different, as is their behavior in the open and closed form of the switch. Finally, the switches are used to turn on and off energy transfer in fluorescent molecules.

In chapter 5 we investigate how a complex molecular system deals with excess energy. This situation can be mimicked in our laboratory by choosing an excitation fluence that is sufficiently high to excite two or more bacteriochlorophyll a molecules (figure 2). The antenna complex can be damaged under these conditions. Therefore, it is important that a mechanism exists to release this excess energy quickly. One of the routes that is followed is the annihilation of excitation. When two excited molecules meet, one will take up the energy of

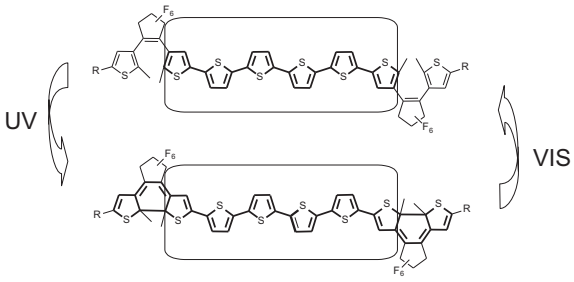

FIGURE 4. Thiophene based molecular wire. The wire, indicated by the box, is at both ends connected to molecular switches. Reversible ring closing and opening can be achieved by irradiation with light in the UV and the visible range of the spectrum.

both while the other is returned to the ground state. A combination of experiments and advanced simulations has shown that annihilation of excitation at high excitation powers occurs within 1.5 ps. The effect of the annihilation of excitation is local heating of the sample with time constants of 10 and 100 ps associated to this process. As a follow up, it was attempted to control and change the natural flow of energy through the antenna. By using a pulse shaper, a complicated phase function can be added to the initial flat phase of a transform limited pulse, to steer the system in a certain direction. By analyzing what kind of phase function is required to change the natural flow of energy, additional information on the excited states of the FMO complex and the dynamics within can be obtained. In an optimization experiment, the system was guided towards a chosen target in a closed learning loop employing an evolutionary algorithm. The goal of the optimization was to prolong the population of the states highest in energy beyond their natural lifetime. Preliminary experiments have been performed showing control of the excited states population. These experiments show that control experiments, possibly even in a coherent fashion using quantum interference effects of excited states, can be used to control the energy transfer pathway in a complex biomolecule.

Chapter 7 describes a series of measurements on switchable molecular wires (figure 4). In the open form of the switch, the wires show interesting temperature dependent behavior. Whereas at room temperature the wires are highly fluorescent and have a lifetime of 500 ps, the fluorescence intensity is greatly reduced upon decreasing the temperature. A combination of optical techniques showed that H-aggregates are formed at lower temperature. In the aggregates intermolecular energy transfer between different wires occurs on a 5 ps timescale and as a result the thiophene fluorescence is quenched. Independent of temperature, upon ring closing, the properties of the wire change dramatically and resemble those of the closed form of a molecular switch. Similar to the switch in the closed form, the wire has a very short lifetime of 5-6 ps and is no longer fluorescent. Hence, this molecular wire is a versatile component of which the properties can be changed reversibly either by changing the temperature or by irradiation.

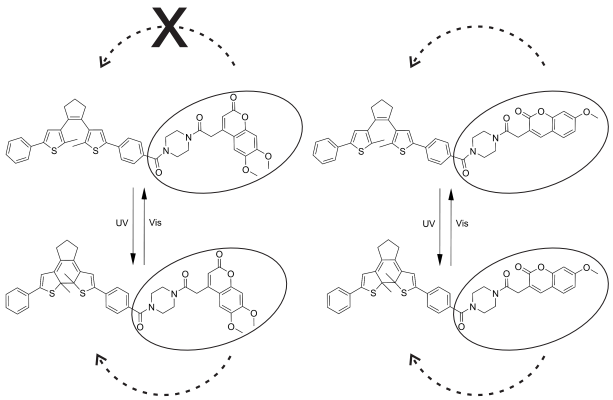

FIGURE 5. Molecular structures of the di-methoxy coumarin functionalized diphenyl switch (DMCS) in the open and closed form (left) and of the mono-methoxy coumarin functionalized diphenyl switch (MMCS) in the open and closed form (right). The coumarin units are pointed out by the solid lines drawn around them. Energy transfer is depicted by the dashed arrows.

In chapter 8, it was shown that two structurally very similar coumarins, covalently attached to a molecular switch, exhibit surprisingly different energy transfer behavior (figure 5). The monomethoxy-coumarin-switch showed energy transfer from the coumarin to the switch both in the ring open and closed form, resulting in a drastic decrease of fluorescence intensity compared to a model monomethoxy-coumarin. In stark contrast, the fluorescence of the dimethoxy-coumarin-switch is completely unquenched in the open form of the switch. Only upon ring closing does energy transfer to the switch occur, fully quenching the coumarin fluorescence. In most cases the design of these types of functional molecules is based on the Förster theory for energy transfer. However, in this chapter it was shown, that for donor-acceptor pairs, that are closely spaced, additional quantum mechanical effects should be taken into account to predict energy transfer pathways.

Finally, in chapter 9 the energy transfer pathways in molecular triads, consisting of two fluorophores connected to a molecular switch, are elucidated as shown in figure 6. A combination of conventional optical techniques such as steady state absorption and fluorescence spectroscopy are combined with time resolved experiments leading to the assignment of energy transfer pathways and the accompanying time constants. It was shown that energy transfer from coumarin and perylene to the closed switch occurs respectively on a 10 and 2 ps timescale.

The studies reported in this thesis have shown that it is not straightforward to design building blocks for molecular devices in which the energy is transferred in a desired direction. Nevertheless, the results described here contribute to a better understanding of the underlying principles on which in the future design of functional molecular devices can be based.

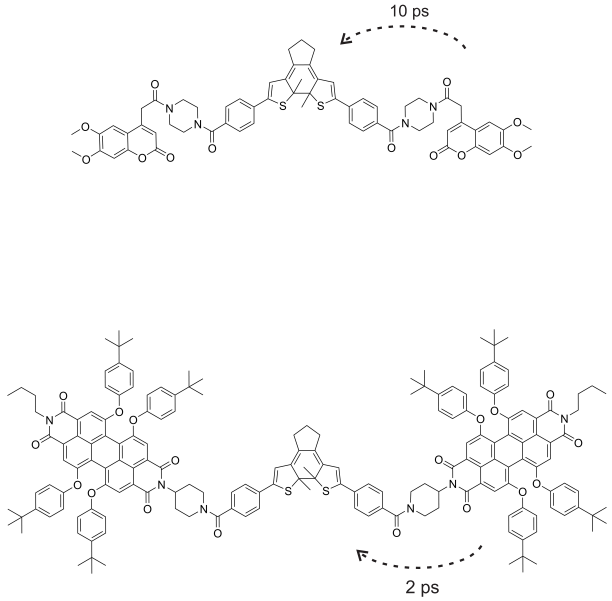

FIGURE 6. Molecular structures of two molecular triads: coumarin-switch-coumarin (top) and perylene-switch-perylene (bottom). The energy transfer pathways, depicted by the dashed arrows, and the energy transfer time constants are shown.

Samenvatting

In dit proefschrift hebben we met verschillende methoden laten zien hoe de energieoverdracht in verschillende bouwstenen voor moleculaire apparaten – een antenne, een moleculaire draad en fluorescentie schakelaars – plaatsvindt. Met behulp van een ultrasnelle tweepulstechniek kunnen we de tijdschaal van deze processen bepalen. De kennis opgedaan in deze experimenten op de bouwstenen kan worden gebruikt voor het ontwerpen van complete moleculaire apparaten. De snelheid en efficiëntie van energieoverdracht binnen de verschillende componenten, zoals in dit proefschrift is beschreven, zal hierbij een belangrijk criterium zijn.

Veel van de huidige eigenschappen van digitale elektronische apparaten zijn te herleiden naar de wet van Moore. Deze zegt ruwweg dat het aantal schakelingen op een chip elke twee jaar verdubbelt. Dit heeft grote gevolgen voor onder andere de opslagcapaciteit van gegevens. Ter vergelijking: waar een floppy in de jaren tachtig slechts enkele honderden kilobytes kon bevatten, past er nu standaard een aantal gigabyte data op een kleine geheugenstick. Het wordt echter steeds moeilijker om de apparatuur verder te verkleinen, omdat de fundamentele grenzen van de techniek waarmee de chips worden gemaakt in zicht komen. Een geheel nieuwe benadering om dit probleem te omzeilen is door elektronica niet langer te verkleinen door de huidige techniek te verbeteren, maar door gebruik te maken van onderdelen die van nature veel kleiner zijn. Een grote groep onderzoekers is bezig met het bouwen van microscopische apparatuur die uit moleculaire bouwstenen bestaat. Het werken met apparaten die slechts uit een aantal moleculen bestaan, brengt allerlei nieuwe uitdagingen met zich mee waarvoor oplossingen moeten worden gezocht. In dit proefschrift hebben we specifiek gekeken naar de energiehuishouding in de bouwstenen die samen een moleculair apparaat kunnen vormen.

Doordat moleculaire apparaten zo klein zijn, kunnen deze apparaten niet met een stekker aan het stopcontact verbonden worden of op een andere eenvoudige manier van energie voorzien worden. We moeten dus een andere manier ontwikkelen om energie in het systeem te brengen en door het systeem heen te laten lopen. Een simpele manier om dit te doen is door middel van absorptie van licht. Als een molecuul licht absorbeert, krijgt het meer energie. Het wordt als het ware een ladder opgeduwd naar een aangeslagen toestand, zoals schematisch is weergegeven in figuur 1. Na verloop van tijd raakt het molecuul die energie vanzelf weer kwijt, bijvoorbeeld door het geabsorbeerde licht weer uit te zenden (fluorescentie) en komt het weer terug in zijn grondtoestand. Voor moleculaire apparaten die uit meerdere bouwstenen bestaan, is het belangrijk dat de energie tussen de verschillende onderdelen wordt gedistribueerd, voordat het verloren gaat door uitzending van licht of door andere processen. In het algemeen wor-

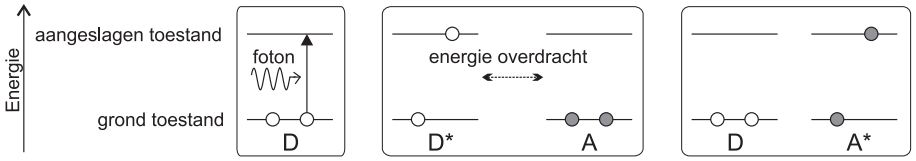

FIGUUR 1. Absorptie van licht (foton) brengt een elektron (weergegeven als balletje) in het donormolecuul naar een aangeslagen toestand (D*). Hierdoor neemt de energie in het molecuul toe. Als er een molecuul in de buurt is dat deze energie kan accepteren, kan de energie worden overgedragen, waardoor de acceptor in de aangeslagen toestand komt (A*). Bij dit proces blijven de elektronen op hetzelfde molecuul.

den bouwstenen die de energie afgeven aangeduid als donor (D) en bouwstenen die deze energie accepteren als acceptor (A). Deze bouwstenen kunnen zowel los van elkaar voorkomen als met elkaar verbonden zijn. Een voorbeeld van de energieoverdracht tussen donor- en acceptormoleculen is geschetst in figuur 1. Dit figuur laat zien dat energieoverdracht kan plaatsvinden van een aangeslagen donormolecuul naar een acceptormolecuul. Tijdens dit proces keert donor terug naar de grondtoestand en gaat de acceptor naar de aangeslagen toestand. Omdat een donormolecuul de energie binnen een nanoseconde (10^{-9} s, dat is een miljardste van een seconde) weer kwijt kan raken door uitzending van licht moet de energieoverdracht snel plaatsvinden. Aangezien de efficiëntie van energieoverdracht sterk afhankelijk is van de afstand tussen de donor en acceptor, betekent dit dat we moleculaire apparaten moeten ontwerpen waarbij de verschillende onderdelen heel dicht bij elkaar zitten of zelfs met elkaar verbonden zijn.

Om het proces van energieoverdracht in moleculaire bouwstenen te kunnen volgen moet er heel snel gekeken worden. Er is echter geen enkele conventionele techniek die snel genoeg is om dit vast te kunnen leggen. Voor het juiste perspectief, de opname snelheid van een digitale camera is ongeveer 25 beelden per seconde. Om energieoverdracht te kunnen volgen hebben we echter een methode nodig die bijna een miljard keer sneller is. In dit proefschrift maken we gebruik van een sequentie van twee ultrasnelle lichtpulsen (pomp en opname) afkomstig van een laser. De eerste puls slaat de moleculaire bouwstenen aan, vervolgens maakt de tweede puls als het ware de opname van het systeem, het 'ziet' hoeveel moleculen er nog aangeslagen zijn (figuur 2). Door nu de tijd tussen pomp en opname te variëren, kijken we, telkens een stukje later in de tijd, wat er met de energie, die we in de bouwsteen hebben gebracht, is gebeurd. Door al deze plaatjes achter elkaar te plakken krijgen we een goed en volledig beeld van het hele proces. Dit is te vergelijken met een stroboscoop waarmee in een disco telkens een klein stukje van de beweging van een persoon te zien is, maar dan veel sneller. Al die stukjes achter elkaar geven een goed beeld van de volledige beweging.

In dit proefschrift hebben we gekeken naar energieoverdracht binnen verschillende bouwstenen die nodig zijn om een moleculair apparaat te maken; een antenne een draad en een schakelaar. Van de laatste hebben we verschillende

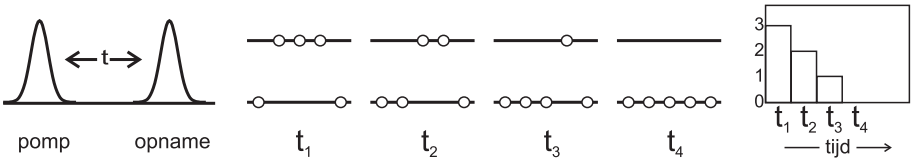

FIGUUR 2. Ultrasnelle twee puls techniek met een pomp en opname puls. Op verschillende tijdstippen t nadat de pomp puls het systeem heeft aangeslagen, wordt een opname gemaakt. Dit resulteert in een plaatje, uiterst rechts, waarbij de hoeveelheid aangeslagen toestanden uitgezet is tegen de tijd.

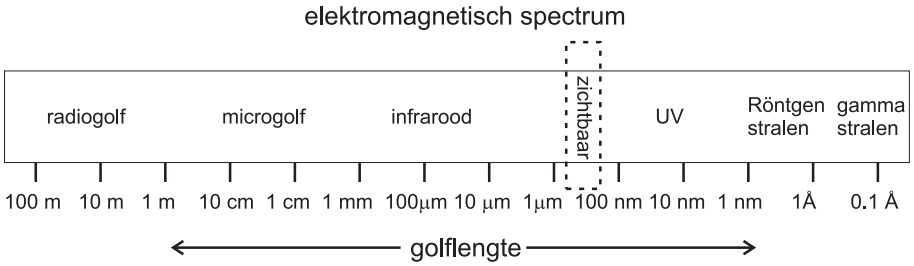

FIGUUR 3. Schematische weergave van het elektromagnetisch spectrum met de bijbehorende golflengten. Het spectrale gebied –zichtbaar– waar het FMO eiwit en de schakelaars licht absorberen is aangegeven met de stippellijn.

versies bestudeerd. Het eerste deel van dit proefschrift beschrijft energieoverdracht in een biologische bouwsteen die dient als antenne. Het FMO eiwit, genoemd naar de ontdekkers Fenna, Matthews en Olson, is afkomstig uit groene zwavelbacteriën en is er mede verantwoordelijk voor dat deze bacteriën licht als energiebron kunnen gebruiken om organisch materiaal te maken. Het FMO eiwit heeft de specifieke functie om zoveel mogelijk energie in de vorm van licht te vangen. In feite heeft dit molecuul dezelfde functie als een antenne die aan een radio zit, alleen worden nu geen radiogolven, maar golven in het zichtbare deel van het spectrum opgevangen (zie figuur 3). Het FMO eiwit is bijzonder vanwege de efficiëntie en de hoge snelheid waarmee de opgevangen energie doorgesluisd wordt naar een volgende bouwsteen, die vervolgens de energie zal vastleggen in de vorm van koolstofverbindingen. De energieoverdracht in dit eiwit is in het verleden al uitgebreid onderzocht met verschillende methoden zoals beschreven is in hoofdstuk 4. Een onderdeel dat bij deze studies is onderbelicht is welke processen optreden in een molecuul als er teveel licht wordt geabsorbeerd. In dit geval kan het voorkomen dat er twee moleculen bij elkaar in de buurt zijn die zich alletwee in de aangeslagen toestand bevinden. Dit overschot aan energie kan het eiwit beschadigen waardoor het niet meer functioneert, wat nadelige gevolgen heeft voor de bacterie. Daarom is het van belang dat er een mechanisme bestaat om snel het energieoverschot kwijt te raken. In hoofdstuk 5 hebben we beschreven hoe snel het energie overschot verdwijnt als

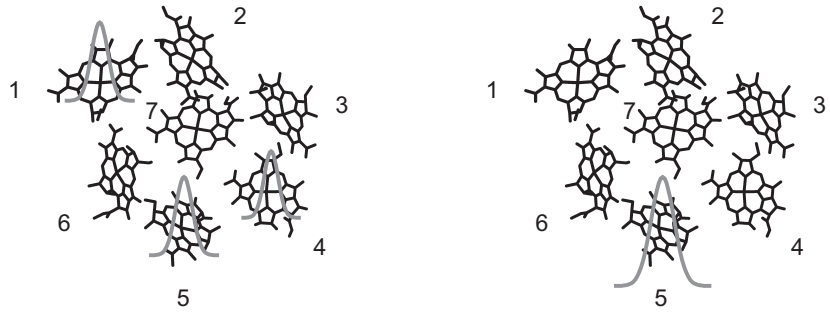

FIGUUR 4. Schematische weergave van de sturing van het energieoverdracht proces in het FMO eiwit. De energie is uitgebeeld met een grijze klokvorm. [Links] Na absorptie van een 'gewone' lichtpuls is de energie enigszins verspreid in het eiwit. [Rechts] Een speciale lichtpuls stuurt de energieoverdracht zodat de energie wordt gelokaliseerd.

er teveel licht op het FMO eiwit valt. Het blijkt uit een combinatie van experimenten en geavanceerde simulaties dat het overschot is weggewerkt binnen 1.5 picoseconde (10^{-12} seconde). Uit simulaties komt ook naar voren dat hierdoor de lokale omgeving van het eiwit langzaam wordt opgewarmd met tijdsconstanten van 10 en 100 picoseconden. Deze vorm van energie is niet schadelijk voor de bacterie. Om meer informatie over de verschillende aangeslagen toestanden van het FMO eiwit te krijgen hebben we geprobeerd de natuurlijke route van energieoverdracht te beïnvloeden. Door met de pomppuls te spelen, door er bijvoorbeeld een treintje van pulsen van te maken, kunnen we het molecuul een figuurlijk zetje geven en de energieoverdracht in een bepaalde richting sturen. De energie zal zich dan op een bepaalde tijd op een andere plek in het eiwit bevinden dan na absorptie van een 'gewone' lichtpuls. Dit is geïllustreerd in figuur 4. Dit experiment staat nog in de kinderschoenen, maar we hebben in hoofdstuk 5 aangetoond dat het mogelijk is om onder moeilijke experimentele condities deze hele snelle processen te sturen in complexe moleculen zoals eiwitten.

In het tweede deel van dit proefschrift wort een ander type bouwsteen voor een moleculair apparaat beschreven. De studies naar moleculaire schakelaars en de resultaten hiervan zijn beschreven in de hoofdstukken 7 tot en met 9. Schakelaars zijn moleculen die reversibel een chemische binding vormen of breken afhankelijk van de kleur van het licht waarmee ze bestraald worden (figuur 5). De open en gesloten vorm van deze schakelaars zijn beide stabiel en er kan een groot aantal keer heen en weer geschakeld worden, voordat er slijtage optreedt. De schakelaars kunnen verder gefunctionaliseerd worden door middel van zijgroepen. In hoofdstuk 7 wordt een schakelbare moleculaire draad beschreven. Deze draad bestaat uit zes thiofeenmoleculen met aan beide uiteinden een schakelaar (figuur 6). In de open vorm van de schakelaars vertoont deze draad interessante temperatuursafhankelijke fluorescentie: bij kamertem-

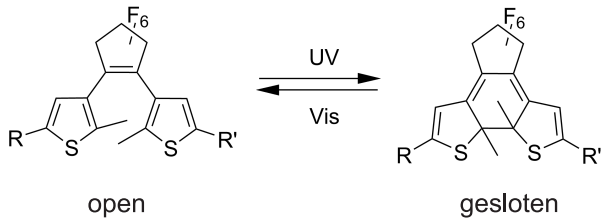

FIGUUR 5. De structuur van een moleculaire schakelaar. In de linker vorm is de ring in het centrum van het molecuul geopend. Als deze vorm met UV licht wordt bestraald, sluit de ring en heeft het molecuul de structuur rechts. Het molecuul kan worden heropend door middel van bestraling met zichtbaar licht. Aan de schakelaars kunnen verschillende zijgroepen gehangen worden, aangeduid met R and R'.

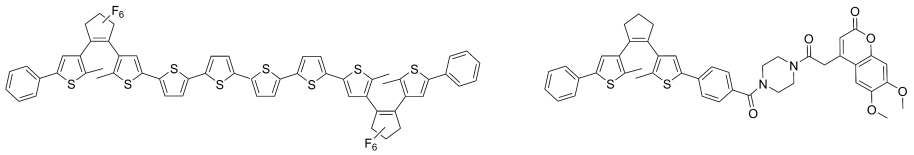

FIGUUR 6. De structuur van twee gefunctionaliseerde moleculaire schakelaars. [Links] De moleculaire draad bestaand uit zes thiofeen moleculen aan beide uiteinden gebonden aan een schakelaar. [Rechts] Een van de moleculaire schakelaars gebonden aan een fluorescent molecuul (coumarine).

peratuur zendt de draad de opgenomen energie efficiënt weer uit en is zeer fluorescent. Als de oplossing waarin de draden zich bevinden wordt afgekoeld neemt de intensiteit van de fluorescentie heel snel af. Zo'n steile afname van de intensiteit duidt op de vorming van een specifieke formatie van de draden waarbij de draden parallel aan elkaar 'geplakt' zitten. We hebben de energieoverdracht bij kamer- en lage temperatuur gemeten met de ultrasnelle twee puls techniek. Hieruit blijkt dat bij kamertemperatuur de draden het geabsorbeerde licht efficiënt weer uitzenden. Bij lage temperatuur, als de draden dicht bij elkaar zitten, is de energieoverdracht tussen de draden of naar foutjes in de formatie sneller dan het uitzenden van licht, waardoor de fluorescentie nauwelijks meer zichtbaar is. Een tweede bijzondere eigenschap van de moleculaire draad komt aan het licht als het gedrag in de open en gesloten vorm wordt vergeleken: in de open vorm is de draad zeer fluorescent, echter na bestraling met UV licht, wat leidt tot ringsluiting, is hier niets meer van over. Er is een nieuwe route bijgekomen om de energie snel af te voeren. We kunnen dus eenvoudigweg en reversibel kiezen voor een moleculaire draad die fluoresceert of niet. Wel of geen fluorescentie (aan en uit) kan vergeleken worden met de code (1 en 0) die gebruikt wordt in het geheugen van elektronica. Wellicht kunnen in de toekomst schakelbare fluorescente moleculen, die veel minder ruimte innemen dan de huidige techniek, gebruikt worden om gegevens op te slaan.

Het tweede soort schakelaars dat we bestudeerd hebben in de hoofdstukken 8 en 9 heeft een fluorescent molecuul (fluorofoor) als zijgroep (figuur 6 rechts). Als de schakelaar gesloten is, kan er energieoverdracht plaatsvinden van het fluorescente molecuul naar de schakelaar. De fluorescentie kan geheel worden uitgedoofd als de energieoverdracht van fluorofoor naar de schakelaar veel sneller is dan de uitzending van licht aangezien energie altijd via de snelste route een molecuul verlaat. Hoofdstuk 8 gaat dieper in op de principes die gehanteerd worden om fluorescente schakelaars te maken. Vaak worden deze moleculen ontworpen aan de hand van een aantal simpele vuistregels. In dit hoofdstuk laten we zien dat voor systemen waarbij de fluorofoor en de schakelaar (de donor en acceptor) zeer dicht bij elkaar of zelfs aan elkaar zitten deze regels niet altijd opgaan. Het blijkt dat ook rekening gehouden moet worden met extra kwantum mechanische effecten om energieoverdracht te voorspellen. In hoofdstuk 9 worden schakelaars met twee dezelfde of twee verschillende fluoroforen beschreven. In deze systemen zijn er verschillende routes voor energieoverdracht: tussen de fluoroforen en van de fluoroforen naar de schakelaar. We hebben ontdekt dat dit laatste proces heel snel is en afhankelijk van de fluorofoor binnen enkele picoseconden plaatsvindt. Dit betekent ook dat we de fluorescentie van de fluoroforen in deze system gecontroleerd kunnen uitdoven.

Het is niet eenvoudig om moleculaire apparaten te ontwerpen waarin de energie gecontroleerd tussen de verschillende componenten gedistribueerd wordt. Het onderzoek beschreven in dit proefschrift draagt bij aan een beter begrip over de verschillende routes die gebruikt kunnen worden om de energieoverdracht tussen de componenten te sturen.

Dankwoord

Promoveren is een groot avontuur dat vier jaar duurt. Grote stukken hiervan leg je alleen af, maar altijd kom je weer nieuwe, interessante mensen tegen die een stuk met je meereizen. Een persoon is er van begin tot eind bij geweest en heeft richting aan mijn onderzoek gegeven en heeft waar nodig bijgestuurd en moed ingesproken. Dear Jennifer, thank you for hiring me when I arrived on the AMOLF doorstep in 2000 and for having the confidence in me that I could succeed staying behind in Amsterdam. If ever I need moral support for whatever reason I know whom to turn to. It is truly inspirational to see what you have achieved with your group at the University of Twente in such a short period of time. Nog twee mensen zijn van groot belang geweest tijdens mijn promotie. Beste Mischa, ik heb je weinig artikelen opgeleverd, maar de rol die jouw groep voor mij gespeeld heeft in de afgelopen vier jaar is onvergetelijk. Bedankt dat je me onder je vleugels hebt genomen, het heeft enorm bijgedragen aan een mooie tijd op AMOLF. Special thanks should be addressed to Wesley, who jumped in when my original project did not work out the way we wanted it to and produced an endless supply of amazing molecules whose behavior needed to be unraveled. Besides being a good friend, you turned out to be a perfect mentor. I will always remember with fondness the heated discussions we had over some of our data and papers. Meeting someone who can be as stubborn as I am and as willing to persevere is an invigorating experience.

The first part of this thesis could not have been written without the help of Mette Miller from the University of Southern Denmark in Odense. I had a great time learning how to purify the FMO protein in your lab and returned with enough protein for another couple of years worth of experiments. Dear Ben, your contributions to my thesis work are truly invaluable. Together we managed to write the most extensive review about the FMO protein to date and with your simulations we will also add to the existing literature on this topic.

De moleculaire schakelaars uit het tweede deel van dit proefschrift zijn gesynthetiseerd door twee organisch chemici wiens magie met moleculen ik nooit zal evenaren. Dear Jetsuda, on a couple of occasions I had the pleasure of sharing your fumehood. Where I was merely preparing some samples for measurements, right beside me you were working your magic. I wish you all the best in Geneva and you should expect a visit from me when you become a professor in Thailand. Beste Joost, de laatste twee hoofdstukken van mijn proefschrift zijn grotendeels aan jou toe te schrijven. Wat een wonderlijke moleculen heb jij geproduceerd. Op dit moment begrijpen we nog steeds niet helemaal hoe ze werken, maar hopelijk hebben we deze raadsels opgelost en omgezet in een aantal mooie publicaties bij het ter perse gaan van dit proefschrift.

Dear members of the biomolecular control group I could not have done this without you. Riccardo, without your teaching skills I would have never grown to become a proper scientist. Niels, ook jouw programmeer kennis heeft mij enorm geholpen, ik hoop dat je een mooie carrière als marinier tegemoet gaat. Janne, thanks for showing me how it is done, being the first PhD student to graduate under Jennifer's supervision. Peter, vaak was ik de trap naar mijn kantoor nog niet eens af of je had mijn matlab probleem al opgelost. Bedankt voor alle hulp binnen en buiten het lab en de solidariteit tijdens de afgelopen jaren. Dear members of the Optical Sciences group, you have made my stays in Enschede very pleasant. I wish you all the best with your research.

Dear members of the BaBo groups, over the years I have seen many of you come and go. It has been a pleasure to reside in your midst during the past four years. I have made many new friends and have enjoyed all the scientific and non-science related discussions and outings. Furthermore, I would like to thank all the other AMOLF residents that have made my PhD very agreeable during, but also after, working hours. I am glad I could share some of my hobbies with you. With the risk of forgetting events worth mentioning I hold warm memories to: the Romania group outing, the many dinners (especially Indian), movie nights, Thirsty Thursdays, organizing and taking part in PV activities, Sinterklaas parties, concerts and dancing and listening to music from all over the world.

Ruim een jaar geleden heb ik mij aangemeld als lid van de ondernemingsraad van AMOLF en heb ik ook zitting genomen in de centrale ondernemingsraad van FOM. Dit is voor mij een zeer leerzame en tegelijkertijd erg leuke ervaring geweest, waarvoor ik mijn dank uit wil spreken aan al mijn medeleden.

Beste lichting'96, alle feestjes, uitjes, housewarmings en skivakanties hebben het leven bijzonder aangenaam gemaakt de afgelopen jaren. Velen van jullie hebben al laten zien hoe promoveren in zijn werk gaat. Ik hoop dan ook dat jullie er bij zullen zijn, om zelf te kunnen aanschouwen dat ik goed op heb gelet tijdens jullie ceremonies. Beste Hester, Jan Pieter, Johan, Maaike, Marinda en aanhang, wie had dat gedacht, dat we bijna tien jaar na het binnenstappen van Nijenborgh 4 nog steeds bij elkaar over de vloer komen. Ondanks dat we allemaal over de wereld zijn uitgewaaierd, hoop ik dat onze vriendschappen standhouden.

Lieve familie, ik hoop dat jullie nu een beter beeld hebben van wat ik de afgelopen vier jaar heb uitgevoerd. Bedankt voor alle steun en toeverlaat, jullie zijn het einde!